

Sheffield Hallam University

Light scattering models for real-time bacteria characterisation in water based environments.

CHLIVEROS, Georgios.

Available from the Sheffield Hallam University Research Archive (SHURA) at:

<http://shura.shu.ac.uk/19461/>

A Sheffield Hallam University thesis

This thesis is protected by copyright which belongs to the author.

The content must not be changed in any way or sold commercially in any format or medium without the formal permission of the author.

When referring to this work, full bibliographic details including the author, title, awarding institution and date of the thesis must be given.

Please visit <http://shura.shu.ac.uk/19461/> and <http://shura.shu.ac.uk/information.html> for further details about copyright and re-use permissions.

300 ... STREET,
SHEPHERD, 01 142.



2076

Fin:

REFERENCE

ProQuest Number: 10694342

All rights reserved

INFORMATION TO ALL USERS

The quality of this reproduction is dependent upon the quality of the copy submitted.

In the unlikely event that the author did not send a complete manuscript and there are missing pages, these will be noted. Also, if material had to be removed, a note will indicate the deletion.



ProQuest 10694342

Published by ProQuest LLC (2017). Copyright of the Dissertation is held by the Author.

All rights reserved.

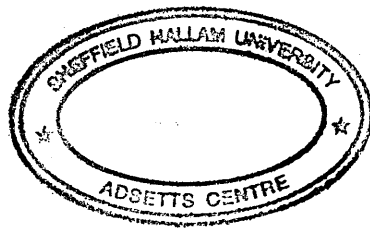
This work is protected against unauthorized copying under Title 17, United States Code
Microform Edition © ProQuest LLC.

ProQuest LLC.
789 East Eisenhower Parkway
P.O. Box 1346
Ann Arbor, MI 48106 – 1346

**Light Scattering Models for Real-Time Bacteria Characterisation in
Water based Environments**

Georgios Chliveros

A thesis submitted in partial fulfilment of the requirements of
Sheffield Hallam University
for the degree of Doctor of Philosophy



Submitted: 14 January 2005

Sheffield Hallam University
Materials & Engineering Research Institute

The undersigned hereby certify that they have read and recommend to the Faculty of Arts, Computing, Engineering and Sciences for acceptance a thesis entitled "**Light Scattering Models for Real-Time Bacteria Characterisation in Water based Environments**" by **Georgios Chliveros** in partial fulfillment of the requirements for the degree of **Doctor of Philosophy**.

Dated: Submitted: 14 January 2005

Research Supervisors: _____
Professor M. A. Rodrigues

Dr D. Cooper

Examining Committee: _____
Dr A. Augousti, Kingston University

Dr D. Cleaver, Sheffield Hallam University

*Dedicated to my parents, Evagelia and Konstantinos,
for providing me with the opportunities they did not have.*

Contents

List of Tables	viii
List of Figures	ix
Abstract	xvi
Acknowledgements	xvii
List of Publications	xviii
1 Introduction	1
2 A review of light scattering: functions, patterns and bacterial cells	7
2.1 Introduction	8
2.2 Bacterial cells: morphology and relation to optical properties	9
2.3 Candidates for drinking water abstraction: Bacterial Ecosystem	17
2.4 Application of Light Scattering theory to biological cells	22
2.5 Mie scattering and the Rayleigh-Debye approximation	29
2.6 On equipment based on light scattering	33
2.7 Discussion	35
3 On inhomogeneous particles of spherical symmetry	37
3.1 Introduction	38
3.2 The exact solution of the n -layer problem	42
3.3 Approximate solution for near-index particles	50
3.4 Evaluation of the approximation model	67
3.5 Validation and applicability limits of the approximation model	72
3.6 Conclusions	77

4	The generalised ellipsoidal Rayleigh-Debye approximation	79
4.1	Introduction	80
4.2	Approximate solutions on near-index ellipsoidal geometries	81
4.3	Geometrical properties and the n -layer approximation	90
4.4	Evaluation of the ellipsoidal approximation model	98
4.5	Theoretical considerations and problems	107
4.6	Conclusions	108
5	On the violation of the independent scattering condition	110
5.1	Introduction	111
5.2	A stochastic algorithm for multi-particle simulation	111
5.3	A procedure for calculating the intensity profile	119
5.4	Conclusion	126
6	Conclusions and further development	128
6.1	Conclusions	129
6.2	Further development	133
	References	136
A	MATLAB Implementation of the n-layer Mie scattering problem	146
A.1	Comments on functions	147
A.2	Generating Functions	148
	A.2.1 The functions RB1 and RB2	148
	A.2.2 The function ALegendr	149
A.3	Main Routines	149
	A.3.1 The function nLayerAmp	149
	A.3.2 The function nlayerScaCoeff	151
A.4	End Result Functions	154
	A.4.1 The Function nlayerIntensity	154
	A.4.2 The Function nlayerEfficiencies	155
	A.4.3 The Function DegreeOfPolarisation	155
A.5	General Comments	156
A.6	Calculation of Scattered Intensity	157
A.7	Calculation and Plots for Degree of Polarisation	159

B	Matlab implementation of a 2-layer model	161
B.1	Impementation of Wyatt's Rayleigh-Debye model	161
C	Matlab Implementation of n-layer generalised Rayleigh-Debye models	163
C.1	Implementation of the n -layer spherical model	163
C.1.1	Finding the coefficients for the Scattering Functions	163
C.1.2	The scattering amplitude function	164
C.1.3	Calculation of the Intensity	165
C.1.4	Calculating the Relative Difference: generalised mRDG versus Mie exact solution	165
C.2	Implementation of the n -layer ellipsoidal model	167
C.2.1	The Assymmetric Size Distribution	167
C.2.2	Input estimation functions	169
C.2.3	Calculation of Scattering Amplitude and Intensity	170
D	Matlab Implementation of Monte Carlo	172
D.1	Description of the MC algorithm and initial parameters	172
D.2	Matlab code for generation of positions in 3D space	175
E	Realisation of Experimental Setup	183

List of Tables

2.1	EU directive 79/869/EEC: Only the bacteriological content for examination from possible sources of potable samples is shown. The sample container's material is required to be sterilized glass. Salmonella numbers indicate the necessity for absence per 1000ml. The remainder as indicated is taken from recent additions as per [1, 2], the <i>Central Disease Control</i> , USA security code.	21
2.2	Literature Summary for values of optical properties derived from light scattering	30
4.1	An example for calculating the values for orientation angle β depending on θ and for $\alpha = \pi/4$, $\phi = \pi/3$	92

List of Figures

2.1	A commonly used configuration for multi angle light scattering measurements. The detectors and laser source are placed on the horizontal plane so as to cover the range for $\theta \in (0, \pi)$. Note that the laser source is coplanar with the array of detectors.	8
2.2	A classification system based on the Gram reaction of the cell; that is to say the behaviour, structure of the cell wall	10
2.3	A Gram (+) cell wall: Chemical composition. Notice that the <i>capsule</i> layer only appears if condensed polymers form; this is an indication of virulence.	11
2.4	Most common bacterial cells in relation to their external morphology. Corresponding microscopic images are also provided: Reprinted with permission from Dr D. Kunkel (Dennis Kunkel Microscopy ©)	13
2.5	Schematic of the true structure of the prokaryotic cell. Note that features are not shown to scale and have been emphasised to illustrate the multi-layered structure.	14
2.6	The electron microscopy image of cross section of the <i>Bacillus subtilis</i> endospore (right). A typical model that appears in most textbooks of microbiology to explain its structure can be seen on the left. Note phase light and phase dark regions of the microscopy image and the clear relationship with the diagrammatic illustration as shown here.	16
2.7	A freshwater lake eco-system and the distribution of bacteria on the layers. Waters above the thermocline layer (indicated by the arrow) constitute the <i>epilimnion</i> and below the said layer is the <i>hypolimnion</i>	20

2.8	Light scattering theoretical models and applicability. Note that Mie scattering would potentially solve most problems involving small particles provided that a rigorous solution could be obtained. On the diagram, (GO): Geometrical Optics and (AD): Anomalous Diffraction. We use GO and AD as examples of approximations that would be applied for particles having a largest dimension $d > 40\mu\text{m}$; for spheres this would be the radius for other external morphologies this would mean the major axis. By x we denote the size parameter defined by $x = 2k_0d$, where d is the scatterer's largest linear dimension.	22
2.9	Diagrammatic depiction of the cross section of a 2-layered spherical model. The outer layer is placed at distance r_2 from the centre and has a thickness $\Delta r = r_2 - r_1$ within which a relative index of refraction m_2 is assumed; the inner core has a radius r_1 and relative refractive index m_1	28
3.1	An n-layered concentric sphere: $i = 1, 2, \dots, n, \dots, N$	43
3.2	A 2-layer sphere intensity pattern, following the results for <i>B.sphaericus</i> spores at $\lambda = 0.514\mu\text{m}$ [3]. Left: Light Intensity Pattern; Right: Polar plot at $\theta \in (0, 180^\circ)$	47
3.3	Light Intensity Patterns of 2 to 5 layer particles at multi-angle and variable wavelength	48
3.4	Scattering Geometry for the modified Rayleigh-Debye approximation . .	50
3.5	Depiction of the Scattering Plane in two dimensions: diffraction occurs at direction \mathbf{k}_s , with respect to the incident field of direction \mathbf{k}_i . The angle between scattering and incidence is denoted by Θ . Far-field assumptions satisfied if observation plane P is placed at distance much greater than the dimension of scatterer.	51
3.6	A scattering particle of arbitrary shape with volume V_o , finite size. The infinitesimal volume dV_j is also indicated	52
3.7	Relationship between \mathbf{k}_i , \mathbf{k}_s and \mathbf{k}_d	56
3.8	Following Fig.3.5 for infinitesimal volumes dV , indicating projections of \mathbf{r} on corresponding vector wave paths	57

3.9	Behaviour of the solution for the n -th layer, using Bessel functions of order $3/2$. The scattering amplitude of the function (E_s) for the n -th layer, is indicated on the z -axis at all detection points (Θ) and increments of radius $r_n \in [0, 4]\mu\text{m}$. The relative refractive index value for the n -th layer is $m_n = 1.12$. The contour of the 3D plot is drawn on the xy plane (Θ, r_n).	63
3.10	A diagrammatic expression of the physical meaning of generalised n -layer Rayleigh-Debye spherical approximation. Note the similarities of this depiction with other disciplines, for example telecommunications engineering, from which the notation has been adopted.	65
3.11	Illustrating patterns of angular dependence for 2-layer equivalent models of spherical bacteria: From top to bottom: the generalised Rayleigh-Debye approximation, the exact Mie theory and the Rayleigh-Debye approximation. Note that the number of minima of the generalised mRDG appears to resemble the Mie solution more closely than the Rayleigh-Debye model scattering pattern.	68
3.12	A comparison between 2-layer equivalent models on backscattering ($\Theta \in (\pi/2, \pi)$): the Rayleigh-Debye approximation (dotted line), the exact Mie theory (solid line) and the generalised mRDG approximation (dashed line). Note that the last minimum in the curve of the generalised mRDG is closer to Mie model than the Rayleigh-Debye prediction (illustrated in the figure via projection of dotted line on the axis of Θ).	69
3.13	A two layer model from the exact solution indicated by the solid line and from the mRDG indicated by the dotted line. The core is assumed to be of radius $1\mu\text{m}$ and corresponding relative refractive index 1.1 whilst the outer layer has radius $1.1\mu\text{m}$ and corresponding relative refractive index 1.3	70
3.14	Resulting scattering patterns of angular dependence for the generalised Rayleigh-Debye approximation. The solid line depicts the result for 2 layers, the dotted line represents results for 4 layers and the dashed line corresponds to 5 layers.	71
3.15	$n = 2$. Relative difference mapping between generalised RDG and Mie scattering for a two layer spherical model with corresponding point histogram.	74

3.16	Relative difference mapping between generalised RDG and Mie scattering for a 6 layer spherical model. Both the result for indexed and its mapping to sorted values of (r, m) are indicated	75
3.17	From Left to Right relative difference maps between generalised Rayleigh-Debye and Mie scattering for: 3-layers hence $n = 3$ and 5-layers hence $n = 5$. At the top we have the indexed relative difference mapping and at the bottom the corresponding averaged sorted indexed values.	76
4.1	Illustration of integrating by taking cross sections of the solid found by planes perpendicular to the line of the bisectrix. The cross section shown here in detail has an area A and infinitesimal thickness dp , where p is the projection of the positioning vector r on the bisectrix. Note a change in the assumption of incidence; the incident direction denoted by k_i is parallel to the z axis of a global coordinate system, and the scattering angle is the polar angle θ , and as a result, linking this to Chapter 3, $\theta = \Theta$.	84
4.2	Cross section of the n -layered ellipsoid. Note that the $n - 1$ layer is at distance ϱ_{n-1} from the centre of the ellipsoid; whilst the n -th layer area is placed between ϱ_{n-1} and ϱ_n with relative refractive index m_n	87
4.3	A diagrammatic illustration of the generalised n -layer Rayleigh-Debye ellipsoidal approximation as a graph network. Once again we use the formalism of notation from other engineering principles. The node denoted by \odot means the $i - 1$ value with respect to the array of values and for the largest linear dimension only.	89
4.4	Spherical triangle showing the position of the major axis of the ellipsoid (v) with respect to the directions of incidence (i) and scattering (s). The bisectrix has the direction (p).	91
4.5	On the example for calculating values for orientation angle. A non-linear relationship between the cosines of $\beta, (\theta/2)$ is revealed in the plot between the cosines (bottom). The plot situated on the top of this figure, clearly illustrates the lag between the cosines and for values of $\theta \in (0, 2\pi)$. We have used the values of the example of Table 4.1, that is $\alpha = 45^\circ \equiv \pi/4$ and $\phi = 60^\circ \equiv \pi/3$	93

4.6	Scattered intensity from an ellipsoid with different source radiation at incidences of $\alpha = [0, \pi/4, 7\pi/4]$ resulting in the plots indicated from top to bottom respectively, with the equivalent polar plots on the right. For the cell it is assumed a 3-layered structure with relative refractive index array of values $m_i = [1.04 \ 1.1 \ 1.01]$ and array of values for the distances from the centre of the cell $\rho_i = [0.88 \ 1.045 \ 1.1]$	95
4.7	The 3D scattering patterns from three distinct cases of 3-layer prolate spheroids: The prolate spheroid type I, where the axial ratio is such that $t = 1.4$; the prolate spheroid type II, where $t = 2.8$; and a prolate spheroid type III, where $t = 14$. Note that the angle of incidence is constant at $\alpha = 90^\circ$. The volume of all spheroids is $1.1\mu\text{m}^3$ whilst the values for relative refractive index equal those of the example in Figure 4.6.	97
4.8	An ensemble of N_o particles within a volume ΔV that is within the ‘cone of reception’ of detector. The detector in this depiction is assumed within the solid angle formed by its cone of reception as cast in the total volume V_t	99
4.9	Size distributions with $\kappa_{\text{left}} + \kappa_{\text{right}} = 0.30$. The solid line curve depicts the symmetrical size distribution, $\kappa_{\text{left}} = \kappa_{\text{right}}$. The dashed line curve depicts an asymmetric size distribution with negative skewness, $\kappa_{\text{left}} = 0.2$, $\kappa_{\text{right}} = 0.1$. The dotted line curve depicts an asymmetric size distribution with positive skewness, $\kappa_{\text{left}} = 0.1$, $\kappa_{\text{right}} = 0.2$	103
4.10	The angular dependence of the scattering ratio for an n-layer ellipsoid. Top: n=3, a three layer ellipsoid model with different axial ratios (dashed line: $t < 1$, solid line: $t = 1$, dotted line: $t > 1$). Middle: n=4, a four layer ellipsoid model with different axial ratios. Bottom: n=6, a six layer ellipsoid model with different axial ratios.	105
4.11	Isolating prominent peaks from the simulation results of Figure 4.10. The cutoff point for selection of a peak is set at 2 arbitrary units. The three layered particles’ ensemble peaks are denoted by 50% grey-scale, the four layered ensemble by 25% grey-scale and finally the six layered ensemble by 75% greyscale.	106

5.1	Absolute global coordinate system and Scattering local coordinate system. For i scattering events to take place with m being the last one. Note that incident radiation or photons with direction k_i , coincide with direction of the Z axis of the global coordinates system whilst the last scattering event follows the direction k_{N_o} at polar angles θ_{N_o}, ϕ_{N_o} of the local coordinate system.	113
5.2	Calculating the separation $d_{j,j+1}$ between a successive pair of ellipsoids placed at points $O_j(X_j, Y_j, Z_j)$ and $O_{j+1}(X_{j+1}, Y_{j+1}, Z_{j+1})$, enclosed within spherical boundaries of corresponding radii R_j and R_{j+1} . The radii correspond to the largest linear dimension of the ellipsoids.	115
5.3	Assuming an ensemble of 40 scattering particles with maximum separation 0.25 mm. Note that we have assumed prolate spheroids where $c = s$ and $a = b = ts$, with the axial ratio t being a real number uniformly distributed in the range (0.1, 12). The sizes s for the spheroids in the illustrations at the bottom, have been overemphasized by a factor 10 so as to be visible. We illustrate for different orientation randomly selected, for the 40 scattering particles.	117
5.4	An ensemble of 50 scattering particles with maximum separation 0.25 mm. The point cloud is indicated at the top whilst the Pair Occurrence distribution function of d/\mathcal{L} is provided at the bottom.	118
5.5	Pair Occurrence distribution function of d/\mathcal{L} for an ensemble of 100 scattering particles. Note that in contrast to the function with 50 particles (Figure 5.4) it tends towards resembling an exponentially decreasing function.	119
5.6	Results for the normalised scattered intensity profile as a continuous function approximated from discrete scattering exit events. We have assumed 10^9 injected photons and spheroidal geometry for the bacterial cells. We illustrate results for $N_o = 5 \times 10^8$ at the top and $N_o = 50 \times 10^8$ at the bottom. The ensemble has particles of the same number (n) of layers internal structure; namely $n = 2, 3, 4, 5$ and $n = 10$ indicated by successive lines from solid to increased dotted lines.	125
A.1	Structure of interaction between the Matlab functions: Generating Functions \rightarrow Main Routines \rightarrow Resulting Functions	147
A.2	Example of a 2-layer Mie scattering model for unpolarised incidence. . .	158

A.3	A 2-layer Mie scattering model for unpolarised incidence but with a denser cell wall.	159
A.4	For a 2-layer Mie scattering model: (Left) The scattered intensity's degree of polarisation; (Right) he scattered intensity's polarisation ratio for 2-layer Mie scattering model.	160
D.1	Positions and ellipsoidal particles generated by the Metropolis MC algorithm. There are 400 particles with maximum acceptance rate set at 60%.	174

Abstract

Bacteria can be said to be small particles in terms of their volume and can be modelled as near-index particles when the average refractive index of their body is close to that of the medium in which they are suspended. This is the case with water based environments whereas the bacterial scatterer is said to be a ‘soft particle’ and within the Rayleigh-Debye experimental bounds of applicability. However, discrepancies in the past have illustrated insufficiency of geometric assumptions, such as spherical symmetry and simplistic internal structures, as well as the assumption of ‘transparency’ of the particle.

The aim of this work is to generalize the Rayleigh-Debye approximation in order to apply them to a wider class of not necessarily soft scatterers, hence departing from $|m - 1| \ll 1$ to $|m - 1| < 1$. We start by establishing a connection between the assumption on the functional expression of the internal field of small particles and that of the function of refractive index, to a *generalisation for arbitrary number of layers* within a *particle* of spherical symmetry. Based on the modification of the Rayleigh-Debye approximation (mRDG) with Bessel functions we proceed to formulate an extended version of the *arbitrary layers particle* for ellipsoidal forms. An application of this *n-layer generalised mRDG* to the bacterial domain optical properties via simulation, re-establishes the limits of the Rayleigh-Debye approximation as a result of the internal field modification.

Finally, we consider the problem of populations of cells modelled as multilayered geometrical structure, consistent with assumptions from bacteriology concerning size distributions and their relationship to statistical frequency functions. The latter problem is examined both when the independent scattering condition is satisfied and when it is violated, leading to increased probability of multiple scattering. Examination of ensembles of inhomogeneous particles was possible due to our generalised approximation which is essentially acting on any infinitesimal volume, within the boundaries of the said layered structured particles, and is the main result of this work. The mathematical treatment presented within this thesis acts as an extension of the known near-index techniques in the theory of scattering for unlimited number of layers and internal distributions of refractive index.

Acknowledgements

I would like to thank professor M.A. Rodrigues, my director of studies, for providing me with the opportunity to engage into research and his constant support during my studies. I am also thankful to Dr D. Cooper, my supervisor, and Dr J. Mills, research advisor, for their guidance through the early months of chaos and confusion. To Ms L. Harrison, A. Cooper and Jo Laughton, of 'ACES' administration, goes my outmost respect for having the patience to continuously offer their help and advice. The same applies for Mr Ian Morrey, 'ACES' research tutor, for his continuous efforts to establish and promote a research culture.

This research would have not been possible if it was not for Dr Lyuba Alboul's crucial comments, Dr Jacques Penders' advice and the numerous discussions I had with Dr Alan Robinson. I am grateful to my past tutors, professor H. Rowlands (University of Wales) and Dr P. White (University of the West of England) for they shaped my academic ability and encouraged me to undertake this research programme.

I should acknowledge Dr Dennis Kunkel (Kunkel Microscopy), for providing high-definition microscopy images and Dr Z. Ulanowski (University of Hertfordshire) for sharing his views on light scattering theory and related issues. I should also acknowledge partial financial support from Trident Management Ltd, and financial support for the year 2004 by SHU Enterprise Centre.

Most importantly, I am grateful to my parents for their patience and belief in me, even though they do not necessarily understand why or what I am actually doing. Finally, I wish to thank Panayiotis 'Lord-Xipe', Periklis 'Red-Elf', Nikos 'JP' and Christiana (for constantly reminding me who I am...); Zissis, Panos and Amir (for unconditionally offering their friendship); Christos, Socrates (RIP, 1998) and Petros (for remembering the past kept me focussed).

Sheffield, UK
January, 2005

G. Chliveros

List of Publications

G. Chliveros (2005). 'Characterisation of Endospores through Light Scattering Patterns', *Poster Presentation: Marie Curie Summer School in Knowledge Based Materials*, 2005, Aachen(Germany).

G. Chliveros and M.A. Rodrigues (2004b). '*Method and Apparatus for Particle Analysis*'. Great Britain Patent Application 0406055.4; 2004-03-17.

G. Chliveros, M.A. Rodrigues and D. Cooper (2004a). 'Bacteria Cells as near-index Particles and the Calculation of Light Scattering', *Invited talk: Institute of Physics Workshop on Optical Techniques in Biomedical Instrumentation*, Feb.2004, London(UK).

G. Chliveros, M.A. Rodrigues and D. Cooper (2003b). 'A new n-Layer mRDG Ellipsoidal Model of Light Scattering for Rapid Monitoring Tests of Coliforms in Potable Water Samples', *Institute of Physics Series in Sensors: Proceedings of Sensors and their Applications XII*, Limerick (Ireland), Sept.2003, pp 317-322.

G. Chliveros, M.A. Rodrigues and D. Cooper (2003a). 'Modelling Populations of Prokaryotic Cells: the n-Layered mRDG Approximation', *SCS-Europe Proceedings of the 17th European Simulation Multi Conference [BioMed]*, Nottingham (UK), June2003, pp 338-344.

G. Chliveros and M.A. Rodrigues (2002). '*MATLAB Implementation of the Exact Solution, for the n-layer Sphere, Scattering Problem*', Technical Report (CVPRAI-02-01). Sheffield Hallam University.

Chapter 1

Introduction

"A likely impossibility is always preferable to an unconvincing possibility"
Aristotle, *Rhetoric*

Light scattering is the secondary radiation scattered by the induced oscillatory motion of protons/electrons within an obstacle when illuminated by a light source. This secondary radiation relates to the heterogeneity of the system (i.e. the collection of particles constituting the obstacle). As a result the interaction of a beam of light with any medium will result in the rise of scattering also known as density fluctuations. Other types of fluctuations also appear, for example concentration and orientation fluctuations. However when we are interested in the light scattering by particles, a fluctuation is not a particle in that sense. After all, scattering by fluctuations is usually much less than scattering by particles [4, p 7][5]. However, there have been many attempts to identify the applicability of low angle scattering and the theory of fluctuations but most are limited to studies of biological motion [6] or chemotaxis, that is movement of cells from one band of the liquid media to another, and relating to the swimming speed of motile organisms [7], as well as rotational-translational effects on the scattering spectra at forward scattering angles [8].

Even though we are interested in the microscopic world (small particles), one would in theory solve the heterogeneous particle problem defined within Maxwell equations. In that sense, [9] was the first to provide a solution to the scattering and absorption by homogeneous spheres. Since then several papers have appeared that refine and extend the theory to non-symmetrical particles by assumptions on spherical equivalents, sphere with inclusions and others ([10, for example]).

Under the paradigm of biological cells and in particular bacterial cells, it has been indicated that laser scattering techniques, even though not a panacea, will play a significant role in partial identification, characterisation and clinical examination of such

samples [11]. For example in [12, 13], angular light scattering data obtained from a goniometric module are interpreted by means of a 2-layer Mie model [4, pp 181–184].

However, most prokaryotic cells are of a complex makeup. In general the cell presents a structure that consists mainly of the cell wall, the plasma or cytoplasmic membrane, the cytoplasm and the nucleoid. Therefore, in order to generate a more accurate representation of the cell, one would model it as having various compartments within its volume and within these compartments the refractive index is different from that of the surrounding objects. In cells where the overall morphology can be approximated as that of a sphere (e.g. *cocci*), each of the structures internal or external to the plasma membrane can be modelled as a different layer in an n -layered spherically symmetric inhomogeneous particle. Not many experimental studies appear in the literature, as we report in subsequent chapters. In this work we are interested in *modelling* the bacterial cell as a non-homogeneous body of assumed geometrical shape.

Finally, the models we have developed do not apply only to bacteria. Other examples, within the boundaries of applicability of our models, include characterisation of anthropogenic aerosols from lidar sounding data, which contain multiple layers of soil erosion, salt, soot, organic and other compounds or even that of atmospheric sensing where the raindrop particles can be characterised by multiple layers of water of different thickness and composition (e.g. multiple ice/ liquid/ ice interfaces and so on).

Aims and organisation of the thesis

In the early days of our research we were interested in scattering from bacteria in water at low angles, that is to say when the scattering angle θ is within 10 degrees with respect to the radiation incidence. Some prior experimental work on these instrumentation setups indicated that there is a strong correlation with increased scattering as concentration increases by the use of, say, temperature applied on the sample over some period of time. However, concentrations alone would not lead to at least partial identification. That is to say, we are interested in models that may lead to identification protocols. As a result, we follow the line of research that is indicated in the literature as one that may lead to this aim: hence, scattering patterns of angular dependence. Even so, not many studies for bacteria appear where the bacterium is examined as a strongly inhomogeneous particle. Furthermore, limiting cases in terms of the cell's geometry have been theoretically examined, mainly due to the lack of inhomogeneous models within the *near-index* regime.

As such the general problem we have investigated can be said to be the modelling of the true *physical meaning* of the internal composition of bacteria in terms of scattering in

all directions through mathematical simulation with both deterministic and stochastic elements. By the term ‘physical meaning’ we imply the identification of physical structure rather than the direct identification of a specific bacterium. As such, commonly used models explore the idea by examining the biological cell as having a limited number of layers. In our work we propose that the bacterial cell must be investigated as an n -layer structure by extending a modification on the Rayleigh-Debye or Born approximation applicable in the near-index regime, as is the case with bacteria in water based environments.

Applying our models as proposed within this thesis, that is a ‘predetermined geometrical shape’ with an arbitrary number of layers, one would first explore the effect of altering the parameters of size overall (s) and per layer (s_i), investigating values for the relative refractive index ($m_i, i = 1, 2, \dots, n$) and then infer, using some test statistic, the best model which may lead to partial identification. The predetermined geometric shape which we refer to is in fact either spherical or ellipsoidal/spheroidal. For a sphere of radius r the spherical shape is defined at a centre point (x_o, y_o, z_o) by the expression

$$\frac{(x - x_o)^2}{r^2} + \frac{(y - y_o)^2}{r^2} + \frac{(z - z_o)^2}{r^2} = 1$$

whilst an ellipsoidal shape of semi-axes (a, b, c) is defined by the expression

$$\frac{(x - x_o)^2}{a^2} + \frac{(y - y_o)^2}{b^2} + \frac{(z - z_o)^2}{c^2} = 1$$

A spheroidal shape is an ellipsoid, that has an axis of symmetry. For example, symmetry about the z -axis, whereby $a = b \neq c$, and for other alternative combinations ($b = c$ or $a = c$). To the best of our knowledge we are the first to theoretically examine the cell as an n -layer structure and to propose such a mathematical extension within the near-index boundaries ($m < 1.35$), at the far-field observation points at distance R (where $R \gg s$).

In the first part of this thesis (Chapters 2 and 3), we review literature on light scattering for bacterial cells and develop a model for bacteria that have spherical shapes and inhomogeneous internal structure. We proceed to generalizing a modification to the Rayleigh-Debye approximation, which seeks to extend the applicability limits of the Rayleigh theory. In that respect, we generalise from homogeneous spheres to spherical particles that may be modelled as having an arbitrary number of layers. Following this generalisation, we first establish the relationship between the popular 2-layer spherical models and our generalisation when $n = 2$. This leads to the question of how this affects the applicability limits of our mathematical model. After finding in the literature the exact Mie solution to the problem, known as the Volkov-Kovach solution, we have implemented a computer algorithm that follows this solution and have constructed relative difference mappings for

our approximating mathematical model. In these chapters, there are several notes and observations reported on the physical meaning of our findings on functional behaviour and we relate them to realisations of experimental value.

In the second part of the thesis (Chapters 3 and 4), the aim was to extend the spherical model to any ellipsoidal geometric form using the basis we have built in proofs and discussions. We provide a new method for solving the multi-layered ellipsoidal problem and we show the effect of non-sphericity to the scattering pattern. Hence we illustrate that the relation of the number of peaks of the scattering pattern to size may lead to erroneous results. Furthermore we show that there is a dependence of backscattering on the three-dimensional scattering, hence there is a need for experiments that adapt this feature in the instrumentation setups. Finally, we devise experiments for populations where the condition of independent scattering is not violated. We devise a new frequency function for bacterial size distributions and apply it to a scattering ratio that has been proven to emphasize the backscattering effect. At the end of this part of the thesis we illustrate how our method can be applied to the case of super-spheroids, defined by

$$\frac{|x - x_o|^n}{a^n} + \frac{|y - y_o|^n}{b^n} + \frac{|z - z_o|^n}{c^n} = 1 \quad , \quad n > 2$$

from which we were unable to infer an analytic expression.

In the third part of the thesis (Chapter 5) the aim was to investigate how our models would be used in cases where the independent scattering condition is violated. In that respect we have built an algorithm that generates such positions in three dimensional space, but avoiding the case of binding of cells, which can only be seen in water treatment processes in which we are not interested. That is to say that throughout the thesis, the major assumption is that the mathematical models developed will be used on samples from drinking water networks and in real time. Hence models that require extensive computational power are not considered.

We have also extended the Rayleigh-Debye phase function so as to apply for increased values of relative refractive index and for multiple layers. Incorporating this new function, the multiple scattering effects on simulations of closely packed ensembles was possible. By numerical evaluation we have illustrated once again the need for detecting backscattering even though there is an apparent 'washing-out' of distinct features. Furthermore, asymmetry in the polar scattering pattern also justifies the use of multilayered internal structures of closely packed ellipsoids, even though there is an apparent limit on the number of layers to be used; namely up to 5 layers for increased numbers of cells, within a sample's volume.

Finally, in Chapter 6, the main results and conclusions of the thesis are outlined. Our main contributions are summarised as:

- Implementation of the computer algorithm for the n -layer exact solution
- A generalised solution to the n -layer near index problem based on modification to the Rayleigh-Debye approximation.
- A theoretical verification that limits of our generalised approximation with respect to the average relative refractive index cover a significant part of the bacteria domain.
- A theoretical study on the relative difference between the exact solution and our generalised approximation.
- A new method for determining the scattering amplitude or the form factor from particles of no apparent geometrical symmetry and for multi-layered internal structures.
- A new method for spheroids of multi-layered internal structure, in conjunction with a physical justification for polar asymmetry in the scattering pattern.
- A new procedure for treating populations of cells that exhibit skewed frequencies in their linear dimension, as long as the condition of independent scattering is satisfied.
- Implementation of an algorithm for issuing positions and visualisation of media densely populated with scattering ensembles where the independent scattering criterion is violated.
- Modification of the Rayleigh-Debye phase function for densely packed random media to apply to n -layered ensembles.
- The theoretical finding that asymmetry in the scattering intensity's profile due to orientation and curvature effects is evident, even for densely packed media.
- A numerical evaluation in simulated media closely packed with cells which deploy more than 2 layers indicated that there is still enough information to evaluate the internal structure. As a result, the common belief that using these algorithms to experimental data does not advance our understanding of the internal composition of the cell illustrated that this is not the case.

Areas of future investigation are suggested, such as developing models for comma-shaped particles, for particles with spherical or ellipsoidal inclusions and incorporation of hybrid cores. Optimisation of optical parameters as means of solving the inverse problem by approximation is also suggested.

Chapter 2

A review of light scattering: functions, patterns and bacterial cells

The formulation of the problem of light scattering or diffraction can be said to be simple. Let vector \mathbf{E}_i denote the incident field on a scatterer(s) of volume V ; the re-constructed field inside the scatterer is denoted by $\mathbf{E}(\mathbf{r})$ where vector \mathbf{r} denotes the distances within the boundaries of the cell, and the scattered field by vector \mathbf{E}_s . From Maxwell's equations one should find the total field equal to $\mathbf{E}(\mathbf{r})$ inside V and to $\mathbf{E}_i + \mathbf{E}_s$ outside V such that it satisfies the boundary conditions over V . Despite the simplicity of the scheme the solution depends on the geometric properties of the scatterer and its structure. Biological cells are in general of no specific structure. Furthermore the problem that is of usual experimental interest is defined as:

Definition 2.1. From a collection of sufficiently diluted *cells*, of assumed geometrical and optical properties, suspended in a *liquid medium*, which is illuminated by a laser beam of specified polarisation and *wavelength*, determine the sample's physical *characteristics* in real-time.

In particular, bacteria in water based environments are considered to be 'soft-scatterers', and of no specific morphology in terms of internal structure relating to optical properties. For example, if one assumes a spherical particle, and one models the interior as an anisotropic tensor of relative refractive index, a general solution in a closed form cannot be obtained [14, 15, 4]. In this section we provide information from the literature that results in reasonable assumptions within our problem domain so that the problem can be analytically solved. Finally we attempt to link work from the literature towards characterisation and possible identification of bacterial cells *via* the known instrumentation and *a priori* knowledge for our propositions that follow in subsequent chapters.

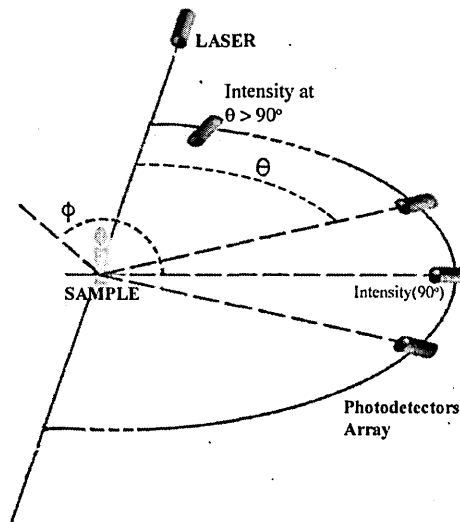


Figure 2.1: A commonly used configuration for multi angle light scattering measurements. The detectors and laser source are placed on the horizontal plane so as to cover the range for $\theta \in (0, \pi)$. Note that the laser source is coplanar with the array of detectors.

2.1 Introduction

To understand what underlies the statements of Definition 2.1 we have to define the terms used. The problem is illustrated in Figure 2.1 where the laser source has a defined wavelength λ and polarisation state. The sample is assumed to be contained in a circular cuvette with a total volume V_t within which there is a number density ρ_o that is occupied by bacteria cells. The concentration of the cells is assumed to be large enough for the scattered light to exceed the background noise ($\rho_o > 10^3 \text{ml}^{-1}$), that is scattering by the liquid itself, and smaller than the critical density $\rho_o < 10^6 \text{ml}^{-1}$ of solution, so that every cell is assumed to scatter light independently. The latter is commonly known as independent scattering and the volume limits have been defined experimentally in several publications [16, 17, and so on] as a theoretically sound limit has been proved difficult or impossible to infer, due to the nature of the geometry and structure of bacteria. Consequently, a size distribution for the scatterers is also assumed, usually being that of the normal Gaussian density function, hence avoiding violation of the statistical assumption of population normality in the parent population. Violation of this assumption would lead to difficulties in inference of statistical significance which is of importance in many applications, for example clinical trials. That is to say, non-parametric testing would have to be employed for every experiment of the kind shown in Figure 2.1.

For real-time identification, following Greenberg *et.al.* in [11, pp 9:22 – 9:24], the most rapid of tests is the fluorometric, by which method the release of carbon dioxide (CO₂) is measured and detection of waterborne faecal coliforms is possible. The test is said to take place in about 1 hour. However it is very specific, that is to say, different protocols must be used for different bacteria genera. As a result the aim of any test in terms of time effectiveness for water samples must be within this time restriction. This applies to all research prototype methods. Concerning light scattering, it has been noted by Ulanowski [18] that light scattering equipment can produce patterns of angular dependence within minutes, and following Wyatt [19] we can determine within another 20 minutes the external morphology, that is to say the geometric shape, of the cell. To characterise the cell, we need to infer the optical properties and correlate them with some microbiological measure. To infer the optical properties from the scattering patterns we then need to use some theoretical background (Section 2.4). A system is said to be real-time when the computation taking place is rapid, that is, fast enough to affect the input as it happens. As a result, the process of characterising bacteria cannot be said to be in real-time. However, the characterisation would be defined as such when a proposed method and computational algorithm do not significantly add in time to the characterisation process. This is what we refer to as real-time: the time taken for the computations within the algorithm.

Finally, by *liquid medium* we refer to the environment of interest, that is to say, water based environments from which abstraction of drinking water is possible. Thus airborne bacterial cells are excluded.

2.2 Bacterial cells: morphology and relation to optical properties

Bacteria are single cell (unicellular) organisms considered to be biologically extremely small in terms of size and multiply by cell division. Some are important agents in the cycles of nitrogen, carbon and other matter whilst others are pathogenic, causing disease to humans and animals. They can be found virtually in all environments and are included in the division of Prokaryotic Cells ¹, and have many important characteristics relating to their shape and internal structure. These features, extracted from the characteristics found, are used in order to name them following the *Bacteriological Code* [20] established by the *International Committee of Systematic Bacteriology*. The description

¹Prokaryotes are considered to be direct descendants of the oldest forms of life, i.e. unicellular organisms. It is noted that in biology the greatest gap, missing link, is the question of how Eukaryotes (multicellular organisms) appeared and how did they evolve.

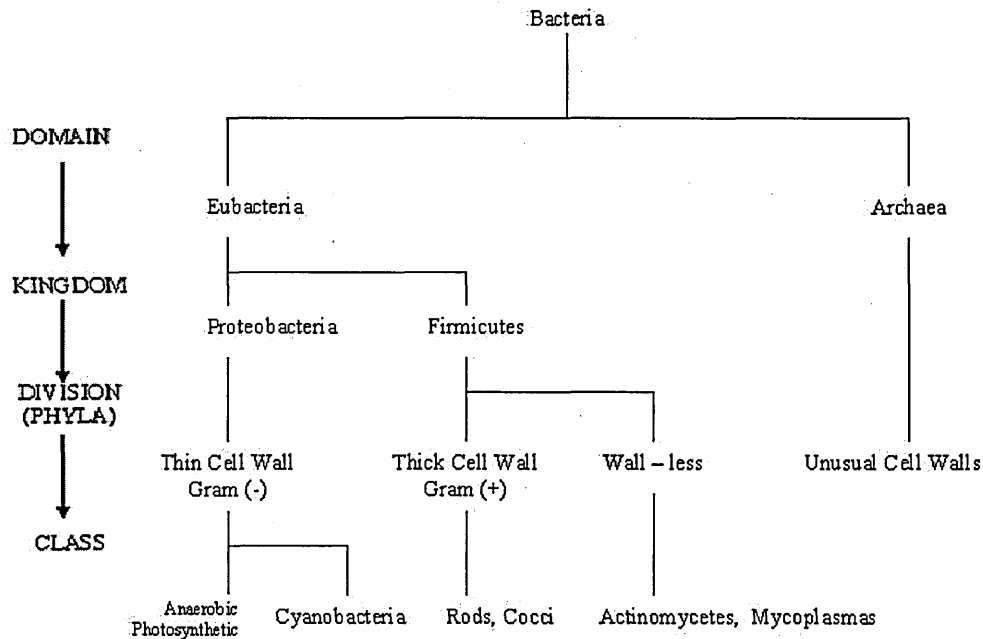


Figure 2.2: A classification system based on the Gram reaction of the cell; that is to say the behaviour, structure of the cell wall

that is attached in this naming code includes, amongst others, morphological characters, occurrence of cells as a result of multiplication by binary-fusion, ability of encapsulating and producing spores, as well as their reaction to Gram stain. What complements these characteristics are the enumeration of physiological and biochemical characteristics, which cannot be directly monitored using light scattering. To avoid the demands of either taxonomy or a phylogenic system of classification, one would resort to a more pragmatic, artificial classification, which groups organisms according to their similarities. The most complete work of such descriptive bacteriology is 'Bergey's manual of Systematic Bacteriology'[21], which contains names, descriptions of morphological and physiological properties with literature citations and the corresponding determinative key of classification. The terminology used is illustrated in Figure 2.2, with an example.

In this classification system, all bacteria can be said to be separated to two domains, that is Eubacteria and Archaea, and further on to five kingdoms, from which two appear for Eubacteria, namely the proteobacteria and firmicutes. From there several procedures have been applied as mentioned earlier to further classify bacteria to corresponding divisions or Phyla. We adopt the most common of them which is separation by Gram staining and the reaction that bacteria have to this process². A fixed bacteria smear, that is the

²Gram reaction is the process of identification through staining, bearing the name of its inventor

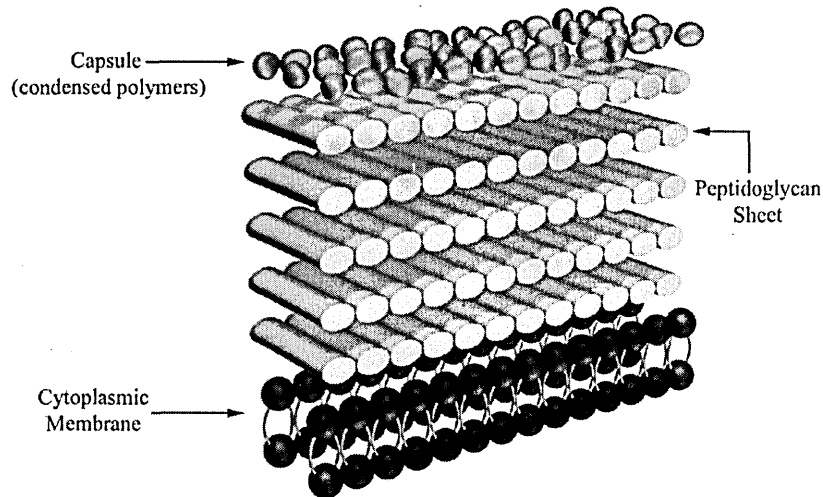


Figure 2.3: A Gram (+) cell wall: Chemical composition. Notice that the *capsule* layer only appears if condensed polymers form; this is an indication of virulence.

bacteria prepared on a glass plate, is stained by violet crystal Gram solution, decolourised with ethanol and counterstained with a contrasting dye. After rinsing with water, some bacteria retain the original stain (Gram positive +) whilst others retain the counterstain (Gram negative -). For identification purposes, the structure of the cell wall plays an important role. A Gram positive cell wall is generally described as a *rigid structure* of chemical composition as in Figure 2.3.

The phenomenon of Gram reaction can be explained by behaviour of the cell wall. Gram (+) cells have a cell wall with multiple layers, forming a thick rigid structure. As a result they are not susceptible to mechanical breakage in that they would sustain the shape and controlled porosity to possibly harmful agents such as antibiotics. In fact [1, 22] it is noted that the cell wall of *Bacillus Anthracis* becomes more rigid with increased doses of chlorine in water distribution systems, resulting in increased resistance to antibiotics, with possible life expectancy of up to two years. On the other hand Gram negative cells have a thin cell wall and are not as dense as their positive counterparts. In terms of light scattering one would, for example, try to link the behaviour of any part of the cell, in the current example the cell wall, with optical properties and in effect try to infer a similar classification system.

By employing the Lorentz-Lorenz formula as derived for optical frequencies commonly known as the Clausius-Mossotti equation [23] so that

$$\frac{m^2 - 1}{m^2 + 2} \frac{M}{D} = \frac{N_A \alpha}{3} \quad (2.1)$$

where the right hand side of the equation is commonly known as the ‘molar refraction’ with M being the molecular weight and D being the molecular density. N_A is the Avogadro’s number, \hat{a} is the polarisability of the molecule and m is the relative refractive index defined as the refractive index of the cell, or cell part, divided by the refractive index of the medium in which it is suspended. Rearranging the terms and taking into account the known fact from analytical chemistry [24] that the molar refraction is solely dependent on the sum of refractions of the bonds present in a given molecule, then for a mixture of different molecules and as a result for particle consisting of several molecules, as is the case with bacteria, it has been shown [25] that for bacteria the average polarisability corresponds to the molar refraction factor

$$a = \frac{m^2 - 1}{m^2 + 2} = \frac{N_A}{3} \sum_i N_i \hat{a}_i \quad (2.2)$$

where N_i is the number concentration in the molecule and \hat{a}_i is the polarisability of the i -th molecule; the bacterium is taken to be a homogeneous body.

Bacteria of volume V are bodies that exceed the molecular level numbers; hence Equation 2.2 would result in [23]

$$\hat{a} = V^{-1} \int \frac{m^2 - 1}{m^2 + 2} dV \approx V^{-1} \int_V \hat{a}(r) dV \quad (2.3)$$

where \hat{a} corresponds to the average polarisability of a bacterium of volume V , which is now assumed to be a non-homogeneous body. This is a generalisation of Equation 2.2, [25], where it was assumed that the cell of volume V is homogeneous.

As a result, using this term explicitly in any modelling procedure would lead to an advance in the sciences related to the biochemical properties of the cell. In theory, inference of such a term could be applied to any internal structure of the cell and could identify apparent contributions. The latter would be true, as long as one establishes an experimental link between the said model and the microbiological properties, for example inference of the proportion of water content of the bacterium as in [3] and [26]. Inference of the water content c_w within bacterial cells of specific volume V_o and refraction increment a_s is performed by using

$$m = 1 + c_s a_s \quad (2.4)$$

$$c_w = D_w (1 - c_s V_o) \quad (2.5)$$

a direct result from Equations 2.2 and 2.3 in the proof of Ulanowski [25, Chapter 2], where c_s is the concentration increment and D_w is the water density. We note that both Wyatt

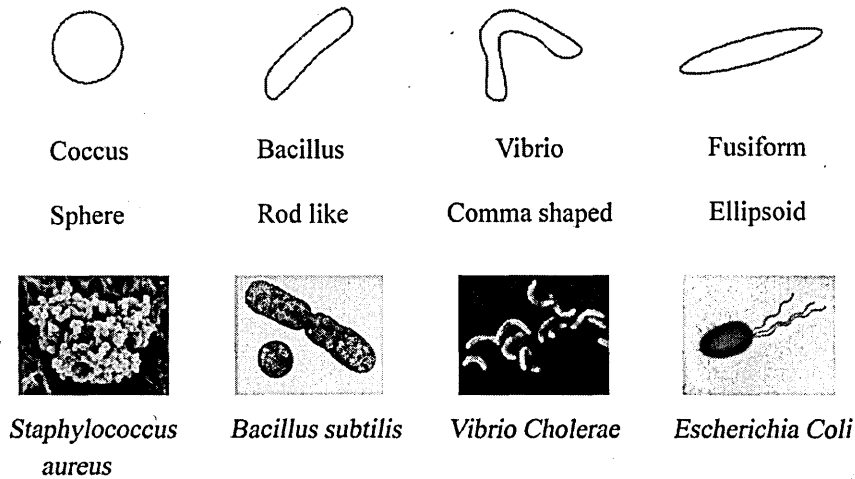


Figure 2.4: Most common bacterial cells in relation to their external morphology. Corresponding microscopic images are also provided: Reprinted with permission from Dr D. Kunkel (Dennis Kunkel Microscopy ©)

and Ulanowski use the assumption $m \rightarrow 1$, so that $[(m^2 - 1)/(m^2 + 2)] \rightarrow 2(m - 1)/3$ and thus accept extremely small phase shifts for light rays entering the medium and body within the cell; assuming ‘transparency’ of near-index particles. The reader is advised that we return to this aspect in Chapter 3, where we infer our main result and introduce our approximation model.

In terms of external morphology, these Prokaryotic cells, which are small in terms of size, can be found in many geometric shapes, but they are mainly distinguished [27] as rod-like, ellipsoids, curved rods or ‘comma-shaped’, and spherical (Figure 2.4). As a result, if one wishes to model bacteria in terms of light scattering or any other type of electro-magnetic radiation field, one should attempt to do so for most, if not all, of the said morphologies. The rod-like, in shape, bacteria such as the genus *Escherichia* are usually not more than $1\mu\text{m}$ wide and $5\mu\text{m}$ long whilst many *Pseudomonads* have a diameter of $0.4 - 0.7\mu\text{m}$ and a length of $2 - 3\mu\text{m}$. Spherically shaped bacteria (hence the name cocci³) have a diameter varying from $0.6\mu\text{m}$, in the case of micrococci, up to $1.1\mu\text{m}$. There are a few larger forms of bacteria, but they are not commonly found in potable water samples and they multiply very slowly [28, 22].

As indicated in Figure 2.5, we have structures internal and external to the cell wall. With reference to Figure 2.3, external to the cell wall we may have a formation of polymers, which may be condensed forming an external slime layer, the capsule. This is an

³derived from the Greek word *κόκκος*, pronounced ‘coccus’

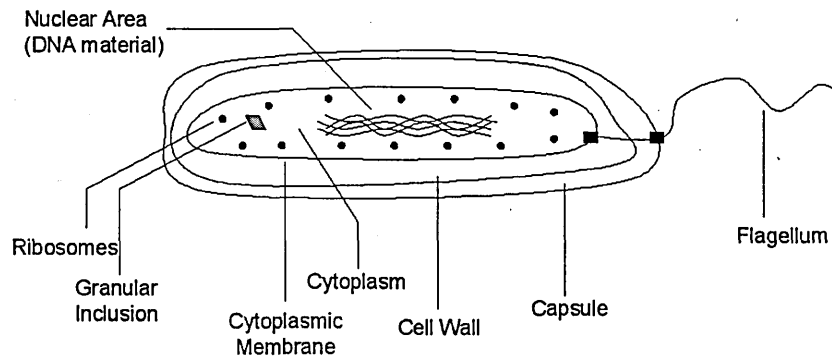


Figure 2.5: Schematic of the true structure of the prokaryotic cell. Note that features are not shown to scale and have been emphasised to illustrate the multi-layered structure.

indication of virulence, that is to say it may be a predictor of the cell's ability to cause disease, causing the cell to be considered as pathogenic. Taking into account that Wyatt, in [19], has shown that polymers in solution can be analytically characterised, indicates that morphological features which have similar composition may need to be taken into account. That is to say, there is no reason to believe that light scattered from the capsule will be negligible, and as a result this morphological feature could be modelled as an additional layer in terms of light scattering. Appearance in the model of such a layer would result in predicting pathogenic bacteria as opposed to possibly harmless ones.

Structures internal to the cell wall are mainly the Cytoplasmic membrane, the Cytoplasm and the nucleoid or *Nuclear area*. The cytoplasmic membrane is a thin structure that encloses the cytoplasm of the cell. It consists primarily of lipids and proteins, but its formation is not a rigid structure. However, looking at the manufacturers of light scattering equipment, both Wyatt [19] and Malvern Instrumentation [29] have shown that characterisation of proteins is feasible using Multi Angle Laser Light Scattering (MALLS). Furthermore, in electron micrographs, the cell wall and the cytoplasmic membrane are visible as two separate layers where a dark line indicates the rigid cell wall (phase dark) whilst a light line (phase light) corresponds to the cytoplasmic membrane. Hence the contribution of such a layer would be considered significant and should be included in a light scattering modelling procedure. Non-appearance of such a membrane would be a predictor of a specific wall-less prokaryote, that is the Actinomycete and the Mycoplasma classes. If the cell wall is destroyed by antimicrobial agents then the cytoplasmic membrane is exposed to injury and the cell's intracellular components are leaked to the external

medium, leading to cell death.

For bacteria the term cytoplasm will refer to the substance of the cell inside the cytoplasmic membrane, that is, enclosed DNA material (nucleoid), ribosomes and so on. Its composition is considered to be mainly water; that is, at least 76% [30] to 80% [27]. As a result if the cell is suspended in a water based environment then it is obvious that the relative refractive index m , defined as the refractive index of the cytoplasm divided by the refractive index of the medium, will be very close to unity, hence $m \rightarrow 1$ or $|m - 1| \ll 1$. The nucleoid of a bacterial cell contributes a single long circular molecule of double-stranded DNA, the bacterial chromosome. The nuclear area can be spherical or elongated depending on the cell's external morphology. As such it can be assumed to follow the overall geometrical structure of the rest of the cell, unlike eukaryotic cells. Following, for example, the experimental work of Newman in [31], and verifications from several simulated nucleoids in the literature, it has been found that the contribution of this internal structure to scattered light is more significant in the backscattering angles. However, the use of simplistic models, as is the case with deployment of no more than 3-layered models, hybrid or otherwise, makes the finds questionable. It is of no dispute, however, that the main structures within the cytoplasm will produce scattering of light, and backscattering will be more emphasised [31, 32] due to the appearance of extra intercellular material, hence layers.

Within the cytoplasm, we also have the appearance of other structures which are exceptionally small and consist of protein and ribosomal RNA (rRNA); hence they have been given the name *ribosomes*. They are not dense and regulate the production of protein within the cell. In prokaryotic cells, they seem not to contribute to light scattering. In any case it would be difficult to model them, as they are randomly dispersed within the cytoplasm, and since their refractive index would be very small as well as their size, theoretically speaking they are usually ignored. This is not the case with other biological cells, hence for the eukaryote cell ribosome modelling must be included, either as a function of refractive index or as separate dipoles within the cytoplasm; that is to say, dipoles with 'size' and optical properties different from those of the surrounding (simulated) matter within the cell. Examples of such a procedure are the hybrid models of simulated cells in [33], stochastic radiation transfer of [34] and a 'black-box' procedure offered in [35]. We follow the procedure normally used where the ribosomes have too small a value of size and refractive index to be taken into account. The same applies for all granules which usually serve as energy, gas or sulphur reserves. They can be said to be of diagnostic significance, but only in terms of biochemical testing, and not directly

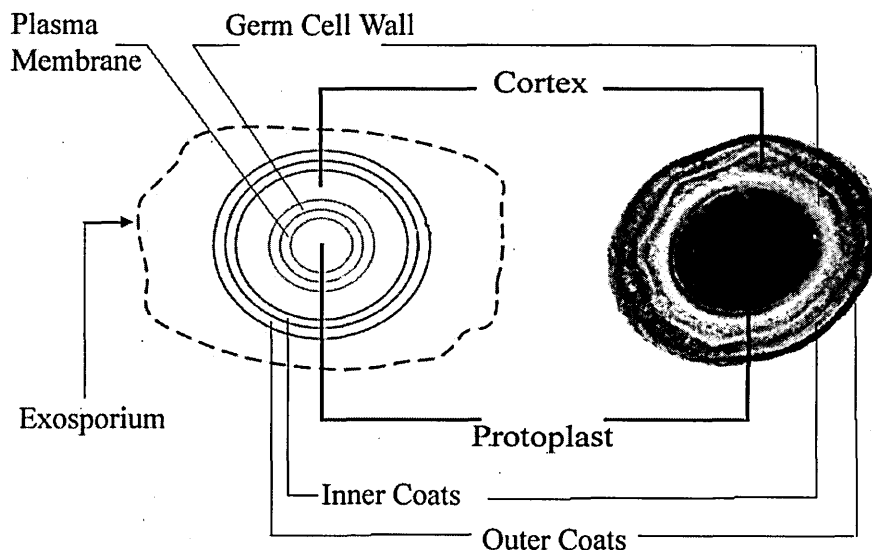


Figure 2.6: The electron microscopy image of cross section of the *Bacillus subtilis* endospore (right). A typical model that appears in most textbooks of microbiology to explain its structure can be seen on the left. Note phase light and phase dark regions of the microscopy image and the clear relationship with the diagrammatic illustration as shown here.

observable by MALLS or light scattering in general.

However, a significant inclusion is the spore, also referred to as endospore. These structures are unique to bacteria and are highly durable with thick cell walls. Furthermore, following most microbiology textbooks, endospores have ‘... *additional internal layers*’ [36][27]. They are formed as structures internal to the cell membrane via the process of sporulation, and they are released into their environment from the parent cell at the germination stage. The free spores may eventually be the same or larger than the parent cell’s size, or may be smaller. When they are within the cell they occur either terminally, that is at the end of the cell, or centrally, and are significantly smaller in size. The free spores can in theory remain dormant [37] for many years and every vegetative cell produces only one spore. After germination the spore is released, and the parent cell dies; hence it is not a process of multiplication. Furthermore, the spore itself does not hold a mechanism for multiplication. As a result, techniques which are based on the outgrowth or multiplication of cells will fail. Furthermore the spore is very difficult to stain, hence optical microscopy counting and resulting induction trees of identification are difficult, if not impossible, to perform and obtain [38].

How to decide whether the spore is dormant, that is, remains alive but does not alter

its metabolism or size, or dead is a research question of great experimental interest and has yet to be answered. Under the hypothesis that dormancy can be linked with highly dehydrated spores, there is still an issue involving the 'wet' spore's water content. The total volumetric water content of such spores greatly varies, between 60 and 85%. If one takes into account that the 'wet' spore is probably completely permeable to water, finding the equilibrium of water in say the dominant internal features of Figure 2.6, namely the cortex / protoplast ratio of size and volumetric proportion of water, is problematic. By examining a summary of finds for the refractive index by light scattering (Section 2.4, Table 2.4) one would observe that vegetative, non-dormant spores have a small relative refractive index value which effectively means a less dense cortex (outer layer in the 2-layer spherical model); hence they are more permeable, suggesting a larger free water content in the protoplast. Even so, in the studies of Jones and Weiss [39] the spores of *B. megaterium* were subjected to high pulses of high energy, i.e. electron radiation. Acquiring corresponding spectra from wet and dry spores via a spectrometer, it was found that the spores following radiation had spectral signatures which were very similar. As a result, it was concluded that it was more likely that the spores normally maintained relatively dry regions within. Translating this to the question of how many layers should one use in a modelling procedure is open to interpretation; however it should be clear that a 2-layer model is too simplistic. It should be clear that the spore is a special case of inclusion, one which would be used for separation between bacteria that are able to sporulate and those which do not possess this ability, hence providing a taxonomic feature of identification [38]. However, in the same work it is noted that the *Bacillus* genus, given its name from the structure within which the spore is enclosed before sporulation, is commonly referred to as a rod-like particle when, in fact, it may be more realistic if one depicts it as an ellipsoid. Even for Group II *Bacillus* spores the author notes that they are not spherical but ellipsoidal, and that the common misconception derives from the 2-dimensionality of most microscopic observation techniques.

2.3 Candidates for drinking water abstraction:

Bacterial Ecosystem

To understand the complexity involved in the kinds of bacterial species that appear in the drinking water environment we present an ecosystem. We then proceed to the legal framework that governs the abstraction of drinking water, and procedures involved

in the quality monitoring of networks of potable waters. Biological processes in the natural environment that can be used in theory for abstraction of drinking water to a human consumption potable supply network [11] are strongly influencing the physical state and quality of water. Such ecosystems are freshwater lakes, water deposits and rivers. Bacteria numbers are influenced mainly by the density of water and the nutrients to be found. Water has a maximum density at 4°C however this varies greatly depending upon the environment.

Every cell in a bacterial ecosystem has an age and size. The relationship between the two is not well understood and has been proved to be exceptionally complicated due to the complex biochemical interactions that take place. Furthermore there still exists a debate as to whether the mathematical relationship is deterministic or stochastic or a combination of the two. However when a cell population grows exponentially there is a greater number of smaller cells relative to the population size than that of larger cells. In general large cells are considered to be older than smaller cells, but once again this is taken as a heuristic result. When cells have reached a steady state of growth then a greater size of larger cells as opposed to smaller ones appears. This heuristic observation leads many researchers to model populations using the normal distribution where the variability, that is the spread of the curve, depends on the rate of inter-divisions of the cells [40] [22, pp253-277]. In particular, Stull in [41], by using differential light scattering measurements on 141 individual bacterial suspensions of *Staphylococcus epidermidis* and assuming a spherical homogeneous body with an average refractive index of 1.388, infers a discrete size distribution that closely matches, in the continuous sense, the normal frequency function. He relies on the assumption that the set of maxima angles in the scattering pattern for a particular radius value is unambiguous and he solves the direct problem in two steps. In the first step, depending on the number of peaks in the measured data, an appropriate range of radii is selected; in the second step, the set of measured peaked angles is fitted to the theoretical pattern of scattering. However, the model he employs is homogeneous and of spherical symmetry. As we will see in Chapter 4, Figure 4.6, this is not the case if theoretical patterns to be fitted on experimental data do not assume an axis of symmetry with respect to the incident radiation (Figure 2.1).

However, Cullum in [42] and Koch in [43] make the case for distributions that incorporate the skewness effect. Koch, by deploying a number of discrete distributions, proposes the use of the Binomial and Poisson frequency distributions for modelling size of bacteria in liquid samples. He concludes that the normal distribution should be used only when there are many independent sources of random fluctuations. That is to say, even

between two sister cells of *Escherichia coli*, there can be identified at least five different sources of random fluctuations. To summarise:

1. Change fluctuations: these arise in the synthesis or partitioning of critical macromolecules that depend on the bacteria growth
2. Systematic physiological changes: these may have arisen due to environmental variability (as we will see later in this section) or due to individual variability in cells due to inequality in separation during the growth cycle.
3. Behavioural changes: due to regulatory mechanisms of, for example, DNA replication
4. Mutational changes: as bacteria progress in their evolution, random mutations take place so as to adapt to changes in their environment. This may affect the size variability directly or indirectly.
5. Genetic change: that is groups of genes may change and production of new species may be rendered with new growth, size and division cycle properties.

These five sources of variation are not the only ones [44] but they have been identified to be the major contributors. They involve stochastic as well as deterministic elements [43] and the distinction as to whether one of the two process modelling procedures should be applied may be dependent on the number of critical events. If a few of those sources are dominant then distributions that emphasize positive or negative skewness must be used. Finally it is stated that continuous distributions, such as the Gamma frequency distribution, would be a useful alternative, but one should be cautious in the way the continuous distribution is fitted to the experimental data [45]. That is to say, when a number of samples has been taken there is an associated risk which stems from the sampling procedure, because if most samples are selected from within a specific range then this may not represent the true nature of the distribution (skewness effects may not be evident) ⁴. A model would be inferred if the events per sample are considered to be independent. Otherwise, the influence of correlation effects has to be determined in order to investigate the underlying relationships before averaging over the whole population.

Freshwater lakes present seasonal variations and temperature zones. For example in spring the cold water of a lake is warmed by the sun. As a result, the surface layer is warmed up and water in this layer decreases in density. The boundaries between zones can

⁴Note that this problem is not restricted to continuous distributions

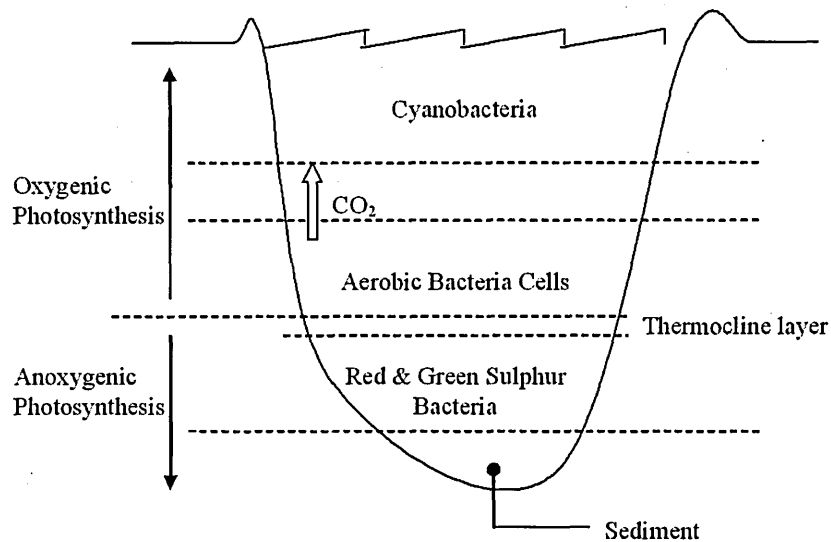


Figure 2.7: A freshwater lake eco-system and the distribution of bacteria on the layers. Waters above the thermocline layer (indicated by the arrow) constitute the *epilimnion* and below the said layer is the *hypolimnion*.

be very abrupt but, depending on depth, they may persist throughout the seasonal changes. However changes in temperature produce an increase of chemical compounds and nutrient concentration. Consequently, when deep waters become cooler, the nutrients rise to the surface and the bacteria population increases accordingly; the population that resides per layer of Figure 2.7 will increase rapidly depending on the nutrient concentrations. The metabolism and multiplication of bacteria will increase the biomass production, hence bacterial cells will increase in size/volume, as well as in their numbers per *ml* of water.

In the upper layers (*epilimnion*) which are penetrated by light, production of biomass will be increased and so will phototropic bacteria, for example the Cyanobacteria. In this case, oxygen is consumed and aerobic bacteria appear. However, in the lower layers (*hypolimnion*) only bacteria that have the ability to utilise methane emissions will be present. This is because the *hypolimnion* will eventually stop producing oxygen, rendering it completely anaerobic, and only methane will escape in the form of bubbles. As a result, anaerobic microbial processes take over. This results eventually in storage of a large portion of hydrogen sulphide and, if illumination is suitable, then purple and green sulphur bacteria will grow and form the primary biomass production. In this zone, appearance of Genera containing gas vacuoles, for example *Amoebobacter*, as well as flagella-propelled, for example *Chromatium*, is evident.

Natural running waters (streams, rivers), assuming they are not polluted, are in general

Bio-Agent	Detection Limit (per 100ml)	Reference Measurement Method
Total Coliforms	500 cells	Culture at 37°C and colony counts or Dilution in at least three tubes and sub-culturing of the positive tubes on a confirmation medium with Most Probable Number as the statistic
Faecal Coliforms	200 cells	As above but culture at 44°C is recommended
Faecal Streptococci	200 cells	Culture at 37°C but for dilution use of sodium azide broth is a requirement
Salmonella	≪ 1 cell	Concentration by filtration or inoculation(s) into pre-enrichment medium
Security Related Examination	Bacillus anthracis (anthrax), Vibrio Cholerae, E.coli O157:H7, Yersinia Pestis (plague), Shigella dysenteriae, Variola major (smallpox)	Rapid identification / Average Stability of bio-agents in water ranges from 6 days to 11 months

Table 2.1: EU directive 79/869/EEC: Only the bacteriological content for examination from possible sources of potable samples is shown. The sample container's material is required to be sterilized glass. Salmonella numbers indicate the necessity for absence per 1000ml. The remainder as indicated is taken from recent additions as per [1, 2], the *Central Disease Control*, USA security code.

suitable for human consumption, as concentrations of unicellular organisms appear to be very low. However even a suspension of 10^5 bacterial cells per ml of water does not appear turbid to the naked eye. In terms of bacteria, the presence of coliforms, such as the *Escherichia* genus, and other genera (*Salmonella* and *Streptococcus*), and sulphur utilising bacteria in conjunction with the appearance of a strong smell of hydrogen sulphide, should serve as a strong warning signal of the poor water quality.

Until water reaches the human consumption network, several chemical treatment processes will have taken place. However there is still a need for microbial screening. Following the European Union Directive 79/869/EEC [46], water companies sample water, to comply with this call for screening of 46 substances, of which 4 are bacteria. To these four biological agents (or parameters as preferred in the EU terminology), one should add the security related screening protocol of the American Public Health Association [1], which calls for further screening of bacteria that present a threat to public health and safety. We summarise these findings in Table 2.1.

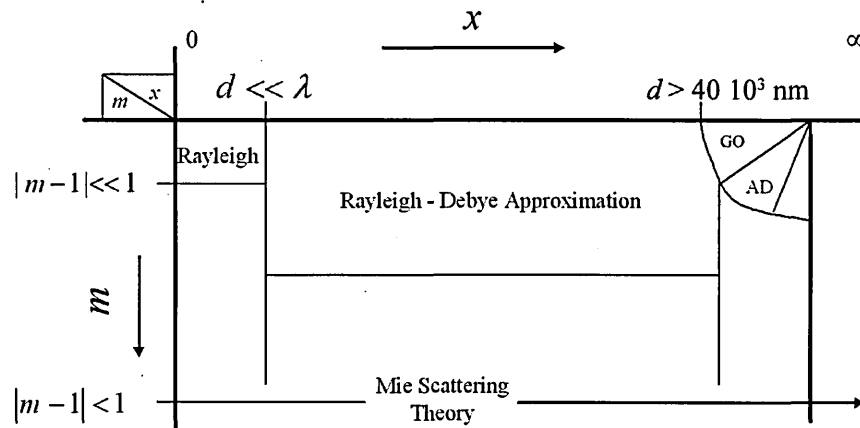


Figure 2.8: Light scattering theoretical models and applicability. Note that Mie scattering would potentially solve most problems involving small particles provided that a rigorous solution could be obtained. On the diagram, (GO): Geometrical Optics and (AD): Anomalous Diffraction. We use GO and AD as examples of approximations that would be applied for particles having a largest dimension $d > 40\mu\text{m}$; for spheres this would be the radius for other external morphologies this would mean the major axis. By x we denote the size parameter defined by $x = 2k_0d$, where d is the scatterer's largest linear dimension.

2.4 Application of Light Scattering theory to biological cells

In general models derived from light scattering by small particles can be applied to the domain of biological cells such as bacteria. However the latter depends on the applicability boundaries of the theory to be used. Various methods have been developed throughout the years but in most cases they relied on simplifying assumptions on the internal structure of the cell. In general Mie theory, which is a rigorous solution, has the widest applicability range (Figure 2.8) as opposed to, for example, approximating theories, such as the Anomalous Diffraction (AD) and Geometrical Optics (GO). In Figure 2.8 the range of applicability for these theories has been related to the size parameter denoted by x and the relative refractive index, denoted by m . The size parameter is directly proportional to the largest linear dimension d of the particle, since by definition $x = 2k_0d$, where k_0 is the propagation constant at a fixed wavelength λ (in vacuo) of incident radiation.

Most commonly used is a two layer model of spherical symmetry and variants of Mie scattering as is the case for the problem of a sphere with an irregular inclusion [47] or a sphere containing multiple spherical inclusions [48]. These variants would have been applied for explaining light scattered from biological cells, and in particular from bacteria with spore inclusions. Unfortunately, in the literature we could not trace such works. The

theory of scattering and absorption by small particles can be said to fall under four main categories:

1. Exact Methods: In the literature there appear to be three dominant theories. That is, solutions from separation of variables (Mie scattering), the T-matrix method and the integral equation method.
2. Numerical Methods: The theories that dominate the field are the Coupled Dipole Method (CDM - Purcell & Pennypacker) and Discrete Dipole Approximation (DDA - Draine & Flatau)
3. Approximate Methods: four dominant theories appear in the literature, that is, Rayleigh-Debye or Born approximation (RDG), Anomalous Diffraction (AD), Geometrical Optics (GO) and the WKB or higher energy approximation
4. Hybrid Methods: that is, appropriate combinations of the above

The most famous and widely used are Mie scattering [9] and the generalised Mie solutions [49, for example] as well as its variants, which fall under the separation of variables category. An example is the solution of scattering by spheres that are placed at close distances (agglomerates) illuminated by a Gaussian beam [50] and presented as a superposition of field components method. Any analytic solution depends on the number of terms required to terminate the scattering series, with the most commonly used criteria outlined in [10]. To take into account inhomogeneities in cells, it is obvious that the model had to be extended. In that respect, a solution for the 2-layer model, but for a variable outer layer refractive index, has been reported in [5] in the context of bacteria and similarly sized biological cells. Most often cited is the simplistic model of a two-layer sphere, in [51, 52] and more often in reprints of Bohren-Huffman's book [4], which has been applied throughout the 1970's. In order to infer optical properties from biological cells using this model, in [53, 54, 3, 55] the particle is considered to be a sphere consisting of two concentric layers. This model continues to be extensively used, for example in [12, 13, 56], even though the n -layer spherical problem has been proved to have an exact solution provided in [57, 58, for example]⁵. Other solution methods to the concentric multi-layered sphere problem have been provided in the literature [59, 60], but the reader is warned that the expressions therein are not explicit.

Unfortunately, the cell is being depicted as having two contributing parts: the core or nucleus and the cell wall or cytoplasm. It must be noted that Wyatt and Ulanowski were

⁵The codes are not generally available

the first to link ⁶ the two layer model with the water content within the cells [12, 61], and to perform the first experiments in that respect, but in general we can already intuitively understand issues arising from its use. On one hand, a microbiologist or biophysicist would immediately identify that the cell wall should be modelled as a separate structure (outer layer) and the cytoplasm as an internal layer which incorporates the nuclear area. Using this as prior knowledge one should model the cell as having at least three layers. Using this assumption, that is a three-layer Mie scattering model as applied to biological cells, it may be surprising that only the works of Lopatin [62, 63, ex-USSR publications in Russian] are found and are largely unknown, possibly due to the fact that an English translation cannot be found. On the other hand, it is often reported in all works cited above that on average 20% of the experimental scattering patterns obtained provide ambiguous results. This is often attributed to asymmetry, deviation from spherical symmetry, or inhomogeneity of the cells. The ambiguous results can be attributed to the inferiority of 2-layer or 3-layer models as descriptors of the extinction and scattering of light by biological particles/cells even in cases where the cell is expected to be spherical (for example, the *cocci* family of bacteria⁷ or sporulating bacterial cells⁸). This is clearly supported in [64] where, using electron microscopy, images of cross-sections of *Bacillus* spores were produced. In this study the electron microscopy images were taken after negative staining, thin-sectioning and freeze-etching. As a result any inferred values, on size or otherwise, are of no use since a destructive technique has been applied; however the finds on structure are significant. For it was reported that the *Bacillus* spores present a structure resembling a 4-layer model, where the cell wall structure is observed to be that of two-periodic layers (resulting in a total of 5 layers). Clearly an n -layer model in conjunction with multi-angle scattering equipment might have been adequate to identify this novel feature and relate to other characteristics of such a spore. That is to say, if this feature were unique, as is the case with Wahlberg's finds, then this would be used as an identification protocol for the specific strain⁹.

The CDM and DDA [65] have been extensively used in astronomy and related disciplines. In effect a lattice of dipoles (or targets as preferred in the DDA terminology) generates a model of the particle under consideration. Assigning optical properties for each dipole, the lattice is then calculated by iteration and all fields are calculated. As should be obvious, the parameter space increases with the number of 'targets' needed to

⁶This refers to their experimental efforts and the use of the Clausius-Mossotti equation

⁷as is the case with *Staphylococcus aureus* and MRSA, which is the Multiple or Methicillin Resistant *Staphylococcus aureus* and presents a uniquely denser cell wall

⁸as is the case with *Bacillus Sphaericus*

⁹It should be evident that prior knowledge plays a significant role in any chosen model

approximate a particle's geometry more closely. For example Bronk *et.al.* in [66] used a DDA model geometrically defined as a cylinder and capped with hemispheres of the same radius as that of the cylinder, for measuring the diameters of rod-shaped bacteria, using the paradigm of *E.coli* in the log-phase of growth¹⁰. This was subsequently utilised in [67] as a means to monitor the rod-like bacterial cells' sensitivity in metal toxicity, that is to say non-rapid decrements of radius translated as a negative effect. However, in the theoretical work of Druger and Bronk [68] the number of dipoles n_d required for a two-layer sphere with size parameter $x = 1.5$, was $n_d \geq 46000$ and this leads to a space of approximately 92000 estimation parameters. Agreement with the BH-code in [4] was good for forward-scattering $(0, \pi/6)$ and side-scattering $(\pi/6, 7\pi/12)$ but increased difference from Mie theory was reported for back scattering. It is emphasized that back-scattering relates more closely to the internal structure than to sizes.

Returning to the experimental work of Bronk *et.al.* [66], 10000 dipoles were used (*E.coli* model), resulting in an error of $\pm 0.1\mu\text{m}$ in diameter, and the authors report that for a better resolution the number of dipoles has to be increased. The significance of the error in inference of diameter relates to the log-phase of growth from which phase *E.coli* cells have been sampled. Within this stage of growth, the cells may exhibit very small variation in size ($< 0.1\mu\text{m}$). As a result using the said number of dipoles would fail to successfully infer the size distribution within a narrow size range. However, it is noted that increasing the number of dipoles by a factor of 10 will also '*increase the time of the calculations by a significant factor*'¹¹. Similar experimental work, [69, for example] required even more dipoles for the characterisation of more complex bacteria, modelled as ellipsoids and assuming a log-phase for growth, where the dimension of the scatterer is almost constant, but increasing the computational power required. It may be true that in the coming years the CDM and DDA will become very popular [70] but the computational complexity and hence time required before results are obtained, prohibits real-time characterisation. The latter is the reason why most light scattering instrumentation manufacturers [19, 29] for whom the real-time characterisation problem is of great commercial importance. These manufacturers are insisting on the use of Mie hybrids or RDG theoretical models in conjunction with the Zimm plot or fitting method [71, 72, 73].

The Zimm [71] or Debye [72] fitting methods rely upon the construction of a plot of

¹⁰bacteria in the log-phase present growth such that the change in diameter is not rapid and the 'shoot-out' phenomenon is not observed

¹¹We can only postulate that this may mean an exponential increase in algorithmic complexity

the ratio of the experimentally acquired angular intensity pattern over the sample concentration against $\sin(\theta/2)$, where θ is the scattering angle mentioned earlier in this Chapter. Subsequently, a polynomial in $\sin(\theta/2)$ is fitted to the data, thereby obtaining the molecular weight and molar mass in conjunction with the average radius of gyration¹² from interpolation at $\theta = 0^\circ$. The latter quantities are inferred by the use of optical properties (average refractive index in the sample concentration) which are linked by an experimentally set curve known as the refraction increment, with known concentration. A Zimm/Debye conformation plot [73], that is a plot of the average radius of gyration against the molar mass acquired by the Zimm/Debye method, serves as an indication of shape. That is linear for spherical particles and non-linear otherwise.

In terms of hybrid methods, an example would be to use the basis of RDG and AD approximations so that an analogy can be found between the formulas for scattering functions, hence the characteristics of spheres and, for example, oriented spheroids [74, 75]. Another basis for building an analogy would be from the Geometrical Optics approximation, as is the case of Harada *et.al.* in [76], where a simple method, in which only two dominant rays describe the interference within the particle, is provided for determining the size and refractive index of a spheroidal ‘transparent’ particle larger than the wavelength, based on the use of Fresnel coefficients. From any theoretical analogy, one postulates a certain relationship between, on one side, the radius and refractive index of an ‘equivalent’ sphere in volume and on the other the spheroid parameters including orientation. The parameter space for the equivalent spherical model is then used under the Mie scattering theory from where all properties are now calculated. Such approximations have little or no physical justification, as the geometry of the particle and the function of refractive index cannot be taken into account. Furthermore, depending on the hybrid method, the algorithmic complexity increases. To illustrate this we borrow an example from astronomy, where a three layer spherical model is used in which the core is assumed to have several inclusions which are in turn modelled using the DDA [77]. This model was found to be useful for calculating the optical properties of interstellar grains and was linked with the porosity of the material, that is inclusions within the core. The model reduces complexity and increases the time efficiency of the algorithm; however it is still out of the bounds of what would be considered in the bacteria domain to be a real time method. A similar procedure for biological particles, via simulation, is described in [33] where a Finite Difference Time Domain (FDTD) method has been used. However, due to

¹²The term ‘radius of gyration’ is a misnomer for the *root mean square radius*, which is a measure of particle size weighted by the mass distribution about its centre of mass.

the use of FDTD, the memory requirements are reported to be particularly high. That is to say, a three-dimensional 2-layer cell, of radius $4\mu\text{m}$, with inclusions in the outer layer, requires at least 60MBytes of memory per cell. Clearly the computational power required is out of the bounds for a portable, real-time system, even under today's rapid technological advancements in computing power. For a three-dimensional simplified model (homogeneous sphere with inclusions) the authors report that the time required to obtain a solution was 90 minutes. It should be noted however that the application of the FDTD to biological cells has not been extensive, due, we suspect, to time complexity and computational power required.

The main ideas of all approximate methods are related to certain regions of the values of the basic diffraction parameters; namely, the size parameter x and the relative refractive index m . For Rayleigh Scattering the conditions are $x \ll 1$ and $x|m| \ll 1$ whilst for RDG these conditions improve to $2x|m - 1| \ll 1$ whilst $|m - 1| \ll 1$. The first condition can be interpreted as specifying that the phase shift within the particle is assumed to be very small. That is to say, the incident radiation field's behaviour and form outside the particle, neglecting the effects of the sample's interface, remains almost unchanged within the particle. The second condition describes particles that have a refractive index very close to that of the medium they are suspended in. This limits the applicability to particles that have a small size to wavelength ratio and are optically soft (we will later refer to this as near-index but in a broader sense). Since bacteria have at least 70% of their body consisting of water [30], if they are suspended in a water based medium then the optically soft assumption is satisfied. However their sizes are larger than say visible wavelength and so with respect to the visible spectrum, any theoretical model is bound to be erroneous. However, Wyatt was the first to examine RDG theory derived models and apply this to experimental multi-angle scattering data in the visible spectrum [61, 16, 3]. The derived models ranged from 2-layer spherical models, to homogeneous ellipsoids and rods, as well as ellipsoids and rods with a spherical inclusion. With respect to the 2-layer model it follows that such a spherical particle can be predicted to scatter light with amplitude $S(\theta)$ described mathematically as

$$S(\theta) = \frac{jk_o^3}{2\pi} ((m_1 - 1) \frac{4\pi r_1^3}{3} \sqrt{\frac{9\pi}{(2k_o a \sin(\theta/2))^2}} J_{3/2}(2k_o a \sin(\theta/2)) + (m_2 - m_1) \frac{4\pi (r_1 - \Delta r)^3}{3} \sqrt{\frac{9\pi}{(2k_o (r_1 - \Delta r) \sin(\theta/2))^2}} J_{3/2}(2k_o (r_1 - \Delta r) \sin(\theta/2))) \quad (2.6)$$

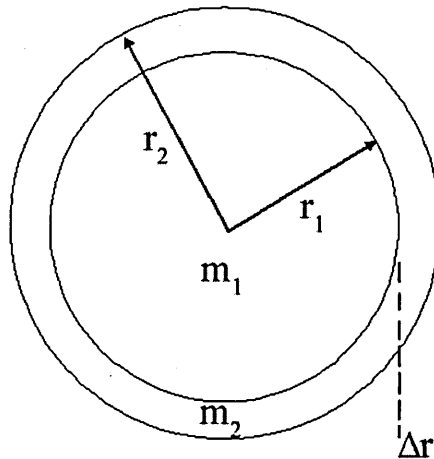


Figure 2.9: Diagrammatic depiction of the cross section of a 2-layered spherical model. The outer layer is placed at distance r_2 from the centre and has a thickness $\Delta r = r_2 - r_1$ within which a relative index of refraction m_2 is assumed; the inner core has a radius r_1 and relative refractive index m_1 .

where $\Delta r = r_2 - r_1$ models the thickness of the cell wall of the cell with overall radius r_2 and internal core (cytoplasm) radius r_1 . The corresponding relative refractive indices are denoted by m_1 and m_2 , θ is the scattering angle and $j^2 = -1$. The function $J_{3/2}$ is the Bessel function of order $3/2$. An illustration of such a 2-layer model can be seen in Figure 2.9 and our implementation of the mathematical model in Matlab of Equation 2.6 can be seen in Annex B.

Using the studies referred to above and the RDG derived models, Sethi and Patnaik [78] performed viability studies for RDG in conjunction with multi-angle light scattering. They confirmed that the RDG can analyse in real time light scattering patterns even from ‘washed-out’ peaks and valleys associated with high concentrations, that is to say, seemingly featureless curves of angular dependence, where it appeared that at least $10^4 - 10^5$ cells per ml of solution was evident in the total volume. Even though they relied for the analysis on homogeneous models, he reports a good agreement with microscopy on the sizes of bacteria, even when the RDG should in theory fail due to exceeding the applicability boundaries. However they omit results for the refractive index and only provide some estimated results in air. It may be the case that sizes can be successfully estimated but, since values for m are only estimated in air, this leaves the applicability of a homogeneous model open to debate. For example, if the refractive index distribution within the cell is highly irregular then an average refractive index would not be a good measure. The

same applies for highly skewed and exponential m -distributions. Finally, as is warned in [3, 79, 80], bacterial cells that are stored in water based environments will become rapidly dehydrated if introduced to a sealed or open air environment. This makes most measurements invalid for one who wishes to examine the cell in its growth cycle phase. An interesting find in the studies of Leuschner [81, 80] is the experimental realisation of the impossibility of identification of a cell in the bacteria domain based on the hypothesis of either a volumetric or size measurement for homogeneous models. This is due to the fact that in certain phases the change is negligible and because of the initial postulate that the predefined spherical shape of say a spore may be violated. An ovoid may have been a better model for bacterial spores. As a result one would monitor water content [82] or the protoplast/sporoplast volume ratio [83] within the spore by examining the mathematical relationships of certain optical properties [25, 84, 85] but it is doubtful whether this leads to identification or viability counting.

Findings of the above scattering theories and for patterns of angular dependence are summarised in Table 2.2. It should be noted that the values reported here are only the findings of the corresponding authors and only those that are directly related to the domain of bacteria. These values have been derived experimentally. There are many other references in the literature, as noted in this section, but either they are not derived directly from light scattering or have been found to agree with previous findings and as such are not included.

2.5 Mie scattering and the Rayleigh-Debye approximation

As we have mentioned earlier the simplest representation of a scattering particle is a homogeneous sphere. Scattering by such a particle is often referred to as **Mie theory** due to Gustav Mie's treatise of the scattering of light by particles of gold and the exact solution

¹wavelength in nm

² n/r : not reported

³[78]: The DAWN-EOS light scattering equipment of WyattTech was used. Refractive index value estimated in air.

⁴[25]: Laser interferometry, 2-layer Mie model.

⁵[80]: A goniometric module was used for collecting scattering patterns.

⁶[70]: Parametric fit to experimental data.

⁷[16]: Sealed chamber, single particle measurement; Refractive index was an 'air equivalent estimation'.

⁸[86]: Effect of heat on optical properties. The parameters indicate reduction in size, increase of refractive index with increasing temperature.

⁹[26]: A two layer concentric sphere model from Mie theory used to generate 10,000 theoretical patterns. Experimental data acquired from differential interferometry, and used to acquire the 4 parameters by non-linear least squares.

¹⁰[41]: the values reported are the average over 141 samples; size ranges obey the normal frequency distribution

Microorganism	Wavelength ¹	Medium	Refractive Index (RI)	Size (μm)/Shape
<i>Streptococcus bovis</i>	655	Water	n/r ²	0.8 – 0.99 (Ovoid) ³
<i>Bacillus subtilis</i>	655	water	1.44	0.67 × 1.17 (Rod) ³
<i>Escherichia coli</i>	655	water	1.35	0.99 × 1.1 (Rod) ³
<i>Bacillus sphaericus</i> spores	514	water	RI _{core} = 1.49 ± .02 RI _{cw} = 1.44 ± .01	r _{core} = 0.35 ± .04 r _{cell} = 0.50 ± .05 (Sphere) ⁴
<i>Bacillus sphaericus</i>	690	water	n/r	0.9 ± 0.06 (Sphere) ⁵
<i>Staphylococcus aureus</i>	633	water	1.66 ± 0.15	r _{core} = 0.954 r _{cell} = 1.04 (Sphere) ⁶
<i>Bacillus sphaericus</i> spores	515	Water/Air	RI _{core} = 1.54 ± .01 RI _{cw} = 1.47 ± .01	r _{core} = 0.43 ± .012 r _{cell} = 0.48 ± .007 (Rod) ⁷
<i>Clostridium filamentojum</i>	515	Water/Air	RI _{core} = 1.54 ± .01 RI _{cw} = 1.47 ± .02	r _{core} = 0.44 ± .011 r _{cell} = 0.49 ± .008 (Sphere) ⁷
<i>Staphylococcus epidermidis</i>	633	Water	1.54(±0.45) → (±0.22)	0.864 → 0.806 (Sphere) ⁸
<i>Lycoperdon pyriforme</i> spores	514	Water	RI _{core} = 1.43 ± .04 RI _{cw} = 1.49 ± .04	r _{core} = 1.37 ± .16 r _{cell} = 1.71 ± .11 (Sphere) ⁹
<i>Staphylococcus epidermidis</i>	514	Water	1.388	0.36 (homogeneous sphere) ¹⁰

Table 2.2: Literature Summary for values of optical properties derived from light scattering

offered therein [9]. Mie theory is a *separation of variables* approach to the solution of the scattering problem from Maxwell equations [87, pp365-367]. That is to say, from Maxwell equations and by performing appropriate eliminations and applying some simplifying assumptions, Mie describes the problem as a second order (partial) differential equation of the scattered field \mathbf{E}_s relating to the size parameter x , producing

$$\frac{\partial^2(x^2\mathbf{E}_s)}{\partial x^2} + \frac{1}{\sin\theta} \frac{\partial}{\partial\theta} \left(\sin\theta \frac{\partial}{\partial\theta} \left(\sin\theta \frac{\partial\mathbf{E}_s}{\partial\theta} \right) \right) + \frac{1}{\sin^2\theta} \frac{\partial^2\mathbf{E}_s}{\partial\phi^2} + x^2\mathbf{E}_s = 0 \quad (2.7)$$

In Equation 2.7 the scattering field (\mathbf{E}_s) is described as a series of electric (H) and magnetic (M) oscillations ($\mathbf{E}_s \sim (\mathbf{H}_s, \mathbf{M}_s)$). The simplifying assumptions mentioned earlier are the boundary conditions which must hold at the surface of the sphere. That is to say, the magnetic field and permittivity being unchanged inside and outside the particle.

As a result the *separation of variables* can be identified by grouping candidate solutions of Equation 2.7 to

- Electrical oscillations only; $|\mathbf{M}_s| = 0$.
- Magnetic oscillations only; $|\mathbf{H}_s| = 0$.
- Regular periodic oscillations; that is, addition of the integrals resulting from the above two cases.

By relating the above solutions he then formulates the scattering series and the scattering elements accordingly. These scattering coefficients for the Mie (scattering) series are described in Section 3.2, page 43, for the solution provided by Volkov and Kovach [57] of which Mie's solution is nowadays the subcase of a homogeneous sphere. That is to say, for n layers, the scattering coefficients are found by putting $n = 1$. In Section 3.2 all elements are described for the case of n -layered concentric sphere and so further details will not be given in this section. However, we should report two main results that are provided within the work of Mie in [9], and constitute the physical basis of Mie scattering. For the particulars, the reader is referred to the English translation from Mie's original manuscript by Sandia Laboratories [88]¹³.

Mie Axiom: The radiation reflected from a small (homogeneous) sphere essentially comprises a finite number of partial waves, but the number of partial waves and their intensity increases as the sphere becomes larger.

¹³In particular the theorems in pages 52 and 53.

Mie's Theorem: Given a constant concentration and a very fine distribution the scattered radiation increases as particle diameter increases. However, when particles become quite large, it reaches a maximum (at the forward direction) and then decreases rapidly; with weaker and weaker maxima (in the angular pattern) which may still appear.

To summarise we would say that the Mie scattering theory is applicable for spherical particles and is a direct solution from Maxwell equations by separation of variables. It calculates the field inside and outside the particle and as a result there is no need for making an assumption concerning the total internal field. However solving in the same manner for non-spherical particles or inhomogeneous particles is difficult, if not impossible. Alternatively, one would assume the functional behaviour of the internal field and solve by approximation.

The latter method is the essence of the **Born** or **Rayleigh-Debye approximation**. That is to say, one would rewrite the scattering equation as an integral over the particle's volume [89, for example] by invoking the far-field form of the Green's function (G_o). As such, to calculate from

$$\mathbf{E}_s = \nabla \times \nabla \times \int_{V_o} (m(\mathbf{r}) - 1)E(\mathbf{r})G_o(\mathbf{k}_s, \mathbf{k}_i)dV \quad (2.8)$$

where the unit vectors $\mathbf{k}_s, \mathbf{k}_i$ designate the direction of scattering and incidence respectively. The functional G_o is Green's function defined as $G_o(\mathbf{k}_s, \mathbf{k}_i) = \exp(jk_o|\mathbf{k}_s - \mathbf{k}_i|)/4\pi|\mathbf{k}_s - \mathbf{k}_i|$ and $m(\mathbf{r})$ is the refractive index distribution. The total internal field of the particle $E(\mathbf{r})$ is unknown.

Born from a quantum mechanics perspective, and *Debye* whilst working on extending the Rayleigh scattering of light theory, assumed that within the particle there are relatively weak interactions between the invoked potentials and so only single scattering events from infinitesimal volume scatterers are to be taken into account. In effect, the field inside the particle is taken to be approximately equal to that of incidence. That is to say,

$$E(\mathbf{r}) \cong E_i(\mathbf{r})$$

which can now be substituted to Equation 2.8 to get an *approximate solution* for the scattering field at 'infinite' distance from the scatterers (far-field). This is the case, for example, with Wyatt's two layer spherical model of page 27, resulting in the approximate solution of the scattering amplitude function of Equation 2.6.

In a sense, the Rayleigh-Debye approximation translates to the incident field being 'distorted' with a very small phase shift within the particle ($2x|m - 1| \ll 1$) and subsequently producing the scattered field. The latter can only apply to particles that have a refractive index very close to that of the medium they are suspended in, hence the condition $|m - 1| \ll 1$ (near-index).

2.6 On equipment based on light scattering

As we have seen in Section 2.4, in theory, the detailed light intensity pattern of angular dependence, scattered by an individual particle, is a complex function of size, shape, orientation and internal structure. In the Rayleigh region, the amount scattered at a specific angle is primarily a function of volume of the particle, but is insensitive to the particle shape. This sets an upper limit on the sizes of particles whose shape can be investigated using visible radiation, and in practical terms it cannot exceed a few tenths of a micrometer. However at sizes larger than 0.7 of a μm , the Rayleigh-Debye theory would be applied. For particle sizes greater than about $40\mu\text{m}$, the spatial scattering profile becomes increasingly complex, until for particles much larger than the wavelength of the illuminating incident source concepts from geometrical optics can be used to describe the spatial scattering and infer particle properties. The delivery of particles singly [18] into the illumination measurement space has an upper limit in size in the order of $100\mu\text{m}$ and is described in terms of polar scattering, that is to say $0 - 180^\circ$ in the plane of the axis of the incident illumination and the azimuthal scattering (i.e. at 360° revolution around the illumination axis).

Measuring light scattering in a single azimuthal plane, that is to say intensity measurements in a single plane containing the illumination source, is the most common approach. The polar intensity variation from an unknown particle led Wyatt to postulate that bacteria can be identified by the manner in which they scatter light [86]. This work led to the first commercial instrument [61] and a succession of other researchers who refined and optimised this technology with the latest advances: by Malvern Instruments [29] which uses a goniometric module for 'scanning' from $12^\circ - 152^\circ$ at a travel speed of 20° per second; and [18] which uses an array of optical fibres to record scattering throughout the polar arc of approximately 180° about scattering particles in a cuvette, liquid flow, or electro-rotation assembly. However these instrumental geometries have the limitation that they do not record the effect that orientation has on the light scattering pattern and as a result

cannot necessarily infer the characteristics of a non-spherical particle. Hence in their initial works both Wyatt and Ulanowski [3][13] work with cells of approximately spherical shape as is the case with spore inclusions. As result, Wyatt later on incorporates a 360° polar scanning module of photodetectors placed symmetrically opposite one another [19] so as to capture the effect of orientation. This allowed for the characterisation of spheres, rods and generally labelled non-spherical particles.

In the DAWN-A light scattering instrument of Wyatt Technologies, an alternative to the instrument presented in [19], a spherical metal chamber was pierced by 72 small and 2 large detector apertures. The small apertures were arranged in 4 azimuthal planes of 18 apertures each set at intervals of 45°. Each small aperture was linked to an optical fibre which transmitted light to a photodetector unit. The two large apertures were used for intensity measurements on the horizontal plane with reference to the incident light source. This instrumentation setup was the culmination of trying to combine polar and azimuthal scattering studies. Further research on this geometric instrumentation setup has been made by the National Institute of Standards and Technology (USA) in [90] and [91], and it is currently under refinement.

In this instrument (Multi-detector Hemispherical Polarised Optical Scattering Instrument, MHPOSI) three lasers at different wavelengths allow for multi-wavelength investigations. The laser passes through a power stabiliser, a polariser, a retarder at half the wavelength of the selected illumination source, a lens and a pinhole before being directed to and focused with a concave mirror through the centre of the light detector/receiver. The hemispherical detector holder consists of a hemisphere of inner radius 75mm with 3mm removed from its opening end. On its surface 31 apertures are placed of which one is left open for the insertion of the light incident beam whilst the opposite aperture allows the forward beam to exit the system and is subsequently blocked by a beam trap. In order to facilitate fundamental studies of the spatial light scattering behaviour of individual spherical and non-spherical particles, a high resolution CCD intensifier camera, in combination with a retractable low power microscope with $\times 6$ objective, also uses one of the said apertures. The 28 scattering detection points cover 45% of the scattering hemisphere. With this instrument two applications have been covered; namely, microroughness of silicon, and particulate contaminants from 181nm to about $20\mu\text{m}$ modelled by polystyrene latex spheres. It must be noted that the half-way retarders are used for measuring the Mueller matrix elements, a subset of it to be exact, in order to improve the sensitivity of detection and for switching the polarisation state of the observed scattering intensities. Finally, the output is normalised by the signal acquired from the incident source so as to compensate

for intensity variations.

The most recent development in terms of hemispherical scattering acquisition arrangements has been reported by Micro Imaging Technology Incorporated (California, US). In their implementation [92], an array of optical sensors at polar and azimuthal angular positions is utilised to detect scattering from a glass sample vial which incorporates a heater at its bottom so as to circulate matter within the cuvette. For each bacterial species, the intensity curve is mapped to a probability density function, where the frequency of occurrence of a number of intensity curves can be found. Subsequently the derived signal is compared with the histograms of known curves to identify qualitatively the microscopic particles present. The occurrences, as defined in the invention, are event descriptors, that is, a library of scattering patterns that have been already tested and found to be true, eliminating the need for frequent calibration. The discrimination procedure is the known statistical techniques of Discriminant Functions [93], but they are not mentioned explicitly.

Consequently, it must be clear that there has been quite extensive research on the instrumentation of angular light scattering and all manufacturers agree that in all cases the light scattering pattern of polar and azimuthal planes can be measured and the angular resolution will depend upon the number of detector points used. Furthermore, single particle scattering measurements are possible. It may be preferable to use supporting devices such as electro-rotation or electrophoresis, but it is not essential, depending on how long the particle stays in the field of view of the incident radiation. Advances in terms of light scattering measurements lie predominantly in the refinement of theories to interpret such data as described in Section 2.4, and in reducing the background noise from artefacts within the sample. In the bacteria characterisation case in water environments, this may range from dead cells to particulate matter of water that has undergone treatment, for example 'clouds' of particles of chlorine.

2.7 Discussion

It should be evident that bacteria are of great diversity in terms of size, the processes by which they exhibit growth through division and environmental effects due to changes in light, oxygen, temperature, pH and others. Furthermore there is a need for experimental studies that consider the inhomogeneous nature of the cell in terms of the inference of the internal optical properties of the cell. From the studies that we have cited we draw the following conclusions, which are treated as reasonable assumptions and aims within our

work.

1. Bacteria in water based mediums have a refractive index close to that of water. As a result they can be modelled as near-index cells where absorption can be considered to be negligible.
2. The sizes for bacteria are indeed diverse but for drinking water, they can be considered to be from approximately $1\mu\text{m}$ to $4\mu\text{m}$.
3. The size distributions for modelling populations must also be examined and in a way that incorporate skewness measures.
4. The commonly used cytoplasm-wall model for bacterial cells is limiting and has to be extended to incorporate at least most of the dominant features of the cell.
5. Spherical models or spherical equivalents do not incorporate physical justification of inferred properties and do not explore the effect of non-sphericity on the scattering patterns.
6. There exist cases where ambiguous results indicate the need for extension of any mathematical solution to other characteristic external morphologies, as in the case of ellipsoidal particles.
7. Forward scattering has been investigated and seems to offer no contribution towards identification. The same is true for exploring concentrations or volumetric inference. That is to say, by simply inferring sizes of bacteria, since too many of them present the same volume, it may be impossible to infer a characterisation or partial identification protocol.
8. Incorporation of the average polarisability of the cell within a proposed model would lead to a better understanding of the internal structure contributions to light scattering.

Chapter 3

On inhomogeneous particles of spherical symmetry

In this chapter we indirectly use the Bohren-Huffman solution to the coated (2-layer) sphere problem [4, pp 181-183; 483-489] which leads to the Volkov-Kovach solution of the n -layer sphere problem [57], in order to validate our solution (Section 3.3) for the near-index particle problem, as is the case with bacteria in water based environments. We strongly emphasize the fact that we are mostly interested in potable water, as in drinking water distribution systems [94]. For the reasons outlined in Chapter 2 we provide solutions to the problem definition:

Definition 3.1. From a particle/cell, of assumed *size* and *spherical shape*, which is illuminated by a (laser) beam, of specified *intensity* (I_0), *wavelength* (λ) and *polarisation*, determine the secondary radiation (scattered light intensity) in all directions, assuming that the internal composition resembles a multi-layered concentric structure.

Our main result (Section 3.3) generalizes a modification to the Rayleigh-Debye approximation (mRDG)¹, also known as the Born approximation in the quantum mechanics field, developed in [95] and used by Sloot in [96] in the problem domain of blood cells (2-layer model). The approximation model developed in this chapter has a direct application to the problem of Definition 3.1 for virtually all spherical bacterial cells in water and is, to the best of our knowledge, the first generalisation to n concentric layers. Finally, the Mie scattering program code (Annex A) developed in Matlab, as part of our validation procedure, outlined in Section 3.2, is the first to appear².

¹The G in mRDG relates to the Gans approximation which is used within the R-D approximation. This is done for historical reasons and in order to keep in line with most of the bibliographic materials used within

²Most of what is said in the subsequent sections has been published in the European Society for Modelling and Simulation Proceedings of June 2003.

3.1 Introduction

We start by briefly introducing a simplified terminology used in the absorption and scattering by small particles, in the form of definitions that are consistent with the previous chapters, where the corresponding terms are used in a more general (laser) optics setting. We provide explanations for the use of such definitions that are based on specific assumptions, which will be used throughout this thesis.

A plane wave is usually found to be a good approximation to most light waves [97] and is one where the direction of the magnetic and electric fields are confined to the propagation direction. Since the plane is two-dimensional the electric vector at a point in space can be decomposed into two orthogonal components. These two components may differ in amplitude and phase. By considering the locus of points, that is to say the shape of the curve traced out in a fixed plane by the electric vector, we obtain a description of the polarisation state.

Definition 3.2. **Polarisation** is a property of electromagnetic radiation, such as light, by which a harmonic plane wave exhibits a specific curve (the locus of points of the electric field) with respect to the end point of the electric vector.

If the two orthogonal components are in phase then the polarisation is said to be linear. If the orthogonal components have the same amplitude but with a phase difference $\pi/2$, then we have circular polarisation because the sum of these components will rotate in a circle. Depending on the way the electric vector rotates we have right-hand or left-hand circular polarisation. If the two components either do not have the same amplitude or do not exhibit a phase difference $\pi/2$ (or both), then the electric vector will generate a locus of points described by an ellipse. This is known as the polarisation ellipse.

Light can be polarised by reflection, refraction or by oblique transmission via circular or elliptical glass surfaces. In that sense, coherent, polarised light, as in the case of lasers in the visible spectrum, which illuminate a suspension of particles, may become partially polarised. This can be interpreted as a statistical correlation between the components of the electric field. The collection of particles is always assumed to follow a particular size distribution describing the largest linear dimension, and it is often assumed that a particular polarisation state has taken place with reference to the scattering plane.

Definition 3.3. A measure of linear spatial extent, that is the magnitude of width, height or length in a straight line, in a dimensional space is called the **linear dimension**.

A small particle is an invisible unit of matter to the naked eye, but not in the traditional particle physics sense, where a small particle is also a ‘fundamental’ particle. Experimental considerations have also to be taken into account, so that low light levels produced by scattering can be observed for a source in the visible spectrum and with detectors placed at angular positions. Small particles are defined so as to have a size of largest linear dimension, in terms of length, height or width depending on the spatial viewpoint. In that sense the far ends of a size distribution may include particles with size ranging from that of individual molecules to prokaryotic cells and protozoa. In as much,

Definition 3.4. Let d be the largest linear dimension of the particle and m its relative refractive index with respect to the surrounding medium, and let λ denote the incident light wavelength. If a particle’s linear dimension obeys the rule, $d \leq \frac{20\lambda}{|m-1|}$, then the particle is said to be a **small particle**.

This does not mean that there is a need to attempt to cover the whole of this range, as this lies within the applicability boundaries of a theory or approximation model. As mentioned earlier, bacteria have a maximum linear dimension of only a few microns (μm); whilst the largest of its aggregates, say a chain like or a self-similar structure, is usually not much larger than about $40-60\mu\text{m}$, but this is a rarity in potable water supply networks [30, 11].

Definition 3.5. Index of refraction or the **refractive index** for radiation of some frequency, is defined as the ratio of the speed of the electromagnetic wave (as in the case of light), in free space to its speed in a medium.

It can be easily shown that Definition 3.5 is equivalent to an alternative definition given in terms of angles of incidence and refraction of the wave [87, pp377-378] at a plane boundary; that is to say, either expressed as the ratio (number) of the sine of angle of incidence to the sine of the angle of refraction, or by the expression $\sqrt{\epsilon\mu}$ attributed to Maxwell³. For example, Kou in [98], calculated that the index of refraction for pure/distilled water solution, at 20°C and for $\lambda = 589\text{nm}$, is 1.33. This effectively means that when light passes out of air into water, the sine of the angle of incidence is 1.33 times the sine of the angle of refraction. For particle(s) suspended in water that may have the greatest part of their bodies composed of water, then the refractive index closely matches that of 1.33. This results in a *relative refractive index* close to unity ($m \rightarrow 1$).

³ ϵ is the electric permittivity, μ is the magnetic permeability

A complex index of refraction can be defined for particles that absorb as well as scatter light and it is related to the wavelength of incidence. The imaginary part of the complex (relative) refractive index number accounts for the amount of absorption, that is to say a decrease in the intensity of light. The real part of the complex (relative) refractive index has been shown to relate to the amount of water present within a particle or cell [25, Chapter 2].

Definition 3.6. If m is the relative refractive index, taken to be in the case of an inhomogeneous particle the average over its volume, of a small particle relative to that of its surrounding medium, then a **near-index particle** will satisfy the condition $|m - 1| \ll 1$.

Depending on the theory used, this condition is to be taken in a rather heuristic sense. As such, a near-index particle is a particle that ‘closely’ matches⁴ the refractive index of the medium it is suspended in. Hence, even if the condition of Definition 3.6 is relaxed to $|m - 1| < 1$, then the particle is still considered to be a near-index particle. As a result, it is often assumed that, for the near-index regime, the Lorentz-Lorenz formula⁵

$$\frac{m^2 - 1}{m^2 + 2} \approx \frac{\mu^2 - 1}{\mu^2 + 2} \frac{V_t}{V_o} \quad (3.1)$$

where μ is the magnetic permeability, can be simplified since $m + 1 \rightarrow 2$ and $m^2 + 1 \rightarrow 2$. It follows that $m^2 + 2 \rightarrow 3$ and bearing in mind that $m \neq 1$, Equation 3.1 simplifies to

$$\frac{m^2 - 1}{m^2 + 2} = \frac{m + 1}{m^2 + 2} (m - 1) \xrightarrow{m \neq 1} \frac{2}{3} (m - 1) \quad (3.2)$$

$$\frac{2}{3} (m - 1) \approx \frac{\mu^2 - 1}{\mu^2 + 2} \frac{V_t}{V_o} \quad (3.3)$$

where V_o is the volume occupied by the particles in a total volume V_t . A number ratio or density is often used instead, which is the number of particles per unit volume. For example, the absorption or decrease in intensity by a slab would be approximated by $2\pi N k^{-3} \Re\{S(0)\}$ (refer to Equations 3.4, 3.5 and Definition 3.8). Here \Re is the real part of $S(0)$. An additional assumption for Equation 3.2 is that of the far-field.

Definition 3.7. Assume a number of observation points placed on the circumference of a circle of radius R , where the sample, which includes the particle under observation, is

⁴needless to say the term is used loosely

⁵Maxwell has also derived the same formula but the two scientists, Lorentz and Lorenz, derived it independently and at about the same time, but their result was published first.

placed at the centre. If the largest linear dimension d of the particle under observation is much smaller than that of the distance vector \mathbf{R} , with magnitude R , hence $d \ll R$, then the total number of angular observations portrays measurement of the long-distance field of the scattered light and will be called the **far-field** measurement.

Experimentally speaking we always refer to remote sensing in the sense that the detector is always at a distance larger than that of the largest linear dimension, which in our case is also true in the sense of a far-field. Additionally, the assumption of a far-field quite often simplifies mathematical manipulation on the estimation of Scattering Fields and Light Intensity (in arbitrary units). The latter is due to the fact that if the magnitude of the observation vector \mathbf{R} is $R < d^2/\lambda$, then the scattered field from a particle $\mathbf{E}_s(\mathbf{r})$ has complicated amplitude and phase variations because of interference between different parts of the particle. At the far-field observation point (we will illustrate this later for plane P in Figure 3.5) the scattering field behaves as a spherical wave, so that

$$\mathbf{E}_s(\mathbf{r}) = \mathbf{S}(\mathbf{k}_i, \mathbf{k}_s) \frac{e^{jkR}}{R} \mathbf{E}_i(\mathbf{r}) \quad (3.4)$$

where \mathbf{S} denotes the scattering matrix, which takes the place of the transformation matrix in the Stokes matrix formulation [99, p123] [100, p34] [101, pp33–36]. The scattered field \mathbf{E}_s is observed at the direction of the unit vector \mathbf{k}_s and is expressed in terms of the incident field $\mathbf{E}_i(\mathbf{r})$ which in turn follows the direction of a unit vector \mathbf{k}_i . The scattering matrix \mathbf{S} explains the phase and magnitude of the scattering fields by means of four amplitude functions S_1, S_2, S_3, S_4 , all functions of (θ, ϕ) . Depending on the orientation of a particle and assuming that the initial position is such that the amplitude functions give the form of scattering matrix

$$\mathbf{S} = \begin{bmatrix} S_2 & S_3 \\ S_4 & S_1 \end{bmatrix} \quad (3.5)$$

then the relationship with the scattering matrix of Equation 3.5 and for the same particle being rotated by 180° is such that,

$$\mathbf{S} = \begin{bmatrix} S_2 & -S_4 \\ -S_3 & S_1 \end{bmatrix} \quad (3.6)$$

The reader is referred to [100, pp.47–49] for the details on selection of the matrix form. It is noted that the reciprocal position, that is the rotation of the particle by 180° , results in change of the sign and transpose for S_3 and S_4 , but the scattering matrix form

remains unchanged since the conjugate is symmetric. The proof follows by the reciprocity theorem [102, p17, p171 and lemmas therein] for vector waves. By definition [4, p112]:

Definition 3.8. Spherical particles and in general any cylindrically symmetrical particle with respect to the direction of propagation of the incident light, result in S_1, S_2 being dependent only on the scattering angle (say θ), and not on the ‘rotational’ (azimuthal) angle (say ϕ), due to absence of particle orientation effects, whilst $S_3 = S_4 = 0$ and S will be diagonal.

The proof follows from symmetry on the plane of the source incidence with reference to that of scattering.

3.2 The exact solution of the n -layer problem

In this section we outline a recursive solution to the problem of scattering by multi-layered spherical particles ⁶, provided by means of Mie scattering series. We are using convergence criteria and the usual functions and notation, as do most of the well known solutions to lesser problems; the properties of the particles are provided in a form applicable to validating the near-index particle solution. The Mie theory or exact solution to this problem is valid in a much larger range of the size parameter and refractive index. As a matter of fact it is often referred to as ‘*rigorous scattering theory for spheres of arbitrary size*’. Since it is an exact solution it can be used for validation of any model which may be a special case (as in the near-index case) or any type of approximate solution.

In any definition of the problem the prerequisite for sphericity is essential if the solution is to be taken as being exact in the true sense. That is to say, it would be used as an approximation depending only on volume to an asymmetric, non-spherical particle, but that would only be used as an approximate spherical ‘*equivalent*’ to an otherwise different (in geometrical shape) particle [75].

Even though we are interested in the microscopic world (small particles), one would in theory solve the heterogeneous particle problem defined by Maxwell’s equations. As we have seen in Section 2.5, Gustav Mie [9] was the first to provide a solution to the scattering and absorption by homogeneous spheres in that sense. Since then several papers

⁶The code we have developed, which is provided in Annex A is the first set of Mie functions to appear, developed in MATLAB (v6, R12; ©Mathworks). When this manuscript was written, it had been featured in T. Wriedt’s *e-Library EM Scattering codes*, and has been used as a validation program against other codes/methods by Dr Hu Cang of Stanford University (USA) and professor M. Brio of University of Arizona in Tucson, USA.

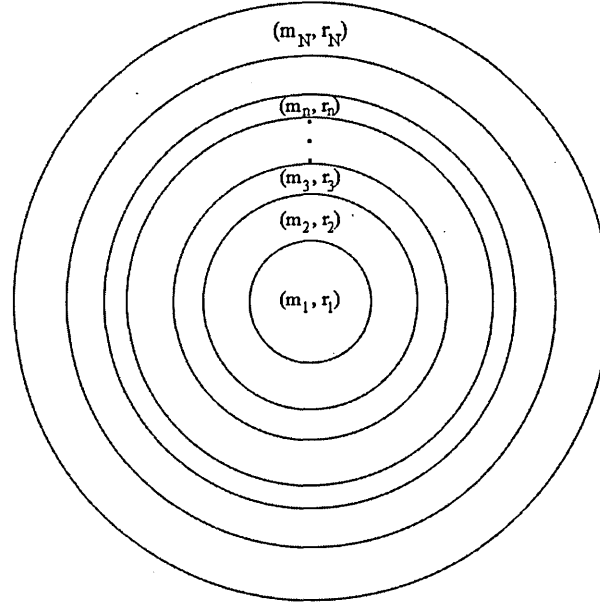


Figure 3.1: An n -layered concentric sphere: $i = 1, 2, \dots, n, \dots, N$

have appeared that refine the theory in terms of computational complexity, approximate for spheres with inclusions [101] and so on. However it should be emphasised that in spite of the advances of processing power, to use Mie theory variants in populations of cells or multiple models still involves a great amount of calculations. As a result, Mie theory for inhomogeneous particles still is computationally expensive and cannot be used for real-time analysis of bacteria.

The problem of Definition 3.1 is illustrated in Figure 3.1. In general, we have $i = 1, 2, \dots, n, \dots, N$ spherical compartments placed concentrically around the core with radius r_1 and relative refractive index m_1 . For simplicity we are using the size parameter notation x_i where $x_i = (2\pi r_i/\lambda)$, with λ being the wavelength of the incident light source. It is assumed that the magnetisation of the particle is governed by the magnetisation of the ambient medium, and hence the magnetic permeability between the particle (μ_i) and the medium (μ) is unchanged (i.e. $\mu = \mu_1 = \dots = \mu_N$).

The explicit equations for the Mie coefficients a_n and b_n of the scattering series of the n -layered inhomogeneous sphere [57], can be used in that respect. In general these equations have the form

$$a_n = \frac{\psi_N^n ((\psi)_{N,N}^n - A_{N-1}^n (\kappa)_{N,N}^n) - m_N (\psi)_{N,N}^n (\psi_{N,N}^n - A_{N-1}^n \kappa_{N,N}^n)}{\xi_N^n ((\psi)_{N,N}^n - A_{N-1}^n (\kappa)_{N,N}^n) - m_N (\xi)_{N,N}^n (\psi_{N,N}^n - A_{N-1}^n \kappa_{N,N}^n)} \quad (3.7)$$

$$b_n = \frac{m_N \psi_N^n ((\psi)_{N,N}^n - B_{N-1}^n (\kappa)_{N,N}^n) - (\psi)_N^n (\psi_{N,N}^n - B_{N-1}^n \kappa_{N,N}^n)}{m_N \xi_N^n ((\psi)_{N,N}^n - B_{N-1}^n (\kappa)_{N,N}^n) - (\xi)_N^n (\psi_{N,N}^n - B_{N-1}^n \kappa_{N,N}^n)} \quad (3.8)$$

where

$$A_i^n = \frac{m_{i+1} \psi_{i+1,i}^n (\psi)_{i,i}^n - m_i (\psi)_{i+1,i}^n \psi_{i,i}^n + A_{i-1}^n a_i^n}{m_{i+1} \kappa_{i+1,i}^n (\psi)_{i,i}^n - m_i (\kappa)_{i+1,i}^n \psi_{i,i}^n + A_{i-1}^n \bar{a}_i^n} \quad (3.9)$$

$$B_i^n = \frac{m_{i+1} \psi_{i,i}^n (\psi)_{i+1,i}^n - m_i \psi_{i+1,i}^n (\psi)_{i,i}^n + B_{i-1}^n b_i^n}{m_{i+1} \psi_{i,i}^n (\kappa)_{i+1,i}^n - m_i (\psi)_{i,i}^n \kappa_{i+1,i}^n + B_{i-1}^n \bar{b}_i^n} \quad (3.10)$$

and

$$\begin{aligned} a_i^n &= m_i \kappa_{i,i}^n (\psi)_{i+1,i}^n - m_{i+1} (\kappa)_{i,i}^n \psi_{i+1,i}^n \\ \bar{a}_i^n &= m_i \kappa_{i,i}^n (\kappa)_{i+1,i}^n - m_{i+1} (\kappa)_{i,i}^n \kappa_{i+1,i}^n \\ b_i^n &= m_i (\kappa)_{i,i}^n \psi_{i+1,i}^n - m_{i+1} \kappa_{i+1,i}^n (\psi)_{i+1,i}^n \\ \bar{b}_i^n &= m_i (\kappa)_{i,i}^n (\kappa)_{i+1,i}^n - m_{i+1} \kappa_{i,i}^n (\kappa)_{i+1,i}^n \\ A_0^n &= B_0^n = 0 \\ 1 &\leq i \leq N-1 \end{aligned} \quad (3.11)$$

In Equations 3.7-3.11, the notation used is such that $\psi(m_L, x_i) = \psi_{L,i}^n$; $\psi_n(x_i) = \psi_i^n$; $\psi'(m_L, x_i) = (\psi)_{L,i}^n$; $\psi'_n(x_i) = \psi_i^n$; and similarly for the functions κ and ξ . The reader is reminded that the functions ${}^7 \psi(\varepsilon)$ and $\kappa(\varepsilon)$ follow the Ricatti-Bessel function of the first kind (implemented in Matlab function: RB1) and second kind (implemented in Matlab function: RB2) respectively in Annex A.2, whilst $\xi(\varepsilon)$ follows the Hankel function [103], internally set in the Matlab function: nlayerScaCoeff, Annex A.3. It follows that, $\xi(\varepsilon) = \psi(\varepsilon) + j \kappa(\varepsilon)$, for $n \in \mathbb{N}$. The reader should also bear in mind the recurrence relations used in the code of Annex A,

$$z_{n-1}(\varepsilon) + z_{n+1}(\varepsilon) = \frac{2n+1}{\varepsilon} z_n(\varepsilon) \quad (3.12)$$

$$(2n+1) \frac{d}{d\varepsilon} z_n(\varepsilon) = n z_{n-1}(\varepsilon) - (n+1) z_{n+1}(\varepsilon) \quad (3.13)$$

where z denotes either of the said Bessel functions.

An important consideration to be made is the number of terms (a_n, b_n) required to get a good approximation to the limit of the scattering series. The convergence criterion of [10] is used, even though it was derived and it is considered to be optimal only for the

⁷note that $z'(\varepsilon) \equiv \frac{d}{d\varepsilon} z(\varepsilon)$

homogeneous sphere problem. There is no evidence in the literature that this criterion is flawed for n layers and so it is adopted here. In effect, the maximum number of terms n_c to be calculated, for $x = x_N$, follows the schema

$$n_c = \begin{cases} x + 4x^{1/3} + 1, & x \in [0.02, 8] \\ x + 4.05x^{1/3} + 2, & x \in (8, 4200] \\ x + 4x^{1/3} + 2, & x \in (4200, 20000] \end{cases} \quad (3.14)$$

However, it should be emphasized that it has been indicated in many publications (e.g. [104]) that even if only the criterion $(x + 4.05x^{1/3} + 2)$ is used, the difference in the results, for ‘small particles’, is negligible.

Equations 3.7-3.8 in conjunction with Equation 3.14, can be used to determine the scattering (C_{sca}), extinction (C_{ext}) and backscattering (C_{bac}) cross sections and therefore the corresponding efficiencies. These *efficiencies* are dimensionless cross sections in their true meaning. For example, the extinction efficiency, denoted by Q_{ext} , may be interpreted as the proportion of the area C_{ext} which is in the ‘shadow’ cast upon a detector by a particle. That is to say, we assume that a particle or a collection of particles illuminated by a light source generates light scattered within the cone of detection of a detector. The proportion of the area by which the incoming radiation will be reduced on the detector is C_{ext} with an efficiency Q_{ext} . Following the same series form for that of a homogeneous particle but taking into account that the radius of the multi-layered sphere is r_N (corresponding size parameter x_N), we have

$$\begin{aligned} Q_{sca} &= \frac{2}{x_N^2} \sum_{n=1}^{n_c} (2n+1) (|a_n|^2 + |b_n|^2) \\ Q_{ext} &= \frac{2}{x_N^2} \sum_{n=1}^{n_c} (2n+1) \Re\{a_n + b_n\} \\ Q_{bac} &= \frac{1}{x_N^2} \left| \sum_{n=1}^{n_c} (2n+1) (-1)^n (a_n - b_n) \right|^2 \end{aligned} \quad (3.15)$$

where \Re denotes the real part of the resulting complex number $(a_n + b_n)$. From Equations 3.15 we can now approximate the Absorption Efficiency Q_{abs} as $Q_{abs} \cong Q_{ext} - Q_{sca}$. Note that the condition $C_{abs} \leq C_{ext}$ must always be satisfied.

For obtaining detailed information on the shape of the angular scattering pattern, there is a need to calculate the scattering functions ⁸, denoted here by S_1 and S_2 . These functions describe the scattered field and can be used when we approximate the so-called *far-field*; that is to say, the scattering observation is made at a distance sufficiently larger than that of the particle’s largest linear dimension. These expressions follow the functional form,

⁸see Equation 3.5 and the discussion that follows straight after

$$S_1(\theta) = \sum_{n=1}^{n_c} \frac{2n+1}{n(n+1)} (a_n \pi_n + b_n \tau_n) \quad (3.16)$$

$$S_2(\theta) = \sum_{n=1}^{n_c} \frac{2n+1}{n(n+1)} (a_n \tau_n + b_n \pi_n) \quad (3.17)$$

and have been implemented as a Matlab function (`nlayerAmp`) in Annex A.3. Here the functions π and τ are the Associated Legendre Polynomials (calculated in Matlab function: `ALegendr`, implemented in Annex A.2). That is to say, π and τ are the angle (θ) dependent functions and can be computed by upward recurrence [4, p95] from the relations

$$\pi_n = \frac{2n-1}{n-1} \pi_{n-1} \cos \theta - \frac{n}{n-1} \pi_{n-2} \quad (3.18)$$

$$\tau_n = n \pi_n \cos \theta - (n+1) \pi_{n-1} \quad (3.19)$$

beginning with $\pi_0 = 0$ and $\pi_1 = 1$. The maximum number of terms (n_c) to be calculated in the series of Equations 3.16 - 3.17 follows the schema of Equation 3.14. Consequently, the relevant Stokes parameters can be computed by applying [4, p65]

$$\begin{aligned} S_{11} &= \frac{1}{2}(S_2 \tilde{S}_2 + S_1 \tilde{S}_1) = \frac{1}{2}(|S_1|^2 + |S_2|^2) \\ S_{12} &= \frac{1}{2}(S_2 \tilde{S}_2 - S_1 \tilde{S}_1) = \frac{1}{2}(|S_1|^2 - |S_2|^2) \\ S_{33} &= \frac{1}{2}(\tilde{S}_2 S_1 + S_2 \tilde{S}_1) \\ S_{34} &= \frac{1}{2}(S_1 \tilde{S}_2 - S_2 \tilde{S}_1) \end{aligned} \quad (3.20)$$

where the symbol \tilde{S} denotes the complex conjugate of S and $j^2 = -1$. The physical meaning of the scattering amplitudes S_1 and S_2 relates to the incident light being polarised perpendicular and parallel to the scattering plane, respectively. Furthermore they describe the amplitude and the phase of the scattering waves. As a result, using the scattering elements as defined in Equations 3.20 one would, in theory, calculate all relevant information about the particle and its optical behaviour; for example, the light intensity scattered by a multilayered spherical particle for any state of polarisation (Matlab function: `nlayerIntensity` implemented in Annex A.2).

Since the scattered intensity, denoted by $I_s(\theta)$, is directly related to the state of polarisation of the incident light intensity I_o to a particular scattering plane⁹, we often need to obtain results for *parallel* and *perpendicular* polarisation as well as *unpolarised* incidence. The latter is of particular interest in experimental work. In this case, it can be shown [100, p35] that

⁹in most cases this would imply the horizontal scattering plane and is also adopted here

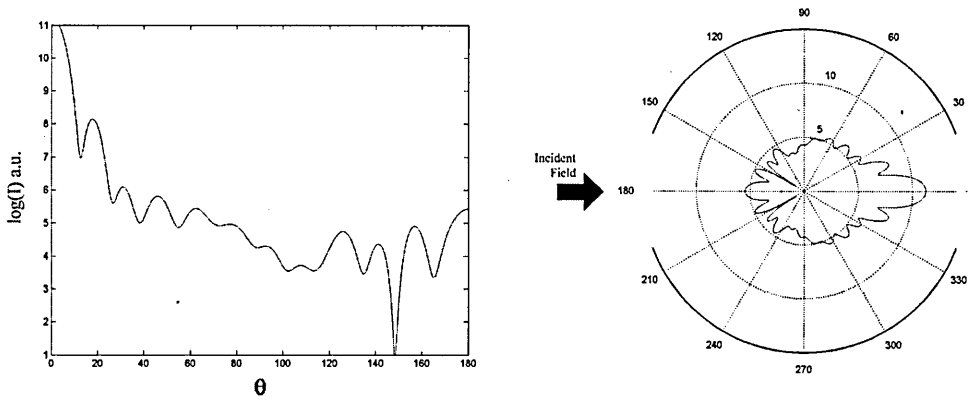


Figure 3.2: A 2-layer sphere intensity pattern, following the results for *B.sphaericus* spores at $\lambda = 0.514\mu\text{m}$ [3]. Left: Light Intensity Pattern; Right: Polar plot at $\theta \in (0, 180^\circ)$.

$$I_s(\theta) = \begin{cases} \frac{1}{X^2}(S_{11} + S_{12})I_o, & \text{parallel polarisation} \\ \frac{1}{X^2}(S_{11} - S_{12})I_o, & \text{perpendicular polarisation} \\ \frac{1}{X^2}(S_{11})I_o, & \text{unpolarised} \end{cases} \quad (3.21)$$

and it is assumed that the point of observation R is such that $r \ll R$, whilst $X = k_o R$, where $k_o = 2\pi/\lambda$ with λ the wavelength of the source in vacuum.

It is often noted, in most scientific papers, that the intensity (or irradiance, in the optics field) is reported in arbitrary units, without a specific explanation as to why this is the case. Furthermore, intensity can be said to be the energy flux per unit area, that is to say, it is measured in Watt per cm^2 in the MKS units system. However there are exceptions such as when $I_s(\theta)$ is expressed directly in terms of electric and magnetic fields (see Definition 3.5). Additionally, it is assumed that the incident and scattered waves at the far field are confined to a small solid angle, usually taken to be that of the detector area, and to a small frequency interval. It is our understanding that it is due to this that the terminology *arbitrary units* is often preferable.

A typical scattering pattern can be seen in Figure 3.2. It should be noted that the pattern shown here closely resembles that of Wyatt [3], except for the deep minimum at $\theta \approx 150^\circ$ which is not reported. This is often the case. That is to say only the values that correspond to the ‘best’ solution (goodness-of-fit) are reported. This is due to the fact that a unique solution cannot be found as the approximation problem is an ill-posed problem. In the spherical particle case, irrespectively of the number of layers, the pattern is an even function of Θ as illustrated in the polar plot in Figure 3.2[Right]. This property is extensively used by many manufacturers of Multi Angle Light Scattering instruments [19, for example]. For particles of spherical symmetry will produce a differential pattern that

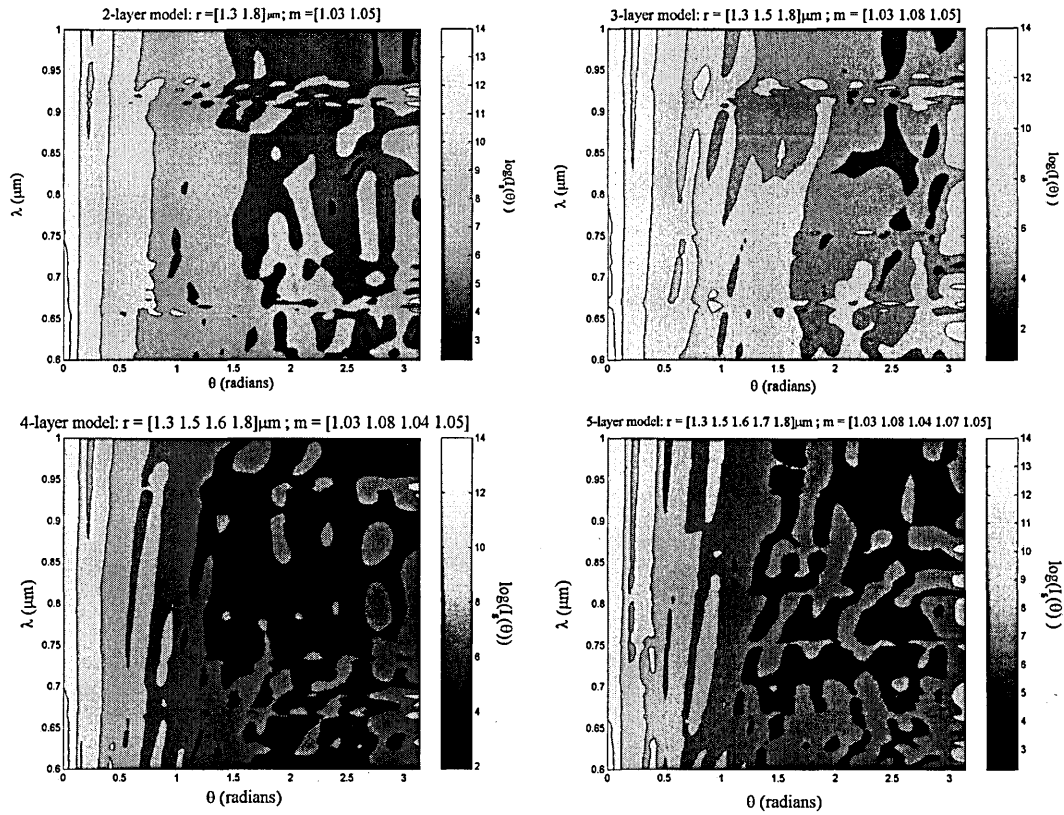


Figure 3.3: Light Intensity Patterns of 2 to 5 layer particles at multi-angle and variable wavelength

will be linear or equivalent to a linear plot in either the Zimm/Debye conformation plot (Section 2.4, page 26) or polar plot sense, whilst asymmetry will deviate from linearity [3, 19, 74]. By differential pattern we mean the subtraction of the averaged signal for $\theta \in (0, \pi)$ from that for $\theta \in (\pi, 2\pi)$. If only noise appears then the average will lead to a linear Zimm/Debye conformation plot, whilst it will be non-linear otherwise.

Remark 3.1. Particles of spherical symmetry will always produce a linear differential light scattering pattern irrespectively of their internal inhomogeneities, whilst non-spherical particles, that is to say those that do not present any form of spherical symmetry, will present a non-linear differential light scattering pattern.

In Figure 3.3, we have generated several patterns of angular dependence for different values of incident source wavelength. This is a contour plot of different λ values that produce several intensity patterns of angular dependence; namely, $\lambda \in [0.6, 1]\mu\text{m}$, that is from red to infra-red laser light source. Referring to Remark 3.1, spheres produce a linear differential pattern, but, for multiple wavelengths, and for different layered models of the

same size and spherical structure, the results are very different. The scattered intensity $I_s(\theta)$ is predicted to be stronger in the near-forward angles (0, 0.5) radians (equivalent to approximately 0, 30°), depicted by lighter shades of grey, independently of wavelength, but it has no significant variability, depicted by closely matched levels of grey-scale in Figure 3.3. However this is not true when examining the angular scattering pattern as a whole. The scattered intensity changes dramatically in response to the effect of additional internal layers, hence to the change of internal composition. As the number of layers increases, the intensity overall decreases. This can be verified by the appearance of darker patches in the contour plots of Figure 3.3. Even so, these changes are clearly evident close to the visible spectrum, where those darker patches appear to occupy a lesser area of the contour plot, hence the intensity signal can be said to be, at least theoretically, stronger, which in turn justifies the fact that most manufacturers and experimenters are insisting on the use of sources in the visible spectrum. In terms of experimentation however, it would be expected that a variable wavelength laser source would be preferred, since different internal structures from similarly sized, spherical objects would be recognised much faster and in real-time. Assuming that these variable wavelength patterns of intensity will reappear for a cell of the same species, hence employing the same number of layers, then, by selecting a few wavelength values in the visible spectrum and examining the scattering pattern as a whole, it may be possible to recognise the particle's signature, rendering a possible partial identification protocol.

Finally, it is also evident from Figure 3.3 that the patterns produced in the forward direction, that is to say from 0.05 to approximately 0.5 radians and within the optical spectrum, are similarly distributed in terms of intensity values. Similar arguments can be made for near-infra and infra red wavelength. This in effect predicts the fact that if only one observation point is used within this angular range and spectrum then it would be impossible to characterise, let alone identify, the particle under examination. This is obvious when one takes into account the fact that most of the variation of the scattered light intensity takes place from 0.65 to π ; that is to say, several patterns of different shades of grey occur within this region of Figure 3.3. This implies use of the intensity patterns only. It is true that some properties may be estimated using a unique detector point, but to do this one should rely on the scattering of fluctuations, which is neither appropriate in terms of biological particles [105] nor the subject of this thesis.

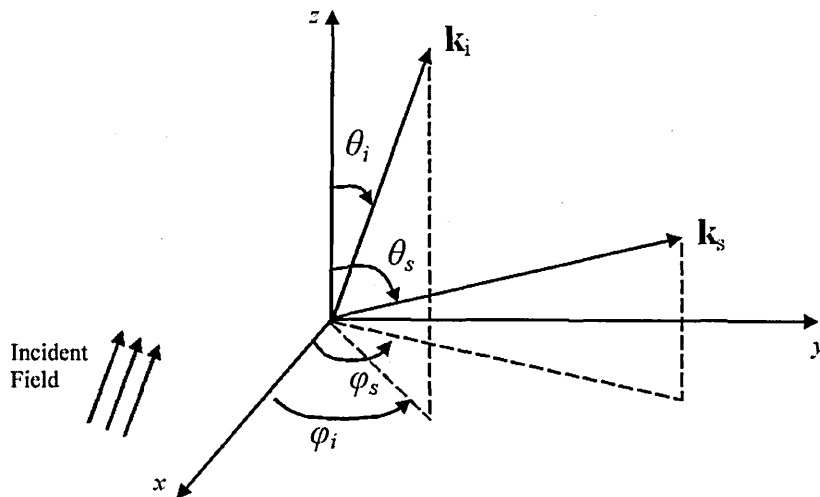


Figure 3.4: Scattering Geometry for the modified Rayleigh-Debye approximation

3.3 Approximate solution for near-index particles

The interest in the near-index problem does not stem only from its mathematical interest. The subject of this thesis is bacterial cells in water environments where $|m(r) - 1| < 1$. However a plethora of applications has been identified for potential solutions to this problem, as in the case of proteins in water [19], water drops in air [76] and interstellar grains [106, 77] to name just a few. We proceed in formally presenting our solution and generalise for multiple layers, from a modification based on including the effect that the propagation constant has on the passage of light through the ‘soft’ material of the cell.

The Problem Definition 3.1, illustrated in Figure 3.1, can be solved in the near-index case and for small ‘phase shifts’ between wavelets, satisfying $2kd|m - 1| \ll 1$, that pass through the body of the particle, using the Rayleigh-Debye Approximation (or RDG). The size restriction is such that if d is the largest linear dimension then the approximation is applicable for $d \ll \lambda/|m - 1|$. This restriction means that bacteria cannot be modelled. However it has been used in several publications [86, 5, 107, 105] with great success, which clearly indicates that the RDG limits [108] do not apply in practice. The latter has been investigated theoretically in [109] for fractal, self-similar aggregates. We will return to this issue in Section 3.5.

Following the physical basis of the Born approximation, and referring to Figure 3.4, a particle illuminated by incident light with direction that of a unit vector \mathbf{k}_i will scatter light

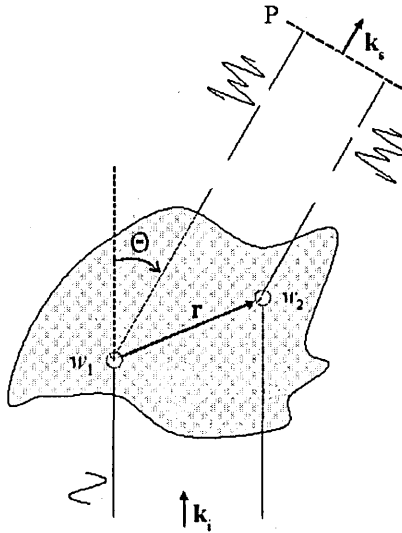


Figure 3.5: Depiction of the Scattering Plane in two dimensions: diffraction occurs at direction k_s , with respect to the incident field of direction k_i . The angle between scattering and incidence is denoted by Θ . Far-field assumptions satisfied if observation plane P is placed at distance much greater than the dimension of scatterer.

independently within the particle. The scattered light has the direction of the unit vector k_s . That is to say the wavelets w_1 and w_2 (Figure 3.5) will not be changed or distorted, and will only undergo a phase lag δ . However this assumption considers the particle to be ‘semi-transparent’ which is not necessarily the case [31, 66, 33]. Furthermore, due to this assumption the range of applicability is also limited. Using Definitions 3.4 and 3.6, we propose that

Proposition 3.1. *A near-index, small particle will scatter light such that the wavelet of any infinitesimal volume dV within the particle will distort light as a function of refractive index $F(k_o, m(\mathbf{r}))$.*

The physical meaning of such a proposition implies that the phase lag which the scattered light will undergo at w_1 and w_2 depends not only on the larger distance that one wavelet will undertake as opposed to another, but also on the functional F . That is to say,

$$\delta = sF(k, m(\mathbf{r})) \quad (3.22)$$

where k , as we will see later, can be related to the difference of the distance that a wavelet

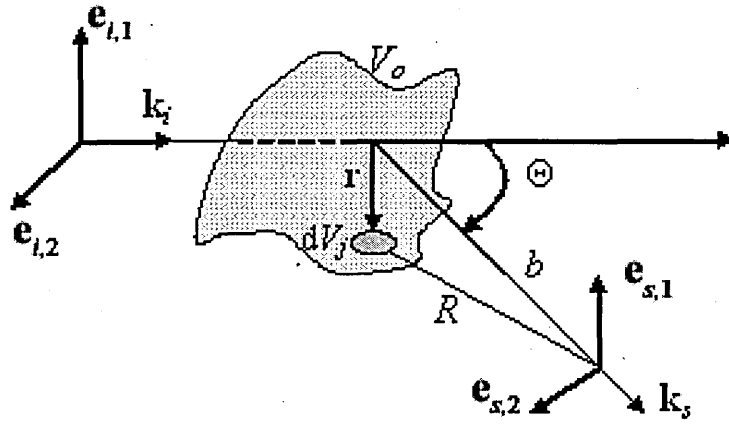


Figure 3.6: A scattering particle of arbitrary shape with volume V_o , finite size. The infinitesimal volume dV_j is also indicated

through w_1 will have to travel further away to the one that would travel via w_2 . In Figure 3.4 the unit vector k_i is assumed to be coplanar with the unit vector k_s , which is the direction of scattering. In Figure 3.5 the angle between these two vectors is Θ . For r in this plane, and without loss of generality, the observation plane P is normal to the direction of scattering, hence to the unit vector k_s . Similar argument applies for the incident wave, following the direction of the unit vector k_i . It should be noted that, for the far-field assumptions to be satisfied, the distance to the observation plane P must be much greater than the linear dimension of the scatterer.

In order to verify Proposition 3.1, we follow a derivation similar to when solving from Maxwell's equations. Consequently, it is known that the scattered field E_s at an observation point P situated at distance R in (Figure 3.6) and assumed to be at the far-field, is given by

$$\mathbf{E}_s = -\frac{k^2 \exp(jk_o R)}{4\pi R} (\mathbf{k}_s \times \mathbf{k}_s \times \bar{\mathbf{p}}) \quad (3.23)$$

where $\bar{\mathbf{p}}$ denotes the dipole moment, following the effect of a far-field radiated from any dipole at direction \mathbf{k}_s . If $\mathbf{E}(\mathbf{r})$ is the field inside the particle, then the polarisation per unit volume within the particle is

$$\bar{\mathbf{P}} = (m(r) - 1)\mathbf{E}(\mathbf{r})$$

with dipole moment $\bar{\mathbf{p}} = V_j \bar{\mathbf{P}}$, hence

$$\bar{\mathbf{p}} = V_j(m(r) - 1)\mathbf{E}(\mathbf{r})$$

As a result scattering at the far-field will be given by

$$\mathbf{E}_s = -\frac{k^2 \exp(jk_o R)}{4\pi R} V_j \left[\mathbf{k}_s \times \mathbf{k}_s \times (m(\mathbf{r}) - 1)\mathbf{E}(\mathbf{r}) \right]$$

where the scatterer is of finite size, arbitrary shape and is an inhomogeneous body. Due to this inhomogeneity, the relative refractive index m is a function of distance within the cell, $m(\mathbf{r})$. Let dV_j be the infinitesimal volume around the point of \mathbf{r} , with relative refractive index $m(\mathbf{r})$. The differential contribution to the far-field will be

$$d\mathbf{E}_s = -\frac{k^2 \exp(jk_o R)}{4\pi R} \left[\mathbf{k}_s \times \mathbf{k}_s \times (m(\mathbf{r}) - 1)\mathbf{E}(\mathbf{r}) \right] dV_j \quad (3.24)$$

The physical meaning of a far-field can be visualised in Figure 3.6. It implies that $|\mathbf{r}| \ll |\mathbf{K}_s| = b$ due to positioning of the detectors at some point which makes their distance much larger than the linear dimension of the scatterer. Following Figure 3.6 it is easy to see that,

$$\begin{aligned} R &= |\mathbf{K}_s - \mathbf{r}| = \sqrt{(\mathbf{K}_s - \mathbf{r}) \cdot (\mathbf{K}_s - \mathbf{r})} \\ R &= \sqrt{|\mathbf{K}_s|^2 - 2\mathbf{K}_s \cdot \mathbf{r} + |\mathbf{r}|^2} \end{aligned} \quad (3.25)$$

Due to the far field assumption $|\mathbf{K}_s| \gg |\mathbf{r}|$ it follows that $|\mathbf{K}_s|^2 + |\mathbf{r}|^2 \cong |\mathbf{K}_s|^2$. Hence

$$R \cong \sqrt{|\mathbf{K}_s|^2 - 2\mathbf{K}_s \cdot \mathbf{r}} \quad (3.26)$$

equivalently

$$R \cong |\mathbf{K}_s| \left(1 - \frac{2\mathbf{K}_s \cdot \mathbf{r}}{|\mathbf{K}_s|^2} \right)^{1/2} \quad (3.27)$$

Using the Taylor expansion [103, p135] and noting that in this case higher powers will be negligible

$$\begin{aligned} \left(1 - \frac{2\mathbf{K}_s \cdot \mathbf{r}}{|\mathbf{K}_s|^2} \right)^{1/2} &= 1 - \frac{1}{2} \frac{2\mathbf{K}_s \cdot \mathbf{r}}{|\mathbf{K}_s|^2} + \left[\frac{\frac{1}{2}(\frac{1}{2} - 1)}{2!} \left(\frac{2\mathbf{K}_s \cdot \mathbf{r}}{|\mathbf{K}_s|^2} \right)^2 + \dots \right] \\ &\cong 1 - \frac{\mathbf{K}_s \cdot \mathbf{r}}{|\mathbf{K}_s|^2} \end{aligned}$$

and from Equation 3.27 it follows that

$$R \cong |\mathbf{K}_s| - \frac{\mathbf{K}_s \cdot \mathbf{r}}{|\mathbf{K}_s|} \quad (3.28)$$

Since $\mathbf{K}_s = |\mathbf{K}_s| \mathbf{k}_s$ we have that

$$R \cong |\mathbf{K}_s| - \mathbf{k}_s \cdot \mathbf{r} \quad (3.29)$$

As indicated in Figure 3.6, we denote the magnitude of \mathbf{K}_s by $|\mathbf{K}_s| = b$. From Equation 3.29 it follows that

$$R \cong b - \mathbf{k}_s \cdot \mathbf{r} \quad (3.30)$$

As a result the prerequisite of far field is satisfied by altering the phase term $\exp(jkR)$ in Equation 3.24. That is to say, we approximate the phase term by $\exp(jkb - j\mathbf{k}_s \cdot \mathbf{r})$ and the amplitude by $1/R \approx 1/b$.

To calculate the scattering field and incorporating the far-field constraint (Equation 3.30), we have to integrate over the volume V_o of the scatterer. This results in

$$\mathbf{E}_s = - \int_{V_o} \frac{k^2 \exp(jkb - j\mathbf{k}_s \cdot \mathbf{r})}{4\pi b} \mathbf{k}_s \times \left[\mathbf{k}_s \times (m(\mathbf{r}) - 1) \mathbf{E}(\mathbf{r}) \right] dV \quad (3.31)$$

and it is obvious that

$$\mathbf{E}_s = - \frac{k^2 \exp(jkb)}{4\pi b} \mathbf{k}_s \times \left[\mathbf{k}_s \times \int_{V_o} (m(\mathbf{r}) - 1) \mathbf{E}(\mathbf{r}) \exp(-j\mathbf{k}_s \cdot \mathbf{r}) dV \right]$$

hence

$$\mathbf{E}_s = - \frac{k^2 \exp(jkb)}{4\pi b} \mathbf{k}_s \times \left[\mathbf{k}_s \times \iiint (m(\mathbf{r}) - 1) \mathbf{E}(\mathbf{r}) \exp(-j\mathbf{k}_s \cdot \mathbf{r}) dx dy dz \right] \quad (3.32)$$

bearing in mind that in Equation 3.32 the triple integral is a consequence of the three-dimensional form.

The internal field $E(\mathbf{r})$ is dependent upon the coherent wave interaction (wavelets) amongst different parts of the cell/particle. It is an unknown quantity, and to calculate it rigorously, we have to solve from Maxwell equations to establish

$$\mathbf{E}_s = \nabla \times \nabla \times \int_{V_o} (m(\mathbf{r}) - 1) E(\mathbf{r}) G_o(\mathbf{k}_s, \mathbf{k}_i) dV \quad (3.33)$$

where $G_o(\mathbf{k}_s, \mathbf{k}_i) = \exp(jk|\mathbf{k}_s - \mathbf{k}_i|)/4\pi|\mathbf{k}_s - \mathbf{k}_i|$, is the free-space Green function and $E(\mathbf{r})$ is the total field inside the particle.

Using the solution from Equation 3.33 would be to use the Mie solution as in Section 3.2 or variants, that is to say approximating by recurrence on the scattering series. The alternative is to use simplifying assumptions, such as the case with the Rayleigh-Debye approximation, where it is assumed that $E(\mathbf{r}) \approx E_{inc}(\mathbf{r}) = \mathbf{e}_i \exp(jk_o \mathbf{r} \cdot \mathbf{k}_i)$. Hence the internal field equals that of the incident $E_{inc}(\mathbf{r})$, which implies that the particle is ‘transparent’. However, the origin of the positioning vector \mathbf{r} must be placed close to all the infinitesimal volume scatterers if one wishes to accurately compute the scattering/absorption caused by the particle. Clearly, most of the phase difference (lag) falls inside the scatterer. As a result, the assumption that incidence equals the internal field of the cell is not an optimal approximation procedure and it limits the applicability of any model produced.

To extend the range of the RDG, and by using the assumptions of Definitions 3.4, 3.6, and in conjunction with Shimizu in [95], it follows

$$E(\mathbf{r}) \approx \mathbf{e}_i \exp(jm(r)k_o \mathbf{r} \cdot \mathbf{k}_i)$$

where the electric field has the direction of \mathbf{e}_i , assumed perpendicular to \mathbf{k}_i . This modification, ‘forces’ in Equation 3.33 the internal field to be taken into account. Substituting in Equation 3.23 we now have that

$$\mathbf{E}_s = -\frac{k^2 \exp(jkb)}{4\pi b} \mathbf{k}_s \times \left[\mathbf{k}_s \times \right. \\ \left. \times \iiint (m(\mathbf{r}) - 1) \mathbf{e}_i \exp(jk_o m(r) \mathbf{r} \cdot \mathbf{k}_i - jk_o m(r) \mathbf{r} \cdot \mathbf{k}_s) dx dy dz \right]$$

hence

$$\mathbf{E}_s = -\frac{k^2 \exp(jkb)}{4\pi b} \mathbf{k}_s \times [\mathbf{k}_s \times \mathbf{e}_i] \\ \iiint (m(\mathbf{r}) - 1) \exp(jk_o m(r) \mathbf{r} \cdot (\mathbf{k}_i - \mathbf{k}_s)) dx dy dz \quad (3.34)$$

The new phase term $\delta = k_o m(r) \mathbf{r} \cdot (\mathbf{k}_i - \mathbf{k}_s)$ relates to the difference between vectors that indicate incident field and scattering field. This vector subtraction can be visualised in Figure 3.7. A useful way to relate the difference $\mathbf{k}_d = k(\mathbf{k}_i - \mathbf{k}_s)$, where $k = k_o m(r)$, to a physical meaning is by taking into account the additional distance that needs to be travelled by different wavelets within the particle, until a detection (destination) point has been reached.

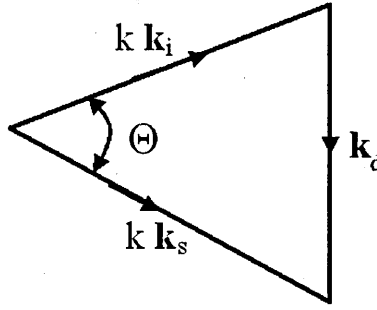


Figure 3.7: Relationship between k_i , k_s and k_d

Corollary 3.2. *Let vector r designate a path within the boundaries of the near-index particle. For any two infinitesimal volumes dV_i , dV_j placed on the origin and ends of a vector r respectively, the additional distance that a wavelet described by scattered vector wave of direction k_s will have to travel as opposed to the wavelet of incidence of direction k_i will be:*

$$k_d = |k_d| = 2k \sin(\Theta/2) \quad (3.35)$$

That is to say, k_d has a linear relation to the sin of scattering angle Θ and is parallel to the projection of r onto the bisectrix of the complement of Θ .

Proof: Let Θ be as indicated in Figures 3.6 and 3.7. Let $\text{Pr}_{kk_i}r$ be the projection of the vector r onto a vector K_i , where $K_i = kk_i$, and $\text{Pr}_{kk_s}r$ be the projection of the vector r onto a vector K_s , where $K_s = kk_s$. It follows from Figure 3.8 that

$$\begin{aligned} k_d &= \text{Pr}_{kk_i}r - \text{Pr}_{kk_s}r \\ &= r \cdot k_i - r \cdot k_s \\ &= r \cdot (k_i - k_s) \end{aligned}$$

It is evident that the angle between k_i , $-k_s$ is also Θ . The vector $(k_i - k_s)$ lies on the base of the isosceles triangle denoted as ABC. If by $\gamma = \hat{A}CB$ we denote the angle between k_i and $k_i - k_s$ then it follows that $\Theta + 2\gamma = \pi \equiv 180^\circ$. Clearly, $\gamma = 90^\circ - \Theta/2$, hence $k_i - k_s$ will lie parallel to the bisectrix of the complement of Θ . *As a result, k_d lies parallel to the bisectrix.*

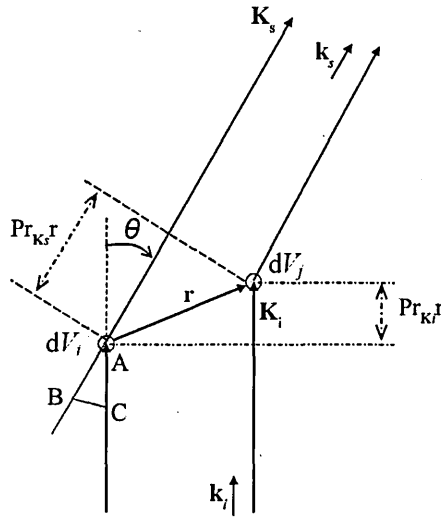


Figure 3.8: Following Fig.3.5 for infinitesimal volumes dV , indicating projections of r on corresponding vector wave paths

From the isosceles triangle ABC and equivalently in Figure 3.7, the bisector of Θ separates k_d at two equal segments $k_d/2$. As a result, for the far-field approximation $\sin(\Theta/2) \doteq (k_d/2)/k = k_d/(2k)$; therefore $k_d = 2k \sin(\Theta/2)$. ■

In many applications the use of Equation 3.34 would be to treat this as the Fourier transform in three dimensions, as a function of $m(r)$. Taking however the inverse transform would mean reconstructing the relative refractive index. As a result, k_d would have to be evaluated for all k_{d_x} , k_{d_y} , k_{d_z} and from Corollary 3.2, for k_d up to $2k$. The latter follows from Equation 3.35 where the maximum of k_d is at $\Theta = 180^\circ$. The reconstructed relative refractive index will be limited to spatial frequencies $< 2k$.

However inversion complicates the algorithmic development which would depend on the function of refractive index calculated by an inverse Fourier transform. We proceed therefore in trying to obtain a closed expression that depends only on the properties of the particle at the scattering points of detection. In polar coordinates, $x = r \sin \theta \cos \phi$, $y = r \sin \theta \sin \phi$ and $z = r \cos \theta$. Changing the variable representation from Cartesian to polar coordinates we need to evaluate the discriminant

$$\begin{aligned}
\begin{vmatrix} \frac{\partial x}{\partial r} & \frac{\partial y}{\partial r} & \frac{\partial z}{\partial r} \\ \frac{\partial x}{\partial \theta} & \frac{\partial y}{\partial \theta} & \frac{\partial z}{\partial \theta} \\ \frac{\partial x}{\partial \phi} & \frac{\partial y}{\partial \phi} & \frac{\partial z}{\partial \phi} \end{vmatrix} &= \begin{vmatrix} \sin \theta \cos \phi & \sin \theta \sin \phi & \cos \theta \\ r \cos \theta \cos \phi & r \cos \theta \sin \phi & -r \sin \theta \\ -r \sin \theta \sin \phi & r \sin \theta \cos \phi & 0 \end{vmatrix} = \\
&= -r \sin \theta \sin \phi \begin{vmatrix} \sin \theta \sin \phi & \cos \theta \\ r \cos \theta \sin \phi & -r \sin \theta \end{vmatrix} - r \sin \theta \cos \phi \begin{vmatrix} \sin \theta \cos \phi & \cos \theta \\ r \cos \theta \cos \phi & -r \sin \theta \end{vmatrix}
\end{aligned}$$

and as a result

$$\begin{vmatrix} \frac{\partial x}{\partial r} & \frac{\partial y}{\partial r} & \frac{\partial z}{\partial r} \\ \frac{\partial x}{\partial \theta} & \frac{\partial y}{\partial \theta} & \frac{\partial z}{\partial \theta} \\ \frac{\partial x}{\partial \phi} & \frac{\partial y}{\partial \phi} & \frac{\partial z}{\partial \phi} \end{vmatrix} = r^2 \sin \theta \sin^2 \phi + r^2 \sin \theta \cos^2 \phi = r^2 \sin \theta$$

Using this transformation of Cartesian to polar coordinates we now have that Equation 3.34 will become

$$\begin{aligned}
\mathbf{E}_s &= -\frac{k^2 \exp(jkb)}{4\pi b} [\mathbf{k}_s \times \mathbf{k}_s \times \mathbf{e}_i] \\
&\iiint (m(\mathbf{r}) - 1) \exp(j\mathbf{r} \cdot \mathbf{k}_d) r^2 \sin \theta dr d\theta d\phi
\end{aligned}$$

hence

$$\begin{aligned}
\mathbf{E}_s &= -\frac{k^2 \exp(jkb)}{4\pi b} [\mathbf{k}_s \times \mathbf{k}_s \times \mathbf{e}_i] \\
&\iiint (m(\mathbf{r}) - 1) \exp(jk_d r \cos \theta) r^2 \sin \theta dr d\theta d\phi \quad (3.36)
\end{aligned}$$

Solving the problem for a multilayered sphere of radius d and relative refractive index distribution such that it portrays a radially changing $m(r)$,

$$m(r) = \begin{cases} m_1, & r \in (0, r_1] \\ m_2, & r \in (r_1, r_2] \\ \vdots & \\ m_n, & r \in (r_{n-1}, r_n]; d = r_n \end{cases} \quad (3.37)$$

we consider the case of a spherical model for the prokaryotic cell as an inhomogeneous particle consisting of a multi-layered sphere with an arbitrary refractive index within each layer. In effect one would assume that there are n layers, such that the i th layer has outer radius r_i and relative refractive index m_i .

Taking into account that there is no dependency on ϕ , Equation 3.36 will become

$$\begin{aligned}
\mathbf{E}_s &= -\frac{k^2 \exp(jkb)}{4\pi b} \mathbf{k}_s \times [\mathbf{k}_s \times \mathbf{e}_i] \\
&\quad \int_0^d \int_0^\pi \int_0^{2\pi} (m(\mathbf{r}) - 1) \exp(j2k_o m(r) \sin(\Theta/2)r \cos \theta) r^2 \sin \theta dr d\theta d\phi \\
\mathbf{E}_s &= -\frac{k^2 \exp(jkb)}{4\pi b} \mathbf{k}_s \times [\mathbf{k}_s \times \mathbf{e}_i] \\
&\quad 2\pi \int_0^d \int_0^\pi (m(\mathbf{r}) - 1) \exp(j2k_o m(r) \sin(\Theta/2)r \cos \theta) r^2 \sin \theta dr d\theta \quad (3.38)
\end{aligned}$$

By taking $v = \cos \theta$, therefore $-dv = \sin \theta d\theta$ we have that

$$\begin{aligned}
\mathbf{E}_s &= -\frac{k^2 \exp(jkb)}{4\pi b} \mathbf{k}_s \times [\mathbf{k}_s \times \mathbf{e}_i] \\
&\quad 2\pi \int_0^d \int_{-1}^1 (m(\mathbf{r}) - 1) \exp(j2k_o m(r) \sin(\Theta/2)rv) r^2 dr dv \quad (3.39)
\end{aligned}$$

and it follows that

$$\begin{aligned}
\mathbf{E}_s &= -\frac{k^2 \exp(jkb)}{4\pi b} \mathbf{k}_s \times [\mathbf{k}_s \times \mathbf{e}_i] \\
&\quad 2\pi \int_0^d r^2 (m(\mathbf{r}) - 1) \int_{-1}^1 \exp(j2k_o m(r) \sin(\Theta/2)rv) dr dv \quad (3.40)
\end{aligned}$$

Integration over v would now result in integration for the exponential (phase) term, and as a result Equation 3.40 can now be simplified.

That is to say either by using the Euler identities or by substitution of $\exp(\pm j\alpha) = \cos \alpha \pm j \sin \alpha$ in conjunction with the trigonometric identities $\cos(-\alpha) = \cos \alpha$, $\sin(-\alpha) = -\sin \alpha$, we now have

$$\begin{aligned}
\mathbf{E}_s &= -\frac{k^2 \exp(jkb)}{4\pi b} \mathbf{k}_s \times [\mathbf{k}_s \times \mathbf{e}_i] \\
&\quad 4\pi \int_0^d r^2 (m(\mathbf{r}) - 1) \frac{\sin(2k_o m(r) \sin(\Theta/2)r)}{2k_o m(r) \sin(\Theta/2)r} dr \quad (3.41)
\end{aligned}$$

As a result we have proved that, within the cell's volume, the triple integral of Equation 3.32 becomes such that \mathbf{E}_s for an inhomogeneous spherical cell/particle will only depend on the relative refractive index as a function of distance r from its origin in its local coordinate system, as well as r (Equation 3.41). To formalise this result:

Corollary 3.3. *Assume a near-index, small particle of spherical morphology and observation point at the far-field. The particle will scatter light such that the wavelet w_j of*

any infinitesimal volume dV_j of direction from origin \mathbf{r} , inside the boundaries, will distort light primarily as a function of refractive index

Proof: From Equations 3.38 and 3.41 we have that any scattered light signal will depend upon a kernel which can be identified as

$$u = 2k_o m(r) \sin(\Theta/2)r$$

Within the boundaries of the cell all contributions from infinitesimal volumes will lie within radius r . As to whether Equation 3.41 is directly solvable depends on the r and the distribution for the relative refractive index over the radial distance of the sphere. The relative refractive index distribution may be a non-linear function of radius. As a result \mathbf{E}_s and solutions for the amplitude of the scattered field, as well as its behaviour, will depend upon $m(r)$; hence the particle will distort light primarily as a function of refractive index. ■

We can now use the schema described in Equation 3.37 and calculate the integral over r . However evaluating the integral as such would mean that we accept the *narrow* approximation $m \rightarrow 1$ and the outcome of Equation 3.2, which is no longer valid due to Theorem 3.3. As per discussion on Definition 3.6 we wish to generalise our model to include the range $|m - 1| < 1$ (*generalised* approximation). To take this into perspective, Hoekstra in [110, 111] in an effort to examine the latter effect for the homogeneous spherical particle case and under the generalised near-index regime, built an error map based on the standardised difference between intensities for the Rayleigh-Debye model, as well as the equivalent model from [95], as opposed to the Mie solution in [4]. It was found that almost 5% of the relative difference would be attributed to the narrow near-index assumption $|m - 1| \ll 1$. In order to avoid these problems and effectively increase the ‘phase-change’ limits in our model we reinstate the term $(m^2 - 1)/(m^2 + 2)$ for n -layers, that is to say $(m_i^2 - 1)/(m_i^2 + 2)$. This term is commonly referred to as the ‘volume polarisability’ of the particle and is denoted by $\hat{a}(r)$, defined by

$$\hat{a} = V^{-1} \int_V \hat{a}(r) dV \quad (3.42)$$

For the schema of Equation 3.37 the averaging effect on the polarisability will be such that $\hat{a} \rightarrow \hat{a}_i = V_i^{-1} \sum_i [(m_i^2 - 1)/(m_i^2 + 2)]$. This is approximated as being equivalent to the discrete average over the whole of the layered structure, and has been used in the past under different theoretical models, for example in [112] and partially in [106]. In our case we adopt the weighted average over the whole volume of the multilayered sphere as

found by integration of Equation 3.42 either with respect to r , by applying $dV = 4\pi r^2 dr$, or directly with respect to V , and will yield

$$\hat{a} = \frac{1}{V} \int_V \frac{m^2(r) - 1}{m^2(r) + 2} dV = \frac{1}{V_n} \left[\frac{m_1^2 - 1}{m_1^2 + 2} V_1 + \dots + \frac{m_n^2 - 1}{m_n^2 + 2} (V_n - V_{n-1}) \right] \quad (3.43)$$

It follows from Eq. 3.42 and 3.43, that the weighted average polarisability for the n -th layer would be expressed as

$$\begin{aligned} V_n \hat{a} &= (V_n - V_{n-1}) \hat{a}_n + V_{n-1}^{-1} \sum_{i=1}^{n-1} \frac{m_i^2 - 1}{m_i^2 + 2} (V_i - V_{i-1}) \\ \hat{a}_n &= \frac{V_n}{V_n - V_{n-1}} \hat{a} - [V_{n-1} (V_n - V_{n-1})]^{-1} \sum_{i=1}^{n-1} \frac{m_i^2 - 1}{m_i^2 + 2} (V_i - V_{i-1}) \end{aligned} \quad (3.44)$$

For example, for a homogeneous sphere it follows that $n = 1$ and so $V_{n-1} = V_0 = 0$, and since

$$\hat{a} = \frac{1}{V_1} \frac{m_1^2 - 1}{m_1^2 + 2} V_1 = \frac{m_1^2 - 1}{m_1^2 + 2} \quad (= a)$$

it follows that

$$\hat{a}_1 = \frac{V_1}{V_1 - 0} a = \frac{m_1^2 - 1}{m_1^2 + 2}$$

in agreement with Equation 2.2; that is to say, a bacterium of volume V , modelled as a homogeneous body.

As a result, using Schema 3.37 and bearing in mind from Equation 3.44 that for \hat{a}_i applied as a weight on the terms for the solution of the scattering field, evaluation of Equation 3.41 over r will result in

$$\mathbf{E}_s = -\frac{k^2 \exp(jk_o b)}{4\pi b} \mathbf{k}_s \times [\mathbf{k}_s \times \mathbf{e}_i] \sum_{i=1}^n 4\pi \hat{a}_i \int_0^{r_n} r \frac{\sin(2k_o m_i \sin(\Theta/2) r)}{2k_o m_i \sin(\Theta/2)} dr \quad (3.45)$$

It is customary to formulate scattering functions in terms of Bessel functions. The Bessel function of order $3/2$ is denoted as $J_{3/2}$ and given by the formula [103]

$$J_{3/2}(u) = \sqrt{\frac{2}{\pi u}} \frac{\sin u - u \cos u}{u}$$

Evaluating for the n -th layer by using the notation from the proof of Corollary 3.3, so that now $u_{i,i} = 2k_o m_i r_i \sin(\Theta/2)$ and $u_{i,i-1} = 2k_o m_i r_{i-1} \sin(\Theta/2)$, the integral of Equation 3.45 would result in

$$\int_{r_{n-1}}^{r_n} r \frac{\sin(2k_o m_i \sin(\Theta/2)r)}{2k_o m_i \sin(\Theta/2)} dr = \frac{(\sin(u_{n,n}) - u_{n,n} \cos(u_{n,n})) - (\sin(u_{n,n-1}) - u_{n,n-1} \cos(u_{n,n-1}))}{(2k_o m_n \sin(\Theta/2))^3} \quad (3.46)$$

whilst using the Bessel function of the three half order it follows

$$\int_{r_{n-1}}^{r_n} r \frac{\sin(2k_o m_i \sin(\Theta/2)r)}{2k_o m_i \sin(\Theta/2)} dr = \left(r_n^3 \sqrt{\frac{\pi}{2u_{n,n}^3}} J_{3/2}(u_{n,n}) - r_{n-1}^3 \sqrt{\frac{\pi}{2u_{n,n-1}^3}} J_{3/2}(u_{n,n-1}) \right) \quad (3.47)$$

whereas for $n = 1$ then $n - 1 = 0$ and we write $r_0 = 0$, so that only the first term in Equation 3.47, dependent on r_n , appears whilst the second term is considered as ‘non-existent’. As a result,

$$\int_{r_0}^{r_1} r \frac{\sin(2k_o m_i \sin(\Theta/2)r)}{2k_o m_i \sin(\Theta/2)} dr = r_1^3 \sqrt{\frac{\pi}{2u_{1,1}^3}} J_{3/2}(u_{1,1}) \quad (3.48)$$

and $u_{1,1} = 2k_o m_1 r_1 \sin(\Theta/2)$.

The behaviour of the expression in Equation 3.47 is depicted in three dimensions in Figure 3.9. This figure illustrates the amplitude variability of the scattered field’s energy at angular detection points $\Theta \in (0, \pi)$, issued for different values of radius (r_i) and for a relative refractive index of $m_i = 1.2$. The incident wavelength is assumed to be $0.690\mu\text{m}$. A contour plot is also shown in order to further illustrate the increased amplitude variability for equal increments of radius at the boundary of the n -th layer.

It is obvious that the amplitude increases as the radius of the particle increases. In effect the function predicts that larger particles of the same refractive index index will scatter more light at any detection point. Consequently, observing Figure 3.9, the prediction is that for r_n increasing, the scattering amplitude will also increase at the angular detection points Θ . Furthermore, by observing the contour plot, it is evident that the number of extrema increases with increased radius values. The latter two observations are in agreement with the general observation from the exact solution (Mie Axiom) as stated in page 31. Even though in this example we have not considered the effect of concentration of particles, we should also observe that for increased values of radius the angular scattering patterns present maxima at the forward direction and with decreasing amplitude thereafter but with weaker and weaker maxima which still appear. This is in agreement with Mie’s theorem in page 31 of Chapter 2. As a result this serves as a numerical verification of the derived model’s validity, since it satisfies, in general, the exact solution’s

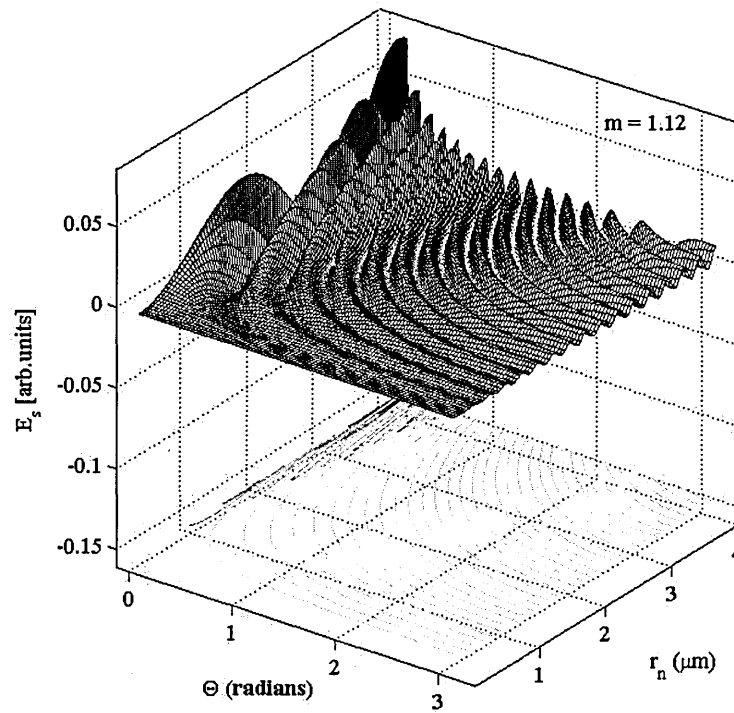


Figure 3.9: Behaviour of the solution for the n -th layer, using Bessel functions of order $3/2$. The scattering amplitude of the function (E_s) for the n -th layer, is indicated on the z -axis at all detection points (Θ) and increments of radius $r_n \in [0, 4]\mu\text{m}$. The relative refractive index value for the n -th layer is $m_n = 1.12$. The contour of the 3D plot is drawn on the xy plane (Θ, r_n).

hypothesis concerning increasing radius [113, pp.18-20], which is not immediately apparent within the expression.

However it should be noted that it is expected that our n -layer mRDG spherical model would behave better for near index values of relative refractive index, due to its derivation from the Rayleigh-Debye regime (weak interactions between induced potentials). The latter is due to the fact that the curve will present unexpected high values of amplitude for increased values of relative refractive index at some detection points, and in particular at the forward direction.

It should be evident that $u \rightarrow 0$ as $\Theta \rightarrow 0$ and the amplitude will tend to reach its highest peak, verifying that most of the scattering will take place in the near-forward direction. We adopt the simplification of Berry in [24], where it follows by definition that if $\Theta = 0$ then any derived *Form Factor* (commonly denoted as $P(\Theta)$ in such expressions where $S(\Theta) = jk_o^3 a(r)P(\Theta)$) results in a value of unity. Finally, the amplitude $\sqrt{\Re(S(0))^2 + \Im(S(0))^2}$, with \Re, \Im being the real and imaginary part of S respectively, will depend only upon the propagation constant k_o outside the particle, the distance from the observation point and the linear dimension of the scatterer.

The scattering amplitude matrix S of Equation 3.4 and its elements can now be easily formulated by accepting the scattering plane coordinate system to represent the scattering amplitude matrix elements. It follows, since $\mathbf{k}_s \times (\mathbf{k}_s \times \mathbf{e}_{i,1}) = -\mathbf{e}_{s,1}$ and $\mathbf{k}_s \times (\mathbf{k}_s \times \mathbf{e}_{i,2}) = -\mathbf{e}_{s,2} \cos \Theta$, bearing in mind the particle's spherical symmetry and taking into account Equation 3.47, that Equation 3.45 can be expressed as

$$\mathbf{E}_s = \frac{k_o^2 \exp(jk_o b)}{b} \mathbf{e}_s \sum_{i=1}^n \left(\hat{a}_i r_i^3 \sqrt{\frac{\pi}{2u_{i,i}^3}} J_{3/2}(u_{i,i}) - \hat{a}_i r_{i-1}^3 \sqrt{\frac{\pi}{2u_{i,i-1}^3}} J_{3/2}(u_{i,i-1}) \right) \begin{bmatrix} 1 & 0 \\ 0 & \cos(\Theta) \end{bmatrix} \quad (3.49)$$

from where it should be evident that the scattering amplitude matrix relates to the scattering field so that

$$\mathbf{S} = jk_o^3 \mathbf{S}(\mathbf{k}_s, \mathbf{k}_i) \begin{bmatrix} 1 & 0 \\ 0 & \cos(\Theta) \end{bmatrix} \quad (3.50)$$

where the scattering amplitude component $S(\mathbf{k}_s, \mathbf{k}_i)$ is expressed by

$$S(\mathbf{k}_s, \mathbf{k}_i) = (2\pi)^{3/2} \sum_{i=1}^n \left(\hat{a}_i r_i^3 u_{i,i}^{-3/2} J_{3/2}(u_{i,i}) - \hat{a}_i r_{i-1}^3 u_{i,i-1}^{-3/2} J_{3/2}(u_{i,i-1}) \right) \quad (3.51)$$

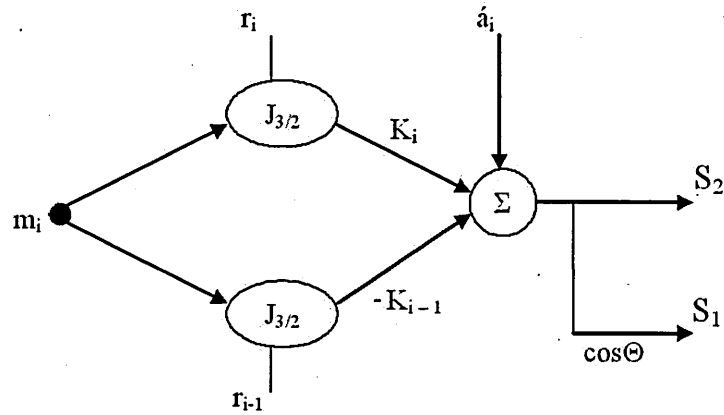


Figure 3.10: A diagrammatic expression of the physical meaning of generalised n -layer Rayleigh-Debye spherical approximation. Note the similarities of this depiction with other disciplines, for example telecommunications engineering, from which the notation has been adopted.

The expression in Equations 3.50, 3.51 and 3.44 predicts the amplitude of light scattered from a single cell and it is the n -layered sphere extension model, which we will refer to as the generalised mRDG spherical model. The reader is reminded that $u_{i,i} = 2k_o m_i r_i \sin(\Theta/2)$ and $u_{i,i-1} = 2k_o m_i r_{i-1} \sin(\Theta/2)$.

This generalised expression can be applied to any population of n -layered spheres and would lead to better approximations of light scattered phenomena on real cells by simulated models. In effect its physical meaning (Figure 3.10) corresponds to the fact that a cell of n layers will scatter light proportional to the sum of n homogeneous spheres of corresponding r_n and m_n , by subtraction of contributions arising from the $(n - 1)$ homogeneous spheres of corresponding r_{n-1} but having the same refractive index, that is m_n . To visualise this result, we proceed in graph depiction of Equation 3.51 illustrated in Figure 3.10. For $K_{i,i} = r_i^3 u_{i,i}^{-3/2}$ and $K_{i,i-1} = r_{i-1}^3 u_{i,i-1}^{-3/2}$, where it is retained that $(i - 1)$ in $(u_{i,i-1})$ and consequently to $(K_{i,i-1})$, corresponds to the radius that encloses the said layer of the cell r_{i-1} . It follows that we have two corresponding constants per layer which are multiplied with the corresponding Bessel functions. The input to these Bessel functions is, in computational terms, an array of values (numbers) of relative refractive index in conjunction with an array of radius values for each layer which we employ in the model. This results in two contributing terms that are in turn subtracted after being multiplied by the polarisability of the layer in question. This is a significant outcome, not only because of the prediction/proposition that our generalised Rayleigh-Debye spherical approximation results in, but also because of its depiction. In effect, if one wishes to solve

the inverse problem, that is to say from a set of experimental intensity values to obtain the optical properties of the cell, one would only need to employ an optimisation procedure where the ‘network’ will be such that multiples as in Figure 3.10. A test statistic to examine the goodness of fit, as is for example the standardised difference

$$E_R = \frac{\sum_{p_m=1}^N |\log I_{p_m} - \log I_{p_m}^{model}|}{(N+1)(\log I_{max} - \log I_{max}^{model})} \quad (3.52)$$

where $\log I_{p_m}^{model}$ is $\log I(\Theta)$, where $I(\Theta)$ is given in Equation 3.53 and I_{p_m} is the array of experimental data points. As a result, if the array for experimentally acquired intensity values I_{p_m} is of dimensionality $I \in \mathbb{R}^{p_m}$ then the solution space will be \mathbb{R}^{p_n} where the problem has now been mapped so that $\mathbb{R}^{p_m} \rightarrow \mathbb{R}^{p_n}$, and therefore p_n is the number of values needed to be found per layer: $2n$ minus one in which ‘one’ represents the parameter of overall radius to be estimated by population inference. As a result, $p_n = 2n - 1$ and we assume that $p_m > p_n$. Clearly, this results in a great reduction in the complexity of the problem, as in effect multiple models would be built and then compared to experimental data.

Furthermore, our approximation procedure correctly predicts the effect of removing layers. Putting $m_{k-1} = m_k$ will result in a multi-layered sphere where the $(k-1)$ th layer will disappear. This is true since the previous $(k-1)$ th and k th layers will merge to a new layer with $m_{new} = m_k = m_{k-1}$, of thickness¹⁰ t_{new} such that $t_{new} = t_k + t_{k-1}$. Finally, if $m_k = 1$ then the k^{th} layer becomes ‘redundant’, in the sense that the polarisability of this layer \hat{a}_k will only depend on the average polarisability of the cell with $r = r_k$, and the contributions resulting from the layer will cancel each other. This can easily be verified by observation of Equation 3.51 and Figure 3.10. Consequently, the k -th layer becomes transparent to incoming light and as such does not contribute to the scattering amplitude.

To finalise our main result, that is the *generalised mRDG* multi-layered spherical *approximation*, and proceed to examination of our findings, we produce the formula for the scattering light intensity for Θ . This would be considered identical to Equation 3.21 and as a result, the light intensity from such a cell can be expressed in terms of the elements of the scattering matrix \mathbf{S} using the expression :

$$I(\Theta) = \frac{I_i}{2(kR)^2} (|\mathbf{S}(\mathbf{k}_s, \mathbf{k}_i)|^2 + |\mathbf{S}(\mathbf{k}_s, \mathbf{k}_i) \cos \Theta|^2) \quad (3.53)$$

where $\mathbf{S}(\mathbf{k}_s, \mathbf{k}_i)$ is calculated via Equation 3.51 with $d = r_n$ being the overall radius of

¹⁰Note that, for example, $t_k = r_k - r_{k-1}$

the spherical cell and I_i is the intensity of the incident light.

3.4 Evaluation of the approximation model

In the absence of experimental data, we proceed to evaluate our main result by relying on simulated models, that is patterns acquired from well established methods, and in particular the Rayleigh-Debye approximation as used and derived for a two layer model in [86] and the two layer Mie solution of [4]. In Figure 3.11, we provide the resulting patterns and for a two-layer sphere with outer radius $1\mu\text{m}$ and core (internal) radius $0.9\mu\text{m}$, where the core has a relative refractive index of 1.203 and the external concentric layer 1.128; hence the core is more dense than the cell wall. Since we simulate using a wavelength of $0.514\mu\text{m}$ the refractive index of water assumes its commonly used value 1.336. The said model would correspond to depicting the cell with the inner sphere (core) simulating the behaviour of the bacterium's cytoplasm whilst the outer layer simulates the cell wall.

By observing in Figure 3.11 the scattering patterns from the generalised Rayleigh-Debye and the corresponding exact Mie solution, it can be seen that the numbers of maxima are the same even though we have selected (on purpose) the case for which our model differs most profoundly from that of Mie. However, taking into account the pattern provided by the RDG approximation, it is evident that our result is not only closer to that of Mie scattering in terms of the number of maxima/minima but also in terms of the intensity amplitude levels predicted. As a result, it should be expected that fitting our model to experimental data would result to fit more closely than that of RDG, particularly if one takes into account the log scale difference. That is to say, the absolute difference by which the RDG 'misses' the Mie scattering curve, is 4 orders of magnitude, whilst the generalised Rayleigh-Debye has a difference of 2 orders of magnitude. This is a problem often noted in terms of the orders of magnitude that approximation patterns cover [111]. Unfortunately, this problem is also apparent here: the orders of magnitude our generalisation covers is greater than those of the exact solution and for all angles. It is evident that in both the Rayleigh-Debye 2-layer model and the generalisation that we outlined in the previous section, that they cover more orders of magnitude than the parameters' equivalent of the 2-layer Mie solution.

The latter is more prominent for Θ being less than approximately 15° where our generalised model is producing too much light intensity (radiant power) and exceeds the Mie prediction by at least 3 orders of magnitude. This poor fit at low angles may be explained

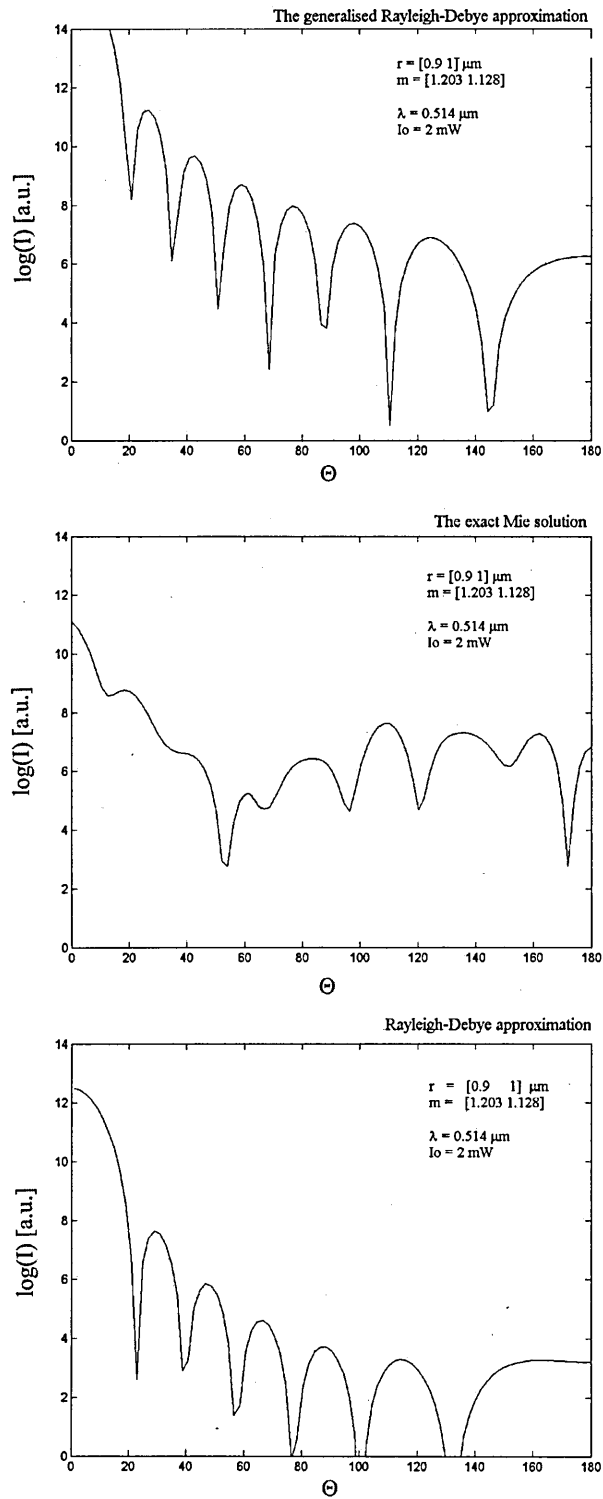


Figure 3.11: Illustrating patterns of angular dependence for 2-layer equivalent models of spherical bacteria: From top to bottom: the generalised Rayleigh-Debye approximation, the exact Mie theory and the Rayleigh-Debye approximation. Note that the number of minima of the generalised mRDG appears to resemble the Mie solution more closely than the Rayleigh-Debye model scattering pattern.

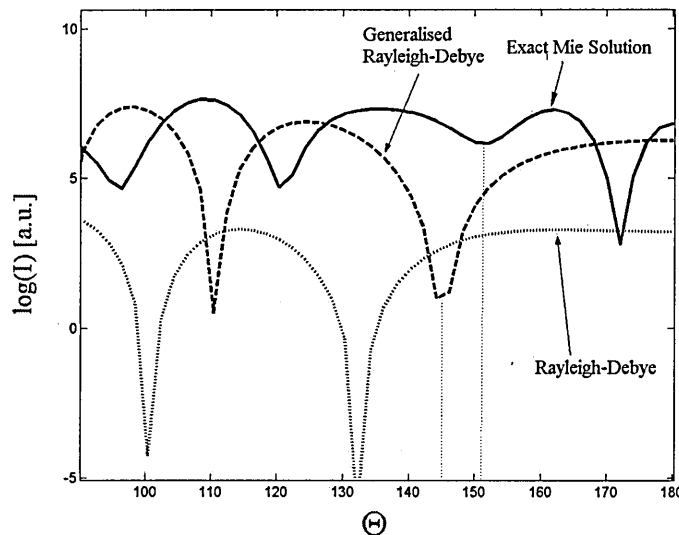


Figure 3.12: A comparison between 2-layer equivalent models on backscattering ($\Theta \in (\pi/2, \pi)$): the Rayleigh-Debye approximation (dotted line), the exact Mie theory (solid line) and the generalised mRDG approximation (dashed line). Note that the last minimum in the curve of the generalised mRDG is closer to Mie model than the Rayleigh-Debye prediction (illustrated in the figure via projection of dotted line on the axis of Θ).

by the fact that the weighted average polarisability term that we have inserted in our models has an adverse cumulative effect at forward direction predictions. That is to say, upon multiplication of the weighted polarisability terms the intensity amplitude of the outer layers will increase by a factor defined by the outer layers' relative refractive indices. The reader is reminded that outer layers and overall radius are primarily responsible for most of scattering at forward directions.

However, there are improvements over RDG models in terms of the appearance of the angular scattering extrema (maximum/minimum of the intensity values) at $\Theta > 90^\circ$, which can be observed in Figure 3.12. For example, by examining the last minimum appearing on the pattern of the generalised RDG, we can see that the generalised model follows the minima of Mie scattering closer than that of the RDG. We illustrate this by the use of a dashed line projection on the axis of Θ . The minimum for Mie is approximately 151° whilst the RDG minimum is approximately 132° , resulting in an angular phase difference of 19° . The generalised prediction has its minimum at approximately 146° resulting in angular difference of 5° . This improvement in backscattering has resulted from insertion of the polarisability term, as well as employing an internal field function that depends on the relative refractive index within the cell. That is to say, Proposition 3.1, as

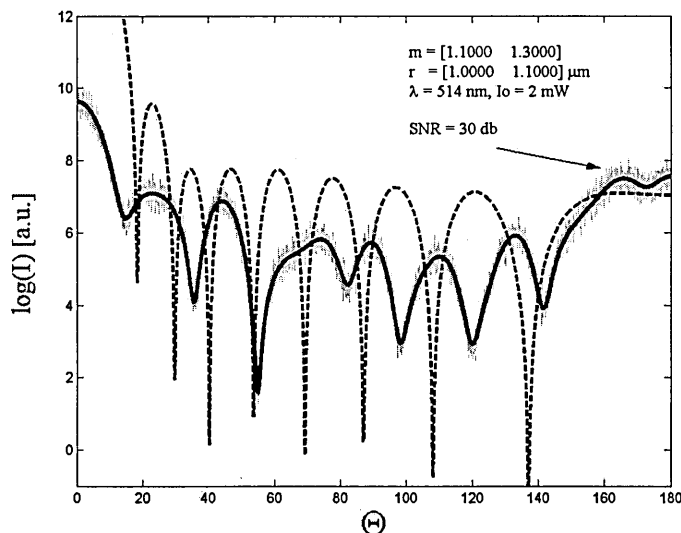


Figure 3.13: A two layer model from the exact solution indicated by the solid line and from the mRDG indicated by the dotted line. The core is assumed to be of radius $1\mu\text{m}$ and corresponding relative refractive index 1.1 whilst the outer layer has radius $1.1\mu\text{m}$ and corresponding relative refractive index 1.3

expressed in Equation 3.51, seems to work better on predictions for backscattering and for near-index particles; this is the case for bacteria in water based environments.

To illustrate the overall behaviour in predictions, another bacterium is modelled, as a two-layer cell, but we increase the values for the optical properties. That is to say, the core is assumed to be of radius $1\mu\text{m}$ and corresponding relative refractive index 1.1, whilst the outer layer enclosed within the radius $1.1\mu\text{m}$ of the cell has a relative refractive index 1.3. The physical meaning of such a value corresponds to a cell wall that is more dense than the internal material of the cell. Again, in Figure 3.13 we note the similarities between the two patterns in terms of the values of Θ at which extrema¹¹ occur, and also for the intensity amplitude. We remind the reader that the values for the optical properties used here have been experimentally derived by Berckman and Wyatt [70], also included in Table 2.2.

Finally we have to note the effect that additional numbers of layers has on backscattering. That is to say, in Figure 3.14 and for the generalised Rayleigh-Debye approximation. We have devised an experiment whereby the radius of the core of the cell remains the same but the number of layers increases from 2 to 5 for radius increments of $0.1\mu\text{m}$. That is to

¹¹By the term *extrema* we mean a maximum or minimum of a function. For example, the total number of minima and maxima that appear in a curve is the number of extrema.

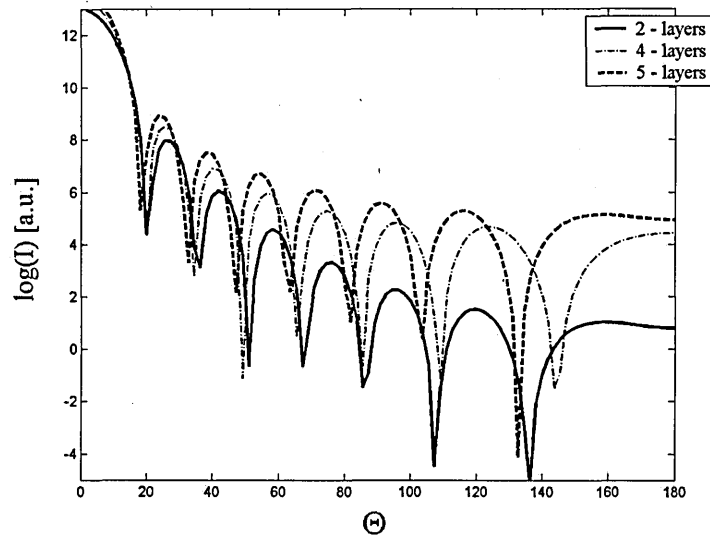


Figure 3.14: Resulting scattering patterns of angular dependence for the generalised Rayleigh-Debye approximation. The solid line depicts the result for 2 layers, the dotted line represents results for 4 layers and the dashed line corresponds to 5 layers.

say for a 2-layer model the internal radius $r_1 = 1\mu\text{m}$ and external $r_2 = 1.1\mu\text{m}$ and as a result for a 4-layer layer structure it follows that $[r_1 \ r_2 \ r_3 \ r_4] = [1 \ 1.1 \ 1.2 \ 1.3]$. A similar procedure is applied to the relative refractive index values except that now the applied increment is of $m_k \pm 0.05$. It is commonly understood that, when a cell is suspended in a medium of a lower refractive index, the cell itself is responsible for small angle scattering. We can clearly see that this is true for our approximation procedure as well, due to the fact that most high amplitude scattering is situated at small angles. This has been used in areas such as flow cytometry to estimate the sizes and concentrations of cells. However, this is not the case for multiple layers, where one could postulate that the cell can be considered as having multiple concentric inclusions, all of which are surrounded by a cell wall. In this case most of the scattering is attributable to the particular structures within the cells [33].

Again we can clearly see in Figure 3.14 that the scattering amplitude increases with increasing number of layers and overall radius. Furthermore the inhomogeneities within the cell increase the amount of backscattering, that is the amplitude of scattering at angles larger than 90° . This illustrates the potential application of light scattering to elucidate whether scattering originates from inhomogeneous or uniform depictions of the cell. In the current example we observe that, at larger angles, scattering is mainly attributed to the inhomogeneity of the cell, and as a result this provides a possible means of real-time

characterisation by observing backscattering. Depending on the relative refractive index of the core, that is to say the nucleus of the cell, and the number of layers employed, most scattering contributions can be decomposed by the procedure of Figure 3.10, hence solving the problem by fitting the experimental data to the model presented in this chapter.

Finally, another significant point to be made is by observing the 2-layer model of Figure 3.14, with a refractive index array of $m = [1.1 \quad 1.21]$, and the one of Figure 3.13, where $m = [1.1 \quad 1.3]$. The latter corresponds to a model for a coccoid bacterium, with a cell wall denser, that is more rigid, than the one with a smaller value of refractive index for the cell wall. Note that the number of maxima for the dense cell wall increases from 8 to 9, as a result of increasing the number of oscillations within the nucleous/cytoplasm interface. This observation can also be verified from the Mie exact model. Theoretically speaking for a denser cell wall one would expect an increase in the number of oscillations observed in the angular scattering pattern. This becomes clearer if we contrast the results with those for a similar sized object but for different composition of the cell wall. This would be of great experimental value for determining either the Gram reaction of the cell or the issue of dormancy for bacterial spores, even though it is almost certain that more layers have to be deployed in the model. However a number of experiments would have to be done so that a database of such experiments is effectively constructed.

3.5 Validation and applicability limits of the approximation model

As mentioned earlier (Section 2.4) there have been several methods of solving the problem of light scattering by spherical particles in general. However, fewer are suggested for the n -layer radially symmetric particle. A careful algorithmic analysis of even the most popular of approaches (for example in [57, 114, 58, 106]), is absent. Because of this, as we have seen earlier (Section 3.2, Equation 3.14), the limits for calculation of the number of terms in the Mie series is based on older convergence criteria [10, 4] with questionable applicability to the n -layer problem. In such a situation, systematic checking rather than a few particular individual tests is needed to assess the validity of a theoretical method/numerical code. Unfortunately, a solution may provide an acceptable result in certain cases but fail under slightly different experimental circumstances. The parameter space for bacterial cells was reported in Section 2.2.

Bacteria sizes vary considerably, from half a micrometre up to several micrometres. In particular, cocci (spherical morphology) would be said to have a radius r within the range $0.5\mu\text{m} \leq r \leq 1.2\mu\text{m}$ with a few exceptions, such as *Sarcina ventriculi* with a $4\mu\text{m}$ radius

and spore inclusions. In scattering experiments, cells are usually suspended in water based media and so the relative refractive index m is close to unity and the cytoplasm's refractive index value is close to 1.35, resulting in a selected range for m in the studies reported here as $1 < m < 1.3$.

Following the criteria set by [110], we present a relative error study for values of relative refractive index and radius as discussed. However, since we are dealing with multiple layers, the examination of single particle scattering is introduced in more detail. Hence, for each cell size defined by an overall radius, the thickness of each layer is proportionally assigned by the use of uniform random numbers in the range $(0, 1)$ (written $U(0, 1)$), so that for the k -th layer the radius will be $r_k = r_{k+1} - r_{k+1}U(0, 1)$. The relative error is estimated over an average of R runs, where for each run a corresponding random relative refractive index value has been provided within the range of interest. We insist on the use of uniform random numbers because in such way we do not bias our results. That is to say, any number within the said range has equal probability of being selected. In the analysis, only the average refractive index m of the cell is illustrated for each value of overall radius r .

The relative difference metric E_R is similar to the one reported in [110] but here we examine the light scattering intensity as opposed to the phase matrix relations. In particular, the error is a measure of the difference between intensities estimated by Mie and mRDG models and is normalised as:

$$E_R = \frac{\sum_{i=0}^N |\log I^{Mie}(i\Delta\theta) - \log I^{mRDG}(i\Delta\theta)|}{(N+1)(\log I^{Mie}(0) - \log I^{Mie}(\theta_o))} \quad (3.54)$$

The values used in the simulations were $N = 100$, $R = 30$ and $\Delta\theta = \pi/N$. Moreover, at a scattering angle θ_o the light intensity of the Mie scattering function (I^{Mie}) is at minimum. Figure 3.13 depicts typical light intensity patterns for the Mie and mRDG models which are the basis for error evaluation through Equation 3.54.

Many authors including Hoekstra *et.al.* [110] have concluded that for a homogeneous sphere the mRDG model covers a significant part of the domain; particularly if one allows for error of 12% as compared to Mie scattering. However, we have found that in the case of multi-layered spheres this relative difference doubles. In particular, Figure 3.15 depicts the error map between Mie scattering model and mRDG for two layer spheres. The grey scale represents the average relative error from 0% (black) to 30% (white). Generally speaking, in Figures 3.15, 3.16 the total average error does not exceed the limit of approximately 19%, even though small areas of 30% do appear. The latter can

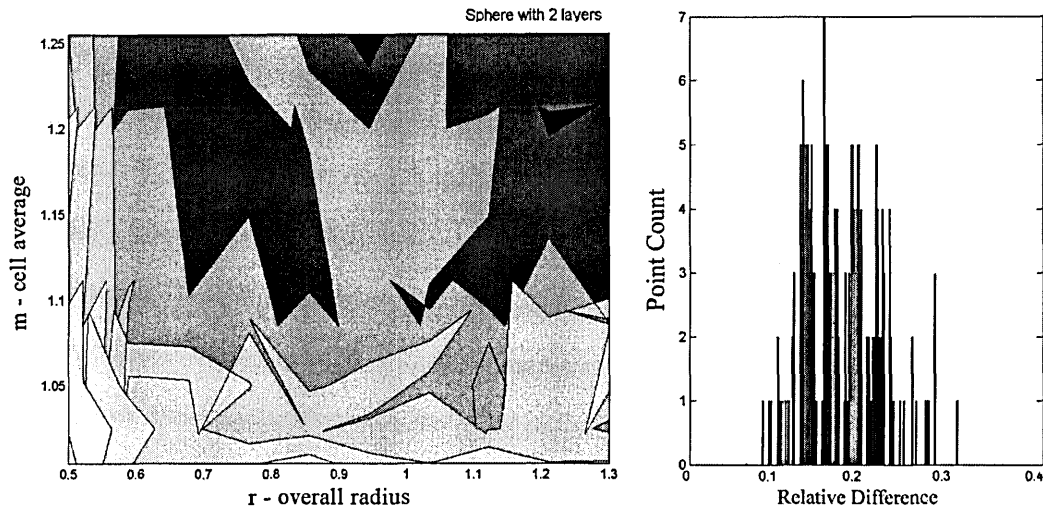


Figure 3.15: $n = 2$. Relative difference mapping between generalised RDG and Mie scattering for a two layer spherical model with corresponding point histogram.

be verified by consulting the error histogram of Figure 3.15 which shows that the greatest difference between the two models lies between 15 and 23%. The ‘error’ or relative difference between Mie and generalised RDG as depicted here shows a very irregular pattern. This is due to the fact that we randomly select values of m_i and an average value over the whole cell is calculated and depicted. A similar argument applies for r_i . The initial result is in effect indexed values of E_R corresponding to indexed values of radius and relative refractive index. A result for $n = 6$ is depicted in Figure 3.16. There are four clear regions in the illustration of the Indexed Relative Difference between the two models. That is to say, a region of approximately 10% difference depicted with a shaded black colour, and three more shaded grey areas of a limit to about 22%. The white coloured areas mapping to a 30% difference appear not because of failure of the generalised approximation but due to sampling of extreme values resulting in outliers within the results, or due to the fact that some in-between values have not been sampled resulting in the maximum error being assigned by our simulation algorithm.

This error or relative difference is consistent throughout the two models for either 2, 3, 4, 5 or 6 layers. Additionally, the generalised Rayleigh-Debye model is an algorithmically faster representation, since Mie algorithms are at least 100 times slower (or more depending on programming skills) than their RDG or generalised Rayleigh-Debye counterparts [4]. As a result, there may be advantages in using the generalised Rayleigh-Debye model in terms of the time taken to infer optical parameters.

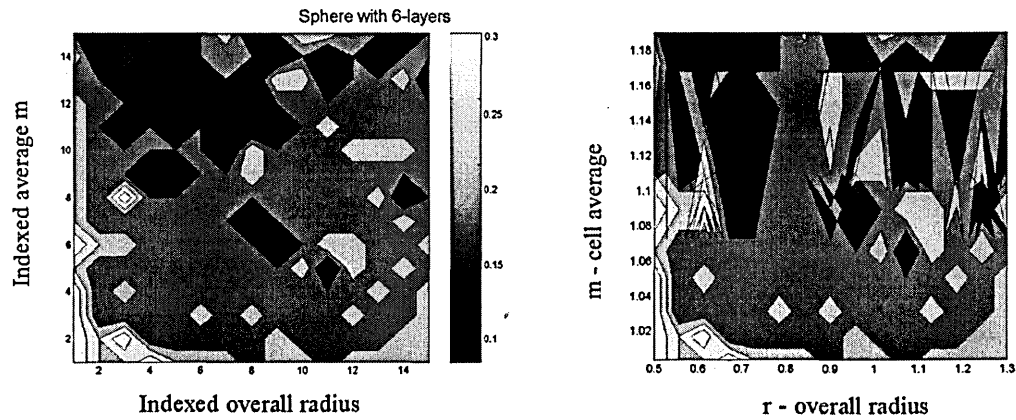


Figure 3.16: Relative difference mapping between generalised RDG and Mie scattering for a 6 layer spherical model. Both the result for indexed and its mapping to sorted values of (r, m) are indicated

In Figure 3.17 it must be emphasized that as the number of layers increases the maximum relative error margin slightly shifts towards higher r values and covering a larger m value margin. As a matter of fact Volkov and Kovach [57] state that for near index particles (high water content) the key factor in the Mie scattering behaviour is the thickness of the layers. Thus it may seem rather surprising that the relative error increases not with increasing r values but with increasing average refractive index, as it is evident in Figure 3.17. This may mean that Mie theory is not particularly sensitive to changes in refractive index for larger values of radius. This indeed may have given rise to the relative error which may be attributed to the generalised Rayleigh-Debye approximation's sensitivity to changes in refractive index. Returning to the earlier rare example of *Sarcina ventriculi*, in a simulation for $r = 4\mu\text{m}$ and for various m values, the average relative error was found to be in the region of 3 to 27%, with the larger relative error arising as $m \rightarrow 1.3$. Finally, within the domain of Prokaryotic cells, such large m -values are not often reported and, hence, the mRDG model may be applicable within the limits of the domain.

Testing the relative error of bacteria populations would also be performed using the same procedure as long as the assumption of independent scattering applies. However since the patterns will be a result of averaging over several sizes, which would minimise the overall difference between the models, the analysis would yield better results and so further illustrations are not included. Therefore, the apparent smoothing of sharp maxima (or minima) in the scattering intensity does not indicate degradation in performance of the n -layer mRDG model. It appears that the difference between the two models is at its maximum at about 25%. We have used the term *relative error*, which does not necessarily

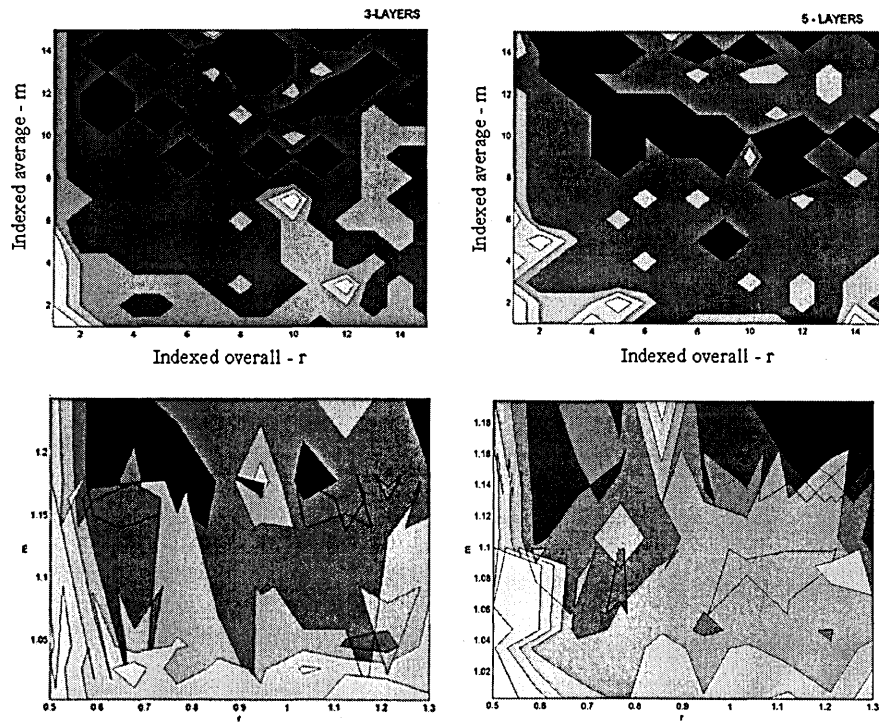


Figure 3.17: From Left to Right relative difference maps between generalised Rayleigh-Debye and Mie scattering for: 3-layers hence $n = 3$ and 5-layers hence $n = 5$. At the top we have the indexed relative difference mapping and at the bottom the corresponding averaged sorted indexed values.

portray the expected error under true experimental conditions. In particular, one has to bear in mind the much faster computation of the generalised Rayleigh-Debye models as opposed to the Mie equivalents. This can be explained as follows: calling t the number of terms to be calculated in the Mie series and n the number of layers, and l_{mie} the scattering coefficients, there would be a minimum of $(l_{mie}nt)$ calculations. The equivalent number for the generalised Rayleigh-Debye scattering would be $(l_{mrdg}(2n - 1))$. In our implementation of both models on the same platform¹², Mie models were at least 100 times slower than the RDG or our generalised approximation counterparts. As a result, for real time or time critical applications the generalised Rayleigh-Debye approximation is expected to be favoured over other more complex theories. The increased computational performance brings obvious advantages to cell characterisation.

3.6 Conclusions

In this chapter we have analysed and derived a model for bacteria that can be characterised as spherical near-index small particles. In that sense we proposed that the cell has to be modelled as an n -layer structure so as to include the contributions arising from all parts of the cell, in agreement with findings on internal structure from electron microscopy. With that in mind four major contributions can be identified:

1. *Implementation of the computer algorithm for the n -layer exact solution.* A verification that for spheres, light scattering patterns present symmetry around the scattering angle (even function of $\Theta \in (0, 2\pi)$), irrespectively of the number of layers deployed for the internal structure.
2. *A generalised solution to the n -layer near index problem* based on modification to the Rayleigh-Debye approximation. We have verified that for the popular model of 2-layers, our solution, the generalised approximation, behaves closer to the exact solution than the model without modification at backscattering. Unfortunately, the problem in the orders of intensity that it covers has not been solved. Increased relative difference at forward-scattering angles increases the overall average difference.
3. We have established that the range of relative refractive index for which our generalised approximation is valid covers a significant part of the bacteria domain.

¹²All implementations are performed in Matlab (Release 12) and executed on a Microsoft Windows based computer system

We have improved the condition for the relative refractive index (in particular for backscattering) from $|m - 1| \ll 1$ to $|m - 1| < 1$.

4. The *relative difference* of the generalised approximation and the exact solution is on average at 19% *irrespective of the number of layers* deployed. Bearing in mind that we uniformly sample within a range $m \in (1, 1.5)$ this difference may become smaller by simply selecting a smaller relative refractive index range of values.

Contribution 1 is important as not many computer programs have been provided, even though many solutions for the said model have been published. However the programs are either not generally available or they can be found in a form that is not easy to use. We have used the Matlab technical computing language to do so, and ever since the publication of our implementation many people have either enquired or have been using the code.

Contribution 2 is of great importance in the domain of near-index cells and consequently for most biological particles that need to be examined *in vivo*. That is to say, all light scattering equipment can adopt the generalised model and infer $2n - 1$ parameters for the cell within the bounds of applicability. As long as the medium in which the bacterium is suspended has an index of refraction close to the one of the particle then identification by the use of the inferred optical parameters may be possible.

Contributions 3 and 4 relate to the applicability limits of the generalised approximation. First we have shown that the relative difference from the exact solution is twice than what was previously believed. That is to say, the belief that modifying the Rayleigh-Debye approximation will result in a relative difference close to 10% does not apply. In fact, by employing multiple layers, the approximation differs from Mie scattering by approximately 20%. However, our significant find is that for our model, thence for the generalised Rayleigh-Debye, this may be true but for increased m and r values. In any case, it has been experimentally shown that for bacteria $m < 1.35$, and as a result the approximation model/procedure that we offer herein may prove to be experimentally successful.

Finally, our procedure would provide results within a few minutes and as such is not expected to significantly add in time to the production of results. We postulate that in real-time applications it is expected to be favoured over more complex alternative theories.

Chapter 4

The generalised ellipsoidal Rayleigh-Debye approximation

It should now be clear that the mathematical and computational problems concerning light scattering theory for bacteria, modeled as small, near-index particles and of spherical geometry can be resolved with either Mie scattering or our generalisation to n -layers of the Rayleigh-Debye approximation. However problems still remain to be tackled in the case of non-spherical particles, and in particular ellipsoidal forms where departure from spherical symmetry can range from negligible to such that the major/minor axis ratio is set to model flat elongated particles, flat disc-like structures in a prolate or oblate spheroidal geometric shape and other forms. Furthermore there is a need to examine the effect on the scattered amplitude when modeling for populations of cells in this extension from spherical to ellipsoidal bacterial forms. The problem would be defined as,

Definition 4.1. From a collection of bacterial cells suspended in a water based liquid medium, which appear alone and resemble an ellipsoidal geometric shape, and which are illuminated by laser radiation, examine the effect that an assumed multilayered internal structure has on the scattered field in all directions.

Using the basis we have built in proofs and discussions for our generalised n -layer spherical Rayleigh-Debye solution, we now extend this to any ellipsoidal geometric form. We then examine the effect of non-sphericity, that is to say the axial ratio, on the scattered field and simulate for diluted suspensions that follow a size distribution ¹. We provide throughout the reasons why backscattering is important even for ‘soft-scatterers’ like bacteria suspended in water, and we theoretically explain the need for development of instrumentation that collects scattered radiation in the three dimensional sense.

¹Most of the said in this Chapter have been published within the Institute of Physics series in Sensors, published in September 2003

4.1 Introduction

In this chapter we will be using a different mathematical procedure to extend our previous model from spherical to ellipsoidal particles. This method is commonly known as the ‘*method of slices*’ and has been used in the past to model homogeneous particles as outlined for example in [100] and in scattering media [115]. However, the terms employed within proofs are defined loosely, and as a result we start by defining the basic terminology that is generally used within our derivations.

Definition 4.2. A **line** is defined in the Cartesian geometry sense as a straight one-dimensional ‘figure’ of infinite length and no thickness, uniquely determined by any pair of points in the three dimensional space \mathbb{R}^3 of which the segment they create is the shortest path between them, hence defining a one dimensional subspace of the vector’s three dimensional space. Vectors are quantities having both magnitude and direction, as opposed to scalar lengths on a line that only have magnitude.

As such if one wishes to take slices of a solid, which are perpendicular to the line that defines the limits within the particle, then one needs firstly to define the line on which these slices are to be taken and secondly to consider the plane of which this line is a member.

Definition 4.3. If an arbitrary solid of volume V is cut at infinite planes perpendicular to some line, in the Cartesian geometry sense, then infinite cross sections will be generated, which are said to have volumes of infinitely many small thicknesses, each of which is called an **infinitesimal thickness**; hence a single slice would be described as the area of small thickness.

As we will see later, an arbitrarily shaped slice results from an arbitrarily shaped solid and if we assume that its thickness is infinitively small, then as a direct consequence of the limit ds , calculating a volume of a slice reduces to calculating the area of the slice.

Definition 4.4. The scattering field amplitude elements in the Maxwell/Stokes formalism for any particle irrespective of external geometrical shape and internal morphology can be separated to two contributions of which one is the **Form Factor**. The Form Factor is defined in this chapter as a function of scattering position (θ, ϕ) that depends on the

geometric properties of the cell; namely the orientation and size in conjunction with the ratio of asymmetry.

However, due to insertion of multiple layers, there is a need for re-exploration of the effect of the Form Factor to the scattering amplitude. That is to say, to the above definition, we need to add the case of non-homogeneity and its effect on refraction.

4.2 Approximate solutions on near-index ellipsoidal geometries

As we have shown in Chapter 3, the generalised Rayleigh-Debye approximation would be applied for a particle of arbitrary shape as any infinitesimal volume at any point within the particle can be utilised so that the particle is a collection of such points with infinitely small volumes. Under the paradigm of our main result, that is to say the generalised Rayleigh-Debye spherical approximation, the extended condition $|m - 1| < 1$ will hold if one allows for a relative difference of 18% from the exact solution and as long as $1 < m < 1.3$. In terms of the scattered field from an arbitrary particle we recall that

$$\mathbf{E}_s = -\frac{k_o^2 \exp(jk_o b)}{4\pi b} \mathbf{k}_s \times [\mathbf{k}_s \times \mathbf{e}_i] \int_V \hat{a}(\mathbf{r}) \exp(j\mathbf{r} \cdot \bar{\mathbf{k}}_d) dV \quad (4.1)$$

If the distribution of relative refractive is considered to be similar to that of the sphere in the schema of Equation 3.37, that is to say, the relative refractive index in polar coordinates at some distance r within the particle will be such that it will have a value $m(r, \theta, \phi) = m_i$, where $i = 1, 2, \dots, n$ denotes a layered structure. Then a further simplification would be performed, so that

$$\mathbf{E}_s = -\frac{k_o^2 \exp(jk_o b)}{4\pi b} \mathbf{k}_s \times [\mathbf{k}_s \times \mathbf{e}_i] \sum_i \hat{a}_i \int_{V_i} \exp(j\mathbf{r} \cdot \bar{\mathbf{k}}_d) dV \quad (4.2)$$

It follows that the amplitude of this field with respect to the scattered field of direction \mathbf{k}_s as opposed to that of incidence with direction \mathbf{k}_i , will be

$$S(\mathbf{k}_s, \mathbf{k}_i) = jk^3 \sum_{i=1}^n \hat{a}_i \int_{V_i} \exp(j\mathbf{r} \cdot \bar{\mathbf{k}}_d) dV \quad (4.3)$$

and relating this to a form factor $P(\mathbf{k}_s, \mathbf{k}_i)$, which is the quantity within the scattered field's amplitude that depends on the geometric shape of the particle and the internal structure, which in our case is a layered particle then

$$P(\mathbf{k}_s, \mathbf{k}_i) = \sum_{i=1}^n \hat{a}_i \int_{V_i} \exp(j\mathbf{r} \cdot \bar{\mathbf{k}}_d) dV \quad (4.4)$$

However as we have illustrated by the proof of Corollary 3.2, the expression within the kernel of Equation 4.3, commonly referred to as the phase lag δ , of any pair of infinitesimal volumes is $\delta = \mathbf{r} \cdot \bar{\mathbf{k}}_d$. In terms of the modification on the Rayleigh-Debye approximation, following Theorem 3.3 and by applying our proposition, from which we consider that the infinitesimal volume will scatter light depending on the relative refractive index of the layer it occupies, then Equation 4.4 becomes

$$P(\mathbf{k}_s, \mathbf{k}_i) = \sum_{i=1}^n \hat{a}_i \int_{V_i} \exp(jk_0 m_i \mathbf{r} \cdot \mathbf{k}_d) dV \quad (4.5)$$

where on this occasion \mathbf{k}_d is a unit vector denoting the direction of $\bar{\mathbf{k}}_d$.

Lemma 4.1. *Let \mathbf{r} denote the direction and distance r between infinitesimal volumes within the boundaries of the cell. If \mathbf{k}_d denotes the direction of the difference between incident and scattering fields, then this difference will lie on the bisectrix of the complement of the scattering angle θ and would be expressed by the distance on the bisectrix (p).*

Proof: From Corollary 3.2 of Chapter 3, it follows that $\mathbf{r} \cdot \mathbf{k}_d$ is a projection of \mathbf{r} onto the difference between unit vectors \mathbf{k}_i (incidence) and \mathbf{k}_s (scattering). The angle between $(\mathbf{k}_i, (-\mathbf{k}_s))$ equals the scattering angle. Since $(\mathbf{k}_i - \mathbf{k}_s)$ lies on the base of an isosceles triangle and denoting the angle between $(\mathbf{k}_i, (\mathbf{k}_i - \mathbf{k}_s))$ by γ , then the total of angles within the isosceles triangle will be $\theta + 2\gamma = 180^\circ$; hence $\gamma = 90^\circ - (\theta/2)$.

It follows that $(\mathbf{k}_i - \mathbf{k}_s)$ can be thought of as being parallel to the bisectrix of the complement of θ . As a result \mathbf{k}_d can be found by assuming that it lies on the bisectrix. Let p to denote the projection of \mathbf{r} on the bisectrix of complement of θ (Figure 4.1). It follows that

$$\begin{aligned} p &= \frac{\mathbf{r} \cdot (\mathbf{k}_i - \mathbf{k}_s)}{|\mathbf{k}_i - \mathbf{k}_s|} \\ \mathbf{r} \cdot (\mathbf{k}_i - \mathbf{k}_s) &= p |\mathbf{k}_i - \mathbf{k}_s| \\ \mathbf{k}_d &= p |\mathbf{k}_i - \mathbf{k}_s| \end{aligned}$$

where

$$|\mathbf{k}_i - \mathbf{k}_s|^2 = 2 - 2\mathbf{k}_i \cdot \mathbf{k}_s = 2(1 - \cos \theta)$$

It follows that

$$|\mathbf{k}_i - \mathbf{k}_s|^2 = 4 \sin^2(\theta/2)$$

and as a result

$$k_d = 2p \sin(\theta/2) \quad (4.6)$$

where the last step follows from the fact that $2 \sin^2 A = 1 - \cos 2A$ and placing $A = \theta/2$. ■

This lemma postulates that the scattering amplitude of the particle could be calculated by taking slices perpendicular to the bisectrix, which are very small in thickness, instead of solving directly over the whole volume of a particle with no axis of symmetry.

However, the integral of any function relating to a solid, for example of functional form $\mathfrak{L}(x, y, z)$, over its volume is defined as the limit of the sum of all elements $\mathfrak{L}(x, y, z)\Delta V$, where ΔV is a subinterval of a partition of an interval of values for \mathfrak{L} , and the limit is taken as the number of subintervals tends to infinity, hence the length of each tends towards zero. As a result the scattering amplitude can be expressed as the infinite sum of infinitesimal areas along a line that passes through the solid (Figure 4.1). Taking this into account, if we now assume, without loss of generality, that \mathbf{k}_i is parallel to the z axis of a global coordinate system then \mathbf{k}_s makes a polar angle θ with respect to it, and on this occasion the scattering angle Θ defined in the previous chapter is equivalent to the polar angle that we defined here. As a result, and by assuming that p is the projection of the positioning vector \mathbf{r} on the bisectrix, then

$$\delta = 2k_o m_i p \sin(\theta/2) \quad (4.7)$$

where the latter follows from $\delta = k_o m_i k_d$, where from Lemma 4.1 we have that $k_d = 2p \sin(\theta/2)$, and here we remind the reader that $k_o = 2\pi/\lambda$. All points along the plane perpendicular to the bisectrix that pass through the endpoint of the positioning vector r will have the same phase lag. As a result, the integrals of the type of Equation 4.5 can be most easily evaluated (Lemma 4.1) by integrating over volume elements which consist of cross sections perpendicular to the bisectrix. Consequently integrating by means of cross sections which occupy an area A and infinitely small thickness, that is to say dp as illustrated in Figure 4.1, will result in Equation 4.5 being much simpler. It can then be evaluated by

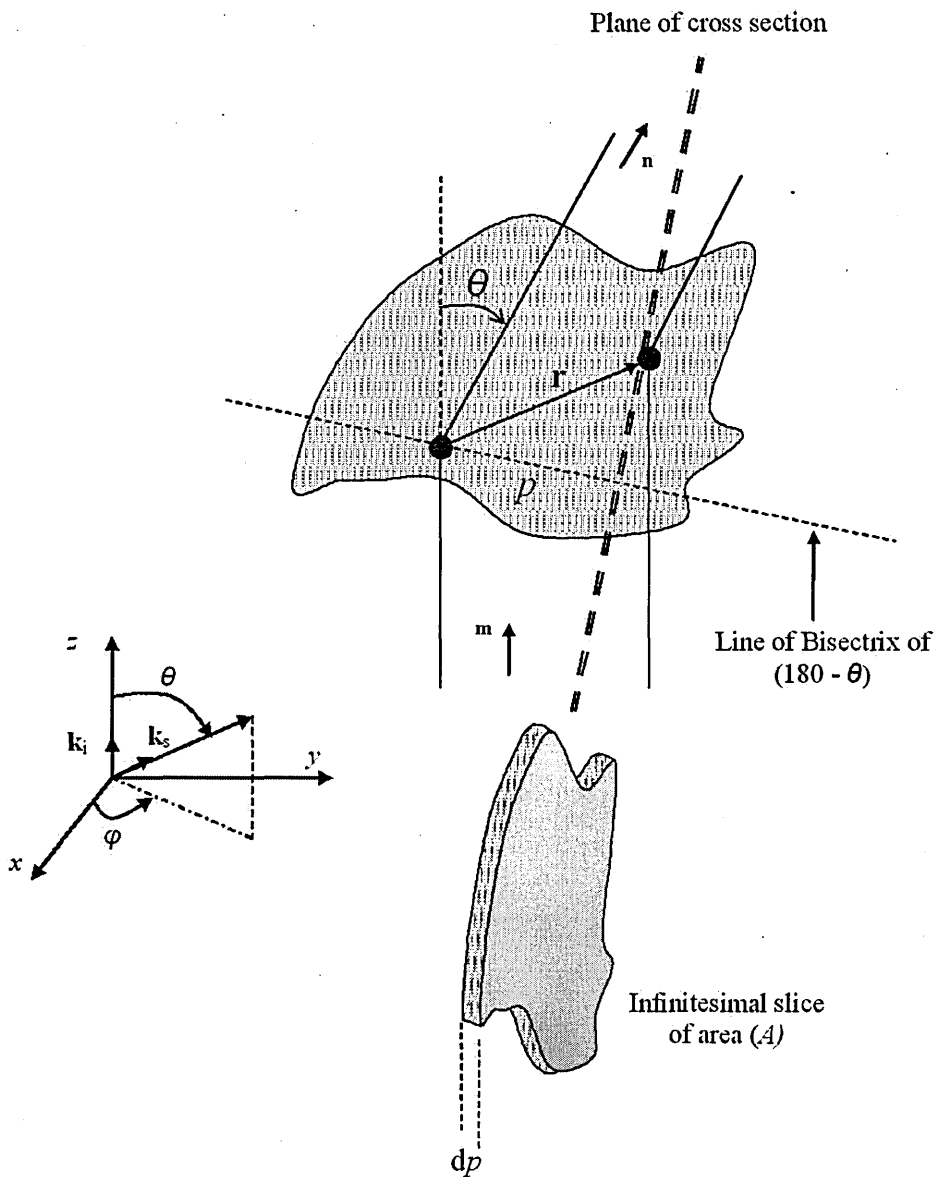


Figure 4.1: Illustration of integrating by taking cross sections of the solid found by planes perpendicular to the line of the bisectrix. The cross section shown here in detail has an area A and infinitesimal thickness dp , where p is the projection of the positioning vector r on the bisectrix. Note a change in the assumption of incidence; the incident direction denoted by k_i is parallel to the z axis of a global coordinate system, and the scattering angle is the polar angle θ , and as a result, linking this to Chapter 3, $\theta = \Theta$.

$$P(\theta, \phi) = \sum_{i=1}^n \acute{a}_i \int_{-\infty}^{\infty} A(p) \exp(j2k_o m_i p \sin(\theta/2)) dp \quad (4.8)$$

Take for example, a homogeneous spherical particle, and note that planes normal to the bisectrix will result in circular cross sections of radius $r = (a^2 - p^2)^{1/2}$, where a is the radius of the sphere and p is the distance along the bisectrix. The area of such circular cross sections will be πr^2 . Taking into account the spherical symmetry of the particle it follows from Equation 4.8 that

$$\begin{aligned} P(\theta, \phi) &= \frac{3m^2 - 1}{4m^2 + 2} \int_{-p}^p \pi(a^2 - p^2) \exp(j2k_o m p \sin(\frac{\theta}{2})) dp \\ P(\theta, \phi) &= \frac{3m^2 - 1}{4m^2 + 2} \int_{-p}^p \pi a^2 (1 - (\frac{p}{a})^2) \exp(j2k_o m p \sin(\theta/2)) dp \end{aligned} \quad (4.9)$$

Let the ratio $q = p/a$ and following the notation from the previous chapter, $u = 2k_o m a \sin(\theta/2)$. Taking into account that the radius of the slice is constant then $dp = a dq$, Equation 4.9 may be written as

$$\begin{aligned} P(\theta, \phi) &= \frac{3m^2 - 1}{4m^2 + 2} \pi a^3 \int_{-1}^1 (1 - q^2) \exp(j2k_o m a \sin(\theta/2) q) dq \therefore \\ P(\theta, \phi) &= \frac{3m^2 - 1}{4m^2 + 2} \pi a^3 \int_{-1}^1 (1 - q^2) \exp(juq) dq \end{aligned} \quad (4.10)$$

Bearing in mind that $\exp(juq) = \cos(uq) - j \sin(uq)$ in conjunction with the fact that $\cos(-uq) = \cos(uq)$, it follows that

$$\begin{aligned} P(\theta, \phi) &= \frac{3m^2 - 1}{4m^2 + 2} \pi a^3 \int_0^1 (1 - q^2) \cos(uq) dq \\ &= \pi a^3 \frac{m^2 - 1}{m^2 + 2} (3/u^3) (\sin u - u \cos u) \end{aligned} \quad (4.11)$$

which is equivalent to the result provided in [95], apart from the fact that we have reinstated in Chapter 3 the term of average volume polarisability. In effect we have a result quite similar to the one obtained for arbitrary incidence, that is, of Equation 3.51 and for $i = 1$. This example can be said to be a theoretical validation of the correctness of the procedure which we used for integration via cross sections through producing similar results. The functional form will not be exactly the same since simplifying assumptions have already been introduced in advance, for example with respect to the angle of incidence and scattering. The latter would be performed, without loss of generality, in order to attempt to solve the problem of ellipsoidal geometries, n -layered structured, and shape.

We are interested in solving the problem for an ellipsoid of semiaxes (a, b, c) in Cartesian coordinates. The equation for such an ellipsoid is given by

$$\left(\frac{x}{a}\right)^2 + \left(\frac{y}{b}\right)^2 + \left(\frac{z}{c}\right)^2 = 1 \quad (4.12)$$

The equation of the plane tangent to this conicoid at the point O on its surface $O(x_1, y_1, z_1)$ is known to be [102]

$$\frac{xx_1}{a^2} + \frac{yy_1}{b^2} + \frac{zz_1}{c^2} = 1 \quad (4.13)$$

Let the direction cosines of the bisectrix as shown in Figure 4.1 be l, m and n respectively, where in vector form it is so that $k_i \equiv n, k_s \equiv m$. The plane normal to this direction and tangent to the ellipsoid at the point $O(x_1, y_1, z_1)$ will be given by the equation

$$lx + my + nz = \rho \quad (4.14)$$

where ρ needs to be determined. However the plane described in Equation 4.13 is equivalent to the plane described in Equation 4.14, and as a result a point O on the surface of the ellipsoid will result in

$$\begin{aligned} x_1 &= \frac{la^2}{\rho} \\ y_1 &= \frac{mb^2}{\rho} \\ z_1 &= \frac{nc^2}{\rho} \end{aligned} \quad (4.15)$$

and as a result substituting the values Equations 4.15 to Equation 4.12, since the said point lies on the ellipsoid, we will have that the expression for calculating the unknown parameter ρ is

$$\rho = \sqrt{(la)^2 + (mb)^2 + (nc)^2} \quad (4.16)$$

The plane perpendicular to the bisectrix whose equation is

$$lx + my + nz = p \leq \rho \quad (4.17)$$

will cut the ellipsoid in an elliptical section whose area is given by [103]

$$A = \pi abc \frac{1 - (p/\rho)^2}{\rho} \quad (4.18)$$

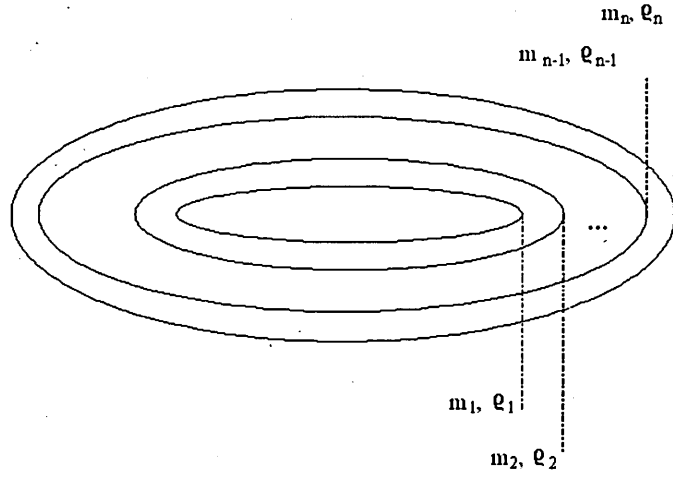


Figure 4.2: Cross section of the n -layered ellipsoid. Note that the $n-1$ layer is at distance ρ_{n-1} from the centre of the ellipsoid; whilst the n -th layer area is placed between ρ_{n-1} and ρ_n with relative refractive index m_n .

It should be clear that p is the distance from the centre of the ellipsoid to this plane measured along the bisectrix. Therefore, recalling Equation 4.8, one would now substitute the area of the ellipsoidal cross section of Equation 4.18 to obtain

$$P(\theta, \phi) = \sum_{i=1}^n \hat{a}_i \int_{-\rho_i}^{\rho_i} \pi abc \frac{1 - (p/\rho_i)^2}{\rho_i} \exp(j2k_o m_i p \sin(\theta/2)) dp \quad (4.19)$$

The integral of Equation 4.19 would be evaluated over each of the homogeneous regions of the n symmetrically placed coatings within an interval $[-\rho_n, \rho_n]$, as denoted in Figure 4.2. For the internal part of the cell, that is to say within the region $[-\rho_1, \rho_1]$ we evaluate as follows.

By noting that, as in the example for the homogeneous sphere that we have provided earlier in this section, the integral depends on variable p and by substituting the ratio p/ρ_1 by a new variable $w = p/\rho_1$ then $dp = \rho_1 dw$

$$P(\theta, \phi) \Big|_{-\rho_1}^{\rho_1} = \pi abc \hat{a}_1 \int_{-1}^1 (1 - w^2) \exp(j2k_o m_1 \rho_1 \sin(\theta/2) w) dw \quad (4.20)$$

and by letting $u_1 = 2k_o m_1 \rho_1 \sin(\theta/2)$, Equation 4.20 is simplified to

$$P(\theta, \phi) \Big|_{-\rho_1}^{\rho_1} = \pi abc \hat{a}_1 \int_{-1}^1 (1 - w^2) \exp(ju_1 w) dw \quad (4.21)$$

It follows that

$$\begin{aligned}
P(\theta, \phi) \Big|_{-\varrho_1}^{\varrho_1} &= 2\pi abc \acute{a}_1 \int_0^1 (1-w^2) \cos(u_1 w) dw \\
P(\theta, \phi) \Big|_{-\varrho_1}^{\varrho_1} &= 2\pi abc \acute{a}_1 \frac{\sqrt{\pi u_1}}{u_1^2} J_{3/2}(u_1)
\end{aligned} \tag{4.22}$$

where $J_{3/2}$ is the Bessel function of order $3/2$. The remaining terms that need to be evaluated in Equation 4.19, correspond to each of the n -layers. Following the model we have developed in Section 3.3, and the reasoning of the generalised Rayleigh-Debye spherical approximation, a layer can be thought of as a collection of elements that will scatter light independently of any collection of elements of another layer. It is therefore a natural consequence that the k -th layer of the cell will scatter light proportionally to that of a homogeneous ellipsoid of corresponding ϱ_k and m_k , by subtraction of the contribution arising from a $(k-1)$ homogeneous ellipsoid of corresponding ϱ_{k-1} but having the same relative refractive index m_k . Bearing this in mind and for the k -th layer we write:

$$\begin{aligned}
P(\theta, \phi) \Big|_{-\varrho_{k-1}}^{\varrho_k} &= 2(P(\theta, \phi) \Big|_0^{\varrho_k} - P(\theta, \phi) \Big|_0^{\varrho_{k-1}}) \\
&= 4\pi abc \acute{a}_k \left(\frac{\sqrt{\pi u_{k,k}}}{u_{k,k}^2} J_{3/2}(u_{k,k}) - \frac{\sqrt{\pi u_{k,k-1}}}{u_{k,k-1}^2} J_{3/2}(u_{k,k-1}) \right)
\end{aligned} \tag{4.23}$$

where $u_{k,\ell} = 2k_o m_i \varrho_\ell \sin(\theta/2)$, which effectively means that the subscript ℓ is taken with respect to the distance from the centre of the ellipsoid $p \in [-\varrho_n, \varrho_n]$. Generalisation for an n -layered ellipsoidal cell is now possible since the form factor of Equation 4.4 can be given by the expression of Equation 4.23, but for n -layers. Returning to the notation for the scattering amplitude from Equation 4.3 we now have the *generalised Rayleigh-Debye ellipsoidal approximation* such that

$$|S(\theta, \phi)| = \sum_{i=1}^n K_i G_{i,i} - K_i G_{i,i-1} \tag{4.24}$$

where $i \in \mathbb{N}^*$ and

$$K_i = 2k_o^3 abc \acute{a}_i, \quad G_{i,\ell} = \frac{\sqrt{\pi u_{i,\ell}}}{u_{i,\ell}^2} J_{3/2}(u_{i,\ell}) \tag{4.25}$$

with initial conditions

$$G_{1,1} = \frac{\sqrt{\pi u_1}}{2u_1^2} J_{3/2}(u_1), \quad G_{1,0} = 0 \tag{4.26}$$

In order to illustrate the physical and functional meaning of the expression in Equations 4.24 to 4.26, of which the internal variables are defined within the text, we refer

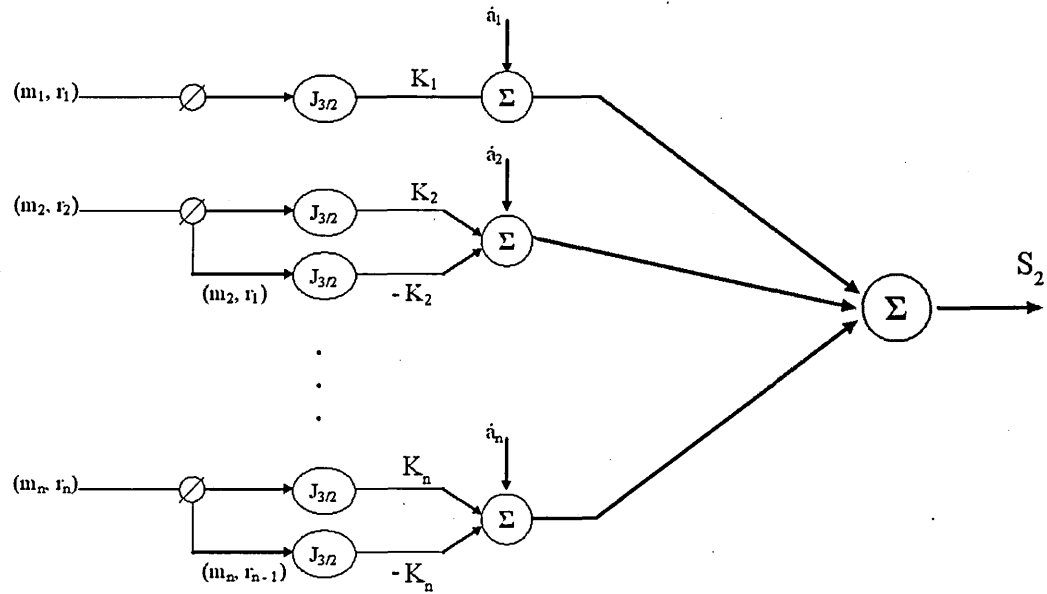


Figure 4.3: A diagrammatic illustration of the generalised n -layer Rayleigh-Debye ellipsoidal approximation as a graph network. Once again we use the formalism of notation from other engineering principles. The node denoted by \oslash means the $i - 1$ value with respect to the array of values and for the largest linear dimension only.

to Figure 4.3. In this graph depiction we have deployed n symmetrically placed layers around the ellipsoidal core. The core's contribution is the same as that of a homogeneous ellipsoid whilst the remainder needs to be taken as two further contributions. As a result we must insert an indexed value $i - 1$ in the input of any layer thereafter and with respect to the array of values for ρ . The two contributions are then following a sum over a multiplicative factor denoted by K_i . The total sum of all contributions results in the scattering amplitude S_2 which is in effect the amplitude of perpendicular polarisation with respect to the scattering plane. To obtain the amplitude of polarisation parallel to the scattering plane S_1 one should multiply by the term $\cos \theta$. The latter is due to the fact that the Rayleigh-Debye approximation derives from Rayleigh theory which states that by definition only the elements (S_1, S_2) are of interest. Consequently, since the generalisation of the Rayleigh-Debye approximation which we offer herein has a point of departure from Rayleigh theory we adopt the *de facto* case as stated, and for the subsequent calculations of the scattering matrix elements.

It should be evident that the result given in Equation 4.24 for ellipsoidal shaped particles/cells, is quite similar to that of Equation 3.51 for spherically shaped cells. The differences in the two models lies on the distance from the centre of the particle and along the bisectrix ρ .

4.3 Geometrical properties and the n -layer approximation

In the previous section we applied our reasoning method to the geometry of general ellipsoids where the major axis of the ellipsoidal linear dimensions that is a, b, c , are related so that $a > b > c$. However, what must be defined per layer is the distance from the bisectrix ρ_i . In turn, to calculate this distance we need to take into account the position of the particle in spatial dimensions, that is to say in its three dimensional space. Clearly, the later depends on the positioning of the ellipsoid, and hence depends on the relationship between the bisectrix and (θ, ϕ) .

Let us assume that the major axis of the ellipsoid is placed along the x -axis. The dependence of the bisectrix on θ and ϕ is made explicit when we define the direction of the major axis of the ellipsoid with respect to that of incident light and scattered light. As such, let α be the angle between the incident beam and the x -axis of the ellipsoid. Furthermore, let β be the angle between the bisectrix and the x -axis of the ellipsoid. We then have the formation of the spherical triangle in Figure 4.4. The expression of dependence between all angles defined follows from the direction cosines as defined earlier and

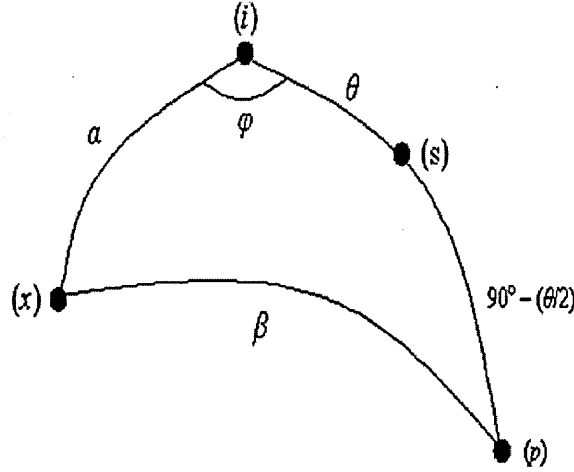


Figure 4.4: Spherical triangle showing the position of the major axis of the ellipsoid (v) with respect to the directions of incidence (i) and scattering (s). The bisectrix has the direction (p).

has been calculated by many. Due to the similarity of the orientation parameters for the ellipsoid we follow [100, p95] and we write

$$\cos \beta = -\cos \alpha \sin \frac{\theta}{2} + \sin \alpha \cos \frac{\theta}{2} \cos \phi \quad (4.27)$$

In this expression, the only angle that needs to be calculated is that of β . We will call this the orientation angle or *aspect*. Angles θ and ϕ are the angles that are characterised in a simulation procedure as inputs. For example if one wishes to map the results for the scattering amplitude on all three spatial dimensions then all points in space must be taken into account. In effect, it should be that $\theta \in (0, 2\pi)$ whilst $\phi \in (0, \pi)$. Consequently, by assuming or randomly selecting a particular angular incidence then this would be considered as a useful procedure for calculating the orientation angle. For example, by letting $\alpha = 45^\circ \equiv \pi/4$ then it follows that $\cos \alpha = \sin \alpha = \sqrt{2}/2$, whilst for say $\phi = 60^\circ \equiv \pi/3$ then $\cos \phi = 1/2$ and from Equation 4.27 we have that

$$\cos \beta = -\frac{\sqrt{2}}{2} \sin \frac{\theta}{2} + \frac{\sqrt{2}}{4} \cos \frac{\theta}{2}$$

By assigning values for θ , one would now calculate the corresponding $\cos \beta$ values and in effect compute the distances ρ_i . Particular discrete values are reported in Table 4.1 and for the resulting dependence on β . The values form of an input array

$$\beta = [1.2094 \quad 1.4116 \quad 1.5148 \quad 1.6178 \quad 1.8235]$$

θ	0	$\pi/6$	$\pi/4$	$\pi/3$	$\pi/2$
$\cos(\theta/2)$	1	0.9659	0.9239	0.866	0.7071
$\sin(\theta/2)$	0	0.2588	0.3827	0.5	0.7071
$\cos(\beta)$	0.3536	0.1585	0.0560	-0.047	-0.25

Table 4.1: An example for calculating the values for orientation angle β depending on θ and for $\alpha = \pi/4, \phi = \pi/3$.

in radians, which is equivalent to [69.29 80.88 86.78 92.69 104.48] degrees. To generalise from this example we have generated a table of values similar to Table 4.1 where $\theta \in (0, 2\pi)$. For the cosine amplitudes of β and $(\theta/2)$ an apparent lag between the two functions is illustrated in Figure 4.5 and as such a non-linear relationship exists. To explain the physical meaning of this relationship one must recall that on the scattering plane we assume that we have a number of detectors placed on a circular surface at the far-field, whilst the plane is defined by θ . Consequently, the scattering angle becomes, in a sense, the observation angle and we can now use this as a visual aid to understanding that as we scan at a different detector perspective and for increasing angular observation θ , then the direction cosine of the bisectrix ($x \cos \beta$) and as such the bisectrix itself gradually moves further away from the viewpoint of the detectors.

To put this into context and to better present resulting patterns of angular dependence from our model we investigate the special case of spheroids. That is to say we parametrically define the geometry of the cell so that $b = c = s$ and $a = ts$, where a, b, c are those of the general expression of the ellipsoid in Cartesian form in Equation 4.12, s is a sample from an array of values for size of some linear dimension and t denotes an axial ratio between the now two major axis of the spheroid. Substituting these values in Equation 4.16 for defining the limits of ϱ , and bearing in mind that the bisectrix forms an angle β with the x -axis, it follows that

$$\varrho = s\sqrt{t^2 \cos^2 \beta + \sin^2 \beta} \quad (4.28)$$

We can now clearly see the difference between the model for spherical particles and that of ellipsoids. The scattering amplitude model for spheres depends on the variable $u_{i,l} \sim r$ where r is the radius of the sphere, whilst the spheroid depends on the variable $u_{i,l} \sim s\sqrt{t^2 \cos^2 \beta + \sin^2 \beta}$. As we have illustrated the relationship between the scattering angle and the aspect of the ellipsoidal volume is non-linear. The relationship of the scattering amplitude with the scattering angle is also expected to be non-linear, resulting in polar scattering patterns of relative asymmetry. Let for example a three layer spheroid to model an Escherichia coli bacterium, for which it is known from Table 2.4, Chapter 2,

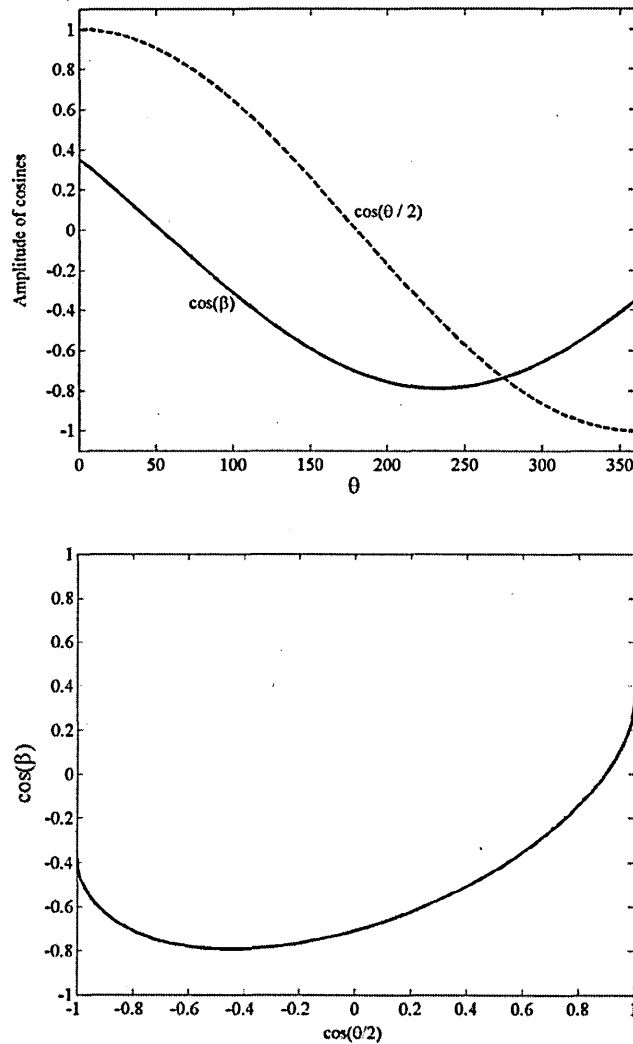


Figure 4.5: On the example for calculating values for orientation angle. A non-linear relationship between the cosines of β , $(\theta/2)$ is revealed in the plot between the cosines (bottom). The plot situated on the top of this figure, clearly illustrates the lag between the cosines and for values of $\theta \in (0, 2\pi)$. We have used the values of the example of Table 4.1, that is $\alpha = 45^\circ \equiv \pi/4$ and $\phi = 60^\circ \equiv \pi/3$.

that the average refractive index is 1.35, hence the average relative refractive index would be 1.02 and for incident wavelength of $\lambda = 0.514\mu\text{m}$. The size is assumed to be inferred from a volume of $1.1\mu\text{m}^3$, hence $s = 1\mu\text{m}$ whilst $a = 1.1\mu\text{m}$. We illustrate our finds in Figure 4.6.

For calculating the values for the dependence of ϱ on β (Equation 4.28), we assume that $\phi = \pi/3$ whilst in Figure 4.6, we have from top to bottom that the incident angle α changes for three distinct cases. That is for $\alpha = 0, \pi/4, 2\pi - \pi/4$. The second case ($\alpha = \pi/4$) is the one that we reported earlier in the example for calculating the term $\cos\beta$. In all graphs the solid line represents scattering at $\theta \in [0, \pi)$ whilst the dashed line represents scattering at $\theta \in (\pi, 2\pi]$. This depiction is also followed in the construction of the polar plots that can be seen on the right of each light intensity pattern and plotted in a logarithmic scale so as to emphasize the extrema of the curves. Note that within these patterns the azimuthal angle ϕ is not taken into account since a single case is only investigated ($\phi = \pi/3$). The relative refractive index values are determined as an array, so that $m_i = [1.04 \quad 1.1 \quad 1.01]$ relating to the three layers, whilst for the sizes of ϱ we have assumed that the core dominates the cell's volume, implying that the cytoplasm is the largest structure within the bacterium. As a result $\varrho_i = [0.8s \quad 0.15s \quad 0.05s]$ where $s = 1.1\mu\text{m}$. As a result the smallest internal structure is the outer shell, implying that the cell wall is of thickness $\varrho_3 = 0.055\mu\text{m}$.

At the topmost plot of Figure 4.6, we have that the polar plot (right) presents a symmetrical pattern. This is what one would expect to find since the axis of symmetry of the particle can be said to be directly illuminated by the incident radiation, which verifies the prediction in Remark 3.1 in conjunction with Definition 3.8 of Chapter 3. This is the reason why the two patterns of the Intensity plot on the left coincide. The remaining two plot explore the asymmetrical case, that is to say when the incidence is not directed to the spheroid's axis of symmetry. It should be evident that the resulting pattern is not symmetric, hence the intensity pattern does not coincide and the polar plots present a significant difference in the number of extrema as well as their amplitude. Note however that at the plot for $\alpha = 2\pi - \pi/4$, we have a reduction on the number of extrema, which leads to the assumption that as the particle rotates around its axis of symmetry then, even though the intensity's amplitude remains on average the same, the oscillations of scattered light tend to become less frequent.

Finally, one should observe the lack of mirror symmetry between the second and third polar plots of Figure 4.6. This feature arises due to the ϕ value ($\phi = \pi/3$) which causes the orientation of the particle to be different. As a result, the surface that the incident

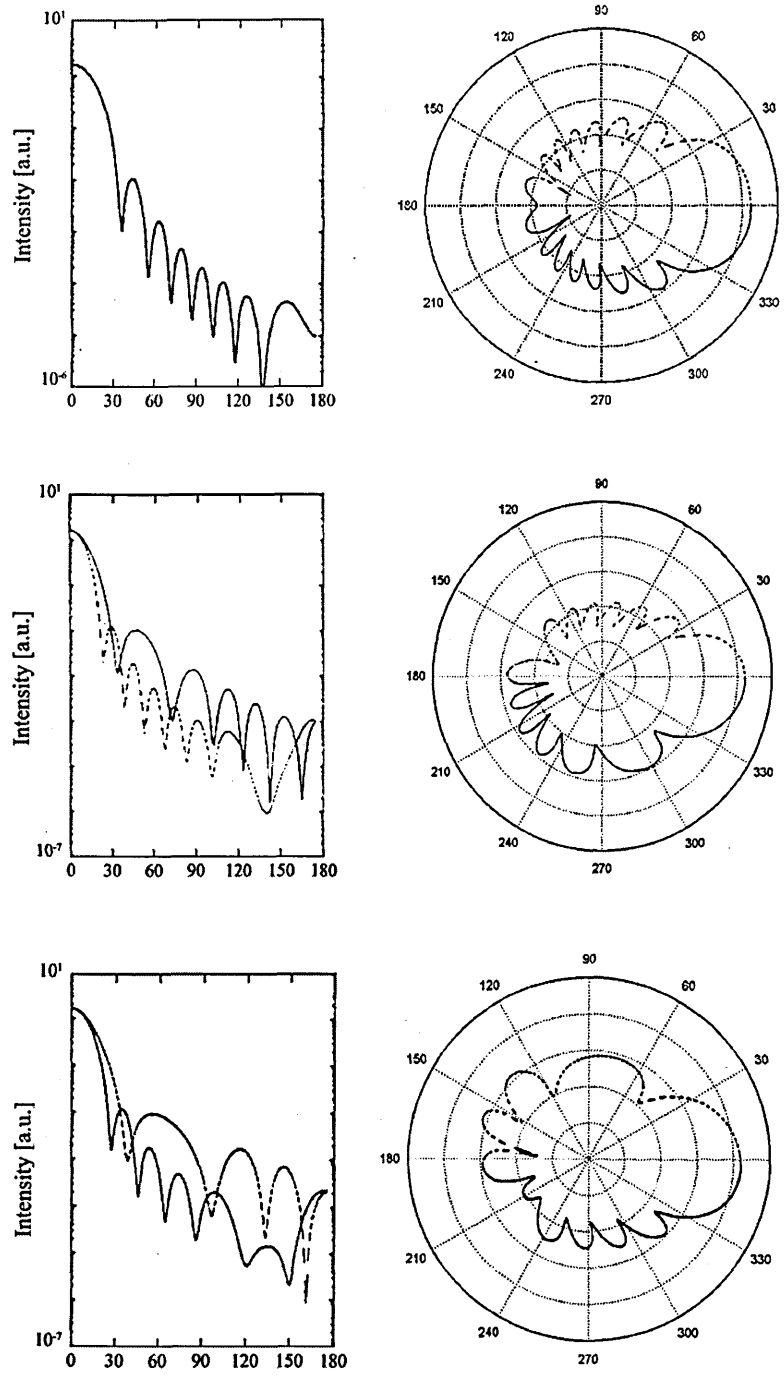


Figure 4.6: Scattered intensity from an ellipsoid with different source radiation at incidences of $\alpha = [0, \pi/4, 7\pi/4]$ resulting in the plots indicated from top to bottom respectively, with the equivalent polar plots on the right. For the cell it is assumed a 3-layered structure with relative refractive index array of values $m_i = [1.04 \ 1.1 \ 1.01]$ and array of values for the distances from the centre of the cell $\rho_i = [0.88 \ 1.045 \ 1.1]$.

radiation illuminates differs between the two cases and so will the two polar plots. It is also related to the polarisability of the cell as incorporated in our generalisation but it is of greater importance in terms of the intensity's amplitude.

This example, illustrates the effect of rotation, and how it would affect inference in terms of size. That is to say, many have linked the number of maxima presented in a scattering curve to that of the size that a particle may have. It should be evident through the observations that we have mentioned, how such a treatment of light scattering patterns may lead to erroneous results.

Remark 4.1. Particles that do not present any form of spherical symmetry, will present on one hand a non-symmetrical polar light scattering pattern which depends primarily on the orientation and shape of the particle whilst on the other hand, the number of oscillations evident in scattered intensity will reduce as the particle rotates around the incident radiation source.

It should be evident that an average over a number of orientations must be included in order to have a more precise prediction on the optical properties of the cell. This however brings another problem that the experimenter will face: that is, whether the number of detectors placed on the scattering planes is sufficient, as well as whether this would be solved by simply adding detectors along several planes of angle ϕ . On this note we devise a new experiment whereby we model prolate spheroids, where the axial ratio is greater than unity, i.e. $t > 1$ and the particle is not spherical. Note that as t increases so will the elongation of the particle. We identify three distinct cases; namely the prolate spheroid which we call type I, where the axial ratio is such that $t = 1.4$, a prolate spheroid type II, where $t = 2.8$ and finally a prolate spheroid of type III, where $t = 14$. We have computed the far-field angular scattering patterns for $\theta \in (0, 2\pi)$ and $\phi \in (0, \pi)$ employing our generalised approximation of Equations 4.24 - 4.26 as depicted in Figure 4.3. The incident radiation is assumed to be at $\alpha = \pi/2$ and the results shown are for parallel polarisation so that the log intensity results will be mapped on the $Z - axis$ and along the $X - Y$ plane as shown in the collection of three dimensional plots of Figure 4.7.

Common to all plots is the irregular pattern behaviour as we move further away from the near forward direction which is placed in this 'laboratory coordinate system' at $X = Y \rightarrow 0$. There appears to be a circular wave structure for the 3D scattered intensity pattern. As expected, the prolate spheroid Type I, exhibits a scattered behaviour close to symmetry due to its small axial ratio value, hence 'mimicking' the behaviour that an

equivalent sphere would have on the said incident radiation. Local extrema are obtained depending on the shape that the incident beam of radiation faces, and it is evident that the dependence on scattering angle θ is dominant on the near-forward and forward scattering on the planar grid. However at the backscattering angles there is a profound dependence on both polar angles (θ, ϕ) , as a result of the curvature that the incident beam faces.

As we have seen earlier increased θ values mean that the bisectrix is moving further away from the scattering plane. The latter refers to taking into account that angular points are used along the plane of θ , and the detectors are placed around this planar grid only, which will result in their viewpoint 'missing' incoming scattered light. Since we have now inserted the azimuthal angle ϕ then the curvature facing the detector points will be enhanced, hence becoming more sensitive to the shape and curvature of the said bacterial cells. Furthermore the peak present at the near forward angles, seems to be slightly broader for the least elongated particles than the ones with increased elongation. It is also clear that the backscattering observed, is more pronounced as the elongation of the cell increases, which again returns to the realisation that there is a strong dependence on the curvature being illuminated by incident radiation.

A strong ϕ dependency is therefore clearly apparent, hence proving, at least theoretically, that there is a need for light scattering instruments that are able to acquire scattered light in both polar angles ². Finally, another significant find is that in the three types of spheroids under examination, the minima of the scattering patterns become deeper with more pronounced elongations similar in a sense to the find as noted for backscattering. The abrupt ripples that can be seen underneath the planar grid have been ignored, since they are expected to be of no experimental importance since averaging over orientations, size distribution, number of layers employed and so on, is expected to diminish such features in the scattering pattern.

4.4 Evaluation of the ellipsoidal approximation model

So far we have seen how our generalised Rayleigh-Debye approximation can be extended for use with particles that exhibit no spherical symmetry, and have explored the effect of orientation and shape under the paradigm of elongated spheroids of a 3-layered internal structure. We have also seen that abrupt artefacts caused by the deep extrema of the scattering patterns, are apparent in any Rayleigh theory variant, as in the case of our generalised spherical and ellipsoidal approximation. However, the use of these models

²This is the basis for our patent submission outlined in Annex E.

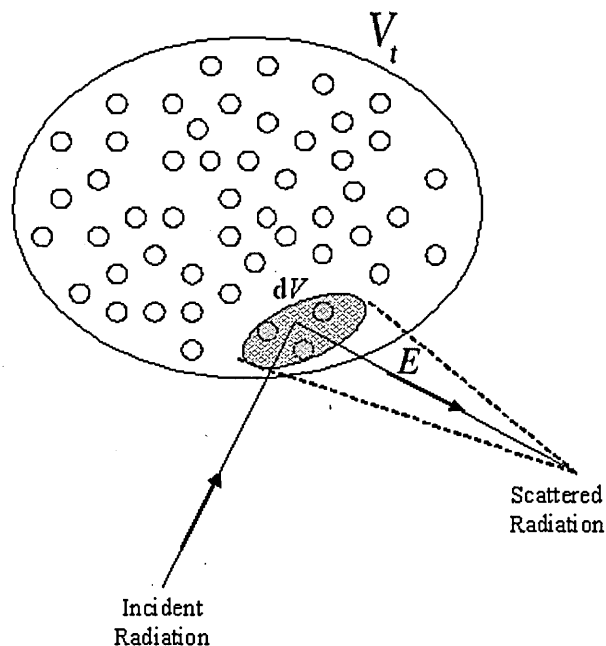


Figure 4.8: An ensemble of N_o particles within a volume ΔV that is within the 'cone of reception' of detector. The detector in this depiction is assumed within the solid angle formed by its cone of reception as cast in the total volume V_t .

for possible identification due to the numerous features they offer should be evident. In particular, the effect of shape and curvature on backscattering angles was also investigated and reported via simulation on single particles. We have left unanswered two fundamental problems:

1. *Populations of bacterial cells in suspension.* In any experimental setup requirement, it is, in general, more desirable to be able to identify distinct features from a suspension of cells in the water medium; hence within a cuvette of some volume, usually a few ml at a time.
2. The effect that the number of layers employed for modelling a particle, would have in an ensemble that would answer the modelling problem posed above.

Consider the ensemble of particles as per Figure 4.8. Let N_o particles in a volume ΔV in such a way, so that we would label the particles as $1, 2, \dots, N_o$. Let \mathbf{E}_j be the scattered field from the particle j . Due to linearity of Maxwell equations we can write

$$\mathbf{E} = \sum_{j=1}^{N_o} \mathbf{E}_j \quad (4.29)$$

The scattered intensity will be

$$|\mathbf{E}|^2 = \sum_{j=1}^{N_o} \mathbf{E}_j \sum_{l=1}^{N_o} \mathbf{E}_l^* \quad (4.30)$$

This double summation should be separated into two terms, since we have two cases, that is $l = j$ and $l \neq j$. As a result,

$$|\mathbf{E}|^2 = \sum_{j=1}^{N_o} |\mathbf{E}_j|^2 + \sum_{j=1}^{N_o} \sum_{l=1}^{N_o} \mathbf{E}_j \mathbf{E}_l^* \quad (4.31)$$

where in the second term, that is the double sum of $(\mathbf{E}_j \mathbf{E}_l^*)$ it should be clear that $l \neq j$.

Denoting the ensemble average by angular brackets, that is to say, by taking the ensemble average over $|\mathbf{E}|^2$ to be $\langle |\mathbf{E}|^2 \rangle$, it follows that

$$\langle |\mathbf{E}|^2 \rangle = \sum_{j=1}^{N_o} \langle |\mathbf{E}_j|^2 \rangle + \sum_{j=1}^{N_o} \sum_{l=1}^{N_o} \langle \mathbf{E}_j \mathbf{E}_l^* \rangle \quad (4.32)$$

The term $\mathbf{E}_j \mathbf{E}_l^*$ deserves extra consideration in terms of the phase lag δ between particles. As we have noted earlier, for the scattered fields of the j -th and l -th particles we would have $\mathbf{E}_j = |\mathbf{E}_j| \exp(j\delta_j)$ and $\mathbf{E}_l = |\mathbf{E}_l| \exp(j\delta_l)$ respectively. Therefore,

$$\langle \mathbf{E}_j \mathbf{E}_l^* \rangle = \langle |\mathbf{E}_j| |\mathbf{E}_l| \exp(j(\delta_j - \delta_l)) \rangle \quad (4.33)$$

As a result, one would come to the conclusion that the lag between the j -th and l -th particles depends in effect on the difference between the paths that their scattered fields will take and consequently on the separation that exists between them. In other words the Euclidean distance d_{jl} that separates the particles. Therefore if we let $\delta_j - \delta_l = \mathcal{O}(kd_{jl})$ then the 'randomness' of this distance is now of interest in the evaluation of Equation 4.33. Allowing for d_{jl} to be considered as a random variable and following a commonly used criterion [101], so that its standard deviation σ is such that $\sigma(d_{jl}) > \lambda^2$, then \mathcal{O} is randomly distributed with a phase lying within $(0, 2\pi)$ radians; hence $\langle \mathbf{E}_j \mathbf{E}_l^* \rangle \rightarrow 0$. Equation 4.32 can now be simplified and it follows that

$$\langle |\mathbf{E}|^2 \rangle = \sum_{j=1}^{N_o} \langle |\mathbf{E}_j|^2 \rangle \quad (4.34)$$

This finding implies that if the separation between particles is large enough then for computing the intensity of the ensemble we only need to consider the sum of scattered fields per particle within the volume of interest. We are using the phrase *volume of interest* since a detector has a 'cone of reception' which is cast over the total volume V . As such,

each detector receives light scattered within this cone of volume V_o , depending on its position in space.

Furthermore, the physical meaning of Equation 4.34 can also be seen in the experimental works of Wyatt in [3], Schimizu in [17] and others [84, 116]. That is to say, given bacteria that appear alone, where there is no binding of cells together (i.e. at low concentrations, that is, when the total volume of the bacterial cells with N_o being their total number does not exceed a total of $N_o < 10^6$ cells per ml of water³ based solution) then the independent scattering assumption is satisfied.

Remark 4.2. When the independent scattering criteria hold true, that is, either the mathematical condition $\mathcal{O}(kd_{jl})$ is randomly distributed and d_{jl} is sufficiently large or the experimental limit of $N_o < 10^6$ cells per ml of water based solution is satisfied, then for computing the total intensity from a number of cells we need only take the average sum of scattered fields per cell within the volume captured by the detector's cone of reception.

Remark 4.2 implies that multiple scattering effects are negligible, and that the scattered field is the sum of the scattered fields from N_o particles. The latter also means that no correlation between the fields scattered from each particle is allowed to take place. As a result the angular brackets within the sums disappear. As a direct consequence we have that the total scattering amplitude element $|S(\theta, \phi)|$ can be calculated by adding the scattered waves from all particles in the detectors' captured volume. As such,

$$|S(\theta, \phi)| = \sum_{j=1}^{N_o} \langle |S_j(\theta, \phi)|^2 \rangle = N_o \langle |S(\theta, \phi)|^2 \rangle \quad (4.35)$$

and if the particles within the ensemble follow a size distribution $\text{Pr}(s)$ then,

$$N_o \langle |S(\theta, \phi)|^2 \rangle = \int_0^\infty |S_j(\theta, \phi)|^2 \text{Pr}(s) ds \quad (4.36)$$

The latter follows by the definition of the size distribution. That is to say, for particles that obey the size distribution $\text{Pr}(s)$ so that the number of particles per unit volume with size between s and $s + \Delta s$ is $\text{Pr}(s)ds$, it follows that

$$N_o = \int_0^\infty \text{Pr}(s) ds \quad (4.37)$$

From Equation 4.36

³This is an experimentally set criteria for example in [16] and is often taken to be loosely defined unlike the distance between cells criterion $\sigma(d_{jl}) > \lambda^2$

$$\langle |S(\theta, \phi)|^2 \rangle = \frac{\int_0^\infty |S_j(\theta, \phi)|^2 \Pr(s) ds}{N_o} \quad (4.38)$$

and by substitution from Equation 4.37,

$$\langle |S(\theta, \phi)|^2 \rangle = \frac{\int_0^\infty |S_j(\theta, \phi)|^2 \Pr(s) ds}{\int_0^\infty \Pr(s) ds} \quad (4.39)$$

In the context of a size distribution, Equation 4.39 can be considered as a summation of both the numerator and denominator, if and only if sufficiently large samples are to be collected from $\Pr(s)$. For example, the statistical Gaussian distribution commonly known as the normal density function $\Pr(s) = \exp(-\frac{s^2}{2})$ can be sufficiently approximated as long as the number of samples collected are no less than 30, a direct consequence of the Central Limit Theorem [117, p231, p238]. That is to say assuming that now N_o depicts the size ranges with midpoints s_1, s_2, \dots, s_{N_o} then the condition $N_o \geq 30$ must be satisfied for reduction of the integral to a summation over ranges of sampled size midpoints. In any case, and where N_o is large enough,

$$\langle |S(\theta, \phi)|^2 \rangle \approx \frac{\sum_{k=1}^{N_o} |S(s_k)|^2 \Pr(s_k)}{\sum_{k=1}^{N_o} \Pr(s_k)} \quad (4.40)$$

However the normal distribution and the gamma distribution, commonly used to model bacteria populations in their natural environments, have unrealistically long tails. That is to say, the array of values for $\Pr(s)$ would not reach zero as $s \rightarrow 0$, even though bacteria sizes do not exceed a specific range. Moreover from a variety of sources of variability that result in the way that bacteria sizes are distributed, only a few are dominant. Even so, a parameter for the effect of population skewness on the left (negative skewness) or right (positive skewness) of a size distribution with mode s_o should be included. Wyatt has inferred such a distribution in [16] such that

$$\Pr(s) = \begin{cases} (1 - z^2)^4 & \text{for } z \in [-1, 1] \\ 0 & \text{for } z \notin [-1, 1] \end{cases} \quad (4.41)$$

where $z = 1.084(s - s_o)/\kappa s_o$, and κ is equivalent to a variability measure.

In order to incorporate the skewness effects, we have allowed for κ in the parameter z of Equation 4.41 to be assigned independently on the left and right of mode s_o . Hence we now re-write the expression for z to be,

$$z = \begin{cases} 1.084(s - s_o)/(\kappa_{\text{left}} s_o) & \text{for } s \leq s_o \\ 1.084(s - s_o)/(\kappa_{\text{right}} s_o) & \text{for } s > s_o \end{cases} \quad (4.42)$$

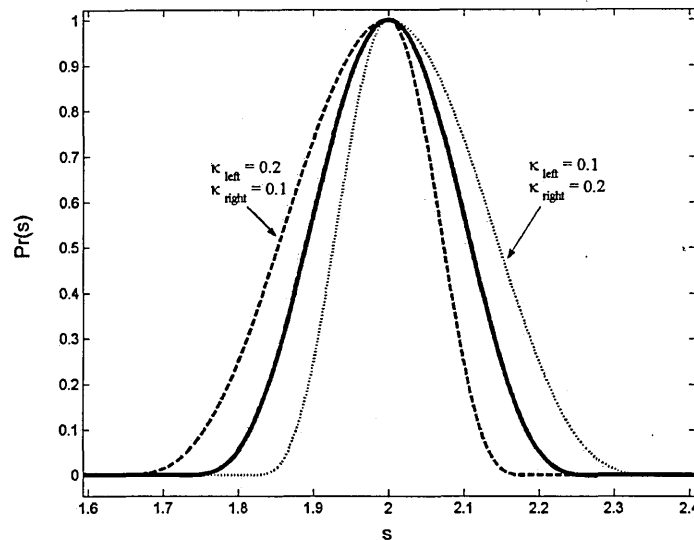


Figure 4.9: Size distributions with $\kappa_{\text{left}} + \kappa_{\text{right}} = 0.30$. The solid line curve depicts the symmetrical size distribution, $\kappa_{\text{left}} = \kappa_{\text{right}}$. The dashed line curve depicts an asymmetric size distribution with negative skewness, $\kappa_{\text{left}} = 0.2$, $\kappa_{\text{right}} = 0.1$. The dotted line curve depicts an asymmetric size distribution with positive skewness, $\kappa_{\text{left}} = 0.1$, $\kappa_{\text{right}} = 0.2$.

The spread of the distribution is dictated by the constant κ which is assigned independently at the left and right of the mode s_0 , resulting in an asymmetric distribution that avoids long tails as shown in Figure 4.9 depicted by dashed and dotted lines. It should be evident that for $\kappa_{\text{left}} = \kappa_{\text{right}}$ the distribution is symmetric (Figure 4.9, solid line) and s_0 becomes the mean, whilst κ is approximately equal to $3\hat{\sigma}/s_0$ with $\hat{\sigma}$ being the variability measure (standard deviation) of the symmetric distribution. It is known that in any unsynchronised culture and in nature we expect a variation in size of at least 30%. This effectively means that $\kappa_{\text{left}} + \kappa_{\text{right}} \geq 0.30$. In Figure 4.9 we have provided an example whereas $\kappa_{\text{left}} + \kappa_{\text{right}} = 0.30$. The distribution as provided here can be applied not only to singlet cells but also to any other configuration of bacteria.

In order to investigate the effect of the number of layers in ensembles of particles as modelled in this section we have implemented, in Matlab, computer simulations for estimation of the light scattered intensity from the asymmetric bacteria populations of Figure 4.9. As noted in Chapter 2, bacterial cells present a structure that consists mainly of the cell wall, cytoplasmic membrane, cytoplasm and nucleoid. Other morphological characteristics may also appear such as a slime layer (capsule) external to the cell wall or spore inclusions in the cytoplasmic area. As such, the use of an n -layered model as

defined here is justified since a more accurate representation of the cell can be achieved when each morphological characteristic is modelled as a separate layer. In the present study it is assumed that $n_{\max} = 6$. Following the findings of many studies (Table 2.2, Chapter 2) for the relative refractive index values that have been found to be true for waterborne biological cells and in line with our findings in Section 3.5 we randomly select an array of values to be deployed within the range $1 < m < 1.3$. Furthermore we randomly assign a number of orientations per cell for which the scattering amplitude would be calculated, and subsequently averaged over these orientations.

The size values are sampled as noted from the size distributions we have shown and for asymmetry such that $\kappa_{left} = 10\%$ and $\kappa_{right} = 20\%$. For every s values sampled we deploy a scheme to assign the array of values for size per layer and for the specific bacterial cell. Since the cytoplasm dominates the internal part of the cell it is assumed that it will always have a size value $\rho_1 = 0.8s$. The remaining layers will have a value $\rho_{i+1} = fs + \rho_i$ so that f is a uniform random number where $f < 0.2$ and relates to the proportion of s allocated for the specific layer thickness, whilst for the outermost layer's compartment it follows that $\rho_n = \rho = s$. To assess the applicability of our models we have concentrated on the examination of the pattern resulting from the ratio of the population averaged scattering matrix elements, $-\langle S_{33} \rangle / \langle S_{11} \rangle$. This ratio has been shown to emphasize the effect of backscattering [56][118] and it is the reason we have adopted it, as well as due to our findings on backscattering as per our discussion in the previous section.

First we investigate the effect of altering the axial ratio (t in Equation 4.28) on the scattering amplitude ratio; that is to say for $t < 1$, $t = 1$ which corresponds to spherical morphology, and $t > 1$. In Figure 4.10, top, results for a three layer model are presented. Note that for the plot of $t > 1$ (dotted line) there are two prominent peaks at angles $\sim 90^\circ$ and 130° ; whilst for $t < 1$ (dashed line) there is a prominent peak at $\sim 142^\circ$. The peaks of $t > 1$ at $90^\circ, 130^\circ$ are unique, as no other pattern presents such a significant local maxima in magnitude. Consulting the results of additional layers in the model, that is for four layers in Figure 4.10, middle, and six layers at the bottom, we verify that there is a consistent appearance of large peaks for each of the patterns for different t values. For example, for $n=6$ the peaks for $t > 1$ appear at $\sim 90^\circ$ and 133° , whilst a magnitude peak for $t < 1$ appears at $\sim 136^\circ$. These results indicate that there will always be a significant difference in the patterns of $-\langle S_{33} \rangle / \langle S_{11} \rangle$ allowing for the morphological characterisation or 'high-level' identification of bacteria in water samples by simply monitoring this ratio. To take this into perspective, cocci present a near-spherical structure whilst coliforms present an

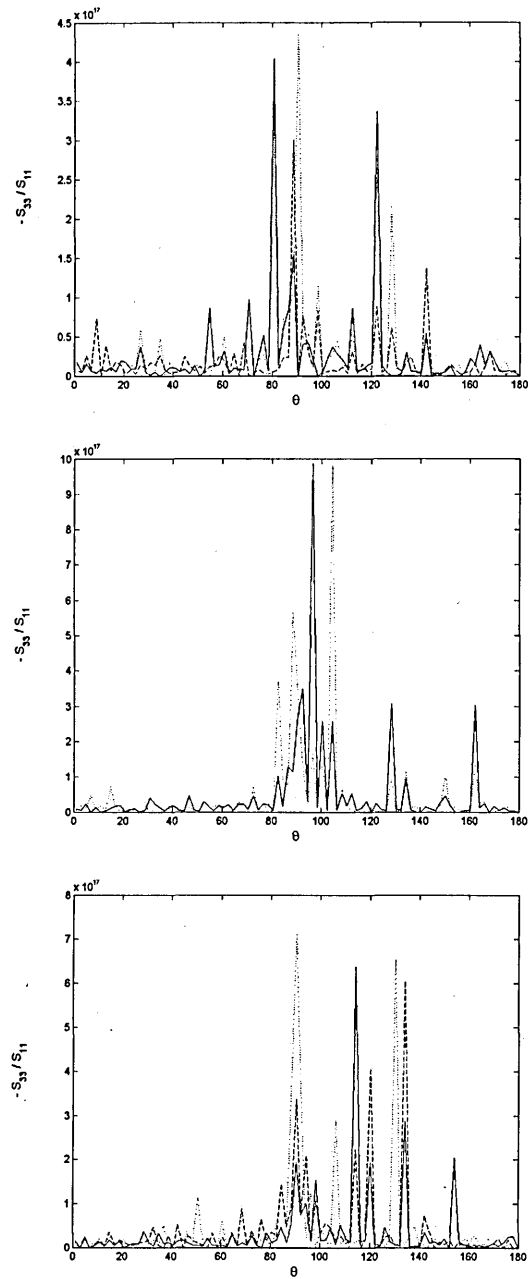


Figure 4.10: The angular dependence of the scattering ratio for an n -layer ellipsoid. Top: $n=3$, a three layer ellipsoid model with different axial ratios (dashed line: $t < 1$, solid line: $t = 1$, dotted line: $t > 1$). Middle: $n=4$, a four layer ellipsoid model with different axial ratios. Bottom: $n=6$, a six layer ellipsoid model with different axial ratios.

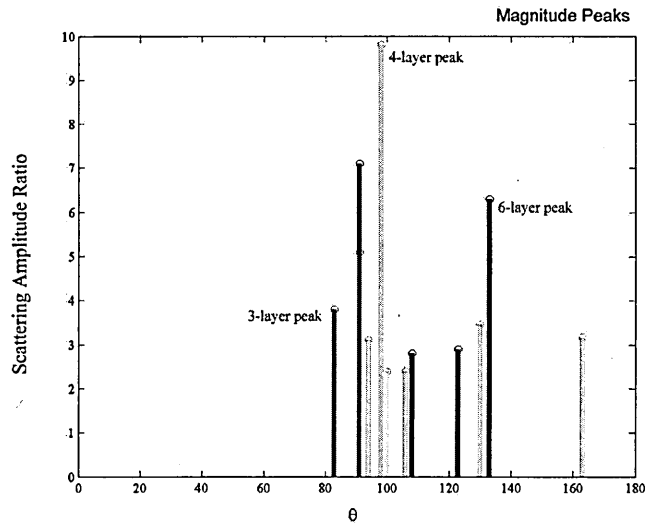


Figure 4.11: Isolating prominent peaks from the simulation results of Figure 4.10. The cutoff point for selection of a peak is set at 2 arbitrary units. The three layered particles' ensemble peaks are denoted by 50% grey-scale, the four layered ensemble by 25% grey-scale and finally the six layered ensemble by 75% greyscale.

elongated spheroidal structure and Bacilli present structures of axis of symmetry. Evidently, this level of differentiation is feasible as shown within our simulation.

This statement is further supported by examining particular peaks of Figure 4.10. Inasmuch, we have isolated specific peaks that are dominant for each ensemble of n -layered particles in the sense that for a cutoff limit set per particular ensemble of internally structured particles, only the peaks that contribute above this cutoff point are selected. The result is indicated in the stem plot of Figure 4.11. When we have a three layer model (denoted by 50% grey-scale) prominent peaks appear at $\sim 82^\circ$ and 90° . By adding one layer to the model, that is for populations of four layer ellipsoid cells ($n = 4$), the magnitude peaks now appear at $\sim 98^\circ$, 130° , 162° . For populations of six layer ellipsoid cells ($n=6$) a further angular shift on the magnitude peak results in a maxima at $\sim 133^\circ$. Similar arguments can be made for particular maxima of the remaining patterns. As a result we can now generalise the statement made above not only to the axial ratio but also to the number of layers that suffice to describe a bacterial cell.

Remark 4.3. Our results indicate that by monitoring the ratio $-\langle S_{33} \rangle / |\langle S_{11} \rangle|$ and for a particular local maxima (peak), a significant difference appears, in these patterns, which allows for identification of geometrical morphology (spheres or ellipsoids) and also their

internal structure (number of layers).

Adding to our earlier discussion concerning the shape of bacteria and possible identification, we can propose that certain species may employ a particular number of layers, even though it has the same volume, axial ratio and shape. In that sense it may be true that further identification may be rendered possible. As a matter of fact inference of relative refractive indices is possible via our generalised Rayleigh-Debye ellipsoidal approximation, hence an extra feature is provided that may be useful for identification purposes and would be used, as outlined.

4.5 Theoretical considerations and problems

Here we report a problem that may be of interest when trying to further extend the generalised approximation to spheroids of the n -th dimension. This problem, whose solution we have outlined in this Chapter, and for n -layers, has yet to be addressed. However, our method would be applied, hence the theoretical value of our procedure is further illustrated. Unfortunately, there may be cases such as the one that follows where analytic expressions are not feasible and computational problems may arise.

Let a super spheroid described by the equation

$$\left(\frac{|x|}{a}\right)^n + \left(\frac{|y|}{b}\right)^n = 1 \quad (4.43)$$

If $n \rightarrow \infty$ then the ends of this subset of super ellipses will flatten out and will closely resemble bacteria from say the Bacillus family. Taking the axis of symmetry to be on the x -axis, we can characterise the shape by this volume of revolution around the x -axis. Cross-sections as taken previously, that is infinitesimal slices perpendicular to this line, will form a circular area. In particular, planes normal to the x axis would be described by the simple equation $x = h$ where h is constant and the slices will be described by

$$y^n + z^n = \left(1 - \left(\frac{x}{a}\right)^n\right)b^n \quad (4.44)$$

and it follows from Equation 4.44

$$z = \pm b\left(1 - (x/a)^n - (y/b)^n\right)^{n/2} \quad (4.45)$$

Elements of the slices as per Equation 4.45 contribute two phase differences. One needs to integrate over a plane that the independent variable is considered to be y with

$y \sin \beta$ being the projection parallel to the bisectrix of an element that has a distance y from the centre of the elliptical section. Hence the first contribution will be

$$\delta_y = 2km(y) \sin(\theta/2)(y \sin \beta) \quad (4.46)$$

The second contribution is from the position of the slice with respect to its projected distance from the origin of the bisectrix, hence $x \cos \beta$. It follows that

$$\delta_x = 2km(x) \sin(\theta/2)(x \cos \beta) \quad (4.47)$$

Hence we can now solve by integrating over the total volume of the multi-layered particle, so that for the i -th layer,

$$\int_{b_i(1-(x/a)^n)^{1/2}}^{-b_i(1-(x/a)^n)^{n/2}} \exp(j\delta_{x,i}) h(1 - (x/a)^n - (y/a)^n)^{n/2} dy \int_{-a}^a \exp(j\delta_{y,i}) dx \quad (4.48)$$

Solving in a manner as per Section 4.2 and by letting $\varepsilon_i = y/b_i$, results in

$$\int_0^1 J_1(u_{x,i}(1 - \varepsilon_i^n)^{1/2}) \cos u_{y,i} \varepsilon_i d\varepsilon \quad (4.49)$$

where $u_{x,i} = 2km_i b_i \sin(\theta/2) \sin \beta$ and $u_{y,i} = 2km_i a_i \sin(\theta/2) \cos \beta$. Unfortunately, the solution of Equation 4.49 is not analytic. Hence a compact expression as provided so far, that may lead to real-time characterisation cannot be given. However, the reader interested in this line of research would in fact deploy a suitable numerical evaluation procedure as long as one takes into consideration that

1. As $u_{x,i} \rightarrow 0$ then $J_1 \rightarrow 0$.
2. or $u_{y,i} \rightarrow \infty$ then $\cos u_{y,i} \rightarrow 0$.

hence normal quadrature techniques will probably fail [119] especially in the above two limiting cases.

4.6 Conclusions

In this chapter we have derived a new model for the ellipsoid and the subcase of spheroids as an n -layered structure. We have found that both the azimuthal and the polar angle (θ, ϕ) in an assumed laboratory Cartesian axis system is important; and in particular the backscattering effects. We have also provided a modelling procedure for population of bacterial cells. Three major contribution are identified:

1. A new method for determining the scattering amplitude or the form factor from particles of no apparent geometrical symmetry and for multi-layered internal structures.
2. A new method for spheroids of multi-layered internal structure, in conjunction with a physical justification for polar asymmetry in the scattering pattern.
3. A new procedure for treating populations of cells that exhibit skewed frequencies on their linear dimension, as long as the condition of independent scattering is satisfied.

Contribution 1 refers to our implementation of the method of slices as a new treatment on the case of multiple internal layers and for ellipsoidal geometry. Taking into consideration the example given in Section 4.5 it can be seen that it has an application to a number of problems of that kind, even if an analytic expression cannot be obtained and one needs to resolve a numerical approximation for the indefinite integral.

Contribution 2 is significant if one considers that, for example, coliforms have been so far modelled as homogeneous bodies. With our model a new line of research may be opened where the experimental data can now be used for inference of n relative refractive indices. A byproduct of our mathematical solution is the theoretical justification that differential scattering patterns are heavily dependent upon orientation and the surface that the incident beam will illuminate. This finding illustrates that since in the three dimensional sense better results may be obtained, then a justification for use of such instruments is provided. Finally it should be clear that back-scattering will play an important role in the characterisation of such particles, even in the case where some axis of symmetry is apparent.

Contribution 3 relates to the problem of populations of cells. The modification that we have applied on the size distribution of Wyatt, incorporates the effect of having several process fluctuations within the environment that the bacteria have been sampled from. Hence, this procedure provides the possibility of having samples directly examined before any calibration takes place, by simply selecting only 2 parameters and the expected size average/mode. In agreement with our findings from the second contribution, we have shown that the scattering amplitude elements ratio and its amplitude peaks at back scattering angles, may be sufficient for immediately being able to identify how many layers there may be within a said sample of bacteria. As such an extra feature towards partial identification has also been offered.

Chapter 5

On the violation of the independent scattering condition

In the previous chapter we have derived a mathematical model for ellipsoidal geometries of an n -layered internal structure. As a result the bacterial cell is considered as an n -layered structure with no apparent axis of symmetry. We have also provided a procedure for modelling populations of cells where the sizes follow a skewed distribution and the independent scattering condition $d_{j,l} > \lambda$ holds true. Here we wish to examine the problem where the bacterial cells are exceeding numbers of 10^6 per ml of solution and as a result $d_{j,l} < \lambda$, hence the assumption of independent scattering is violated. We examine the problem:

Definition 5.1. For bacterial cells of the same species, hence the same internal structure, that exhibit an ellipsoidal external morphology and are densely populating the water based medium, investigate the effect that violation of independent scattering will have on the scattering pattern in relation to the number of layers deployed.

We now use the model developed in Chapter 4 and we investigate suspensions that are not sufficiently diluted. We subsequently establish a limit on the number of layers that can be used by performing stochastic simulations of the behaviour of light that is scattered from particle to particle, i.e. multiple scattering. We numerically illustrate that the asymmetric polar scattering pattern is still evident due to particles' orientation and curvature facing the multiple scattered light. Furthermore we illustrate that backscattering still contributes significantly to the intensity profile despite its apparent washing-out of detailed features, which is due to increased populations, resulting in the increase of the probability of multiple scattering.

5.1 Introduction

When we have a particularly high volume fraction of scatterers, say an ensemble N_o in a participating medium, then correlation, between fields of say a j -th particle or scattering event and the l -th scattering event, will be evident. As a result the total scattering field will now be

$$\langle |\mathbf{E}|^2 \rangle = \sum_{j=1}^{N_o} \langle |\mathbf{E}_j|^2 \rangle + \sum_{j=1}^{N_o} \sum_{l=1}^{N_o} \langle \mathbf{E}_j \mathbf{E}_l^* \rangle \quad l \neq j \quad (5.1)$$

and the interaction $\langle \mathbf{E}_j \mathbf{E}_l^* \rangle$ can no longer be thought of as a vanishing term, since

$$\langle \mathbf{E}_j \mathbf{E}_l^* \rangle = \langle |\mathbf{E}_j| |\mathbf{E}_l| \mathcal{O}(k, d_{jl}) \rangle \quad (5.2)$$

where the phase interaction \mathcal{O} depends directly on the particle separation of the j -th and l -th scattering events, that is $d_{j,l}$. This is again considered to be a random variable but, in contrast to the mathematical modelling of Section 4.4 of Chapter 4 for populations of cells, it now assumes a standard deviation $\sigma(d_{j,l}) < \lambda^2$. Experimentally speaking, for concentrations where the number of cells per 1ml of water based medium, is greater than 10^6 , then this correlation of fields effect is most pronounced and *multiple scattering*, as is commonly known¹, would take place.

Unfortunately, only limited cases of the general multiple scattering problem have appeared, and there is no exact solution [115]. Therefore most rely on probabilistic simulations in order to examine its effect and so we adopt a stochastic procedure in subsequent sections.

5.2 A stochastic algorithm for multi-particle simulation

Taking into account the paradigm of radiative transfer, light can be considered as a packet of photons. When a photon is emitted, it travels some distance and eventually meets a particle where one of two outcomes is possible: the photon will be scattered or absorbed. That is, since the relative refractive index of a particle can have both real and imaginary parts, the relative refractive index would be $m = \Re(m) + j\Im(m)$, where $\Im(m)$ relates to the amount of absorption from the particle.

On stochastic simulations of radiative transfer the absorptivity of a material can be calculated directly from the surface fields [99]. From Ohm's law [87, p114] it is known

¹In some cases, and for dipole potentials, the term *retardation effects* is used, instead of multiple scattering.

that for most materials the steady state of the current density is proportional to its field, at a given temperature, and the steady state density can be calculated from the set of cross sections of such surfaces [97]. The power absorbed in each region of the surface fields is obtained by integration of dissipation in the region of the particle [99, p141, p353]:

$$P_a = \frac{1}{2}\omega \int_{V_o} \Im(m(r))|\mathbf{E}(r)|^2 dr \quad (5.3)$$

where $\mathbf{E}(r)$ is the field within the particle and $dr \equiv (dx, dy, dz)$, hence the integration is to be performed over the three dimensional volume of the particle. The absorption cross section is defined by

$$\sigma_a = \frac{P_a}{|S_j|} \quad (5.4)$$

where $|S_j|$ is the power flow magnitude of the j -th particle and the *albedo* ω , that is a measure of fraction of scattering cross section over the total cross section ($\sigma_a + \sigma_s$) with σ_s being the scattering cross section, will be

$$\omega = \frac{\sigma_a}{\sigma_s + \sigma_a} \quad (5.5)$$

from where it is evident that $\omega \in [0, 1]$.

Since bacteria are assumed to absorb a minute amount of the energy of incident radiation, this is considered to be negligible ($\Im(m(r)) \rightarrow 0$), therefore, in Equation 5.5, only scattering is taken into consideration and from Equation 5.4, $\sigma_a \rightarrow 0$. This effectively means that the probability of a photon being scattered or absorbed by an ensemble of particles, commonly known as the *stationary albedo* [120], becomes

$$\tilde{\omega} = \frac{n_s \tilde{\sigma}_s}{n_s \tilde{\sigma}_s + n_a \tilde{\sigma}_a} = \frac{n_s \tilde{\sigma}_s}{n_s \tilde{\sigma}_s + 0} = 1 \quad (5.6)$$

meaning that all light will be scattered when it meets a particle in its path. This is true both of incident light (injected photons) and of light previously scattered from another particle. In Equation 5.6, (n_s, n_a) denotes the proportion of scattering and absorbing particles respectively with corresponding cross sections (σ_s, σ_a) .

Light propagating in the medium is assumed to be undergoing m successive scattering events $(1, 2, \dots, m)$ from N_o particles located at $\mathbf{d}_1, \mathbf{d}_2, \dots, \mathbf{d}_{N_o}$, generating scattered light with direction of vectors $\mathbf{k}_{s,1}, \mathbf{k}_{s,2}, \dots, \mathbf{k}_{s,m}$ respectively. For the increased populations we will be using later it can be said that the number of scattering events will be at least the number of the scattering particles in the densely packed medium. The absolute coordinates (X, Y, Z) of the Cartesian system are defined with respect to the entrance

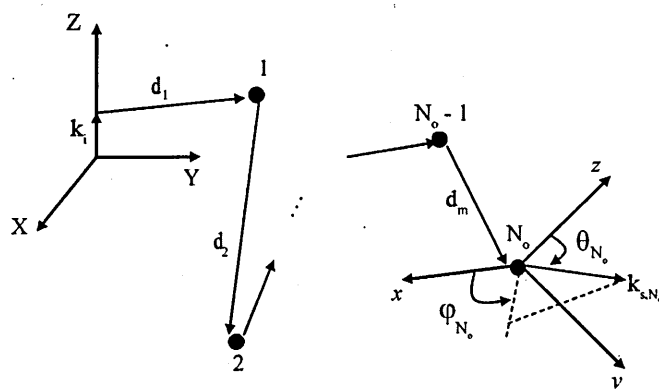


Figure 5.1: Absolute global coordinate system and Scattering local coordinate system. For i scattering events to take place with m being the last one. Note that incident radiation or photons with direction k_i , coincide with direction of the Z axis of the global coordinates system whilst the last scattering event follows the direction k_{N_o} at polar angles θ_{N_o}, ϕ_{N_o} of the local coordinate system.

point of the incident light wave with direction k_i , coinciding with the Z -axis of the global Cartesian system, as indicated in Figure 5.1. The scattering coordinate system is defined with respect to the origin at the m -th scattering point, which corresponds to the last scattering event, with Cartesian coordinate system (x_m, y_m, z_m) . After the series of scattering events has been terminated then the scattered light leaves the medium in direction k_s at a point $d_s(X_l, Y_l, Z_l)$.

The distance vector d between two successive scattering events will be negative exponentially distributed [121], under the assumption of a homogeneous suspension in a solvent (liquid medium; that is water in our case)². Consequently, the probability density function will be given by

$$\text{Pr}(d) = \frac{\exp(-d/\mathcal{L})}{\mathcal{L}} \quad (5.7)$$

where $|d| = d$ and, putting this into the context of the previous section and for the m -th scattering event, $d = d_{m-1,m}$. The parameter \mathcal{L} is defined as the mean free pathlength of the random medium. The random distance between two events or pair of particles, is given by means of the ‘transformation’

$$u = \int_{d_o}^{d_m} \text{Pr}(d) dd = \text{Pc}(d_o, d_m) \quad (5.8)$$

²in molecular modelling this is known as the *canonical ensemble*

where $u = U(0, 1)$ is a random number uniformly distributed in the range $[0, 1]$ and d_o is the lower limit of the range over which d is defined. Note that $Pc(d_o, d_m)$ is in effect the cumulative probability distribution.

Since the issue here is how far a photon will travel before being scattered, the probability that a photon travels an optical depth d without interaction is $\exp(-d)$. Probability of scattering prior to d is $Pc(d) = 1 - \exp(-d)$, therefore sampling from the cumulative probability according to $u = 1 - \exp(-d)$, gives

$$d = -\log(1 - u) \quad (5.9)$$

and as a result d_m can now be calculated from Equation 5.8.

However the latter is not an easy task particularly if one wishes to examine particles of no spherical symmetry, as is the case with ellipsoids. It has been noted that most of the computational time taken from this algorithmic process is due to this computation [122]. The complexity increases exponentially with the number of scattering events or number of particles to be simulated. We have adopted a treatment where the particle's surrounding volume is a sphere with the radius being that of the ellipsoid's largest linear dimension. Since we do not wish to examine the process of aggregation, we seek (d, d_m) such that each successive pair of ellipsoids does not collide or form any binding linear chain, fractal or otherwise structure. Hence they would be very close to one another (agglomerates) so that, depending on numbers of cells in the volume, $d_o < \lambda$ but do not form aggregates. The latter implies that the case where $d \rightarrow 0$ is not examined. As a result we wish to find a *Pair Distribution Function*, by which $Pr(d, d_m)$ is calculated so that by assuming a range $(0, Pr_{max})$ and a range $d \in (d_o, d_{max})$, then we take a sample from a uniform distribution for both ranges and use a rejection criteria: if $Pr(d) > Pc(L)$ then we reject the specific value of d and repeat the procedure [123].

In our implementation, we assume that the largest linear dimension is sampled from the size distribution of Chapter 4, Section 4.4 in Equations 4.41 and 4.42 for every iteration in which the size of the linear dimension of the ellipsoid is defined when calculating a value for d between pairs of scattering events. The total volume of the solvent, that is to say the cuvette's volume, is 1 ml, and the total volume of all the bounding spheres of the ellipsoids is denoted by $V_{total} < 1$. With reference to Figure 5.2, we see that for the j -th scattering particle

$$d_{j,j+1} = \sqrt{(x_{j+1} - x_j)^2 + (y_{j+1} - y_j)^2 + (z_{j+1} - z_j)^2} - (R_j + R_{j+1}) \quad (5.10)$$

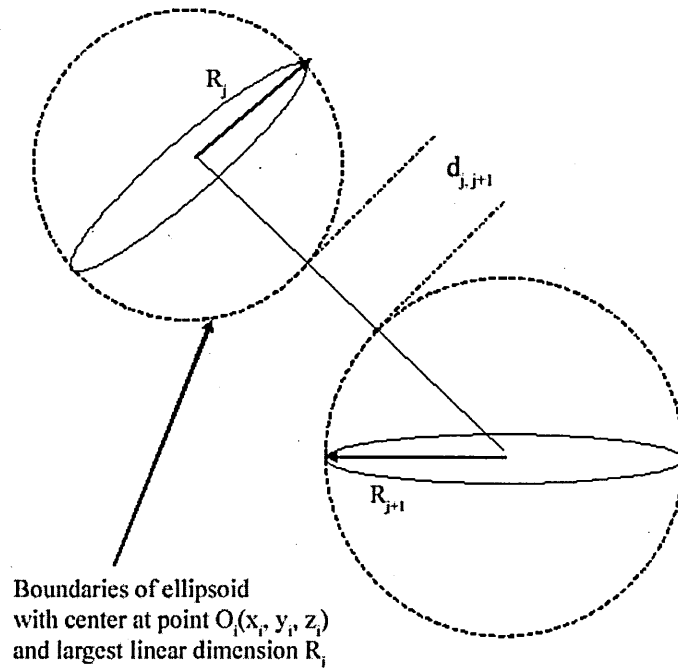


Figure 5.2: Calculating the separation $d_{j,j+1}$ between a successive pair of ellipsoids placed at points $O_j(X_j, Y_j, Z_j)$ and $O_{j+1}(X_{j+1}, Y_{j+1}, Z_{j+1})$, enclosed within spherical boundaries of corresponding radii R_j and R_{j+1} . The radii correspond to the largest linear dimension of the ellipsoids.

and the decision procedure [124] will follow the criterion:

$$\begin{cases} \text{if } \Pr(d_{j,j+1}) > Pc(\mathbf{L}), & \text{reject } d_{j,j+1} \text{ and either } R_j \text{ or } R_{j+1}; \\ \text{if } \Pr(d_{j,j+1}) < Pc(\mathbf{L}), & \text{accept and move to next event.} \end{cases}$$

If the separation between events is accepted then a random orientation for the $(j + 1)$ -th ellipsoidal particle is assigned with respect to the local coordinate system. The advantage of this method is that it applies for any unknown probability distribution if we know its peak value or where this maximum will occur. By selecting a maximum displacement (d_o/\mathbf{L}) between two successive events this problem can be solved. It should also be evident that the procedure we describe resembles the Monte Carlo method where the pairwise interactions between events are described [120] as a sum of occurrences of the complete set of positions and orientations (d_j, d_{j+1}) of the stochastic process $\Phi(d_j, d_{j+1})$. This process follows the conditions of a discrete Markov Chain's evolution, and as such if an exponentially decreasing distribution for d is found then the ensemble is a homogeneous one, since it is a limiting case of the transition matrix of the Markov Chain state evolution. Hence the stochastic process $\Phi(d_j, d_{j+1})$ evolves as a Monte Carlo Markov Chain process if it resembles a distribution such that from a maxima it eventually reaches a minima, that is to say, the steady state.

For example, for easing the visualisation of particles distributed in the three dimensional space of our volume, let $N_o = 40$ and a maximum displacement between each of these 40 particles be 0.25mm. By generating the points for the scattering events we have the result at the top of Figure 5.3. By determining the accepted distances d_i between successive pairs of spherical boundaries and selecting random orientation for the event $(i + 1)$ and for all ellipsoids thereafter, we can now generate the visualisation of their placement in the volume, as indicated at the bottom of Figure 5.3. However, if we need to examine light scattered from the ensemble we need to be able to select a number of new orientations for each photon packet. In our implementation we achieve this by forcing the algorithm to assume new orientation angles but for the same point clouds. Due to our treatment of ellipsoids covering a spherical volume of their largest linear dimension, collisions between them is avoided. Such a new random orientation is provided in Figure 5.3[bottom left], where we still deploy the 40 scattering events of the point cloud shown in Figure 5.3[bottom right]. Increasing the number of scattering events by 10, and using the same parameters, the point cloud will become denser and the pair occurrence condition of the separation between the ellipsoids will become much more difficult to accept as a successful separation candidate. The problem can be seen in the function of occurrences for the pair distribution ratio (d/\mathbf{L}) of Figure 5.4. This effect is even

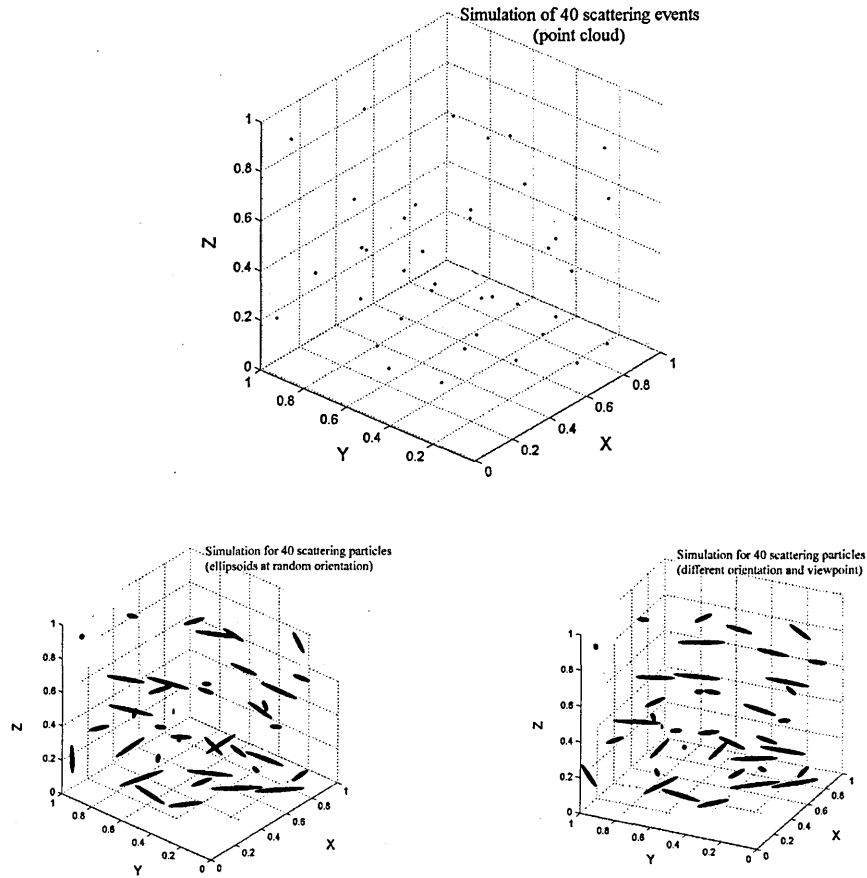


Figure 5.3: Assuming an ensemble of 40 scattering particles with maximum separation 0.25 mm. Note that we have assumed prolate spheroids where $c = s$ and $a = b = ts$, with the axial ratio t being a real number uniformly distributed in the range (0.1, 12). The sizes s for the spheroids in the illustrations at the bottom, have been overemphasized by a factor 10 so as to be visible. We illustrate for different orientation randomly selected, for the 40 scattering particles.

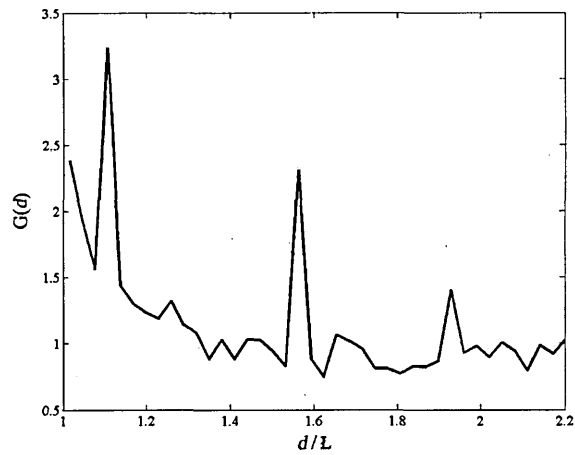
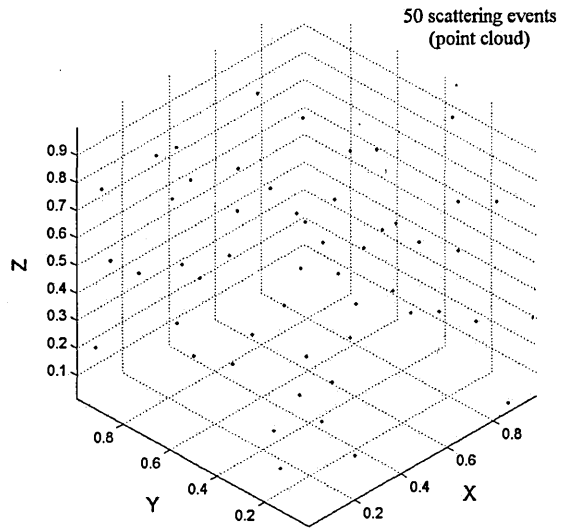


Figure 5.4: An ensemble of 50 scattering particles with maximum separation 0.25 mm. The point cloud is indicated at the top whilst the Pair Occurrence distribution function of d/L is provided at the bottom.

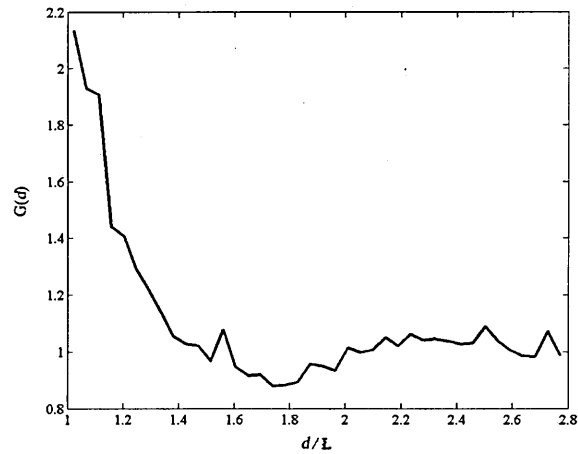


Figure 5.5: Pair Occurrence distribution function of d/L for an ensemble of 100 scattering particles. Note that in contrast to the function with 50 particles (Figure 5.4) it tends towards resembling an exponentially decreasing function.

more pronounced (Figure 5.5) where the number of scatterers in the ensemble doubles to $N_o = 100$, resembling the negative exponential function reported earlier.

Using the decision criteria for acceptance of pair separations, leads to a stochastic process with a function which is exponentially decreasing as N_o increases, for a ratio of d over the mean free pathlength L . This is compatible with a homogeneous distribution of particles, and hence illustrates the validity of this approach.

5.3 A procedure for calculating the intensity profile

As we have explained in the previous section, we consider three dimensional environments consisting of a light source and biological cells within a total volume. The basic form of the algorithm that we employed for the stochastic simulation of photon transfer is as follows.

Step I Decide on the total number of photons to be injected

Step II Decide on the wavelength and number of photons in a packet to be injected from the source, depending on the environment

Step III For each photon repeat steps 1 to 5:

1. Assign wavelength and update intensity, following the source specification

2. Choose initial position
3. Increment count of emission
4. Update intensity profile
5. Repeat steps (a) and (b) until the last scattering event
 - (a) find nearest surface along the photon path
 - (b) If a cell is found along the photon's path:
 - i. determine outgoing intensity
 - ii. assign scattering direction
6. Store outgoing photon's direction (polar angles)

Step IV Calculate normalised intensity.

For an ensemble of N_o particles within this total volume we assume that the transfer of radiation from the light source will be from below. That is to say, photon packets are injected from the origin such that the intensity at any direction of emission of the source is isotropic. For each photon the initial position (Step III.2) is the origin and the direction cosines of the photon are known to be

$$k_{i,x} = \sin \theta \cos \phi \quad k_{i,y} = \sin \theta \sin \phi \quad k_{i,z} = \cos \theta \quad (5.11)$$

and all subsequent photons will follow a direction where we will be considering the case where injection of photons is taking place only in an upward direction. The basic assumptions made in the simulation algorithm are:

1. **Source (emitter):** The laser light source is a 'generator' of photons, which are assigned an initial position on the emitter's surface. The emission strength is uniform over the emitter's surface: photons are generated uniformly over the surface.
2. **Environment:** The environment is assumed to be distilled water illuminated by a source in the visible spectrum (refractive index 1.336). The water environment does not interact with the photons emitted and subsequently scattered.
3. **Scattering events:** Photons will only be scattered and not absorbed when they contact a bacterial surface. The scattering surfaces are described by the three-dimensional mathematical relationship and its orientation with respect to a global coordinate system. The global coordinate system is defined to be that of the source.

4. **Scattering Objects:** These are the ellipsoidal surfaces which model the bacterial cells. The optical properties depend on the internal structure, that is to say, the number of layers employed.

However, it is a reasonable assumption that the particle's ellipsoidal shape affects the polarisation properties and scattered intensity. As we have seen in Chapter 4 for single particles, the intensity profile is affected by the curvature and orientation in particular. Furthermore the number of layers that the ensemble's particles will have may have a significant effect upon the scattering angle selection (Step III.5.b.ii). That is to say, since we are interested in the multiple scattering of non-aggregating species of bacteria, the phase function would in theory affect the way scattered light will be distributed as it passes through each scattering particle. Furthermore, we assume that the medium in the environment (water) does not interact with the photons and that the bacterial cells are described by their bounding surfaces (ellipsoids), and the associated optical properties.

The dependence of the optical properties on a bacterial ensemble that violates the rule $d_{i-1,i} < \lambda$ is investigated by studying the effect that these properties have on the scattering field. For each scattering event, within the densely but homogeneously distributed packed media, the Rayleigh-Debye phase function would be applied, and is provided in [101, pp 22-24].

$$F(\theta) = C(k_o)[V(m-1)]^2 |\bar{\mathbf{P}}| |S(\theta, \phi)|^2 \quad (5.12)$$

where V is the volume and m the relative refractive index of the scattering particle respectively. $C(k_o)$ is a constant depending on the propagation constant's (k_o) behaviour with wavelength λ and magnitude of polarisation $|\bar{\mathbf{P}}|$. The expression for the scattering amplitude S is the one that we have derived in Chapter 4 for ellipsoidal geometries with an arbitrary number of layers (Equations 4.24 to 4.26) and by using the treatment of Section 4.3 for spheroidal shapes of a randomly chosen axial ratio.

However, in Equation 5.12, it is once again assumed that the transparency of the particle $m \rightarrow 1$ holds true and that the particles producing the scattering amplitude are homogeneous. Following the treatment from previous Chapters, we have shown that for an n -layered particle the average weighted polarisability of the scattering cell has to be taken into account defined as

$$\hat{a} = \frac{1}{V_n} \sum_{i=1}^n \frac{m_i^2 - 1}{m_i^2 + 2} (V_i - V_{i-1}); \quad V_o = 0. \quad (5.13)$$

As such Equation 5.12 becomes

$$F(\theta, \phi) = C(k_o)\hat{a}^2|P||S(\theta, \phi)|^2 \quad (5.14)$$

This modification of the phase function makes it possible to examine scattering from n -layered bacterial cells, depending on the derived amplitude function used, for the previously examined geometrical shapes.

In our simulations (in particular Step III.5.b) the azimuth angle ϕ_i at the i -th scattering event is generated as a random number distributed uniformly in the interval $[0, 2\pi]$ such that $\phi_i = 2\pi U(0, 1)$, whilst the zenith angle θ_i at the i -th scattering event is generated as a random real number distributed in the interval $[0, \pi]$ but using the transformation defined as [125, p.22]

$$u = \frac{\int_0^{2\pi} d\phi \int_0^{\theta_i} F(\theta, \phi) \sin \theta d\theta}{\int_0^{2\pi} d\phi \int_0^{\theta_i} \sin \theta d\theta} \quad (5.15)$$

where u and ϕ are sampled as a random real number distributed uniformly so that $u = U(0, 1)$ and $\phi = 2\pi U(0, 1)$.

The polarisation vector \bar{P} is assumed to undertake a sequence of rotations, as a direct consequence of the scattering events. When the last scattered wave with polarisation \bar{P}_{m-1} is incident to the N_o -th particle, the polarisation \bar{P}_{N_o} radiated from the N_o -th particle will be given by

$$\bar{P}_{N_o} = -\bar{k}_{s,N_o} \times (\bar{k}_{s,N_o} \times \bar{P}_{N_o-1}) \quad (5.16)$$

where $\bar{k}_{s,m}$ is a vector notation of the direction cosine of $\mathbf{k}_{s,m}$ defined in the absolute (global) coordinate system. This can be given in a form of a rotation matrix [102], and as such Equation 5.16 will become

$$\bar{P}_{N_o} = \begin{bmatrix} 1 - \bar{k}_{(s,N_o),X}^2 & -\bar{k}_{(s,N_o),X}\bar{k}_{(s,N_o),Y} & -\bar{k}_{(s,N_o),X}\bar{k}_{(s,N_o),Z} \\ -\bar{k}_{(s,N_o),X}\bar{k}_{(s,N_o),Y} & 1 - \bar{k}_{(s,N_o),Y}^2 & -\bar{k}_{(s,N_o),Y}\bar{k}_{(s,N_o),Z} \\ -\bar{k}_{(s,N_o),X}\bar{k}_{(s,N_o),Z} & -\bar{k}_{(s,N_o),Y}\bar{k}_{(s,N_o),Z} & 1 - \bar{k}_{(s,N_o),Z}^2 \end{bmatrix} \bar{P}_{N_o-1} \quad (5.17)$$

where the relation between the direction cosines [103] is such that

$$\bar{k}_{(s,N_o),X}^2 + \bar{k}_{(s,N_o),Y}^2 + \bar{k}_{(s,N_o),Z}^2 = 1. \quad (5.18)$$

where for the N_o event the direction cosine for the X -axis of the global coordinate system is $\bar{k}_{(s,N_o),X}$ and similarly for the global Y - and Z -axes.

In a similar fashion, we assume that the incident wave vector \mathbf{k}_i has a polarisation \mathbf{P}_i and to undergo successive scattering events at least once from its particle, with the last

particle labelled as N_o , would mean that a multiplicative effect would take place so that the final polarisation vector $\bar{\mathbf{P}}$ from all N_o scattering processes would be obtained from

$$\bar{\mathbf{P}}_{N_o} = \prod_{j=N_o}^1 \mathbf{R}_j(X, Y, Z) \bar{\mathbf{P}}_1 \quad (5.19)$$

where $\mathbf{R}(X, Y, Z)$ is the rotation matrix of Equation 5.17. In our simulation, the direction and polarisation of the scattered wave at each event are determined in the scattering coordinate system. However, for simplicity, the product of the rotation matrices is calculated with respect to the global coordinate system so as to reduce the time required for relating the different local coordinate systems per scattering particle.

Every time a new photon is injected from the origin (Step III), our simulation procedure issues a new orientation for a proportion of ellipsoids, as soon as it finishes its travelling path from the ensemble and exits the total volume of the cuvette (note that in our simulations $V_{total} = 1$ ml). Hence the effect we achieve is an average over several orientations. However, when a photon exits the ensemble it has to be placed in a memory matrix with its intensity value and the direction of travel (Step III.6). This is because we are trying to acquire the intensity of the ensemble in the total volume using discrete events, including the exit of a photon. This is equivalent to sampling from a continuous intensity distribution and we infer the intensity profile by producing histograms of its function. For fully three dimensional systems we need to inject (Step I and II) and store (Step III.6) many photons, in the region of 10^5 or more. As is noted by Walker [126], for an algorithmic procedure of the kind we describe here, convergence of pair separation in conjunction with tabulation of scattering angles requires 10^6 histories for acquisition of an intensity profile at $[0, 40^\circ]$ degrees whilst for $[0, 90^\circ]$ the number of photons emitted must be at least 10^8 . As a result, the computational power needed increases rapidly because of the number of random events and calculations that need to be performed within the ensemble³. As a result, we assume that each ϕ direction exit is equally probable and we only compute the intensity over θ in the range $[0, 2\pi]$. As is customary in all Monte Carlo Markov Chain radiative transfer codes, we normalise the intensity so that

$$\tilde{I} = \frac{I(\theta)}{\lim_{\theta \rightarrow 0} I(\theta) - \lim_{\theta \rightarrow \pi} I(\theta)} = \frac{I(\theta)}{I_{max} - I_{min}} \quad (5.20)$$

and we report our results so that scattering in Figure 5.6 has two curves per experiment with each different number of layers, i.e. for the scattering angle in $[\pi, 2\pi]$ and another curve for $[0, \pi]$. Experiments with different number of layers are denoted by curves that

³If the worst case performance is $\mathcal{O}(N_o^3)$ for computation time then the best case scenario for time needed to store results is $\mathcal{O}(N_o^2)$.

have successively changing lines from solid line to dashed, double dashed and so on, depending on the number of layers. It will become evident that asymmetry in the intensity profile is apparent and there is no need for extra visualization aids.

In Figure 5.6 we have shown results for concentrations of cells in the ensemble as $N_o = 5 \times 10^8$ (top) and $N_o = 50 \times 10^8$ (bottom) where clearly the probability of multiple scattering is expected to be sufficiently high. The size distribution from which we have sampled a size (s) for each of the scattering bacterial cells is the one of Figure 4.9 and for $\kappa_{left} = 0.2$, $\kappa_{right} = 0.1$. In this simulation we assume that we have an ensemble of the same species of bacteria, hence for every experiment the cells have the same number of layers, that is for $n = 2, 3, 4, 5$ and $n = 10$. However the distribution of layers, that is to say their thickness, is produced by using a previously noted procedure: for spheroids of equal dimension on their local coordinate system $a = b = ts$ and $c = s$ where for the axial ratio $t = U(0, 1)$, we assume that the first layer is 0.8 of the total radius whilst the remainder are of uniformly distributed random thickness. A similar procedure is also applied for the relative refractive indices using the rule for each layer of the bacterial cell, $m_k = 1.35 - 0.344U(0, 1)$. For an increase in the number of scattering events, the peak of the intensity at near forward angles decreases, whilst the depth increases. This is expected, since for increased concentrations the scattering intensity will decrease rapidly with respect to that of incidence, as we have mathematically shown in earlier chapters (curves have weaker features, i.e. extrema are ‘washed-out’).

However, at backscattering angles we can still observe some extrema features which may be smoothed out owing to the increased concentrations and multiple scattering, but they are evident up to a limit of ensembles with no more than 5 layers. For additional layers the intensity patterns become featureless, predicting that for example if 10 layers are deployed then the scattering pattern becomes almost flat, with features appearing only in near-forward directions $(0, 30^\circ)$ and $(330^\circ, 360^\circ)$. This illustrates that if one is to use our generalised approximation for densely packed media, then the applicability of our model has a limit of no more than 5 layers, assuming an ensemble where all bacteria are of the same species. Within this limit, inference of optical properties is possible.

As we have noted earlier, every time a photon exits the total scattering volume, a new orientation is assigned for the particles. Hence averaging over all orientations is achieved for the intensity profile. However, note that for the polar patterns for the same number of layers, that is to say for patterns from $(0, 180^\circ)$ and $(180^\circ, 360^\circ)$ shown by the same line style in Figure 5.6. Even though for the same number of layers the magnitude is of the same order, there is an apparent polar asymmetry. Therefore, the orientation effects of the

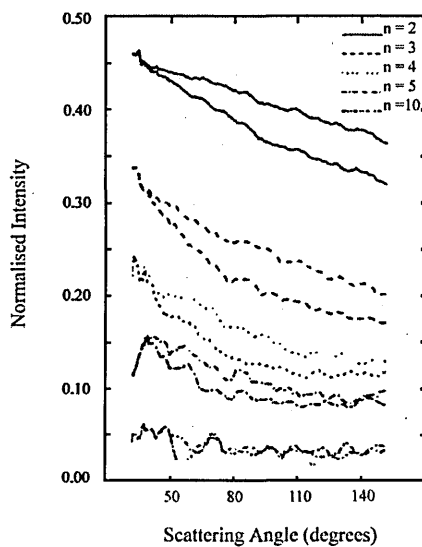
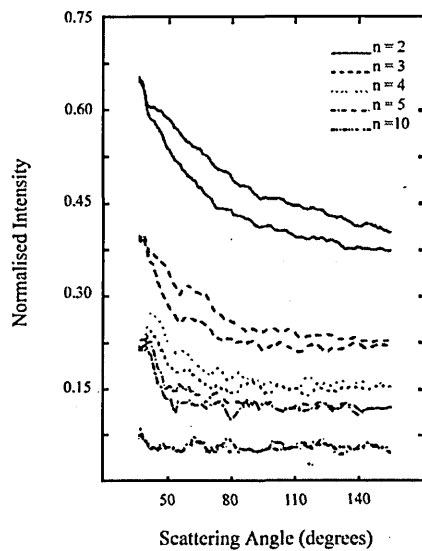


Figure 5.6: Results for the normalised scattered intensity profile as a continuous function approximated from discrete scattering exit events. We have assumed 10^9 injected photons and spheroidal geometry for the bacterial cells. We illustrate results for $N_o = 5 \times 10^8$ at the top and $N_o = 50 \times 10^8$ at the bottom. The ensemble has particles of the same number (n) of layers internal structure; namely $n = 2, 3, 4, 5$ and $n = 10$ indicated by successive lines from solid to increased dotted lines.

spheroidal modelled bacteria seems to be of interest even for high concentrations. Clearly characterisation by means of geometry of the cells is still possible. This finding is in agreement with our finding of Chapter 4, and for asymmetric polar patterns of geometries where the axis of symmetry is less likely to be normal to the incident wave vector. Hence we postulate that for such geometries the curvature faced upon incidence and orientation has a significant effect on multiple scattering. Up to a limit of 5 layers in all scattering particles (i.e. for the same species), this asymmetrical scattering intensity profile would be explored as a possible means of partial identification.

Finally, the width and depth of the intensity cone depends on the distance travelled from the origin to the exit points. We have assumed, in our models for the scattering amplitude, observations in the far field of the exit point of the plane of θ from the random medium. Increasing the number of layers means that, effectively, there are additional shifts within the particle's layers and so the intensity decreases with relation to the mean free pathlength L travelled between scattering events. Unfortunately, due to the fact that the process is stochastic and for each injection of a photon different scattering angles for each particle are selected, we cannot provide a detailed analysis of this relationship and we only report its effect. That is to say, a reduction of the intensity is not only due to number of layers employed but also due to the effect the mean free pathlength has on the intensity.

5.4 Conclusion

In this Chapter we have described mathematically the problem of light scattering in densely occupied media. This is done with particular reference to bacteria in water, hence fulfilling the conditions outlined in Chapter 2. A modelling procedure satisfying these conditions has been provided. Since there is no exact solution to the problem of multiple scattering we have outlined a stochastic procedure for calculating positions of bacteria in a 1ml volume where no binding of cells is expected. To achieve this we have constructed a decision rule with particular reference to ellipsoidal geometries, where the spatial volume occupied by these micro-metre particles is that of a sphere. That is to say, their volume is considered to be the one constructed for the ellipsoid's largest linear dimension enclosed within a sphere of this radius. Hence collision effects are avoided, and there is no binding between particles. This is a minor contribution: the implementation and visualisation of the dense scattering ensembles (Annex D).

The main contribution of this Chapter is our modification of the phase function for

densely packed media. That is to say, using our reasoning method from previous chapters, we have extended this function to apply for relative refractive indices of at least $m < 1.35$, as opposed to $m \rightarrow 1$, by incorporating the average polarisability contribution of the cell and for n -layers. Hence applications of the methods in Chapters 3 and 4 have been rendered possible; that is to say the ensemble's scattering amplitude is considered to be the one outlined in the mathematical expressions for our generalised Rayleigh-Debye approximation and is applied in every scattering event.

This leads us to a major finding: as noted in Chapter 4, asymmetry in the scattering intensity's profile due to orientation and curvature effects is evident, even for this densely populated medium. Hence we propose that, at least theoretically, the asymmetric polar pattern is evident even after the apparent 'wash-out' of distinct features in the light scattering pattern of angular dependence due to increased concentrations. The latter also happens with increasing number of layers employed for each collection of particles in the simulation. This also causes a decrease in the magnitude of the intensity, hence limiting the number of layers that one would use. We suggest that at most 5 layers can be used, enough for characterisation of the bacterium in such media, due to this amplitude decrease.

We have illustrated that, even in high concentrations, it is possible to use the mathematical models, in effect our generalised Rayleigh-Debye approximation, and to infer the optical properties by inference on at most 5 layers. This can be thought of as another minor contribution, since we postulate a departure from the common experimental belief that deploying more than 2 layers in closely packed media does not advance our understanding of the internal composition of the cell.

Chapter 6

Conclusions and further development

The general problem that we have investigated within this thesis can be said to be the modelling of the true physical meaning of the internal composition of bacteria, in terms of scattering in all directions through mathematical simulation, with both deterministic and stochastic elements. Forward scattering has been investigated and seems to offer no contribution towards identification. A similar argument exists for exploration of patterns resulting from different concentrations or from volumetric inference. That is to say, by simply inferring sizes of bacteria, since too many of them present the same volume, then it is not impossible to produce a characterisation or partial identification protocol [27]. Therefore, our research has focused on models that may provide inference of a number of features that have a physical standing; namely the internal structure. As follows from the literature, scattering patterns of angular dependence reveal simplistic internal structures and it is reasonable to assume that following this line of research would lead at least to partial identification.

However, as we have seen in Chapter 2, few studies for bacteria appear where the bacterium is examined as a strongly inhomogeneous particle. Furthermore, limiting cases have been theoretically examined, mainly due to the lack of inhomogeneous models within the *near-index* regime. The commonly used models explore the idea that the biological cell has a limited number of layers. In our work we propose that the bacterial cell must be investigated as an n -layer structure by generalising and extending a modification of the Rayleigh-Debye or Born approximation applicable in the near-index regime, as is the case with bacteria in water based environments.

6.1 Conclusions

In Chapter 2 we have introduced the physiology and biological processes (drinking water ecosystems) in relation to examination of bacteriological content in water based media via light scattering. With this in mind we have also introduced the underlying theory and instrumentation available. It was apparent in the literature that the bacterial cell has a refractive index close to that of water. As a result they can be modelled as near-index cells where absorption can be considered to be negligible. The sizes for bacteria are indeed diverse, but for drinking water, they can be considered to be from approximately $1\mu\text{m}$ to $4\mu\text{m}$. However, solutions in the near-index regime seem not to accommodate these sizes, even though they have been applied in conjunction with light scattering equipment. That is to say, have been successfully applied on the homogeneous model and the simplistic 2-layer model (cytoplasm / cell wall for bacteria or cortex / protoplast for spores). As such, these models can be said to be limiting and have to be extended to incorporate at least most of the dominant features of the cell. Furthermore the spherical models or spherical equivalents do not incorporate physical justification of inferred properties and do not explore the effect of non-sphericity on the scattering patterns.

Following the drinking water ecosystem paradigm we have also found that in the literature there is a call for further examination of the size distributions for modelling populations which must incorporate skewness measures. Another research question is the effect that densely packed media would have on the scattering pattern and how many layers would in theory be applied. Regarding the populations of cells, there exist cases where ambiguous results from light scattering models indicate the need for extension of any mathematical solution to other characteristic external morphologies, as in the case of ellipsoidal particles. This case is particularly evident for spores and coliforms. Finally the assumption of transparency of the particle has to be re-evaluated if one wishes to extend the applicability boundaries of near-index models; incorporation of the average polarisability of the cell within a proposed model would lead to a better understanding of contributions of the internal structure to light scattering.

In Chapter 3 we have analysed and derived a model for bacteria that can be characterised as spherical near-index small particles. In that sense we proposed that the cell has to be modelled as an n -layer spherical structure so as to include the contributions arising from all parts of the cell, in agreement with findings on internal structure from electron microscopy.

The first contribution is our implementation of the computer algorithm for the n -layer

exact solution. From there a major finding is the theoretical verification that, for spheres, patterns of light scattering are symmetric along the scattering angle, irrespective of the number of layers deployed for the internal structure. However for patterns where the wavelength is variable, then within the visible spectrum there seems to be enough information to render possible inference of multiple layers and corresponding optical properties. The implementation of this solution could prove to be an important tool used as a virtual experimental laboratory, as not many computer programs are generally available even though many solutions to the problem have been published. We have used the Matlab technical computing language to do so, and ever since its publication many researchers have either enquired or have been using our code.

The second and major contribution of Chapter 3 is the *generalised solution to the n -layer near index problem* based on modification to the Rayleigh-Debye approximation. Due to the absence of experimental data, we have verified that, at backscattering angles, the popular models of 2-layer Mie and Rayleigh-Debye, our solution, the generalised approximation, behaves much closer to the exact solution compared to the model without a modification. Unfortunately, at forward scattering our model does not yield good results and causes the relative difference from the exact solution to increase since there is a difference of at least 2 orders of magnitude. From the implementation of the n -layer exact solution we have established the limits of our generalised approximation. Hence our third contribution, the generalised Rayleigh-Debye spherical model, with respect to the relative refractive index, covers a significant part of the bacteria domain. Finally, our fourth contribution was an attempt to improve the condition for the relative refractive index from $|m - 1| \ll 1$ to $|m - 1| < 1$ and to incorporate the average weighted polarisability term. It was found that, irrespective of the number of layers we deploy, our mathematical model presents a 19% relative difference from the exact solution when the range of values for the relative refractive index is up to approximately 1.3. This is the reason for our claim that it covers almost the total region of bacteria, since we have already seen in Chapter 2 that most reported values do not exceed the 1.2 limit. Furthermore it is expected that for smaller ranges this relative difference will decrease.

A major finding from this relative difference study shows that the belief that modifying the Rayleigh-Debye approximation will result in a relative difference close to 10% is not true. In fact we have illustrated, by employing multiple layers, that the generalised approximation which is an extended version of the Rayleigh-Debye modification differs from Mie scattering by approximately 20%. However, another significant finding is that, for our model, the generalised Rayleigh-Debye, this may be true but for increased m and r

values. It has been apparent that our model is inferior to the exact solution not necessarily because of increased m values but for consequent increases of size. This validates our earlier claim that smaller values of relative refractive index do appear to decrease the relative difference.

In Chapter 4 we have derived a new model for the ellipsoid and the subcase of spheroids as an n -layered structure. Hence we have provided a contribution in terms of an extension to our generalised near-index approximation from spheres to ellipsoidal geometrical shapes. This contribution is the new method for determining the scattering amplitude or the form factor from particles of no apparent spherical symmetry, as in the case of ellipsoids, and for multi-layered internal structures. This is a significant finding if one considers that, for example, coliforms have been so far modelled as homogeneous bodies and examined using polar patterns of scattering. With our model a new line of research may be opened where the experimental data can now be used for inference of n relative refractive indices.

We have provided a modelling procedure for the population of bacterial cells and through this procedure we illustrate in particular that backscattering effects may lead to real-time characterisation of the internal structure of a bacterium in water. Hence, a contribution that can be said to stem from this Chapter is the new procedure for treating populations of cells that exhibit skewed frequencies of their linear dimension, as long as the condition of independent scattering is satisfied. Hence, this procedure provides the possibility of having samples directly examined before any calibration takes place, by simply selecting only 2 parameters and the expected size average.

A major finding which can be derived from simulation of our mathematical solution is the theoretical justification that differential scattering patterns are heavily dependent upon orientation and the surface that the incident beam will illuminate. We have found that both the azimuthal and the polar angle (θ, ϕ) in an assumed laboratory Cartesian axis system are important. This finding illustrates that since in the three dimensional sense better results may be obtained, a justification for use of instruments that acquire a three-dimensional pattern is provided.

Overall we emphasise that back scattering will play an important role in the characterisation of such particles, even in the case where some axis of symmetry is apparent. As a result, our final contribution in this Chapter is the realisation that the ratio of particular scattering amplitude elements and angular changes at back scattering, may be sufficient for immediately being able to identify how many layers there may be within a sample of bacteria. Thus an extra feature towards partial identification has also been offered.

In Chapter 5 we have described mathematically the problem of light scattering in densely

occupied media. This is done with particular reference to bacteria in water, hence fulfilling the conditions outlined in Chapter 2. A modelling procedure satisfying the previously outlined conditions has been provided.

Since there is no exact solution to the problem of multiple scattering we have outlined a stochastic procedure resembling the Monte Carlo Markov Chain simulation. A minor contribution that stems from this chapter is this very procedure, implementation and visualisation of the dense scattering ensembles, which can be applied to any geometry. This is due to the fact that we have constructed a decision rule, with particular reference to bacteria of ellipsoidal geometry in a 1ml volume where no binding of cells is expected but the distance between them is small enough to increase the probability of multiple scattering. To achieve this, the spatial volume occupied by these micro-meter particles is that of a sphere. That is to say, their volume is considered to be the one constructed for the ellipsoid's largest linear dimension enclosed within a sphere of given radius. Hence collision effects and binding of cells (aggregates) has not been examined.

A major contribution of Chapter 5 is our modification of the phase function for densely packed media and our treatment of multiple scattering within our procedure. That is to say, using our approach from Chapters 3 and 4, we have extended this function to apply for relative refractive indices of at least $m < 1.35$, as opposed to $m \rightarrow 1$, by incorporating the average polarisability contribution of the cell for n layers. This has allowed the methods in Chapters 3 and 4 to be used; that is to say the ensemble's scattering amplitude is considered to be the one outlined in the mathematical expressions for our generalised Rayleigh-Debye approximation and is applied in every scattering event.

This leads to a major finding: as noted in Chapter 4, asymmetry in the scattering intensity's profile due to orientation and curvature effects is evident, even for this dense medium where multiple scattering has a high probability of occurrence. Hence we propose that, at least theoretically, the asymmetric polar pattern is evident even after the apparent 'wash-out' of distinct features in the light scattering pattern of angular dependence due to increased concentrations. The latter is also evident when the number of layers employed for each collection of particles in the ensemble is increased. The latter also causes a decrease in the magnitude of the intensity, hence limiting the number of layers that one would use to at most 5. However, even for this limit, and due to our prior knowledge for the cell, it is evident that characterisation in such media, is possible. Hence, we have provided an extended tool, enhancing the simplistic models of 2 or 3 layers.

Hence, we have illustrated that, even in higher concentrations where smaller separation of pairs takes place, it is possible to use the mathematical models (i.e. generalised

Rayleigh-Debye approximation) and to infer the optical properties by employing at most 5 layers. This signals the final contribution within our work, since we postulate a departure from the common experimental belief that using algorithms that deploy more than 2 layers in closely packed media does not advance our understanding of the internal composition of the cell.

To summarise: applying our models as proposed within, that is to a spherical, ellipsoidal or spheroidal geometrical shape with an arbitrary number of layers, one would first explore the effect of altering the parameters of size overall (s) and per layer (s_i), investigating values for the relative refractive index ($m_i, i = 1, 2, \dots, n$) and then infer, using some test statistic, the best model which may lead to partial identification. To the best of our knowledge we are the first to theoretically examine the cell as a small particle of n -layer structure and to propose such a mathematical extension within the near-index boundaries ($m < 1.35$), at the far-field observation points at distance R (where $R \gg s$).

6.2 Further development

The work described in this Thesis has led to mathematical models for the spherical and ellipsoidal bacterial cell or spore and for populations of bacteria that satisfy or violate the independent scattering condition. Most of the mathematical work that would follow should be within the area of implementing a solution for comma-shaped particles, particles with spherical and/or ellipsoidal inclusions and incorporation of hybrid cores.

That is to say, one would in theory apply the ellipsoidal model that we have provided, and try to solve the problem where the catenary curve is fitted within the kernel of the phase shift, and for the n -layered cell. Hence, in three dimensional space and using the treatment we have illustrated within, we use the equation

$$y = a \cosh \frac{x}{a}$$

to infer the phase shift δ_y over y and by inferring a relationship between this curved ellipsoid over the x -axis, we take infinitesimal cross sections where their plane is parallel to the z -axis and normal to the xy plane. This is not a trivial problem since angular relationships have to be established between the catenary curve and the X and Y axis, as well as with respect to the arbitrary angle of incidence. It may be the case that the problem has no analytic solution, as with the indefinite integral of the super ellipse problem (Section 4.5).

In terms of spherical or ellipsoidal spore inclusions, one would have to calculate from

an integral of the form

$$S_{spore} = \frac{j k_c^3}{2\pi} \hat{a}_i P(\theta, \phi) \exp(jC)$$

where $P(\theta, \phi)$ is the proper amplitude form factor corresponding to the structure of the spore with reference to a local coordinate system with origin at distance C from its centre. Again a procedure has to be constructed so as to incorporate non-symmetrically placed n -layers for both the spore inclusion and the host cell. The procedure is deemed to have no analytical solution for modelling multiple inclusions.

However, one would use a hybrid model, namely an n -layered structure for all parts of the cell using the generalised approximation except for the core, which would be modelled as an ensemble of Discrete Dipoles of different properties. In that sense the internal part would model multiple inclusions that have different optical properties and arbitrary shape. The reader is warned that this procedure may provide difficulties when trying to understand the physical meaning of the cell and its contributions to scattered light. Furthermore, it may prove difficult to keep the computational time required within reasonable limits. It is almost certain that rapid convergence cannot be established.

Another extension of this work may be the stochastic modelling of ensembles that incorporate a time dependent property. That is to say, not to assume that within the ensemble the particles are stationary, but that they are moving in different directions and for random walks, helical motion and Brownian - helical - Brownian combinations. Particular care has to be taken to deal with collisions. That is to say extra criteria have to be set for what happens in the case of collisions of two, three and higher numbers of particles at any given time. We note that the problem is of great biological interest. The same can be said for the cases where some particles form multiple aggregates at different positions, whilst others will continue their free movement. Simulations of this effect may shed light on the process of scattering with time and angular dependence. All these refinements refer to the stochastic simulation process that is provided in Chapter 5, and will lead towards more realistic models for ensembles of bacterial cells.

Most of the experimental work that should follow is to acquire light scattering patterns from several bacteria species and fitting these data to our generalised approximation, so as to infer a number of optical properties for a single cell or populations of cells. Multiple cultures, that is to say, the problem of having multiple species within some total volume, may be of particular experimental interest. By constructing some physical separation procedure, as is the case with size exclusion, applying our models in mixed cultures may be possible. Furthermore, an identification protocol may be possible. We should note that

the production of a library of experimental (raw) data from light scattering experiments that would be publicly available would greatly advance the field of light scattering by small particles as any theory could be directly tested. To the best of our knowledge, no such library exists.

Developing an algorithm that infers models of 2, 3 or more layers, from (raw) light scattering data for the same sample of bacteria, is a fairly straightforward linear or non linear optimisation problem, depending on the objective function to be used. The issue here would be how to decide which model is the best out of a number of candidates. This may be another direction of research which stems from our n -layered models. We advise anyone interested in following this line of research, the employment of inductive learning techniques that incorporate statistical entropy measures, since they will be more sensitive to small changes in a dataset of $[r_i, m_i]$ values. As a result, normal statistical procedures, as is the case with discriminant or logistic functionals and their corresponding decision rules, may fail to incorporate the complexity of the n -layered candidate solution space.

Finally, we have provided, for the mathematical expressions of our models, network graphs comprising a main function, weights and inputs to this function. It is easy to see that in effect one has a stochastic process of Bessel functions. Assuming that we have Bessel functions that take optical properties as 'inputs' and multiply these by the weighted average polarisabilities and the constant terms, then we have a process that is remarkably similar to the one from the neural networks literature. Consequently, by substituting the kernel function of a Radial Basis Artificial Neural Network with that of a Bessel function, and retaining the matrix of weights and corresponding input values, then a close fit of a light scattering pattern from a library of experimental data would be achieved. It is expected that the process would be performed in real time if an adaptive or feedback neural network is used; but now some insight on the physical meaning of the results can be inferred.

References

- [1] M.A. Embrey and R.E. Parkin. *Handbook of CCL Microbes in Drinking Water*. American Public Health Associatio, Washington, 2002.
- [2] A.S. Khan and D.L. Swerdlow. Precautions against biological and chemical terrorism directed at food and water supplies. Technical Report 116, Public Health Report, 2001.
- [3] P.J. Wyatt. Observations on the structure of spores. *Journal of Applied Bacteriology*, 38:47–51, 1975.
- [4] C.F. Bohren and D.R. Huffman. *Absorption and Scattering of Light by Small Particles*. Wiley-Interscience, 1998.
- [5] A.L. Koch. Theory of the angular dependence of light scattered by bacteria and similar sized biological objects. *Journal of Theoretical Biology*, 18:133–156, 1968.
- [6] J.C. Earnshaw and M.W. Steer. *The application of laser light scattering to the study of biological motion*. Plenum - NATO, New York, July 1982.
- [7] R. Nossal. Spectral analysis of laser light scattered from motile organisms. *Biophysical Journal*, 11:341–354, 1971.
- [8] M. Holz and S. Chen. Rotational translational models for interpretation of light scattering spectra of motile bacteria. *Applied Optics*, 17(20), 1978.
- [9] G. Mie. Beitrage zur optic truber madien, speziell kolloidaler metallosungen. *Ann. Phys.*, 25:337–388, 1908.
- [10] W.J. Wiscombe. Improved Mie scattering algorithms. *Applied Optics*, 19:1505–1509, 1980.

- [11] L.S. Clesceri, A.E. Greenberg and A.D. Eaton. *Standard Methods for the examination of Water and Wastewater*. American Public Health Association, Washington, 1998.
- [12] Z. Ulanowski, I.K. Ludlow and W.M.R.S. Waites. Water content and size of spore components determined by laser diffractometry. *FEMS Microbiol. Lett.*, 40:229–232, 1987.
- [13] Z. Ulanowski and I.K. Ludlow. The influence of the cortex on protoplast dehydration in bacterial spores studied with light scattering. *Curr. Microbiol.*, 26:31–35, 1993.
- [14] A.N. Tikhonov and V.Y. Arsenin. *Solutions of Ill-Posed Problems*. Scripta, in Mathematics. Wiley-Hayka, New York, 1977.
- [15] L.P. Bayvel and A.R. Jones. *Electromagnetic Scattering and its Applications*. Applied Science Publishers, London, 1982.
- [16] P.J. Wyatt. *Differential Light Scattering Techniques for Microbiology*, volume 8 of *Methods in Microbiology*, pages 183–263. Academic Press, New York, 1973.
- [17] K. Shimizu and A. Ishimaru. Scattering pattern analysis of bacteria. *Optical Engineering*, 17(2):129–134, 1978.
- [18] Z. Ulanowski, R.S. Greenaway, P.H. Kaye and I.K. Ludlow. Laser diffractometer for single particle scattering measurements. *Measurement Science and Technology*, 13:292–296, 2002.
- [19] P.J. Wyatt. Light scattering and the absolute characterisation of macromolecules. *Analytica Chimica Acta*, 272:1–40, 1993.
- [20] P.H. Sneath. *International Code of Nomenclature of Bacteria: Bacteriological Code*. American Society for Microbiology, ASM Press, Herndon, USA, 1992.
- [21] J.G. Berger and P.H. Sneath. *Bergey's Manual of Determinative Bacteriology*. Williams and Wilkins Publications: Aries Systems, London, 1994.
- [22] S. Cooper. *Bacterial Growth and Division*. Academic Press, New York, 1991.
- [23] M. Klein and T. Furtak. *Optics*. Wiley-Interscience, 1986.

- [24] G.C. Berry. *Light Scattering, Classical: Size and Size Distribution Characterisation*. Encyclopedia of Analytical Chemistry: Instrumentation and Applications. 1998.
- [25] Z. Ulanowski. *Investigations of Microbial Physiology and Cell Structure using Laser Diffractometry*. PhD thesis, Hatfield Polytechnic, Department of Physical Sciences, 1988.
- [26] Z. Ulanowski and I.K. Ludlow. Water distribution, size and wall thickness in *Lycopodon pyriforme* spores. *Mycol. Res.*, 93(1), 1989.
- [27] G.J. Tortora and B.R. Funke. *Microbiology*. Addison Wesley Longman, New York, 7th edition, 1998.
- [28] J. Scaife, D. Leach and A. Galizzi. *Genetics of Bacteria*. Academic Press, London, 1985.
- [29] Malvern Instruments. CGS-3: A goniometric module for light scattering measurements. Technical Report Malvern-MRK493, Malvern Instruments, 2003.
- [30] H.G. Schlegel. *General Microbiology*. Cambridge University Press, London, 1997.
- [31] C.D. Newman. *Measurement of the Scattering Matrix as a means for Bacterial Identification*. PhD thesis, University of New Mexico, 1987.
- [32] A. Diaspro, G. Radicchi and C. Nicolini. Polarised light scattering: A biophysical method for studying bacterial cells. *IEEE Transactions on Biomedical Engineering*, 42(10):1038–1043, October 1995.
- [33] R. Drezek and A. Dunn. A pulsed FDTD method for calculating light scattering from biological cells. *e-Journal of OSA: Opt.Express*, 6(7):147–157, March 2000.
- [34] V.G. Kolinko, F.F.M. de Mul, J. Greve and A.V. Priezzhev. On refraction in Monte-Carlo simulations of light transport through biological tissues. *Med. Biol. Eng. Comput.*, 35:287–288, 1997.
- [35] A. Jones, D. Young, J. Taylor et.al. Quantification of microbial productivity via multi-angle light scattering and supervised learning. *Biotechnology and Bioengineering*, 59(2), 1998.
- [36] A. Hurst and G. Gould. *The Bacterial Spore*, volume 2. Academic Press, London, 1993.

- [37] R. Slepecky and E. Leadbetter. *Mechanisms of resistance and dormancy*, volume 2 of *The Bacterial Spore*, chapter 5, pages 173–209. Academic Press, 1993.
- [38] G. Hobbs and T. Cross. *Identification of endospore forming bacteria*, volume 2 of *The Bacterial Spore*, chapter 2, pages 49–77. Academic Press, 1993.
- [39] W. Jones and H. Weiss. Radiation studies of *B. megaterium* spores. *Dediat. Res.*, 70:657–665, 1977.
- [40] W.D. Donachie and K.J. Begg. Cell length, cell growth and cell division. *Nature*, 264:328–333, 1976.
- [41] V.R. Stull. Size distribution of bacterial cells. *Journal of Bacteriology*, 109(3):1301–1303, 1971.
- [42] J. Cullum and M. Vicente. Cell growth and length distribution of *e. coli*. *Journal of Bacteriology*, 134(1):330–337, 1978.
- [43] A.L. Koch. *The variability of the Bacterium*, volume 2 of *Escherichia Coli and Salmonella Typhimurium*, chapter 101, pages 1606–1614. American Society for Microbiology, Washington DC, 1988.
- [44] J. Ingraham. *Effect of temperature, pH, water activity and pressure on growth*, volume 2 of *Escherichia Coli and Salmonella Typhimurium*, chapter 97, pages 1543–1554. American Society for Microbiology, Washington DC, 1988.
- [45] C.H. Haas. How to average microbial densities to characterize risk. *Water Research*, 30(4):1036–1038, 1996.
- [46] European-Union. Council directive of 9th october 1979: Methods of measurement and frequencies of sampling and analysis of surface water intended for the abstraction of drinking water. *Official Journal of the European Communities*, L(271):44–53, 29 October 1979.
- [47] G. Videen and D. Ngo. Light scattering from a sphere with an irregular inclusion. *JOSA A*, 12(5):922–928, 1995.
- [48] F. Borghese and P. Denti. Optical properties of spheres containing several spherical inclusions. *Applied Optics*, 33(3):484–493, 1994.

- [49] F. Durst and J. Domnick, editors. *Generalised Lorentz-Mie theory for spherical and non-spherical particles with application to phase Doppler anemometry*, 4th International Congress on Optical Particle Sizing. Partec 95, 1995.
- [50] G. Gouesbet and G. Grehan. Generalised Lorentz-Mie theory for assemblies of spheres and aggregates. *J.Opt.A: Pure Appl. Opt.*, 1:706–712, 1999.
- [51] A.L. Aden and M. Kerker. Scattering of electromagnetic waves from two concentric spheres. *J.Appl.Phys.*, 22:1242–1246, 1951.
- [52] M. Kerker. *The Scattering of Light and other electromagnetic radiation*. Academic Press, New York, 1969.
- [53] A. Brunsting and P.F. Mullaney. Scattering of Electro Magnetic waves from two concentric spheres. *J. Appl. Phys.*, 22:1242–1255, 1951.
- [54] A. Brunsting and P.F. Mullaney. Light scattering from coated spheres: model for biological cells. *Applied Optics*, 11:675–680, 1972.
- [55] A.W. Dawkins and N.R. Nightingale. The role of water in microwave absorption by biological material. *Phys.Med.Biol.*, 24:1168–1176, 1979.
- [56] A. Dunn. *Light Scattering Properties of Cells*. PhD thesis, University of Texas at Austin, 1997.
- [57] N.G. Volkov and V.Yu. Kovach. Scattering of light by inhomogeneous spherically symmetrical aerosol particles. *Izvestiya Atmospheric and Oceanic Physics*, 26(5):381–385, 1990.
- [58] Z.P. Wu and Y.P. Wang. EM scattering for multi-layered spheres: recursive algorithms. *Radio Science*, 26:1393–1401, 1991.
- [59] A.Y. Perelman. Scattering by particles with radially variable refractive indices. *Applied Optics*, 35(27):5452–5460, 1996.
- [60] R. Bhandari. Analytic expressions, calculational forms for scattering by a multi-layered sphere. In *SPIE South West Conference in Optics*, volume 540 of *SPIE Proceedings*, pages 500–511. SPIE, 1985.
- [61] P.J. Wyatt and D.T. Phillips. Structure of single bacteria from light scattering. *Journal Of theoretical Biology*, 37:493–501, 1972.

- [62] V.N. Lopatin and F. Sid'ko. Influence of the membrane on the absorption and scattering of light by means of spherical three-layer particle model of cells. *Opt. Spekr.*, 43:930–935, 1977. In Russian: Vliyanie obolochki na oslablenie i rasseyanie sveta sfericheskimi trehslojnymi chastitsami-modelyami kletok.
- [63] V.N. Lopatin and F. Sid'ko. *Introduction to the optics of the suspension of cells*. Nauka, Novosibirsk, 1988. In Russian: 'Vvedenie v optiku vzvesej kletok'.
- [64] J. Wahlberg, S. Tynkkynen and N. Taylor. A novel type of cell wall structure with two periodic layers of *Bacillus sphaericus* strains. *FEMS Microbiology Letters*, 40:75–79, 1987.
- [65] B.T. Draine and P.J. Flatau. Discrete dipole approximation for scattering calculations. *J. Opt. Soc. Am. A*, 11(4):1491–1499, 1994.
- [66] B.V. Bronk, S.S. Druger, J. Czégé and W.P. van de Merwe. Measuring diameters of rod-shaped bacteria in vivo with polarized light scattering. *Biophysical Journal*, 69:1170–1177, 1995.
- [67] B.V. Bronk, Z.Z. Li and J. Czégé. Polarized light scattering as a rapid and sensitive array for metal toxicity to bacteria. *Journal of Applied Toxicology*, 21:107–113, 2001.
- [68] S.D. Druger and B.V. Bronk. Internal and scattered fields in the discrete dipole approximation. *J. Opt. Soc. Am. B*, 16(12):2239–2246, 1999.
- [69] I.C. Felkner and B.E. Worthy. Microbiological detection and quantification of bioactive compounds in vegetation matrix by laser light scattering. *Fresenius' Journal of Analytical Chemistry*, 338:489–494, 1990.
- [70] T. Wriedt. Elastic light scattering theories. *Part.Part.Syst.Charact.*, 15:67–74, 1998.
- [71] B.H. Zimm. The scattering of light and the radial distribution function of high polymer solutions. *Journal of Physics and Colloidal Chemistry*, 16:1093–1116, 1945.
- [72] P. Debye. Molecular weight determination by light scattering. *Journal of Chemical Physics*, 16:1093–1116, 1945.

- [73] J. Jackson, L. Wilson and P.J. Wyatt. Online absolute measurement of radius and molecular weight of polymers using size exclusion chromatography and light scattering. *Journal of Applied Polymer Science*, 45:191–202, 1990.
- [74] P. Latimer, A. Brunsting and B.E. Pyle. Effects of asphericity on single particle scattering. *Applied Optics*, 17(19):3152–3158, 1978.
- [75] A. Rawle. Particle size measurement. *Advances in Colour Science and Technology*, 5(1), 2002.
- [76] Y. Harada, T. Asakura and T. Murakami. Determination of size and refractive index of single spherical particles on the basis of geometrical optics. *Pure Appl. Opt.*, 1, 1992.
- [77] N.V. Voshchinnikov, V.B. Il'in and Th. Henning. Modelling the optical properties of composite and porous interstellar grains. September 2004.
- [78] V. Sethis and P. Patnaik. Evaluation of optical detection methods for waterborne suspensions. *Journal of the American Water Works Association*, 89(2):98–112, February 1997.
- [79] S.E. Harding and P. Johnson. Quasi-elastic light scattering studies on dormant and germinating *Bacillus subtilis* spores. *Biochem. Journal*, 220:117–123, 1984.
- [80] R.G.K. Leuschner and D.P. Ferdinando. Structural analysis of spores of *Bacillus subtilis* during germination and outgrowth. *Colloids and Surfaces B*, 19:31–41, 2000.
- [81] R.G.K. Leuschner and A. Weaver. Rapid particle size distribution analysis of *Bacillus* spore suspensions. *Colloids and Surfaces B*, 13:47–57, 1999.
- [82] Y. Imae and J.L. Strominger. Relationship between cortex content and properties of *Bacillus sphaericus* spores. *Journal of Bacteriology*, 126(2):907–913, May 1976.
- [83] T.C. Beaman and J.T. Greenamyre. Bacterial spore heat resistance correlated with water content, density and protoplast sporeplast volume ratio. *Journal of Bacteriology*, 150(2):870–877, May 1982.
- [84] R.O. Ulloa. *Influence of heterotrophic bacteria and other sub-micrometer particles on light scattering in the ocean*. PhD thesis, Dalhousie University, National Library of Canada, 1993.

- [85] S. Zakovic. *Global optimisation applied to the inverse scattering problem*. PhD thesis, University of Hertfordshire, Department of Physical Sciences, 1997.
- [86] P.J. Wyatt. Differential light scattering: Physical method for identifying living bacterial cells. *Applied Optics*, 7(10), 1968.
- [87] I.S. Grant and W.R. Phillips. *Electromagnetism*. Wiley, 1990.
- [88] P. Newman (Translator). G. Mie(1908): Contributions on the optics of turbid media, particularly colloidal metal solutions. Sandia Laboratories: Translation 79-21946, July 1978.
- [89] R.D. Murch. Extended Born approximation. *Inverse Problems*, 8:L5–L11, 1992.
- [90] T.A. Germer and C.S. Asmail. Goniometric optical scatter instrument for out-of-plane ellipsometry measurements. *Review of Scientific Instruments*, 70:3688, 1999.
- [91] T.A. Germer. Multidetector hemi-spherical polarised optical scattering instrument. *Proceedings of the SPIE*, 3784:304–313, 1999.
- [92] D.L. Haavig and G. Lorden. Method and apparatus for rapid particle identification utilising scattered histograms. European Patent Application: EP 1 367 382 A1, December 2003.
- [93] K. Fukunaga. *Statistical Pattern Recognition*. Academic Press, New York, 1990.
- [94] F.Y. Bois and T. Fahmy. Dynamic modeling of bacteria in a pilot drinking-water distribution system. *Water Research*, 31(12):3146–3156, 1997.
- [95] K. Shimizu. Modification of the Rayleigh-Debye approximation. *J.Opt.Soc.Am. Letters*, 73(4):504–507, 1983.
- [96] P.M.A. Sloot and C.G. Figdor. Elastic light scattering from nucleated blood cells. *Applied Optics*, 25(19):3559–3565, October 1986.
- [97] M. Born and E. Wolf. *Principles of Optics: EM theory of propagation, interference and diffraction of light*. Cambridge University Press, 1997.
- [98] L. Kou, D. Labrie and P. Chylek. Refractive indices of water and ice in the 0.55 to 2.5 micron range. *Applied Optics*, 32:3531–3540, 1993.
- [99] L. Tsang, J.A. Kong and K.-H. Ding. *Scattering of Electromagnetic Waves*. Wiley-Interscience, New York, 2000.

- [100] H.C. van de Hulst. *Light Scattering by Small Particles*. Dover, 1981.
- [101] A. Ishimaru. *Wave Propagation and Scattering in Random Media*. IEEE-OUP, New York, 1997.
- [102] M.R. Spiegel. *Vector Analysis*. McGraw – Hill, New York, 1958.
- [103] W.R. Spiegel and J. Liu. *Mathematical Handbook of Formulas and Tables*. McGraw – Hill, New York, 1999.
- [104] I.K. Ludlow and D. Everitt. Systematic behavior of the Mie scattering coefficients of spheres as a function of order. *Physical Review*, 55(3):2909–2924, 1996.
- [105] S.E. Harding. Microbial laser light scattering. *Biotechnology and Genetic Engineering Reviews*, 14:145–164, April 1997.
- [106] N.V. Voshchinnikov and J.S. Mathis. Calculating cross sections of composite interstellar grains. *Astrophys. J.*, 526:111–125, 1999.
- [107] H.J. Coles, B.R. Jennings and V.J. Morris. Infrared scattering: A method for evaluating the mass and size of bacteria. *Physics in Medicine and Biology*, 20(2):225–234, 1975.
- [108] M. Kerker, W.A. Farone and E. Matijevic. Applicability of Rayleigh-Gans scattering to spherical particles. *JOSA Letters*, 53(6):758–760, July 1963.
- [109] T.L. Farias, U.O. Koylu and M.G. Carvalho. Range of validity of the Rayleigh-Debye-Gans theory for optics of fractal aggregates. *Applied Optics*, 35(33):6560–6567, 1996.
- [110] A.G. Hoekstra and P.M.A. Sloot. *Biophysical and Biomedical Applications of non-spherical Scattering*, pages 585–602. *Light Scattering by Nonspherical Particles*. Academic Press, New York, 2000.
- [111] A.G. Hoekstra and P.M.A. Sloot. Accuracy of (m)RDG calculations of scattering from a sphere. <http://carol.wins.uva.nl/alfons/rdg-vs-mie/rdg.html>, October 2001.
- [112] M. Kerker, D.D. Cooke and H. Chew. Light scattering by structured spheres. *J.Opt.Soc.Am.*, 68:592–599, 1978.
- [113] British Standards ISO. *Particle Size Analysis - Laser Diffraction methods Part I: General Principles*. Number 13220-1. November 1999(E).

- [114] G. Chliveros and M.A. Rodrigues. Matlab implementation of the exact solution, for the n-layer sphere, scattering problem. CVPRAI-TR 01, Sheffield Hallam University, Sheffield, UK, May 2002.
- [115] A.A. Kokhanovsky. *Optics of Light Scattering Media: Problems and Solutions*. Springer-Verlag, London, May 2001.
- [116] V. Sethi. *Experimental Studies in transport of dissolved and suspended contaminants in water distribution systems*. AWWA/USA, University of Cincinnati, 1995.
- [117] A.H. Kvanli and C.S. Guynes. *Statistics: A computer integrated approach*. West Publishing Company, New York, iv edition, 1996.
- [118] N.M. Witriol. Forward scattering and size parameter in layered spherical aerosol particles. *J.Aerosol Sci.*, 23(Suppl.1):349-352, 1992.
- [119] A. Fokas and M. Ablowitz. *Complex variables*. Cambridge University Press, Cambridge, 1997.
- [120] E. Akkermans, P.E. Wolf, R. Waynard and G. Maret. Theoretical study of coherent backscattering of light by disordered media. *J. Phys. France*, 49:77-98, 1988.
- [121] S.A. Prahl and M. Keijzer. A Monte Carlo model of light propagation in tissue. In *SPIE Institute Series*, volume IS 5 of *Dosimetry of Laser Radiation in Medicine and Biology*, pages 102 - 111, 1989.
- [122] C.N. Zeeb and P.J. Burns. Performance enhancements of monte carlo particle tracing algorithms. Technical report, Colorado State University, 2000.
- [123] J.R. Zijp and J. Bosch. Use of cumulative density functions to generate pseudorandom numbers obeying specific distributions for Monte Carlo simulations. *Applied Optics*, 33(3):533-535, 1994.
- [124] W.R. Gilks, S. Richardson and D.J. Spiegelhalter. *Markov Chain Monte Carlo in practice*. Chapman & Hall, Suffolk, 1996.
- [125] W.H. Press and B.P Flannery. *Numerical recipes in C*. Cambridge University Press, New York, 1988.
- [126] P.L. Walker. Modification of Monte Carlo codes for use with sharply peaked phase functions. *Applied Optics*, 32(15):2730-2733, May 1993. Technical Note.

Appendix A

MATLAB Implementation of the n -layer Mie scattering problem

To the best of our knowledge this is the first set of Mie functions to appear, developed in MATLAB (version 6, release 12; ©Mathworks), that tackles the n -layer sphere problem. That is to say it includes functions for the calculation of the Mie coefficients a_n and b_n , efficiencies of extinction, scattering and backscattering, the polarisation ratio and finally the angular scattering elements S_{11} , S_{12} , S_{33} and S_{34} . From the latter, calculation of the light intensity is provided as well as the degree of polarisation. An approximation of the absorption efficiency is also included within (i.e. $Q_{abs} \approx Q_{ext} - Q_{sca}$).

It is assumed that the magnetisation of the particle is governed by the magnetisation of the ambient medium, and as such the magnetic permeability between the particle and the medium is unchanged. Required input parameters is the vector of size parameter ($x = kr$ where $k = 2\pi/\lambda$, λ being the incident wavelength and r the radius vector). The vector of the size parameter has n dimensions, that is to say, as many as the number of layers we employ. Another input is the vector of complex relative refractive indices, corresponding to each of the x -vector values (implied compartments/layers), the angular range in radians ($\theta \in [0, \pi]$) and information about the incident light source; namely the state of polarisation and incident power. All input values must be expressed in the micro units range (e.g. μm , μW).

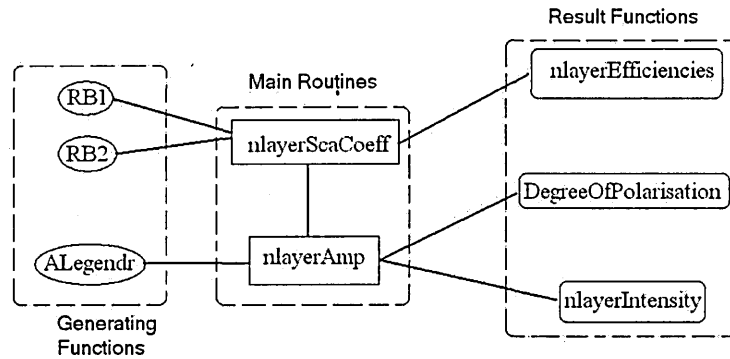


Figure A.1: Structure of interaction between the Matlab functions: Generating Functions → Main Routines → Resulting Functions

A.1 Comments on functions

In terms of the cooperation between the functions and the way they are structured, a generalised view can be seen in Figure A.1. The functions RB1 and RB2 are generating functions to `nlayerScaCoeff`; that is to say, the calculation of the coefficients in the Mie series uses the Ricatti Bessel functions as shown in the corresponding code of Section A.2. Similarly, the Associated Legendre polynomials (function `ALegendr`) are used as a generating function for the calculation of the Scattering Amplitude and the corresponding Scattering Elements (function `nLayerAmp`) in conjunction with the coefficients calculated in the Mie series (function `nlayerScaCoeff`). The number of terms to be calculated obeys the schema described in Equation 3.14 and has been incorporated in `nlayerScaCoeff`. As such the main routines are shown in Figure A.1 to be the Matlab functions `nlayerScaCoeff` and `nLayerAmp`. These main routines provide the results that can be produced using the Resulting Functions: `nlayerEfficiencies`, `DegreeOfPolarisation` and `nlayerIntensity`.

A.2 Generating Functions

A.2.1 The functions RB1 and RB2

```
% RB1 the Ricatti-Bessel function of the first kind
% RB1(rho, nmax) for the value rho from n=1 to n=nmax.
```

```
function phi = RB1(rho, nmax)

rho=rho(:).';

nst = ceil(nmax + sqrt(101+max(rho)));

phi= zeros(nst,length(rho));

phi(nst-1,:) = 1e-10;

for n=nst-2:-1:1
    phi(n,:) = (2*n+3)*phi(n+1,:)./rho - phi(n+2,:);
end

phi0 = 3*phi(1,:)./rho - phi(2,:);

phi0 = sin(rho)./phi0;

phi = phi(1:nmax,:) .* (ones(nmax,1)*phi0);
```

```
=====

% RB2 the Ricatti-Bessel function of the second kind
% RB2(rho, nmax) for the value rho from n=1 to n=nmax.
```

```
function zeta = RB2(rho, nmax)

rho = rho(:).';

zeta = zeros(nmax,length(rho));

zeta(1,:) = -cos(rho)./rho - sin(rho);

zeta(2,:) = 3*zeta(1,:)./rho + cos(rho);

for n=3:nmax
```

```

zeta(n,:) = (2*n-1)*zeta(n-1,:)/rho - zeta(n-2,:);
end

```

A.2.2 The function ALegendr

```

% ALegendr the angular dependent Associated Legendre Polynomials
% [p,t]=ALegendr(ang, nmax)
% produces matrices p and t with rows n=1 to n=nmax
% for pi and tau functions respectively.

function [p,t] = ALegendr(ang, nmax)

p(1,:) = ones(1,size(ang,2));

t(1,:) = cos(ang);

p(2,:) = 3*cos(ang);

t(2,:) = 2*cos(ang).*p(2,)-3;

for n=3:nmax
    p(n,:) = ((2*n-1)*cos(ang).*p(n-1,:) - n*p(n-2,:))/(n-1);
    t(n,:) = n*cos(ang).*p(n,:) - (n+1)*p(n-1,:);
end

```

A.3 Main Routines

A.3.1 The function nLayerAmp

```

% Scattering Amplitude Elements of scattered light.
% nlayerAmp(m,x,Io,ang) returns the scattered Light for
% a sphere, size x, refractive index relative to medium m
% at angle ang.
%

function S = nlayerAmp(m, x, ang)

if length(x)==1
    x = x*ones(size(m));
end if length(m)==1
    m = m*ones(size(x));
end

% criteria for number of terms in Mie Series

```

```

% (Number of coefficients nlayerScaCoeff to be calculated)
% Wiscombe(1980), Applied Optics, 19(9), 1505
nc = ceil(max(x)+4.05*(max(x)^(1/3))+2); n=(1:nc).';

E = ((2*nc+1)/(nc*(nc+1))); [p,t] = ALegendr(ang,nc); W = warning;
warning off [a,b] = nlayerScaCoeff(m,x,nc);
% Check for invalid (NaN) results due to too many terms in
% relatively small particles.
invalid = find(any(isnan([a;b]))); while ~isempty(invalid)
    a(:,invalid) = 0;
    b(:,invalid) = 0;
    nc2 = ceil(max(x(invalid))+4.05*(max(x(invalid))^(1/3))+2);
    [A,B] = nlayerScaCoeff(m(invalid),x(invalid),nc2);
    a(1:nc2,invalid) = A;
    b(1:nc2,invalid) = B;
    invalid = find(any(isnan([a;b])));
    % remove invalidity of zero m or x
    % these _should_ return NaN!
    if length(x)>=max(invalid)
        invalid = invalid(x(invalid)~=0);
    else
        if x==0
            invalid = [];
        end
    end
    if length(m)>=max(invalid)
        invalid = invalid(m(invalid)~=0);
    else
        if m==0
            invalid = [];
        end
    end
end
end warning(W);

a = a.*E; b = b.*E;

% The scattering amplitude functions
S1 = a.'*p + b.'*t; S2 = a.'*t + b.'*p;

% The scattering matrix elements (Mueller Matrix)

S11 = ((S2.*conj(S2))+(S1.*conj(S1)))/2;

S12 = ((S2.*conj(S2))-(S1.*conj(S1)))/2;

```

```

S33 = ((S1.*conj(S2))+(S2.*conj(S1)))/2;

S34 = i*((S1.*conj(S2))-(S2.*conj(S1)))/2;

S = [S11; S12; S33; S34];

```

A.3.2 The function nlayerScaCoeff

```

% Perform calculation of the Scattering Coefficients (Mie Series)
% for the n-layered sphere. Max number of Coeff denoted by nmax
%
%      [a_n,b_n] = nlayerScaCoeff(m,x,nmax,nlayers);
%      x is the vector of size parameter (k.*radius) per compartment relating to
%      the vector of relative refractive indices m function

[a_n,b_n] = nlayerScaCoeff(m,x,nmax,nlayers)

m = m(:).'; x = x(:).'; nlayers = length(x); if length(x)==1
    x = x*ones(size(m));
end if length(m)>1 & length(x)~=length(m)
    error('Dimensions of x & m must be the same or scalar')
end N = ((1:nmax).')*ones(1,length(x));

% Ricatti-Bessel functions

psi = RB1(x, nmax); psim = RB1(m.*x, nmax);

% Ricatti-Bessel function for variable m(k+1)*x(k) of k number of layers

psimKplus1 = zeros(nmax,length(x)); for k = 1:(nlayers-1)
    psimK = RB1(m(k+1)*x(k), nmax);
    psimKplus1(:,k+1) = psimK;
    k=k+1;
end correctpsimn_1 = [0, sin(m(2:nlayers).*x(1:(nlayers-1)))];

% and for (n-1) series terms Ricatti-Bessel

psimKplusln_1 = [correctpsimn_1; psimKplus1(1:(nmax-1),:)];

% Ricatti-Bessel functions

kappa = RB2(x, nmax); kappam = RB2(m.*x, nmax);

```

```

% Ricatti-Bessel function for variable m(k+1)*x(k) of k number of layers

kappamKplus1 = zeros(nmax,length(x)); for k = 1:(nlayers-1)
    kappamK = RB1(m(k+1)*x(k), nmax);
    kappamKplus1(:,k+1) = kappamK;
    k=k+1;
end correctkappan_1 = [0, -cos(m(2:nlayers).*x(1:(nlayers-1)))];
kappamKplus1n_1 = [correctkappan_1;kappamKplus1(1:(nmax-1),:)]; % (n-1) terms

% Hankel function

xi = psi - i * kappa;

% Ricatti-Bessel function for variable m(k+1)*x(k) of k number of layers,
% for (n-1) terms in series

psin_1 = [sin(x);psi(1:(nmax-1),:)]; psimn_1 =
[sin(m.*x);psim(1:(nmax-1),:)]; kappan_1 =
[-cos(x);kappa(1:(nmax-1),:)]; kappamn_1 =
[-cos(m.*x);kappam(1:(nmax-1),:)];

% correction to avoid error in matrix/array dimensions

if length(m)>1
    mm = ones(nmax,1)*m;
end if length(x)>1
    xx = ones(nmax,1)*x;
end

% Calculation of the first derivative of the nth order R-B function

% Refer to Bohren and Huffman (1998), Wiley, pp86-87

dpsi = psin_1-N.*psi./xx; dpsim = psimn_1-N.*psim./(mm.*xx);
correctionA = [ones(1,nmax); (mm(:,2:nlayers).*xx(:,1:(nlayers -
1))).'.']; dpsimKplus1 = psimKplus1n_1 -
N.*psimKplus1./correctionA; dkappa = kappan_1-N.*kappa./xx;
dkappam = kappamn_1-N.*kappam./(mm.*xx); dkappamKplus1 =
kappamKplus1n_1 - N.*kappamKplus1./correctionA; dxi = dpsi - i *
dkappa;

% Main routine. Reference: Volkov and Kovach(1990),
% Izvestiya Atmospheric Oceanic Physics, 26(5), 381-385

```

```

A_k = zeros(nmax,1); B_k = zeros(nmax,1);

for k = 1:(nlayers-1)
    a_k = m(k).*kappam(:,k).*dpsimKplus1(:,k+1) -
        m(k+1).*dkappam(:,k).*psimKplus1(:,k+1);

    dash_a_k = m(k).*kappam(:,k).*dkappamKplus1(:,k+1) -
        m(k+1).*dkappam(:,k).*kappamKplus1(:,k+1);

    b_k = m(k).*dkappam(:,k).*psimKplus1(:,k+1) -
        m(k+1).*kappam(:,k).*dpsimKplus1(:,k+1);

    dash_b_k = m(k).*dkappam(:,k).*dkappamKplus1(:,k+1) -
        m(k+1).*kappam(k).*dkappamKplus1(:,k+1);

    numA_k = (m(k+1).*psimKplus1(:,k+1).*dpsim(k) -
        m(k).*dpsimKplus1(:,k+1).*psim(:,k) + A_k.*a_k);

    denomA_k = (m(k+1).*kappamKplus1(:,k+1).*dpsim(:,k) -
        m(k).*dkappamKplus1(:,k+1).*psim(:,k) + A_k
        .*dash_a_k);

    A_k = numA_k ./ denomA_k;

    numB_k = (m(k+1).*psim(:,k).*dpsimKplus1(:,k+1) -
        m(k).*psimKplus1(:,k+1).*dpsim(:,k) + B_k.*b_k);

    denomB_k = (m(k+1).*psim(:,k).*dkappamKplus1(:,k+1) -
        m(k).*dpsim(:,k).*kappamKplus1(:,k+1) + B_k
        .*dash_b_k);

    B_k = numB_k ./ denomB_k;
end

NUMa_n = psi(:,nlayers) .* (dpsim(:,nlayers) - A_k .*
    dkappam(:,nlayers)) - m(nlayers).*dpsi(:,nlayers) .*
    (psim(:,nlayers) - A_k.*kappam(:,nlayers));

DENOMA_n = xi(:,nlayers) .* (dpsim(:,nlayers) -
    A_k.*dkappam(:,nlayers)) - m(nlayers).*dxi(:,nlayers) .*
    (psi(:,nlayers) - A_k.*kappam(:,nlayers));

NUMb_n = m(nlayers).*psi(:,nlayers) .* (dpsim(:,nlayers) - B_k .*

```

```

dkappam(:,nlayers) - dpsi(:,nlayers) .* (psim(:,nlayers) -
B_k.*kappam(:,nlayers));

DENOMB_n = m(nlayers).*xi(:,nlayers) .* (dpsim(:,nlayers) -
B_k.*dkappam(:,nlayers)) - dxi(:,nlayers) .* (psi(:,nlayers) -
B_k.*kappam(:,nlayers));

% the coefficients...

a_n = NUMa_n ./ DENOMA_n; b_n = NUMb_n ./ DENOMB_n;

```

A.4 End Result Functions

A.4.1 The Function nlayerIntensity

```

%      I = nlayerIntensity(x, m, Io, ang, polarisation);
%
%      Io is the incident light's power.
%      Polarisation is an option for incident light polarisation state
%      as opposed to the reference scattering plane:
%          Polarisation = 0 ==> unpolarised
%          Polarisation = 1 ==> perpendicular
%          Polarisation = 2 ==> parallel

function I = nlayerIntensity(x, m, Io, ang, polarisation)

S = nlayerAmp(m, x, ang);

if polarisation == 0
    % assuming incident light is unpolarised
    I = (1/(max(x))^2) .* S(1,:) .* Io;
elseif polarisation == 1
    % assuming incident light is polarised parallel
    % to the scattering plane
    I = (1/(max(x))^2) .* (S(1,:) + S(2,:)) .* Io;
elseif polarisation == 2
    % assuming incident light is polarised perpendicular
    % to the scattering plane
    I = (1/(max(x))^2) .* (S(1,:) - S(2,:)) .* Io;
end

```

A.4.2 The Function nlayerEfficiencies

```
function [Q_sca,Q_ext,Q_back,Q_abs] = nlayerEfficiencies(m,x)

nc = ceil(max(x)+4.05*(max(x)^(1/3))+2); [a,b] =
nlayerScaCoeff(m,x,nc);

% scattering efficiency
Q_sca = (2/(max(x)^2)) .* (3:2:(2*length(a)+1) .* (abs(a).^2 +
abs(b).^2));

% extinction efficiency
% BEWARE OF THE EXTINCTION PARADOX [Bohren and Huffman 1998, p107]
Q_ext = (2/(max(x)^2)) .* (3:2:(2*length(a)+1) .* (real(a + b)));

% backscatter efficiency
Q_back = (1/(max(x)^2)) .* ((abs(sum((2*length(a)+1) .*
(-1^(length(b))) .* (a - b))))).^2);

% heuristic efficiency for radiation pressure
% (ie the force exerted on the particle by the laser beam)
% Q_h_pressure = Q_ext -
% (4/(max(x)^2)) * (sum( (nc*(nc+2)/(nc+1)) .* real(a .* conj([0 a(nc+1,:)])) +
% b .* conj([0 b(nc+1,:)])) ) + sum((2*nc+1/n^2 + nc) .* real(a.*conj(b))))

% approximate value for the absorption efficiency Q_abs
Q_abs = Q_ext - Q_sca;
```

A.4.3 The Function DegreeOfPolarisation

```
% ratioP = DegreeOfPolarisation(x, m, ang);
%
% Results in ratioP = [magP; P] where
% Polarisation ratio P and Degree of polarisation magP for the scattered light.
%
% In all cases magP <= 1 and P(0)=P(180)=0
% It is known that if
% P > 0 ==> Scattered light is partially polarised parallel to the
% scattering plane
% P < 0 ==> Scattered light is partially polarised perpendicular to the
% scattering plane
```

```

%

function [P, magP] = DegreeOfPolarisation(x, m, ang);

S = nlayerAmp(m, x, ang);

% || scattered irradiance per unit incident irradiance assuming incident light polarised
% perpendicular to the scattering plane
% PerIrradiance = (S(1,:) + S(2,:));
% _|_ scattered irradiance per unit incident irradiance assuming incident light polarised
% parallel to the scattering plane
% ParIrradiance = (S(1,:) - S(2,:));

% Polarisation Ratio
P = - (S(2,:) ./ S(1,:));
% Degree of Polarisation
magP = abs(P);

figure plot(ang, magP)

figure plot(ang, P)

```

A.5 General Comments

It should be noted in this stage that all input parameters have to be expressed in the micro-range. For example and for the input parameter of size x , the wavelength of say $514nm$ has to be re-formulated as $0.514\mu m$. As a result to calculate x at the command prompt one should type

```

>> lambda = 0.514;

>> k = 2 * pi / lambda;

>> r = [1.0 1.1];

```

```
>> x = k .* r;  
>>
```

where the two layered sphere has a core radius of $1\mu m$ and overall radius $1.1\mu m$, i.e. the thickness of the outmost layer is $0.1\mu m$.

The reader is also reminded that MATLAB, calculates angles in radians and as a result all angles must be printed in radians. That is to say, to define the input parameter `theta` one should type

```
>> theta = linspace(0,pi,1000);
```

where a linear space of 1000 discrete values has been generated from 0 to π radians, corresponding to an angle θ of 0° to 180° .

A.6 Calculation of Scattered Intensity

In order to calculate the scattered light intensity from the 2-layer sphere described above, the Matlab function `nlayerIntensity` should be used. However, one must first define the corresponding refractive indices per layer (the remainder of the parameters in the function follow that of Section A.5); an incident laser power (e.g. 2mW) in μW (i.e. 2000) and define the polarisation state. As a result at the command prompt

```
>> m = [1.1 1.3]; Io = 2000;  
  
>> polarisation = 0;  
  
>> I = nlayerIntensity(x, m, Io, theta, polarisation);  
>> logI = log(I);
```

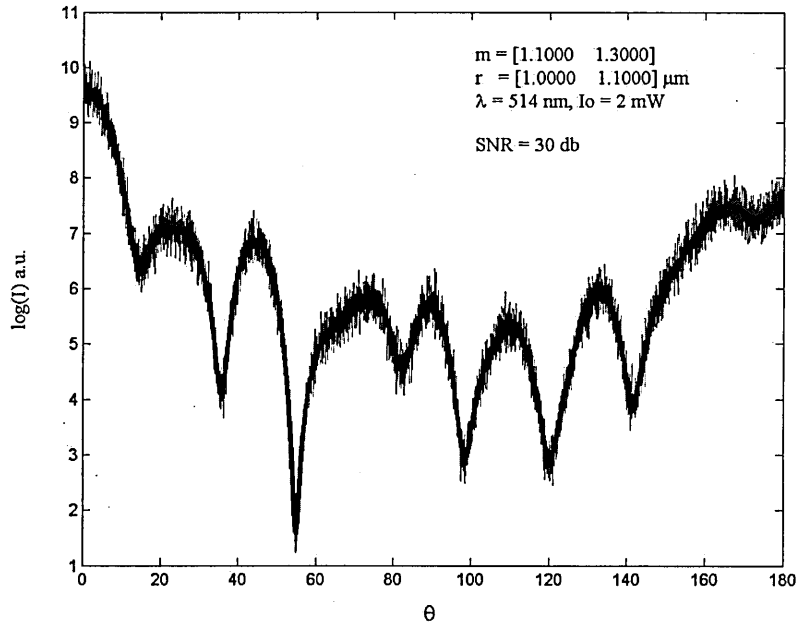


Figure A.2: Example of a 2-layer Mie scattering model for unpolarised incidence.

where the last line has been added so as to emphasize the maxima/minima of the calculated pattern when we need to get a plot. Finally, when we have 'real data' then some noise level is expected, that is to say the signal to noise ratio measured at $\log(I)$ will be assumed to be of some decibels (db). To perform this more realistic depiction, we insert a noise level of 30db and type on the command prompt

```
>> noisyI = awgn(logI, 30, 'measured');
>> plot(ang, logI, ang, noisyI)
```

This results in Figure A.2 where all input parameters as discussed in this chapter have been introduced and the solid line represents the expected Scattered Intensity without noise.

A second example can be seen in Figure A.3. The parameters used are the same apart from the fact that the outer layer is of a thicker (i.e. more dense) composition and so the refractive index is expected to increase. For this example it has been assumed that

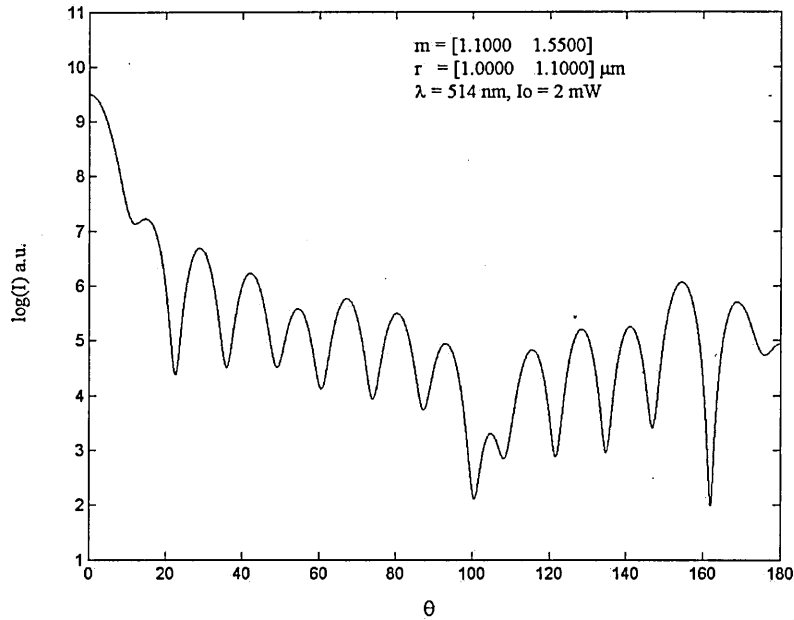


Figure A.3: A 2-layer Mie scattering model for unpolarised incidence but with a denser cell wall.

$m_2 = 1.55$. Note that increasing the outer refractive index resulted in increasing the number of oscillations within the inner cell and as such the number of oscillations that appear in Figure A.3.

A.7 Calculation and Plots for Degree of Polarisation

Using the same values for the input parameters `x`, `m` and `theta` that resulted in Figure A.2, we can now produce a plot of the degree of polarisation and polarisation ratio. That is to say, typing

```
ratioP = DegreeOfPolarisation(x, m, theta);
```

one gets the resulting Figure A.4. According to Figure A.4 (left) and the said in Sections 3.2 and A.6, one would now conclude that a two layer sphere of external radius $1.1\mu m$ and core radius $1\mu m$ of corresponding relative refractive indices of 1.3 and 1.1 respectively, the resulting scattering light will be partially polarised perpendicular to the

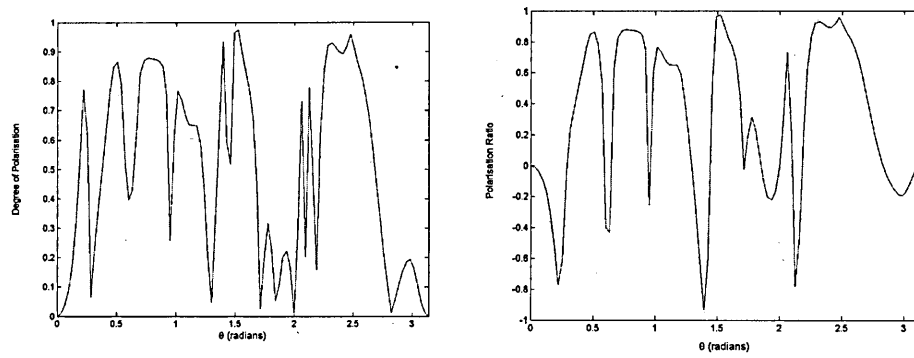


Figure A.4: For a 2-layer Mie scattering model: (Left) The scattered intensity's degree of polarisation; (Right) he scattered intensity's polarisation ratio for 2-layer Mie scattering model.

scattering plane for

$$\theta \in \{[0, 0.3] \cup [0.56, 0.61] \cup [1.36, 1.5] \cup [1.9, 2] \cup [2.08, 2.25] \cup [2.88, 3.12]\} .$$

In all other angular regions the scattered light is partially polarised perpendicular to the scattering plane.

Appendix B

Matlab implementation of a 2-layer model

B.1 Impementation of Wyatt's Rayleigh-Debye model

```
% P.J. Wyatt (1968), App.Opt. 7(10).
% S. aureous (cocci)

fprintf('Structural Information of the Cell... \n')

t = input('cell wall thickness, in micro m : ');

a = input('relative radius of the spherical body, in micro m : ');

m1 = input('nucleus and cytoplasm: relative refractive index (range
from 1.00 to 1.2): ');

m2 = input('cell wall: relative refractive index (range from 1.00 to
1.2): ');

fprintf('Experimental Considerations... \n')

Io = input('power of laser intensity in micro Watt : ');

lamda = input('wavelength in micro m : ');

k = 2*pi/lamda;
```

```

theta = linspace(1,180,91);

theta_rad = (pi/180).*theta;

u = (2*k*a).*(sin(theta_rad./2));

v = (2*k*(a-t)).*(sin(theta_rad./2));

Gu = (3./(u.^3)).*(sin(u)-u.*cos(u));

Gv = (3./(v.^3)).*(sin(v)-v.*cos(v));

R1 = (4/3)*pi*(a^3).*Gu;

R2 = (4/3)*pi*((a-t)^3).*Gv;

ss1 = (k^3).*((m1-1).*R1)+((m2-m1).*R2);

S1 = complex(0, ss1); magS1 = abs(S1);

r = sqrt(a^2-t^2);

IscaWyatt = (Io/(2*((k*r)^2))).*(magS1.^2);

% semilogy(theta,IscaWyatt);
% figure
% semilogy(theta_rad,IscaWyatt);

```

Appendix C

Matlab Implementation of n -layer generalised Rayleigh-Debye models

C.1 Implementation of the n -layer spherical model

We provide the Matlab function for the n -layer spherical model. The programming functions mirror the mathematical expressions of Chapter 2. In as much, we do not go into further explanations or examples as those are reported within the main body of our work. To obtain results please follow procedures similar to those outlined in Appendix A.6.

C.1.1 Finding the coefficients for the Scattering Functions

```
function J = Bessel(m,r,theta)

% The Bessel function of order 2/3, where
% m is the relative refractive index of the ith layer
% and r is the radius of the boundary of the lth compartment

k = 2*pi/0.635;

x = 2*k*m*r.*sin(theta./2);

J = sqrt(2./(pi.*x)) .* ((sin(x) - x .* cos(x)) ./ x);

% =====

function K = Coeff(m,r,theta)
```

```
\% The coefficients to be multiplied on the Scattering Function
```

```
k = 2*pi/0.635;
```

```
K = (m-1) .* sqrt((r./((2*k*m).*sin(theta./2))).^3);
```

C.1.2 The scattering amplitude function

```
function S = nlayerSph(m, r, theta)
```

```
k = 2 * pi / 0.653;
```

```
ang = length(theta);
```

```
n = length(r);
```

```
if length(r) ~= length(m)
```

```
    error('Vectors m and r must have the same dimensions')
```

```
end
```

```
K = zeros(n,ang); G = zeros(n,ang);
```

```
for i = 1:n
```

```
    G(i,:) = Bessel(m(i),r(i),theta);
```

```
    K(i,:) = Coeff(m(i),r(i),theta);
```

```
end
```

```
KG = K .* G;
```

```
Kprevious = zeros(n,ang); Gprevious = zeros(n,ang);
```

```
for i = 2:n
```

```
    Gprevious(i,:) = Bessel(m(i),r(i-1),theta);
```

```
    Kprevious(i,:) = Coeff(m(i),r(i-1),theta);
```

```
end
```

```
KGprevious = Kprevious .* Gprevious;
```

```
Contributions = sum(KG - KGprevious);
```

```
S = [(k*sqrt(2*pi)).*(Contributions)].^2;
```

```
((k*sqrt(2*pi)) .* (Contributions) .* cos(theta)).^2];
```

C.1.3 Calculation of the Intensity

```
% I = nlayerIntensitymRDG(r, m, Io, theta, polarisation);
%
% Io is the incident light's power.
% x is the size parameter given by (2*pi/wavelength).*r
% Polarisation is an option for incident light polarisation
% state as opposed to the reference scattering plane:
%           Polarisation = 0 ==> unpolarised
%           Polarisation = 1 ==> perpendicular
%           Polarisation = 2 ==> parallel

function I = nlayerIntensitymRDG(r, m, Io, theta, polarisation)

k = 2*pi/0.514;

S = nlayerSph(m, r, theta);

R = max(r);

if polarisation == 0
    % assuming incident light is unpolarised
    I = (Io / 2*((k*R)^2)) .* S(1,:) + (Io / 2*((k*R)^2)) .* S(2,:);
elseif polarisation == 1
    % assuming incident light is polarised parallel to the scattering plane
    I = (Io / 2*((k*R)^2)) .* S(2,:);
elseif polarisation == 2
    % assuming incident light is polarised perpendicular to the scattering plane
    I = (Io / 2*((k*R)^2)) .* S(1,:);
end
```

C.1.4 Calculating the Relative Difference: generalised mRDG versus Mie exact solution

```
clc fprintf('THIS WILL TAKE SOME TIME... Please be patient \n')

theta = linspace(0.0175, pi, 91);

k = 2 * pi / 0.635;
```

```

r = linspace(0.5,1.3,15);

nlayers = input('Enter number of layers (integer): ');

nlayers = floor(nlayers);

runs = input('Enter number of runs (integer): ');

runs = floor(runs);

m = linspace(1.005,1.4,15);

error = zeros(length(m),length(r));

m_e = zeros(1,length(m));

for j = 1:length(r)
    for m_values = 1:length(m)
        mlayers = ((m(m_values))-1) .* rand(1, nlayers) + 1;
        m_e(m_values) = mean(mlayers);
        rlayers = zeros(runs, nlayers);
        I_mRDG = zeros(runs,length(theta));
        I_mie = zeros(runs,length(theta));
        I_mie_zero = zeros(1,runs);
        min_I_mRDG = zeros(1,runs);
        for i = 1:runs
            rlayers(i,nlayers) = r(j);
            for l = 1:(nlayers-1)
                index = nlayers-l;
                rlayers(i,index) = rand * rlayers(i,(index+1));
            end

            cd d:\matlabR12\work\nLayersSmRDG
            I_mRDG(i,:) = nlayerIntensitymRDG(rlayers(i,:), mlayers, 200, theta, 0);
            xlayers = k .* rlayers;
            min_I_mRDG(i) = min(I_mRDG(i,:));
            cd D:\matlabR12\work\nLayersMie
            I_mie(i,:) = nlayerIntensity(xlayers(i,:), mlayers, 2000, theta, 0);
            I_mie_zero(i) = nlayerIntensity(xlayers(i,:), mlayers, 2000, 0, 0);
        end

        keeper = abs((log(I_mie) - log(I_mRDG)));
        num_error = (sum(keeper.'));
        den_error = (length(theta)+1) * (log(I_mie_zero) - log(min_I_mRDG));
    end
end

```

```

        run_error = num_error ./ den_error;
        error(j,m_values) = mean(run_error);
    end
    number_iteration = length(r) - j;
    fprintf('processing... Remaining Iterations: %g.\n\n', number_iteration)
end

rel_diff = mean(error); all_rel_diff = mean(rel_diff);
fprintf('END.\b MEAN TOTAL OF RELATIVE DIFFERENCE IS %g.\n', all_rel_diff)

% for better representation we round the error
NewError = error; for i = 1:length(r)
    for j = 1:length(m)
        if NewError(i,j) < 0.1
            NewError(i,j) = 0;
        elseif error(i,j) > 0.1 & error(i,j) < 0.2
            NewError(i,j) = 0.10;
        elseif error(i,j) > 0.2 & error(i,j) < 0.3
            NewError(i,j) = 0.2;
        elseif error(i,j) > 0.3 & error(i,j) < 0.4
            NewError(i,j) = 0.3;
        else
            NewError(i,j) = 0.4;
        end
    end
end

end

% no need to worry about irregularly spaced m,r values
% in response to (error) 10x10 matrix...
% Matlab will take care of it automatically !!!!!
% figure
% contourf(r,m_e,error); colormap gray
% figure
% contourf(r,m_e,NewError); colormap gray

figure contourf(NewError); colormap gray

```

C.2 Implementation of the n -layer ellipsoidal model

C.2.1 The Assymmetric Size Distribution

```
function pD = AsymSizeDistr(D, params)
```

```

%
% SizeDistr(Size, Parameters), is the Asymmetric Size Distribution function.
% This function returns a matrix evaluated at Size values array and with the
% parameters being the three element vector [Do deltaLeft deltaRight].
% To be more specific:
%
% pD = AsymSizeDistr(SizeVariable, [Do deltaL deltaR])
%
% where Do is the average size and delta R and L is the width of the distribution
% (curve) for D < Do and D > Do respectively.
% In general delta is approximately equal to 3*sigma / Do;
% sigma being the variability measure
% of the distribution assuming symmetry...
%

fprintf(' ATTENTION: You must always define the internal variable as
D, in micro meters. \n\n')

if length(params) < 3

    error('The AssymmetricSizeDistribution function needs at least three parameters.');

```

```

elseif D(i) < Do
    Z(i) = 1.0824 * ((D(i) - Do) / (deltaL * Do));
end
end
end

pDo = 0; pD = zeros(1, length(D)); for k = 1:length(D)
    if Z(k) < -1
        pD(k) = pDo;
    elseif Z(k) > 1
        pD(k) = pDo;
    else
        pD(k) = (1 - (Z(k)^2))^4;
    end
end
end

% -----

s_new = sort(s);
Ps_new=zeros(1, sample);

for j=1:sample
    Ps_new(j) = AsymSizeDistr(s_new(j), [1 0.40 0.2]);
end

figure plot(s_new, Ps_new, 'ro')

```

C.2.2 Input estimation functions

```

function K = eCoeff(m,s,t)

% m is the relative refractive index of the compartments
% s is the length of the minor-axis of the ellipsoid form
% t is the axial ratio

k = 2*pi/0.635;

K = 2 * (k^3) * t .* (s.^3) .* (m-1);

%-----

function v = Limits(s_layer, t, alpha, phi, theta)

```

```

% change degrees to radians
alpha = pi .* alpha ./ 180;

theta = pi .* theta ./ 180;

phi = pi .* phi ./ 180;

sqcosinebeta = (-cos(alpha) .* sin(theta./2) + sin(alpha) * cos(phi)
.* cos(theta./2)).^2;

sqsinebeta = 1-(sqcosinebeta);

multiplier = sqrt((t^2) .* sqcosinebeta + sqsinebeta);

v = s_layer .* multiplier;

```

C.2.3 Calculation of Scattering Amplitude and Intensity

```

% s, t, alpha, theta, phi
function S = ScaAmp(s, m, t, alpha, phi, theta)

% orientation of the cell
k = 2*pi/0.635;

K = eCoeff(m,s,t); nlayers = length(s);

KG = zeros(nlayers,length(theta));

for i = 1:nlayers
    v = Limits(s(i), t, alpha, phi, theta);
    u = (2*k*m(i)) .* sin(theta./2) .* v;
    KG(i,:) = K(i) .* ((sin(u) - u.*cos(u)) ./ (u.^3));
end

KGprevious = zeros(nlayers,length(theta));

for i = 2:nlayers
    v = Limits(s(i-1), t, alpha, phi, theta);
    u = (2*k*m(i)) .* sin(theta./2) .* v;
    KGprevious(i,:) = K(i) .* ((sin(u)-u.*cos(u)) ./ (u.^3));
end

Sperp = sum(KG - KGprevious);

```

```

Sparallel = Sperm .* cos(theta);

S = [Sperm; Sparallel];

% -----

function I = nlayerIntensityEmRDG(s, m, t, Io, alpha, phi, theta, polarisation)

%
%
%   Io is the incident light's power.
%   x is the size parameter given by (2*pi/wavelength).*r
%   Polarisation is an option for incident light polarisation
%   state as opposed to the reference scattering plane:
%       Polarisation = 0 ==> unpolarised
%       Polarisation = 1 ==> perpendicular
%       Polarisation = 2 ==> parallel

k = 2*pi/lamda;

S = ScaAmp(s, m, t, alpha, phi, theta);

R = max(s);

if polarisation == 0
    % assuming incident light is unpolarised
    I = (Io / 2*((k*R)^2)) .* abs(S(1,:)) + (Io / 2*((k*R)^2)) .* abs(S(2,:));
elseif polarisation == 1
    % assuming incident light is polarised parallel to the scattering plane
    I = (Io / 2*((k*R)^2)) .* S(2,:);
elseif polarisation == 2
    % assuming incident light is polarised perpendicular to the scattering plane
    I = (Io / 2*((k*R)^2)) .* S(1,:);
end

```

Appendix D

Matlab Implementation of Monte Carlo

The generation of positions in the three-dimensional space of a cubic volume of length ℓ is achieved in this code by employing the Metropolis technique. Due to memory limitations the maximum number of points to be generated is 4000. It starts by issuing initial random positions which are then shuffled to create different realisations. At the final stage of the algorithm the positions are accepted and plotted. However it is assumed that there are no inter-particle forces and inter-penetration is not allowed (see relevant section, Chapter 5).

D.1 Description of the MC algorithm and initial parameters

The experiments are performed on a system of N_o number of particles. These N_o ellipsoids have different sizes and occupy a spherical space of their largest linear dimension. If N_i is the number of particles with largest linear dimension R_i then the number density n_i and fractional volume f_i is

$$n_i = \frac{N_i}{\ell^3} \quad f_i = \frac{4\pi}{3} n_i R_i^3 \quad (\text{D.1})$$

and the total number and fractional volume occupied by the particles is

$$N_o = \sum N_i \quad f = \sum f_i \quad (\text{D.2})$$

The steps that describe the algorithm are

Step I Set initial configuration for the system. All coordinates for the spherical space occupied lie in the range $[0, \ell]$.

Step II Change the system configuration by random displacement of particles sequentially so that: $(x, y, z)_{new} \rightarrow (x, y, z)_{old} + \Delta U(-\ell, \ell)$ where Δ is the maximum displacement allowed to take place. If Δ is too small then most displacements will be accepted; if too large most displacements will be rejected. To avoid this we set the acceptance rate A_c so that: $0.30 < A_c < 0.80$.

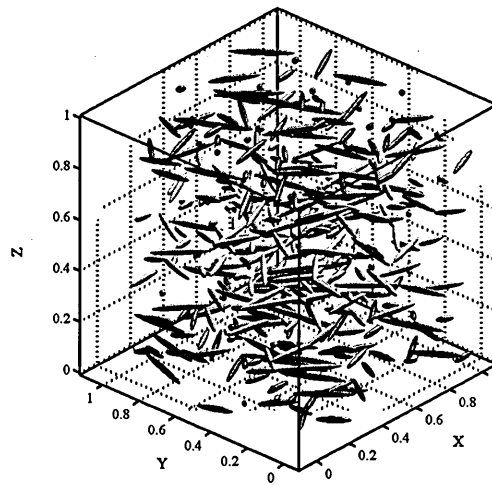
Step III If the displaced particle occupies a spherical space that overlaps with another particle then return to original position. Otherwise:

1. Accept displacement
2. Update the particle's coordinates
3. Calculate distance from closest neighbour.

Step IV Update number of configurations generated.

Step V Count the frequency of occurrence of different pair separations.

At the end of the algorithm several plots are generated. We illustrate here (Figure D.1) the plots of positions with the corresponding ellipsoids. The plot that follows illustrates 400 particles with random orientation in 3D space.



Point Cloud (400 events)

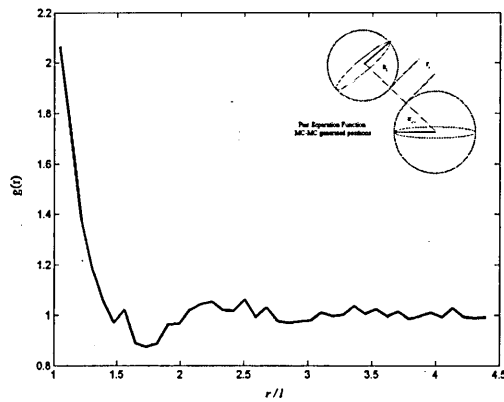
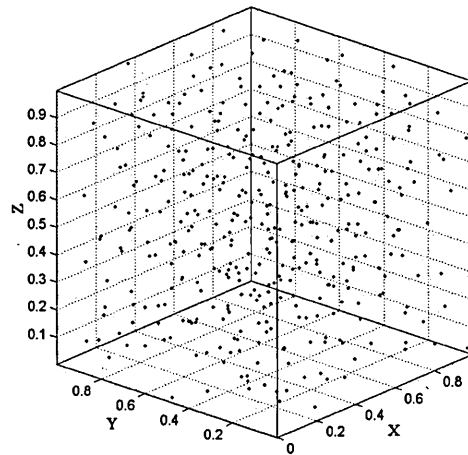


Figure D.1: Positions and ellipsoidal particles generated by the Metropolis MC algorithm. There are 400 particles with maximum acceptance rate set at 60%.

D.2 Matlab code for generation of positions in 3D space

```
%                               montecarloVisual.m
%%
% Main program for the Monte Carlo simulations of pair distribution
% functions and the creation of a series of random realizations of
% particle positions

% with animation,,,,

kk=input('Enter total number of frames : ');

aviobj = avifile('particles.avi','fps',5);

for frame_index=1:kk

% Input Parameters
ntot=input('Enter total number of spheres : ');

fv=input('Enter fractional volume of spheres (< 0.4) : ');

cnst=input('Enter maximum displacement (< 1) : ');

npsr=input('Enter number of passes for each realization : ');

nrlz=input('Enter total number of realizations : ');

seed=input('Enter seed for random numbers : ');

vol=1.0; rho=ntot/vol; da=(6.0*fv/pi/rho)^(1.0/3.0); nd=fix(1.0/da);

ncell=nd*nd*nd;

dl=1.0/nd;

ntpas=npsr*nrlz;

dinc=1.0/ntot/ntpas;

rgmax=5.; srgmax=rgmax*da;

if srgmax >= 0.5
    srgmax=0.5;
```

```

end

rgmax=srgmax/da;

del=cnst*da;

if ncell < ntot
    fprintf('\n Number of Spheres > Number of Cells ==> STOP ! \n');
    break
end

if dl <= da
    fprintf('\n Diameter > Cell Length ==> STOP ! \n');
    break
end

fpos=fopen('pos.dat','w+');

fpdf=fopen('pdf.dat','w+');

% initial regular setting of spheres
xrow=zeros(1,ntot);

yrow=zeros(1,ntot);

zrow=zeros(1,ntot);

da2=ones(ntot,ntot);

da2=da*da*da2;
np=0;

for i=0:nd-1
    if np > ntot
        break
    else
        for j=0:nd-1
            if np > ntot
                break
            else
                for k=0:nd-1
                    np=np+1;
                    if np > ntot
                        break
                    end
                end
            end
        end
    end
end

```

```

else
    xrow(np)=(k+0.5)*dl;
    yrow(np)=(j+0.5)*dl;
    zrow(np)=(i+0.5)*dl;
end
end
end
end
end
end
mg=40; ddcst=4.0*pi*(ntot-1.0)*rho*da*da*da/3.0;
dgr=(rgmax-1.0)/mg; r=zeros(1,mg);
ddr=zeros(1,mg); f=zeros(1,mg);
fnn=zeros(1,mg); g=zeros(1,mg);
for n=1:mg
    r1=1.0+n*dgr;
    rs=r1-dgr;
    r(n)=sqrt((r1*r1+rs*rs)/2.0);
    ddr(n)=r1*r1-rs*rs;
end
rand('seed',seed);
erow=ones(1,ntot); ecol=ones(ntot,1); move=zeros(ntot,1);
stay=ones(ntot,1); rx=zeros(ntot,ntot); ry=zeros(ntot,ntot);
rz=zeros(ntot,ntot); r12=zeros(ntot,ntot); ix=zeros(ntot,ntot);
% initial random setting shuffling
fprintf('\n Initial Shuffling Starts ... \n');
acp=0.0; ovp=0.0;
for ir=1:npsr
    rank=erow-2.0*rand(1,ntot);
    rany=erow-2.0*rand(1,ntot);
    ranz=erow-2.0*rand(1,ntot);
    xtry=xrow+del*ranx;
    ytry=yrow+del*rany;
    ztry=zrow+del*rany;
end

```

```

xtry=xtry-fix(2.0*xtry-erow);
ytry=ytry-fix(2.0*ytry-erow);
ztry=ztry-fix(2.0*ztry-erow);
xtry=xtry-fix(2.0*xtry-erow);
ytry=ytry-fix(2.0*ytry-erow);
ztry=ztry-fix(2.0*ztry-erow);

% check separation between pairs of spheres
rx=xtry'*erow-ecol*xrow;
ry=ytry'*erow-ecol*yrow;
rz=ztry'*erow-ecol*zrow;
rx=rx-fix(2.0*rx);
ry=ry-fix(2.0*ry);
rz=rz-fix(2.0*rz);
rr2=rx.^2+ry.^2+rz.^2;
for i=1:ntot
    rr2(i,i)=da*da;
end
gt=rr2 >= da2;
for i=1:ntot
    move(i)=all(gt(i,:));
end
stay=ecol-move;
xrow=move' .*xtry+stay' .*xrow;
yrow=move' .*ytry+stay' .*yrow;
zrow=move' .*ztry+stay' .*zrow;
for i=1:ntot
    acp=acp+dinc*move(i);
    ovp=ovp+dinc*stay(i);
end
end

fprintf('\n acceptance rate = %8.4f \n',acp);

fprintf(' overlapping rate = %8.4f \n',ovp);

fprintf('\n Initial Shuffling Done !!! \n');

% Monte Carlo shuffling
ir=0; acp=0.0; ovp=0.0;

fprintf('\n Monte Carlo Shuffling Starts ... \n');

for ip=1:ntpas

```

```

ipp=ip-npsr;
while ipp > 0
    ipp=ipp-npsr;
end

ranx=erow-2.0*rand(1,ntot);
rany=erow-2.0*rand(1,ntot);
ranz=erow-2.0*rand(1,ntot);
xtry=xrow+del*ranx;
ytry=yrow+del*rany;
ztry=zrow+del*ranz;
xtry=xtry-fix(2.0*xtry-erow);
ytry=ytry-fix(2.0*ytry-erow);
ztry=ztry-fix(2.0*ztry-erow);
xtry=xtry-fix(2.0*xtry-erow);
ytry=ytry-fix(2.0*ytry-erow);
ztry=ztry-fix(2.0*ztry-erow);

% check separation between pairs of spheres
rx=xtry'*erow-ecol*xrow;
ry=ytry'*erow-ecol*yrow;
rz=ztry'*erow-ecol*zrow;
rx=rx-fix(2.0*rx);
ry=ry-fix(2.0*ry);
rz=rz-fix(2.0*rz);
rr2=rx.^2+ry.^2+rz.^2;
for i=1:ntot
    rr2(i,i)=da+da;
end
gt=rr2 >= da2;
for i=1:ntot
    move(i)=all(gt(i,:));
end
stay=ecol-move;
xrow=move' .*xtry+stay' .*xrow;
yrow=move' .*ytry+stay' .*yrow;
zrow=move' .*ztry+stay' .*zrow;
for i=1:ntot
    acp=acp+dinc*move(i);
    ovp=ovp+dinc*stay(i);
end

% tabulate the occurrence of pair separations
fmn=f;

```

```

rx=xrow'*erow-ecol*xrow;
ry=yrow'*erow-ecol*yrow;
rz=zrow'*erow-ecol*zrow;
rx=rx-fix(2.0*rx);
ry=ry-fix(2.0*ry);
rz=rz-fix(2.0*rz);
rr2=rx.^2+ry.^2+rz.^2;
ix=fix((sqrt(rr2/da/da)-1.0)/dgr)+1;
for i=1:ntot
    for j=1:ntot
        if ix(i,j) >= 1 & ix(i,j) <= mg
            fmn(ix(i,j))=fmn(ix(i,j))+1.0;
        end
    end
end
f=fmn;

if ipp == 0
    ir=ir+1;
    fprintf('\n      realization = %6u \n',ir);
    fprintf('          pass = %6u \n',ip);
    fprintf(' acceptance rate = %8.4f \n',acp);
    fprintf(' overlaping rate = %8.4f \n',ovp);
% output position
    fprintf(fpos,'%6u \n',ir);
    for np=1:ntot
        fprintf(fpos,'%8.4f %8.4f %8.4f \n',xrow(np),yrow(np),zrow(np));
    end
end
end

fprintf(' \n\n');

fprintf(' total acceptance rate = %8.4f \n',acp);

fprintf(' total overlaping rate = %8.4f \n',ovp);

fprintf('\n Monte Carlo Shuffling Done !!! \n');

% output pair distribution function
for jj=1:mg
    g(jj)=f(jj)/ddcst/ddr(jj)/ntpas;
    fprintf(fpdf,'%8.4f %8.4f \n',r(jj),g(jj));
end

```

```

fclose(fpos); fclose(fpdf);

% save the positions of the spheres in 3D space
X = [xrow.',yrow.',zrow.'];
save('Sphere3Dpos.txt','X','-ASCII','-TABS');

% plot all pairs of spheres in 3D space
plot3(xrow,yrow,zrow,'bo') grid on
% and animate
M(frame_index) = getframe;

aviobj = addframe(aviobj,M(frame_index));

% plot pair distribution function
% (requires output of pypdf.m)

load pdf.dat -ascii; figure;

plot(pdf(:,1),pdf(:,2),'b-');

% axis([0.0,5.0,0.0,4.0]);
xlabel('r/d '); ylabel('g(r) ');

legend('Monte Carlo');

end

% end the animating sequence kk

% and preview 10 times at 1 frame per sec

figure grid off axis([0.0,0.2,0.4,0.6,0.8,1]);

xlabel('x'); ylabel('y'); zlabel('z');

box on; movie(M,10,1)

aviobj = close(aviobj); saveas *.avi file

%=====

% Visualise ellipsoids at [xrow, yrow, zrow] from Monte Carlo simulations

```

```
% G. Chliveros, Sheffield Hallam University, MERI,  
% Geometric Modelling & Pattern Recognition Group
```

```
figure
```

```
plot3(xrow,yrow,zrow, '.')
```

```
scale = input('Enter scale of ellipsoid dimension (e.g. 10-3) for  
micrometers): ');
```

```
s = 1.1 * (scale);
```

```
yr = s;
```

```
zr = s;
```

```
for i = 1:length(xrow)
```

```
    t = 0.1 + 12.9 * rand(1,1);
```

```
    xr = t*s;
```

```
    [e1,e2,e3] = ellipsoid(0,0,0, xr,yr,zr);
```

```
    i
```

```
    visual = surf(e1 + xrow(i), e2 + yrow(i), e3 + zrow(i));
```

```
    zdir = [0 0 1];
```

```
    center = [xrow(i) yrow(i) zrow(i)];
```

```
    alpha = 180*rand(1,1)
```

```
    rotate(visual,zdir,alpha,center);
```

```
    for i = 1
```

```
        hold on
```

```
    end
```

```
end
```

Appendix E

Realisation of Experimental Setup

The realisation of the experimental setup is the Great Britain patent application 0406055.4 we have submitted on the 17–th of March, 2004. The patent document outlines a proposed experimental setup with algorithms for data acquisition and preprocessing. The handling of the angular scattering patterns, that is to say, the post-processing, is briefly described and is the n –layered generalised Rayleigh-Debye approximation, our main contribution as outlined in this work.

We have included only the part that state the claims within this patent and a general description. The receipt from our submission the Patent Office is also included.



INVESTOR IN PEOPLE

FILING RECEIPT

Franks & Co
9 President Buildings
Saville Street East
Sheffield
UK
S4 7UQ

The Patent Office

Concept House
Cardiff Road
Newport
South Wales NP10 8QQ

Switchboard: 01633-81400
Minicom: 08459 22250
DX 722540/41 Cleppa Park 3
<http://www.patent.gov.uk>

Your Ref. : MM/P1111

19 March 2004

PATENT APPLICATION NUMBER 0406055.4

The Patent Office confirms receipt of a request for grant of a patent, details of which have been recorded as follows :

Filing Date (See Note)	:	17-MAR-04
Applicants	:	Sheffield Hallam University
Description (No.of Sheets)	:	28
Claims (No.of Sheets)	:	8
Drawings (No.of Sheets)	:	9+9
Abstract	:	1
Statement of Inventorship (Form 7/77)	:	None
Request for Search (Form 9/77)	:	Yes
Request for Examination (Form 10/77)	:	Yes
Priority Documents	:	None
Translation of Priority Documents	:	None
Other Attachments Received	:	None

The application number included in the heading above should be quoted on all correspondence with The Patent Office.

Any queries on this receipt should be addressed to Janine Geran, tel. 01633 814570. All other enquiries should be directed to Central Enquiry Unit, tel. 0845 9 500 505.

Note : The above filing date is provisional and may need to be amended if the provisions of section 15(1) of the Patents Act 1977 are not met.

Claims:

1. Apparatus for particle analysis comprising:

a radiation source;

5

a sample chamber configured to contain a sample, said sample comprising a plurality of particles;

a first array of radiation detectors;

10

a second array of radiation detectors;

said device configured to collect data from said radiation detectors at least at a first time and a second time, wherein said second array occupies a first position at said first time and a second position at said second time;

15

a processor configured to process said collected data, said processing determining at least one predetermined parameter of said particles.

20

2. A device for particle analysis as claimed in claim 1 wherein said radiation source comprises a laser; and

said arrays of radiation detectors are configured to detect visible light.

25

3. A device for particle analysis as claimed in claim 1 or claim 2 wherein each said array of radiation detectors comprises at least one photo-multiplier tube.

30

4. A device for particle analysis as claimed in any preceding claim wherein each said array of radiation detectors comprises:

an array of optical fibres;

a photo-multiplier tube;

means to sequentially connect each optical fibre of said array of optical fibres to said photo-multiplier tube, and collect data at said photo-multiplier tube
5 from each said optical fibre.

5. A device for particle analysis as claimed in any preceding claim wherein said first array of radiation detectors is mounted on a first support, and each radiation detector of said first array of radiation detectors is located at the
10 same distance from said sample chamber;

said second array of radiation detectors is mounted on a second support, and each radiation detector of said second array of radiation detectors is located at the same distance from said sample chamber;
15

6. A device for particle analysis as claimed in any preceding claim wherein said second array of radiation detectors is movable relative to said sample chamber.

7. A device for particle analysis as claimed in any preceding claim wherein said second array of radiation detectors is rotatable about said sample chamber.
20

8. A device for particle analysis as claimed in claim 4 wherein said
25 optical fibres comprise non-coherent polymer fibres.

9. A device for particle analysis as claimed in any preceding claim wherein said predetermined parameter comprises information relating to any one of the following:
30

particle shape

particle size

particle species

particle refractive index

5

refractive index of at least one inferred layer of said particle

particle motion

10 10. A device for particle analysis as claimed in any preceding claim wherein said processing determining at least one predetermined parameter of said particles comprises removing collected data arising from non-motile particles.

15 11. A device for particle analysis as claimed in any preceding claim wherein said processing determining at least one predetermined parameter of said particles comprises comparing a measured predetermined parameter value with a series of predefined parameter values from a database.

20 12. A device for particle analysis as claimed in any preceding claim wherein said processing determining at least one predetermined parameter of said particles comprises:

25 obtaining measured intensity data from said first and second array of radiation detectors

 fitting said measured intensity data to a predicted function of said particles

30 13. A device for particle analysis as claimed in any preceding claim wherein said radiation source is configured to generate radiation at a range of different wavelengths.

14. A device for particle analysis as claimed in any preceding claim wherein said radiation source is configured to generate radiation at a range of different intensities.

5 15. A method of particle analysis comprising:

illuminating a sample with radiation, said sample comprising a plurality of particles;

10 collecting a first data set from a first array of radiation detectors;

collecting a second data set from a second array of radiation detectors;

15 collecting said first data set and said second data set at least at a first time and a second time, wherein said second array occupies a first position at said first time and a second position at said second time;

processing said collected data to determine at least one predetermined parameter of said particles

20

16. A method of particle analysis as claimed in claim 15 further comprising:

providing said illumination using a laser; and

25

said arrays of radiation detectors are configured to detect visible light.

17. A method of particle analysis as claimed in claim 15 or claim 16 wherein each said array of radiation detectors comprises at least one photo-multiplier tube.

30

18. A method of particle analysis as claimed in any one of claims 15 to 17 wherein each said array of radiation detectors comprises:

an array of optical fibres;

a photo-multiplier tube;

5

and said method further comprises sequentially connecting each optical fibre of said array of optical fibres to said photo-multiplier tube, and

collecting data at said photo-multiplier tube from each said optical fibre.

10

19. A method of particle analysis as claimed in any one of claims 15 to 18 comprising:

15 mounting said first array of radiation detectors on a first support such that each radiation detector of said first array of radiation detectors is located at the same distance from said sample;

20 mounting said second array of radiation detectors is on a second support, such that each radiation detector of said second array of radiation detectors is located at the same distance from said sample;

20. A method of particle analysis as claimed in any one of claims 15 to 19 comprising:

25 moving said second array of radiation detectors relative to said sample.

21. A method of particle analysis as claimed in any one of claims 15 to 20 comprising:

30 rotating said second array of radiation detectors about said sample.

22. A method of particle analysis as claimed in claim 18 wherein said optical fibres comprise non-coherent polymer fibres.

23. A method of particle analysis as claimed in any one of claims 15 to 22 wherein said predetermined parameter comprises information relating to any one of the following:

5

particle shape

particle size

10

particle species

particle refractive index

refractive index of at least one inferred layer of said particle

15

particle motion

24. A method of particle analysis as claimed in any one of claims 15 to 23 wherein said processing determining at least one predetermined parameter of said particles comprises removing collected data arising from non-motile particles.

25. A method of particle analysis as claimed in any one of claims 15 to 24 wherein said processing determining at least one predetermined parameter of said particles comprises:

comparing a measured predetermined parameter value with a series of predefined parameter values from a database.

26. A method of particle analysis as claimed in any one of claims 15 to 25 wherein said processing determining at least one predetermined parameter of said particles comprises:

obtaining measured intensity data from said first and second array of radiation detectors

fitting said measured intensity data to a predicted function of said particles

5

27. A method of particle analysis as claimed in any one of claims 15 to 26 comprising illuminating said sample with radiation, said radiation being generated at least at two different wavelengths.

10

28. A method of particle analysis as claimed in any one of claims 15 to 27 comprising illuminating said sample with radiation, said radiation being generated at least at two different intensities.

15

29. A device for particle analysis comprising:

a laser source;

a sample chamber configured to contain a sample comprising a plurality of particles;

20

a first ring,

a second ring;

25

a plurality of radiation detectors disposed on said first ring;

a plurality of radiation detectors disposed on said second ring;

wherein said second ring is rotatable about said sample chamber;

30

means to collect light intensity data from said plurality of radiation detectors

means to process said collected light intensity data to infer information about said particles.

Abstract

METHOD AND APPARATUS FOR PARTICLE ANALYSIS

There is provided a method and apparatus for particle analysis comprising a radiation source, a sample chamber configured to contain a sample, said sample comprising a plurality of particles, a first array of radiation detectors, a second array of radiation detectors, wherein the apparatus is configured to collect data from the radiation detectors at least at a first time and a second time, wherein the second array occupies a first position at the first time and a second position at the second time, and a processor configured to process the collected data, the processing determining at least one predetermined parameter of said particles, such as size, shape, internal morphology or type of particle

15

Fig. 3

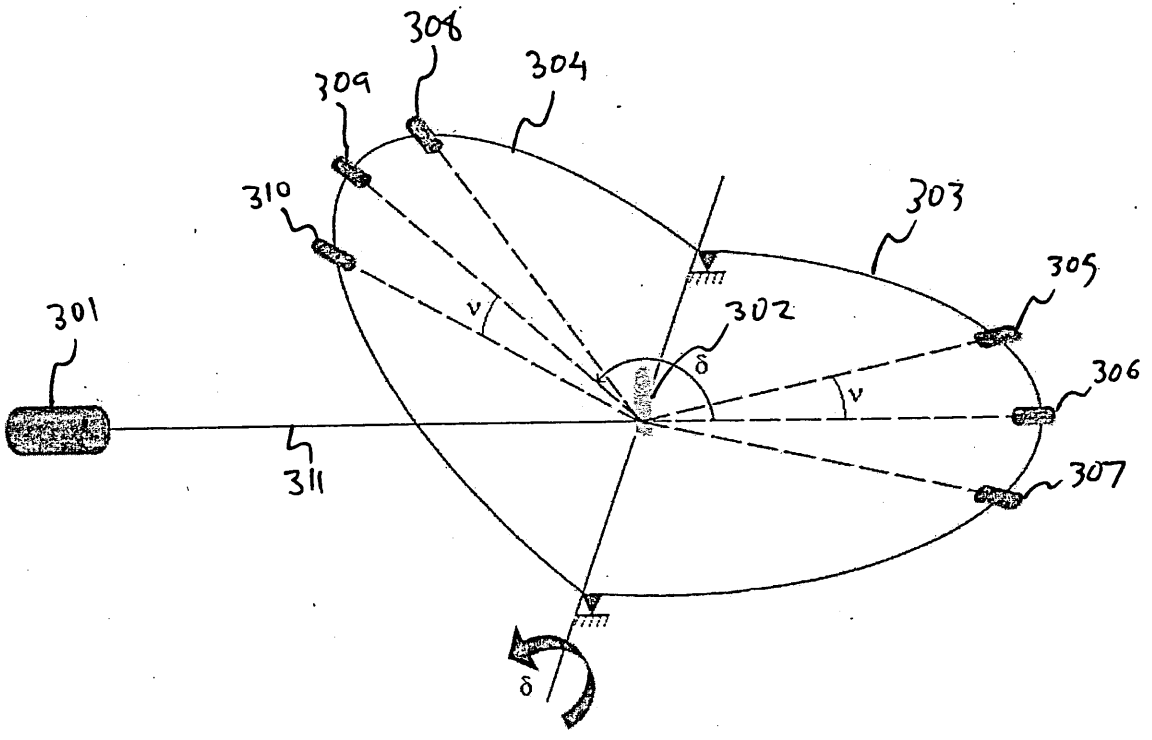


Fig 3